



universität
wien

DISSERTATION / DOCTORAL THESIS

Titel der Dissertation /Title of the Doctoral Thesis

„Measuring and Modelling Night Sky Brightness -
The Impact of Light Pollution“

verfasst von / submitted by

Stefan Wallner, BSc MSc

angestrebter akademischer Grad / in partial fulfilment of the requirements for the degree of
Doktor der Naturwissenschaften (Dr. rer. nat.)

Wien, 2020 / Vienna 2020

Studienkennzahl lt. Studienblatt /
degree programme code as it appears on the student
record sheet:

UA 796 605 413

Dissertationsgebiet lt. Studienblatt /
field of study as it appears on the student record sheet:

Astronomie

Betreut von / Supervisor:

Univ.-Prof. Mag. Dr. Franz Kerschbaum

This is for the man

*who taught me everything,
who brought me everywhere,
who cared for me at every time
and who I loved working with everyday.*

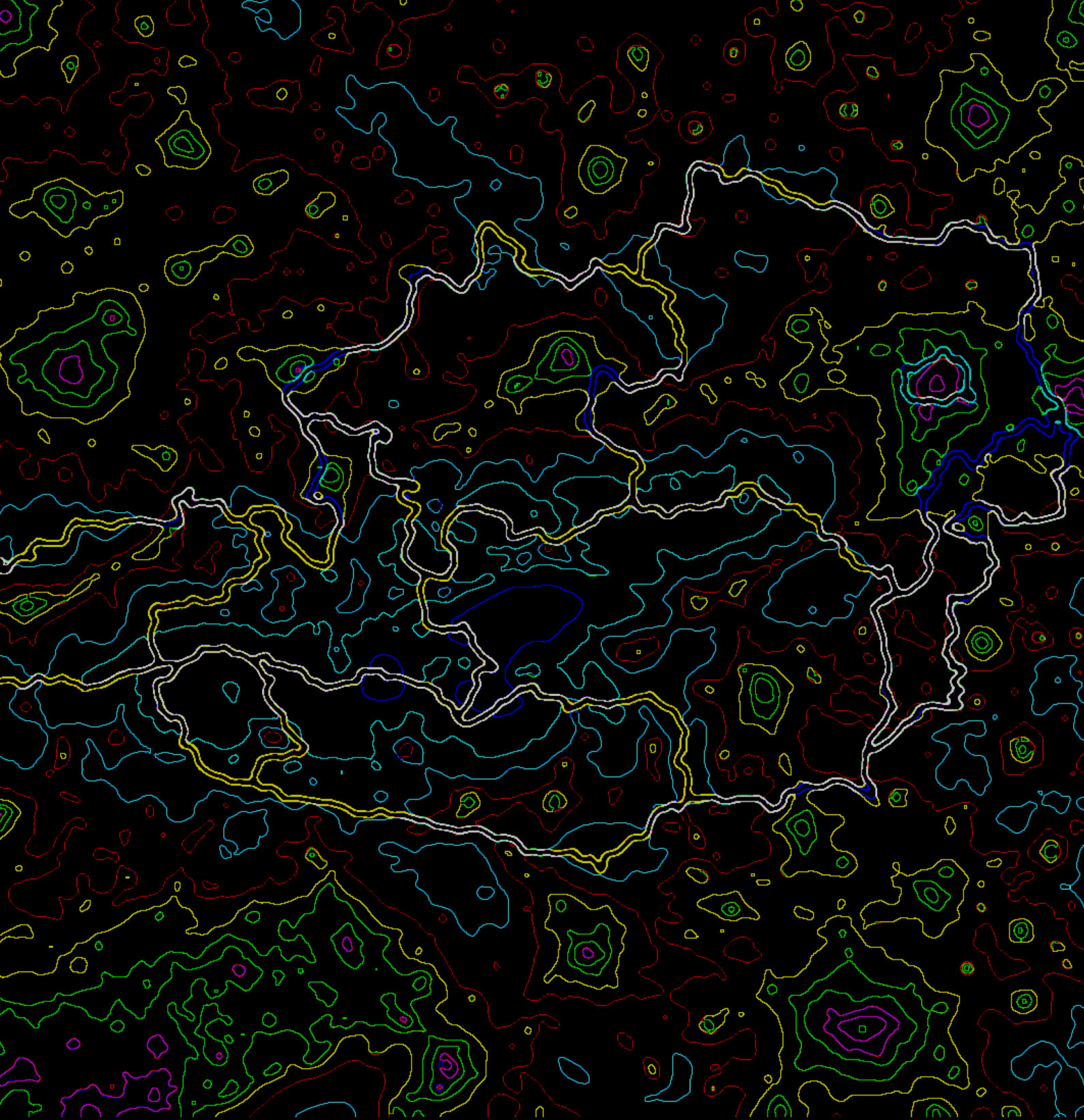
*Thank you for everything, my friend.
May you now rest with the stars you lived and loved.*

Thomas Posch (1974 - 2019)

Contents

1	Introduction	2
1.1	Light and lighting technology	2
1.1.1	Definition and human perception	2
1.1.2	An introduction to lighting engineering	4
1.1.3	History and conversions of lighting systems	9
1.2	Artificial light at night - 'ALAN'	10
1.2.1	What is light pollution?	10
1.2.2	Impacts on astronomy	12
1.2.3	Impacts on human health	13
1.2.4	Impacts on wildlife	14
1.2.5	Impacts on environment & nature	16
1.3	Current status and development	18
1.3.1	Global	18
1.3.2	Special focus on Austria	20
1.4	Potential actions against light pollution	22
1.4.1	Legal situation	22
1.4.2	Environmentally friendly lighting	24
1.4.3	Protection of dark sites	26
2	Measuring Light Pollution	30
2.1	Naked-eye observations	30
2.2	'Sky Quality Meter' and light monitoring networks	32
2.3	All-sky measurements	36
2.4	Vertical fisheye observations	38
2.5	Spectral measurements	39
2.5.1	Influence of various light sources on skyglow	39
2.5.2	Numerical values of spectral impacts	42
2.6	Satellite observations	43
2.6.1	DMSP-OLS	43
2.6.2	NPP-VIIRS	43
2.6.3	Luoja 1-01	44
2.6.4	Comparison	44
3	Modelling Light Pollution	48
3.1	Fundamentals of skyglow modelling I - Basic properties of the atmosphere	48
3.1.1	Aerosols and molecules	48
3.1.2	Scattering orders	51
3.1.3	Light pollution vs. air pollution	53

3.2	Fundamentals of skyglow modelling II - The city emission function	54
3.2.1	Light emitting sources	54
3.2.2	Surface albedo	55
3.2.3	Topography and blockings	56
3.3	Modelling tools	57
3.3.1	Garstang's model	57
3.3.2	ILLUMINA	59
3.3.3	SkyGlow	61
3.3.4	Comparison	63
4	Publications	66
4.1	'An asymptotic formula for skyglow modelling over a large territory'	66
4.2	'Impacts of surface albedo variations on the night sky brightness – A numerical and experimental analysis'	78
4.3	'Usage of Vertical Fisheye-Images to Quantify Urban Light Pollution on Small Scales and the Impact of LED Conversion'	90
4.4	'Circalunar variations of the night sky brightness – an FFT perspective on the impact of light pollution'	116
4.5	'Night sky imaging as potential tool for characterization of total lumen output from small and medium-sized cities'	134
4.6	'Modelled impacts of a potential LED lighting system conversion and the influence of an extremely polluted atmosphere on light pollution in Mexico City'	146
4.7	'Is the lumen output estimate from light-pollution sources suitable for bulk applications if based on population?'	168
5	Conclusions and Outlook	174
5.1	Conclusions	174
5.2	Outlook	175
	References	177
	Acknowledgements	185
	Appendix	186
	Scientific survey towards the establishment of the first official Dark Sky Park in Austria	186
	Reprint Permissions	196
	Curriculum Vitae	197
	Summary	199



INTRODUCTION

1

1 Introduction

1.1 Light and lighting technology

1.1.1 Definition and human perception

The term 'light' marks a multilayered word extensively used in everyday speech. Over time, humans have nurtured a deep attachment to it since it is a byword for emotional connection to commonplace items or emotions. While the sun on the sky, a crackling fire, a gleaming lamp or luminaire are often referred to as 'light', it is also associated with perceptions like brightness, warmth and visualisation. The astronomical reader will further develop this idea and maybe immediately think about its daily work with telescopes, light curves of exoplanets or magnitudes of celestial objects. Nevertheless, even though all those show a logical linking, the true definition of the term 'light' is an essential basis for the science working with and investigating it. Although, this might seem easy to find, some details may differ searching various global sources for information, e.g., online dictionaries. The International Lighting Vocabulary CIE S 017/E:2011 published by the International Commission on Illumination (CIE) provides the definition as:

light

- 1.) characteristic of all sensations and perceptions that is specific to vision;
- 2.) radiation that is considered from the point of view of its ability to excite the human visual system.

To go into more detail of the technical description provided by the CIE, there are three major aspects which determine the definition of light:

i) Light is the part of electromagnetic spectrum visible to the human eye.

Figure 1 illustrates the luminous efficiency functions of the human visual perception. The photopic vision of the human eye is notable for using the cone cells in eye's retinas as photoreceptors. This enables the sense of sight working optimally under well-lit conditions like daylight. An adaptation to such environmental conditions is reaching a luminance of $>30 \text{ cd/m}^2$. The maximum sensibility achieved with photopic vision is reached at 555 nm. Due to the fact that colour perception is the main function of the cone cells, human sensitivity to colour is also at its maximum.

The equivalent to the photopic vision but under dark environmental conditions is the scotopic vision. With an adaption luminance of $<0.01 \text{ cd/m}^2$ its sensibility is shifted to lower wavelengths with the maximum located at 507 nm. Being more sensitive than cone cells, the more intensified use of the rod cells are enabling the adaption under such low light levels. Nevertheless, the colour perception suffers in this process.

By far more complex to retrieve is the luminous efficiency for eyesight at twilight conditions, meaning that an adaption luminance between 0.01 and 30 cd/m^2 is achieved. The sight between photopic and scotopic vision is the mesopic vision and completes the gap between them. Since there are numerous transitions in the usage of cone and rod cells at such conditions, a uniform function is not always readily available (Stockman and Sharpe, 2006). A summary of all illuminance levels compared to processes occurring in the human eye and the resulting visions is illustrated in Figure 2

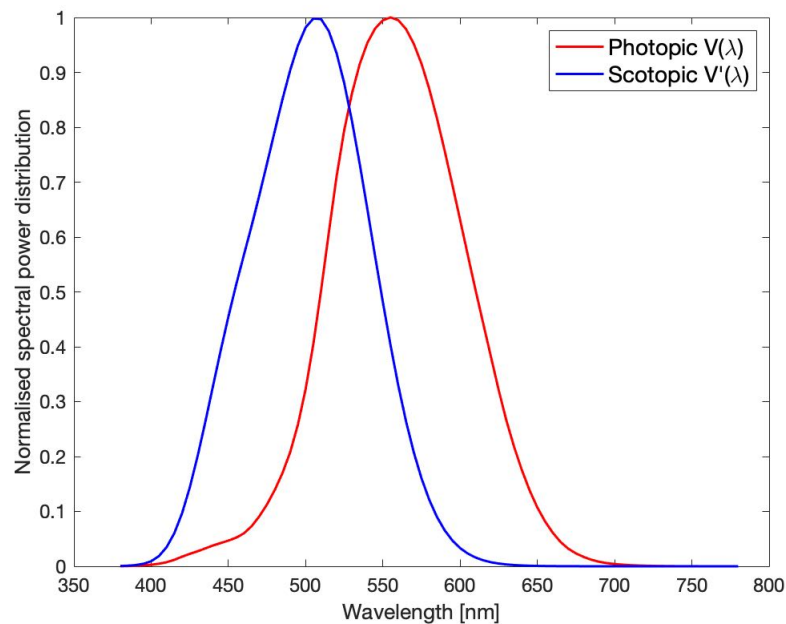


Figure 1 – Luminous efficiency functions of the photopic $V(\lambda)$ -vision under well-lit conditions (red curve) and scotopic $V'(\lambda)$ -vision under low light levels (blue curve). Created by Stefan Wallner. Data obtained from the Lamp Spectral Power Distribution Database (LSPDD) (Roby and Aubé; Aubé et al., 2013).

ii) Wavelength thresholds of visible light range between 380 - 780 nm.

The exact thresholds of visible light to the human eye was very long matter of discussion (Slaney, 2016). With the near-infrared spectral band (IR-A) beginning at 780 nm, the upper threshold of wavelength range was by far not as much a matter of discussion as the lower threshold. Here, human perception seems to overlap with the deep violet UV-A (315-380 nm) between 360 and 400 nm. Still, the International Standards Organization (ISO) published the standard ISO-20473-2007 which clearly separates the two spectral bands, defining the lower threshold as being 380 nm. The CIE standard defining the definitive values of the spectral luminous efficiency functions of the photopic and scotopic vision also provides data in the range of 380 - 780 nm¹.

iii) Light triggers an immediate perception to the (human) visual system.

The third aspect iii) usually plays a tangential role talking about the effects of light. It is clear that a perception of the human visual system is given as soon as something becomes visible solely. Still, as seen above and in Figure 2, light is always connected with the stimulation of physiological processes in the body, with the starting point being the eye. However, this is valid for all living organisms on planet Earth, not only humans. Especially for biological applications, i.e., the perception of animals and nature, which underlie a much higher sensibility in higher wavelengths, the spectral range of infrared radiation was assigned to subclasses (IR-A), (IR-B) and (IR-C) by the CIE and was stan-

¹CIE S 010/E:2004 Photometry - The CIE System of Physical Photometry

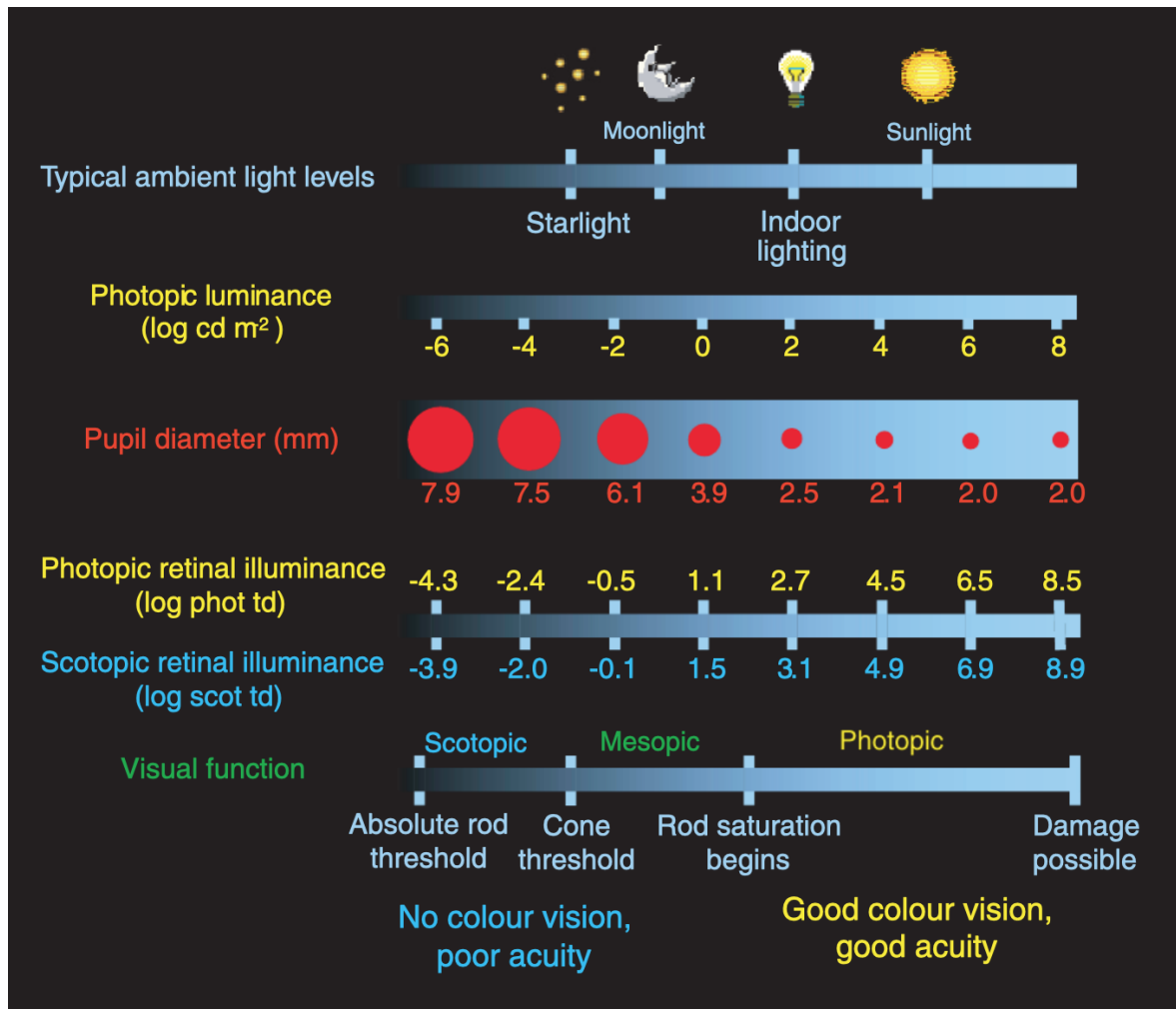


Figure 2 – Comparison of physiological processes and visual functions in the human eye with ambient light levels. From [Stockman and Sharpe \(2006\)](#); [Hood and Finkelstein \(1986\)](#). Reprint with permission.

dardised by the DIN 5031². The ISO 20473³ standard suggests a different classification into the subclasses 'near-infrared' (NIR), 'mid-infrared' (MIR) and 'far infrared' (FIR), commonly used for astronomical purposes. Sections [1.2.3](#), [1.2.4](#) and [1.2.5](#) will discuss the matter of perception in living creatures in more detail.

1.1.2 An introduction to lighting engineering

The aim of the following section is to introduce and characterise the fundamental parameters for light technology. At this point, it is important to do so since the research of light pollution deals with various physical peculiarities originating from lighting engineering not commonly used in astronomy.

²DIN 5031-7:1984-01 Optical radiation physics and illumination engineering; terms for wavebands

³ISO 20473:2007 Optics and photonics - Spectral bands

1.1.2.1 The four fundamental parameters

- Luminous flux Φ

The luminous flux is a parameter which connects the total energy radiated in all directions by a light source and its visual perception. To receive information about the impression of a light source, knowing the total radiant power emitted is not enough since the $V(\lambda)$ -function, discussed in Section 1.1.1, shows a spectral dependency for the human visual system. Therefore, its derivation includes the spectral luminous flux $\Phi_{e,\lambda}$ with regard to a certain wavelength range, and can be written as

$$\Phi = K_m \int_{380\text{nm}}^{780\text{nm}} \Phi_{e,\lambda}(\lambda) V(\lambda) d\lambda, \quad (1)$$

with the result being specified in lumens (lm). Here, K_m characterises a very important physical property, describing the maximum luminous efficacy of the photopic vision which is reached, as a consequence of the $V(\lambda)$ -function, with a monochromatic light emitting source at a wavelength of 555 nm. Its equivalent for the scotopic vision, K'_m , reaches its maximum with a source at 507 nm. Their values as adopted by the CIE and ISO⁴ standards, are as follows

$$K_m \approx 683 \text{ lmW}^{-1} \quad K'_m \approx 1699 \text{ lmW}^{-1}.$$

- Luminous intensity I

The luminous intensity connects the the luminous flux, as defined above, with its emission in a specified direction per unit solid angle Ω (sr). Therefore, its calculation only depends on those parameters, as

$$I = \frac{d\Phi}{d\Omega}. \quad (2)$$

The unit used for I is candela (cd), being part of the International System of Units (SI). The official definition of the candela includes a fixing of its numerical value to 683 for the luminous efficacy of a monochromatic light emitting source, radiating with a frequency of $540 \cdot 10^{12}$ Hz (Newell and Tiesinga, 2019).

- Illuminance E

The illuminance is the total luminous flux radiated onto a specified surface area. Consequently, it is derived as

$$E = \frac{d\Phi}{dA}. \quad (3)$$

Its unit is lux (lx). Since the luminous flux can be transformed to $\Phi = I \cdot Q$ and the solid angle can be seen as surface area dA as part of a spherical cap with distance r , the illuminance can be converted to

$$E = \frac{I \cdot \frac{dA}{r^2}}{dA} = \frac{I}{r^2}, \quad (4)$$

showing that the illuminance is proportional to $1/r^2$.

⁴ISO 23539:2005(E); CIE S 010/E:2004 Photometry - The CIE System of Physical Photometry

- Luminance L

In lighting engineering the luminance is the parameter characterising the impression of brightness perceived by the human eye. Consequently, it is the only value quantifying the visiblence of light to the observer. Its derivation connects the ratio between luminous intensity and light emitting area dA_{rad} , therefore

$$L = \frac{I}{dA_{\text{rad}}}. \quad (5)$$

To go into more detail, its definition also involves that light is emitted by the area dA_{rad} into a specified direction with solid angle $d\Omega_{\text{rad}}$, see Eq. 2. Including the angle α if surface dA_{rad} and radiation direction are not orientated vertically, the standardised definition⁵ of the luminance calculation also includes fluctuations of the luminous intensity in the light emitting area dA_{rad} , it is derived as

$$L = \lim_{d\Omega_{\text{rad}} \rightarrow 0} \lim_{dA_{\text{rad}} \rightarrow 0} \frac{d\Phi}{dA_{\text{rad}} \cdot \cos \alpha \cdot d\Omega_{\text{rad}}} = \frac{d^2\Phi}{dA \cdot \cos \alpha \cdot d\Omega}. \quad (6)$$

Consequently, as seen above, the derivation of the luminance L is no specification of the light emitting source itself, but rather quantifies the illuminated surface. Its unit is candela per square meter (cd/m^2) and can be compared and converted to the astronomical counterpart magnitudes per square arcsecond ($\text{mag}/\text{arcsec}^2$) via

$$[\text{cd}/\text{m}^2] = 10.8 \cdot 10^4 \cdot 10^{-0.4 \cdot [\text{mag}/\text{arcsec}^2]}. \quad (7)$$

1.1.2.2 Luminous efficacy

Lighting type	Luminous efficacy [lm/W]
Tungsten Incandescent	<15
High Pressure Sodium (HPS)*	<140
Low Pressure Sodium (LPS)*	<170
Metal Halide*	<105
Light Emitting Diode (LED)*	<120
Light Emitting Diode (LED)	<200
Maximum for white light	250-370
Monochromatic 555 nm-source	683

Table 1 – Comparison of luminous efficacies of various lighting types. Sources marked by a * are considered as pure streetlighting sources. (Oberösterreichischer Energiesparverband, 2015; Licht-technische Gesellschaft Österreichs, 2012; Murphy, 2012; Pracki, 2011)

As seen above, the luminous efficacy K , or often marked by η in various literature sources, of a lighting system gives valuable information about the energy efficiency. Its unit [lm/W] depicts how a certain luminaire can be characterised, making a clear statement about the lumen output, i.e., luminous flux Φ , with specified power input P , as follows

⁵DIN 5031-3:1982-03 Optical radiation physics and illuminating engineering; quantities, symbols and units of illuminating engineering

$$K = \frac{\Phi}{P}. \quad (8)$$

Consequently, with increasing efficacy the greater the potential for energy savings. Table I demonstrates luminous efficacy values for various lighting types. Especially for Light Emitting Diodes (LEDs) this value highly depends on the spectral power distribution of the emitted light. In comparison to other lighting sources, LEDs can be manufactured with the possibility of dynamically adjust the spectral radiation, i.e., correlated colour temperature.

1.1.2.3 Correlated Colour Temperature

The correlated colour temperature (CCT) represents the temperature of a Planckian radiator, i.e., a hypothetical body with zero reflectance. This body is characterised by its chromaticity being identical to the light source analysed (Valencia et al., 2013). Its definition as registered by the CIE also includes this body being the same brightness and underlies the same viewing conditions as the emitted radiation analysed⁶. Following the Planck radiation law (Planck, 1901), such radiation is defined as

$$I(\lambda, T) = \frac{2\pi hc^2}{\lambda^5} \frac{1}{\exp\left(\frac{hc}{k\lambda T}\right) - 1}, \quad (9)$$

resulting from the constants $h = 6.626 \cdot 10^{-34}$ Js, $c = 2.998 \cdot 10^8$ m/s and $k = 1.381 \cdot 10^{-23}$ J/K. The calculation of the correlated colour temperature is based on the 'CIE 1931 colour space'⁷, connecting the human perception of colour of light with the colour stimuli of the eye. In this diagram, the spectral power distribution as received by an observer, is divided and distinguished in three coordinates quantifying the fundamental colours as specified by the CIE: x (red), y (green) and z (blue), i.e., the 'tristimulus values'. The overarching goal of this categorisation is the characterisation of all colours by the x and y -coordinates of this diagram, as the sum of each part is defined by the white point, being

$$x + y + z = 1. \quad (10)$$

Since the tristimulus values already include the human perception, a tracing back to the colour of the light emitting source can be undertaken by calculating the colour coordinates of the light source X , Y , and Z , respectively. Their derivation include the CIE defined standard observer functions \tilde{x} , \tilde{y} and \tilde{z} , weighing the sensibility of specified colours for the human eye. In general, their derivation (Nassau, 1997) is given by

$$X = k \sum \text{SPD}(\lambda) \tilde{x}(\lambda) R(\lambda), \quad (11)$$

$$Y = k \sum \text{SPD}(\lambda) \tilde{y}(\lambda) R(\lambda), \quad (12)$$

$$Z = k \sum \text{SPD}(\lambda) \tilde{z}(\lambda) R(\lambda), \quad (13)$$

with the constant $k = \frac{100}{\sum P(\lambda) \tilde{y}(\lambda)}$, $\text{SPD}(\lambda)$ being the spectral power distribution of the light source and $R(\lambda)$ a reflectance factor. (Valencia et al., 2013) illustrate a simplification of these calculations to

$$X = K \sum_{\lambda=380\text{nm}}^{\lambda=780\text{nm}} \text{SPD}(\lambda) \tilde{x}(\lambda), \quad (14)$$

⁶VIE/IEC 17.4:1987 International Lighting Vocabulary

⁷CIE 15:2004 Colorimetry

$$Y = K \sum_{\lambda=380\text{nm}}^{\lambda=780\text{nm}} \text{SPD}(\lambda) \tilde{y}(\lambda), \quad (15)$$

$$Z = K \sum_{\lambda=380\text{nm}}^{\lambda=780\text{nm}} \text{SPD}(\lambda) \tilde{z}(\lambda), \quad (16)$$

respectively. Here, K is a constant for the normalisation of Y to 100. With obtained values characterising the emitted light, the tristimulus values can be calculated as

$$x = \frac{X}{X + Y + Z}, \quad (17)$$

$$y = \frac{Y}{X + Y + Z}. \quad (18)$$

As a last step, the correlated colour temperature can be calculated via the approach published by [McCamy \(1992\)](#), as follows

$$CCT = 449n^3 + 3525n^2 + 6823n + 5520, \quad (19)$$

with

$$n = \frac{x - 0.3320}{0.1858 - y}. \quad (20)$$

Figure 3 compares various types of lighting and their correlated colour temperature.

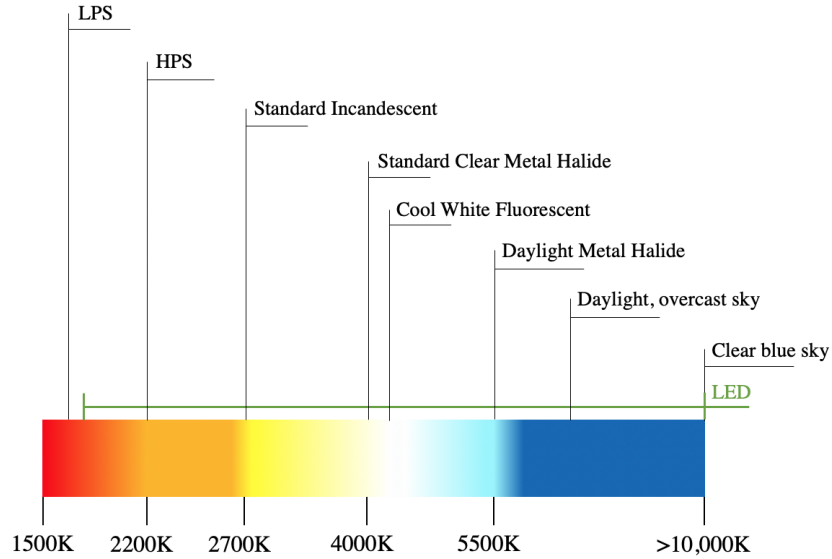


Figure 3 – Comparison of CCT values for various lighting types, including daylight or blue sky. The LED (marked in green) is the only lamp with an adjustable spectral power distribution. Therefore, it enables the possibility of a wide range of colour temperatures for illumination. The value for daylight is an approximated for midday sun, since it depends on location and solar altitude. Created by Stefan Wallner according to [International Dark Sky Association \(2018a\)](#).

1.1.3 History and conversions of lighting systems

The history of illumination, especially focussing on public lighting, shows that the first type of street-lights were oil lanterns, starting in Europe with Paris in 1667. It was installed with the aim of supporting police activities, enhancing of the visibility for pedestrians and to emphasise important sites (Nye, 2018). In 1687, Vienna had adopted a new regulation that obligated to start with the development of an illumination network of tallow candles over the city with 2000 street lamps being installed only one year later (ORF, 2012). The usage of gas and electricity for illumination started in the middle of the 19th century with arc lamps. Since then a large number of different types were manufactured with the goal to increase not only the luminous efficacy but also the durability. Discharging lamps, e.g., the sodium vapour lamp, were established around the 1930s. From a global point of view, the most common lighting types used for street illumination until today are the high pressure sodium lamp (HPS) and the metal-halide lamp (MH).

The history of the invention of the LED started in the early 20th century with the detection of the excitation of inorganic substances when supplying with electrification. this effect was discovered by English engineer Henry J. Round (1881 – 1966) in 1907 (Round, 1907). His finding was revived and reconfirmed in 1921 by Russian scientist Oleg V. Lossev (1903 – 1942). In his publication he discussed the development of a discharge tube with cathodoluminescence of carborundum (Lossev, 1928). As it turned out, his invention should be a forerunner for the modern LED. Naturally, in the course of time some more decisive discoveries were necessary until the first Light Emitting Diode emitting radiation in the visible spectrum at higher wavelengths (red) was manufactured by American engineer Nick Holonyak Jr. in 1962 (Holonyak and Bevacqua, 1962). Until the early 1990s his device was continuously enhances until it was available with a light emission in nearly all colours. The first blue LED (GaN-LED) successfully established in the market for commercial purposes was produced in 1993 by American electrical engineer Shuji Nakamura and Japanese scientists Isamu Akasaki and Hiroshi Amano, receiving the Nobel Price for Physics in 2014 for their development (Royal Swedish Academy of Sciences, 2014).

Today the LED presents the state-of-the-art technology for all areas of application. Currently, as shown in Table I, the luminous efficacy is one of the highest compared to other lighting types. However, even if the efficiency does not reach values of sodium-vapour lamps, the development of the Light Emitting Diode has not yet started to ease off. In fact, its further advancement is one of the uppermost goals in lighting engineering. As also shown above, the theoretical limit of luminous efficacy for LEDs is up to 370 lm/W. Be that as it may, the luminous efficacy solely does not give clear statements about the quality of a lighting source. Even if LPS/HPS lamps show an advantage here, LEDs have far more other benefits, making it by far superior in energy saving purposes: a longer service life (between HPS and LEDs the service life increases by a factor of ~3, the possibility of precise adjustments of targeting light to potential needs and following a reduction of power input, the opportunity to freely choose the colour temperature, low maintenance requirements and the option to dim and immediately switch on or off the light. Compared to lamps of past generations, the energy saving potential of LEDs is at about 60 - 80% (Oberösterreichischer Energiesparverband, 2015).

Already commonly in use for advertising purposes, there is a global trend showing a conversion of outdated street lighting systems to LEDs. Although, its technology is not only a promising approach with encouraging results, it also entails potential threats. Especially the decreasing price of electricity and such benefits as the simple installation or easy operation lead to a serious risk of exaggeration by excessive usage and misapplication. This will be of further discussion in the following Section 1.2

1.2 Artificial light at night - 'ALAN'

1.2.1 What is light pollution?

The term 'light pollution' characterises the influence of artificial light on the natural dark sky. Such phenomenon occurs, if light is emitted to the upward hemisphere (misdirection), if there is an excessive use of light (over-illumination) or usage of environmentally harmful light (impacts by colour temperature).

Light pollution is a worldwide phenomenon and can be dated back at least to the beginning of the 20th century. It is caused by artificial light coming from the ground and comprises phenomena like light trespass, light scattering in the atmosphere and huge 'domes' of light around cities. In 1924, it was Johann Palisa (1848 – 1925), astronomer at the University Observatory of Vienna, who observed nearly four kilometres away from the city centre that if electrical lighting is switched off at midnight normally non-visible stars, that were up to six times fainter, became visible to the naked eye. The original journal article text is shown in Figure 4.

Diese Übelstände wachsen an Stärke von Jahr zu Jahr. Erst besondere Ereignisse bringen dem Beobachter die Steigerung des Übelstandes zum Bewußtsein. So z. B. wurde in Wien vor dem Weltkriege die Ringstraße mit Bogenlampen beleuchtet. Um Mitternacht wurden die Bogenlampen ausgeschaltet, und sofort konnte ich um $1\frac{1}{2}$ bis 2 Größenklassen schwächere Sterne sehen. Ein zweites Ereignis trat im August 1923 ein. Ich hatte im Juli den Planeten 995 [1923 NP] verfolgt und hoffte, auch noch im August ihn sehen und beobachten zu können. Obwohl ich an der richtigen Stelle suchte, konnte ich doch keine Spur von ihm erblicken. Wie erstaunt aber war ich, als mir Dr. Mündler eine ganze Reihe von im August angestellten Beobachtungen desselben Planeten mitteilte. Nun wird jedermann begreifen, wie sehr die Arbeitsfreudigkeit herabgestimmt wird, wenn er sieht, daß der fünfmal mehr Sternlicht auffangende 27-Zöller nicht das zu leisten imstande ist, was der 12-Zöller in Heidelberg leistet. Ich fing an zu glauben, daß meine Sehkraft nachgelassen habe, aber auch das ist nicht der Fall, denn vergleichende Beobachtungen mit einem jüngeren Kollegen, der auch auf schwache Sterne eingeübt ist, ergaben, daß ich immer noch schwächere Sterne wahrnehmen kann. Solche Wahrnehmungen bringen den Beobachter immer wieder auf den Gedanken, daß die Wiener Sternwarte mit ihrem großen Refraktor heute nicht mehr auf dem richtigen Platze steht, und daß es an der Zeit ist, an ihre Verlegung zu denken und zu schreiten.

Wien, 1924 Mai. J. Palisa.

Figure 4 – [Palisa \(1924\)](#) about observations with the 27-inch refractor at the University Observatory Vienna and his recognition about the upcoming light pollution. Translated and reproduced with permission.

[...] The disadvantages are increasing from year to year. Only special events demonstrate its growth rate to the observer. As an example, before the outbreak of the world war, Vienna's ring road was illuminated with arc lamps. At midnight, they were switched off and immediately I was able to see stars being fainter by 1.5 to 2 magnitudes. A second event happened in August 1923. In July I followed the planet 995[1923NP] and hoped to see him in August also. Although, I was searching on the right spot, I was not able to trace him again. How surprised I was, when Dr. Mündler showed a whole string of observations of the same planet from August to me. Now, everybody will understand how the job satisfaction is lowered by knowing that the 27-inch refractor, normally detecting five times more starlight, cannot achieve the same as the 12-inch refractor in Heidelberg. I started to believe it was my visual acuity decreasing, but that is not the case, since similar observations together with a younger colleague, who is experienced in seeing faint stars, showed I was still able to see fainter stars. Such awarenesses suggest to observers the idea that the Vienna Observatory with its large refractor is not in the right place any more and that it is time to think about its relocation and leave. Vienna, 1924 May. J. Palisa.

As the example of Palisa's observation shows, light pollution is a result of anthropogenic activity. Although, it is also a hint for energy wasting and badly installed lightings, it is a threat widely not dealt with since the potential causes, e.g., on human health, are in the long term. However, the increase of areas suffering from artificial light at night was accelerated growing in the near past and still is. Consequently, due to their nighttime environments becoming continuously brighter, people are more and more becoming aware of the phenomenon.



Figure 5 – Examples for streetlights causing light pollution. Left: Illumination of a street by HPS lamps with disturbing glare. Right: Ball light emitting light to nearly all directions, especially to the upper hemisphere. Source: Andreas Hänel, Vereinigung der Sternfreunde - Fachgruppe Dark Sky.

Light pollution is most conspicuous in densely populated areas such as Vienna and its surroundings. Without any light emitting sources, clear night skies provide a measured brightness of approximately $21.8 - 22 \text{ mag arcsec}^{-2}$, Vienna's sky in comparison has at best $18.5 - 19.0 \text{ mag arcsec}^{-2}$ which means a brightness difference of a factor 25 (as a result of the logarithmical definition of astronomical magnitudes). Figures 5 and 6 illustrate examples of various sources producing strong impact on light pollution.



Figure 6 – Examples for illuminated buildings causing light pollution by light going past the facades. Left: Illumination the Business Tower Nürnberg, Germany. Right: Illumination of a church. Source: Andreas Hänel, Vereinigung der Sternfreunde - Fachgruppe Dark Sky.

But light pollution would be a much smaller problem if it were only affecting stellar visibility. It also has life changing impacts on us humans and the wildlife as described by [Posch et al. \(2010\)](#). Since billions of years, life on Earth has adapted to the periodic change of day- and night-time and thus all organisms adopted to this so called 'circadian rhythm'. We as humans for example use the day as an active period while we regenerate at nights for which the hormone melatonin is necessary. It can only be produced in the dark. Light pollution and especially blue parts of the emitting spectrum of lighting prevent the synthesis of this hormone, which is a huge issue for human health. This results for example in more cases of breast- and prostate-cancer of people living in light polluted cities. Animals too are facing many problems with this phenomenon, e.g., migratory birds who get irritated by artificially lit buildings and sea turtles who are attracted to light sources. In both cases the death toll can amount to many thousands of individuals per year and per country.

Sections [1.2.3](#), [1.2.4](#) and [1.2.5](#) discuss influences of ALAN on humans, wildlife and environment in more detail. The work presented in Section [4.3](#) discusses a possibility of quantifying the impact of light pollution by such cases and also characterises the conversion of HPS to LEDs lamps of a city.

1.2.2 Impacts on astronomy

The daily astronomical work suffers from light pollution impacts significantly. As mentioned above, artificial light at night causes, if used in a negligent behaviour, an addition to the natural brightness of the night sky. As discussed later in Section [2.1](#) in more detail, with increasing luminance the less celestial objects are visible to either the naked eye or any other kind of observational detector. Compared to the human eye, astronomical telescopes use larger detector areas aiming to amplify the amount of photons captured, with the consequence of more and more collected artificial light also, becoming prohibitive due to saturation of observations. Such detrimental effects can occur very rapidly, since the loss of visibility is rising exponentially compared to sky brightness magnitudes, as Figure [7](#) illustrates the number of visible stars of the Northern hemisphere compared to the level of light pollution. It is shown that with every magnitude of increasing sky brightness the number of stars still apparent to the human eye is approximately halved.

The International Astronomical Union (IAU) classifies dark skies for existing or planned telescopes in three categories:

A class: telescopes with apertures greater than 6.5 m are already available. The zenith of the night sky is defined as being not effected by light pollution.

B class: telescopes with apertures greater than 6.5 m are in planning or under construction. Also here, the zenith shows no influence do to light pollution.

C class: telescopes with apertures greater than 2.5 m are operating and the zenith shows a slight increase in brightness due to light pollution but less than gained naturally caused by the solar cycle.

All three classes are barely existing in, e.g., Europe or North America, see more in Section [1.3](#). In conclusion, the daily astronomical work is severely restricted due to the impact of ALAN. Locations far away from existing infrastructures have to be chosen as observation sites for telescopes to evade the influence of light pollution.

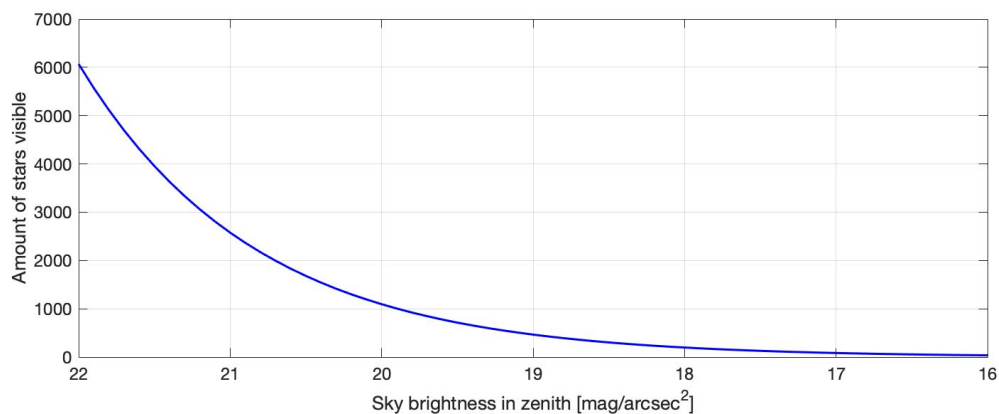


Figure 7 – Number of stars visible to the human eye compared to the sky brightness in zenith. Please note that astronomical magnitude is a logarithmic scale, decreasing with objects appearing brighter. A difference of one magnitude corresponds to a factor of 2.512. Created by Stefan Wallner and Thomas Posch. Data obtained from the Yale Catalog of Bright Stars.

1.2.3 Impacts on human health

Since human beings are inhabiting planet Earth, its life adopted to the motion of the sun. The daily rhythm of constant interaction between day and night, the circadian rhythm, was not only a point of reference, far more the physiology of life bases on its fundament. Society, as it exists today, relies on the usage of electricity across the whole day, throughout the whole year. As night is therefore fading away, sleeping habits have changed significantly. Before a supply with electricity was feasible, sleeping was decidedly connected to start with dusk and end with dawn. There were two sleep phases with a waking phase in between. The modern world shows a completely different picture with the first sleep phase being missed due to a vast range of replacement activities, e.g., shift work, operating electrical devices, or others. Also, the biphasic behaviour is mostly lost, since sleep is compacted into one phase solely (Stevens and Zhu, 2015).

The discussed disruption of the circadian rhythm is not only caused by the human urge of activity, the exposure to ALAN clearly leaves its marks in relevant processes within the human body. Primarily, it is well known that the endocrine system shows serious consequences. Special attention is hereby raised to the hormone melatonin. Also known as 'sleep hormone', it regulates the wake/sleep-rhythm through natural regeneration during the sleep phases and, therefore, preparing the human body for its daylight activity. As a consequence of artificial light replacing the natural darkness at night and furthermore being the only time melatonin is released, a suppression of the hormone is the resulting effect. The higher the intensity of light emissions, the more likely this is the case. But not only the intensity, also the wavelength of radiation influences a potential repression (Falchi et al., 2011).

Figure 11 illustrates spectra of various lighting types compared to the Melatonin Suppression Action Spectrum (MSAS). Latter shows that light arriving at a human observer has impacts on the suppression of melatonin with different strengths depending on the wavelengths. Short wavelengths, especially below 550 nm, seems to have the biggest impact to the hormone repression while radiation above this threshold does not at all. The peak of melatonin suppression occurs at wavelengths ranging between 430 - 460 nm. This process can be explained by ocular light being transmitted by neurones of

the human eye's retina to the suprachiasmatic nucleus (SCN) in the hypothalamus brain region, which is driving the wake/sleep-phase shift. The SCN is located above the optic chiasm, the region where the optic nerves are intersecting, consequently, this explains the sensitivity of the SCN to visible light. The transmission of the originating optical signals is carried forward until ending in the pineal gland, where the acute melatonin suppression takes place (Thapan et al., 2001; Moore et al., 1995).

The consequences of a disrupted circadian rhythm seem to be clear as sleep disorders are the immediate outcomes. Furthermore, there are resultant health issues like metabolic disorders, weakness and performance problems. Moreover, even more dramatic is the support of lowering blood levels with far-reaching implications as breast, prostate, endometrial and colorectal cancer types may arise. The melatonin suppression is hereby the stimulating factor (Falchi et al., 2011; Reiter et al., 2007). Finally, also other long-term consequences like obesity, diabetes and depression are also linked to the chronodisruption but still need further research (Stevens et al., 2007).

Here it is important to state that the sources of light pollution resulting in health issues discussed, must not be seen as being only public lighting. Also if they do play a role, the private usage of light near to the eye, i.e., screens of laptops, mobile phones, tablets, TV, etc., especially at nighttime, are far worse (Cajochen et al., 2011). Still, compared to public sources, each individual is responsible for its actions and activities and therefore, this is actually easy to be solved in theory. However, society today is the major issue by expecting humans being active throughout the day. On the contrary, problems regarding public lighting are usually hardly solvable.

1.2.4 Impacts on wildlife

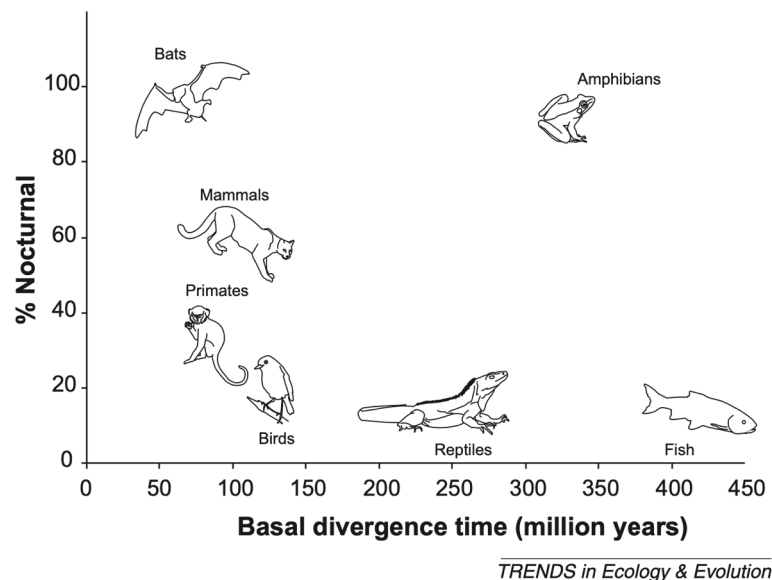


Figure 8 – Comparison of vertebrate classes and their percentage of nocturnal species. From Hölker et al. (2010). Reprint with permission.

Mammals on planet Earth are divided into four groups regarding their daily time of activity: nocturnal, diurnal, cathemeral and crepuscular. In the latter two cases, the activity phases during dusk

and dawn are characterised. The inevitable influence of ALAN on the species becomes abundantly clear looking on the percentage allocation of periods of activity. In fact, 69% of all mammals are nocturnal while only 20% being diurnal (Bennie et al., 2014). With the displacement of the natural night, potential problems for the majority upstream, since, e.g., movements and foraging activity are usually depending on the lunar cycle. With the night sky being illuminated, acting like moonlit conditions, a variety of animals are avoiding leaving their hidden habitats with dying of starvation. With the increase of artificially lit areas, habitats are lost completely and wildlife corridors are drastically comprised (Rich and Longcore, 2006).

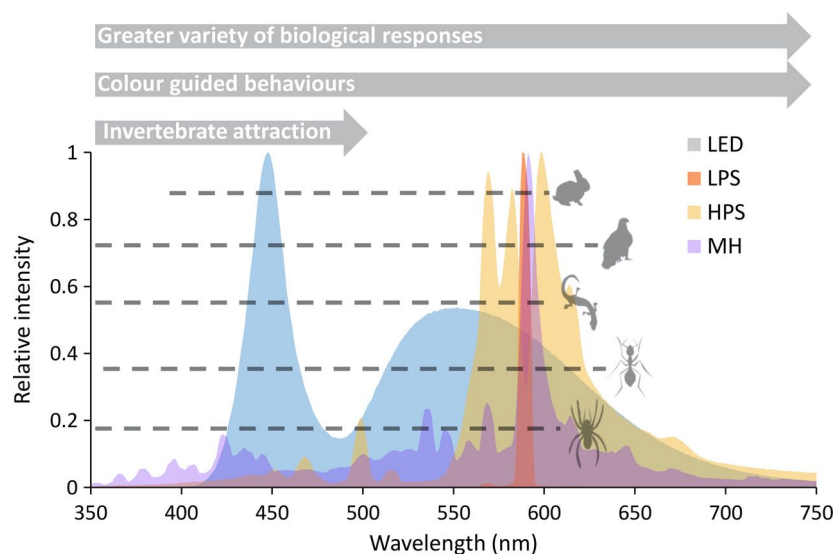


Figure 9 – Comparison of wavelength ranges illustrating the thresholds of light being detected by various species (grey dashed line) with biological responses as observed (grey arrows) and normalised spectral power distributions of lamp spectra of a Light Emitting Diode (LED) with colour temperature of 5000 K, a low pressure sodium lamp (LPS), a high pressure sodium lamp (HPS) and a metal halide lamp (MH). From Davies and Smyth (2018); Davies et al. (2013). Reprint with permission.

Naturally, not only mammals are affected by light pollution, but furthermore every living creature. Figure 8 compares vertebrate classes and their percentage of nocturnal species. It is noticeable that recent radiations provide a higher percentage of nocturnal animals and it is concluded by Hölker et al. (2010) that this validates nocturnality being a profound step in vertebrate evolution. Insects underline the importance of choosing lighting types with certain spectral power distributions, as their number of appearance was halved after converting from high pressure mercury light to high pressure sodium (Eisenbeis and Hänel, 2009). However, even if this is an improvement on the issue of insects congregating around light emitting sources, it still must be noticed that the majority dies of exhaustion and the total biomass is reduced. Strongly connected to this, the same behaviour potentially occurs with birds losing their orientation or sight and collide with structures like buildings or windows (Longcore and Rich, 2004). Even aquatic systems are not excluded from a potential impact with, e.g., periphyton showing a decrease in biomass of around 60% after a conversion to white LED illumination (Grubisic et al., 2018). These are just a few examples among many demonstrating the clear indication of artificial light at night impacting wildlife with great concern. As a last comparison, Figure 9 illustrates the ranges in wavelengths of detectable light for various species compared to the spectral emission of

different sources, clearly indicating animals being more affected in short wavelengths (blue).

In summary, light pollution poses a major threat for ecology since natural patterns are disrupted. Animals react to the influence of ALAN by changing reproductive, predator-prey or migration behaviours, loose the strength of their senses, e.g., orientation, are displaced by wildlife corridors becoming continuously smaller or die with the biomass being reduced noticeable. Animals show a high sensitivity to short-wavelength emissions, i.e., blue light, which should be avoided with the objective of their protection.

1.2.5 Impacts on environment & nature

Not only humans and animals show reactions to light, also other organisms like plants respond to a wide range of radiation. As discussed in the work presented in Section 4.4, plants act upon the lunar cycle, with flowering patterns or movement of leafs being established to it (Ben-Attia et al., 2016; Bünning and Moser, 1969). Consequently, also the environment demonstrates a sensitivity to the brightness of the night sky, even if not being induced artificially. This objective is clear, since the photosynthesis, one of the most important biochemical processes, is based on light as resource. While during the day oxygen is emitted and carbon dioxide absorbed induced by the reception of sunlight, the opposite is the case during nighttime.



Figure 10 – Trees showing clear indications of induced photosynthesis by ALAN as leafs stay green coloured under a street lamp (left) or leafs not falling and continuing the photosynthesis during autumn and winter near a light source (right). Source: International Dark Sky Association (2019)

This process is executed by all green plants and stimulated by light at wavelengths between 380 - 730 nm as shown in the Photosynthesis Action Spectrum (PAS) in Figure 11 in comparison to various light emitting sources. As is shown, the range of the PAS covers nearly the complete visible spectrum and therefore all light sources included to the comparison show emissions in wavelengths overlapping with the photosynthesis spectrum. However, the level of stimulation is varying over this range, with its highest sensibility in short wavelengths around 420 - 460 nm, then a slight decrease more than halving the sensitivity over the green-lighted wavelengths before increasing to a second maximum around 650 - 680 nm. It follows that, if light coming from artificial sources replaces the natural darkness during nighttime, photosynthesis can still be induced without the need of sunlight. The result is a carbon fixation with leafs either staying green throughout the year (no loss of chlorophyll) or not

falling in autumn as a consequence, plants perishing early. Even if the photosynthetically active radiation induced by ALAN was studied to be extremely low relative to sunlight conditions ([Gaston et al., 2013](#)), it are nonetheless single lamps near to leaves which are leaving marks clearly visible, as seen in Figure [10](#).

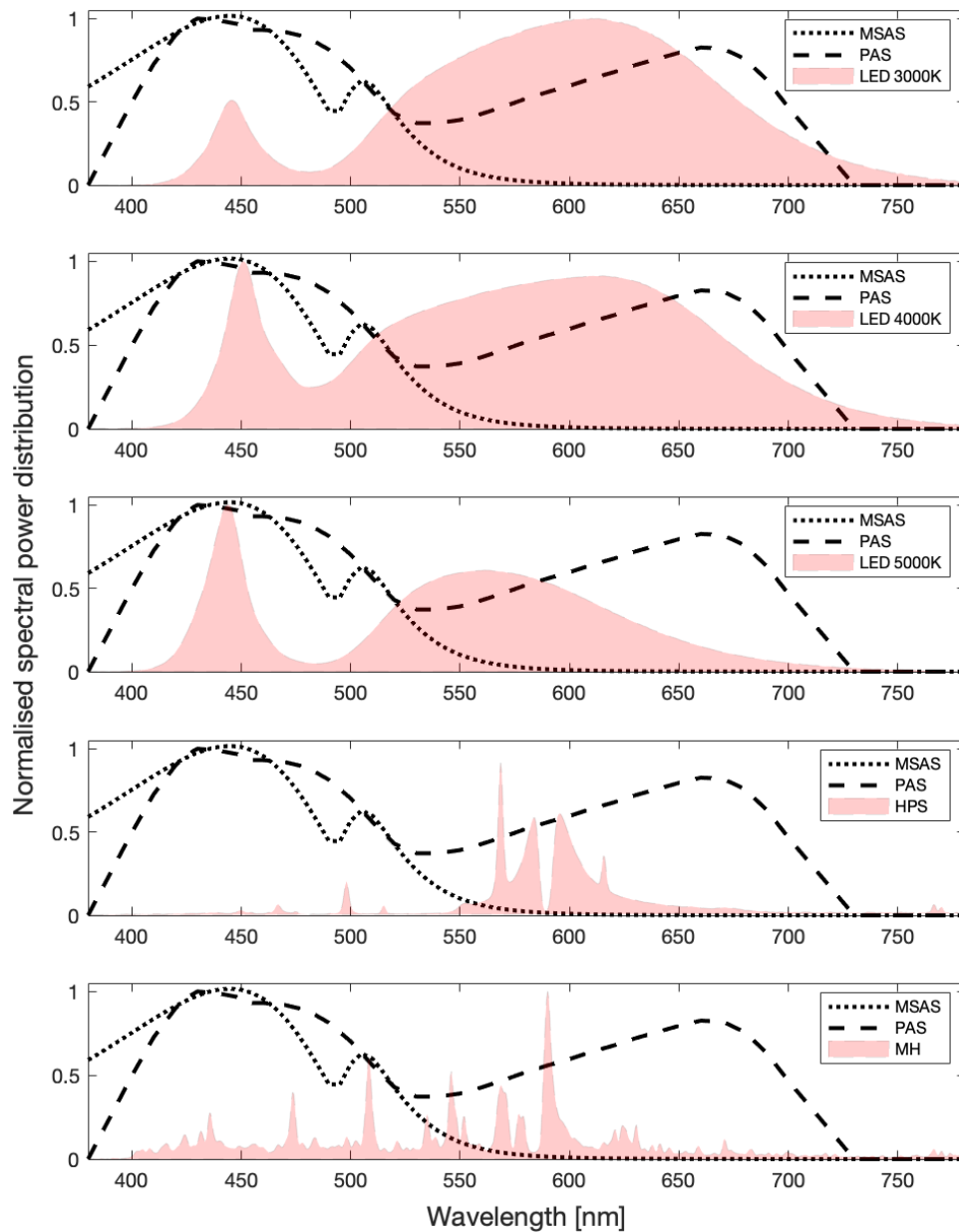


Figure 11 – Comparison of various lamp spectra (3000 K LED, 4000 K LED, 5000 K LED, HPS and MH) with the Melatonin Suppression Action Spectrum (MSAS) and the Photosynthesis Action Spectrum (PAS). Created by Stefan Wallner with data obtained from the Lamp Spectral Power Distribution Database (LSPDD) ([Roby and Aubé](#); [Aubé et al., 2013](#)).

1.3 Current status and development

1.3.1 Global

The phenomenon of light pollution is a global issue. The 'World Atlas of the Artificial Night Sky Brightness' by [Falchi et al. \(2016b\)](#) illustrates a global coverage of satellite data underlining the worldwide distribution, see Figure [12](#). As might be expected, countries with a higher population density also show a higher amount of artificially lit areas, obviously. The data clearly indicates the problem being large scaled: About 83% of Earth's population live under skies polluted by ALAN. Europe and North America are standing out in this regard, here the number increases to more than 99% of their citizens. At this point, it is important to state that a night sky is considered to be light-polluted with the artificial sky brightness reaching values $>14 \mu\text{cd}/\text{m}^2$, as defined by IAU Commission 50. To receive the total sky brightness, the value of artificial pollution must be added to the natural sky brightness, defined as $170 \mu\text{cd}/\text{m}^2$, corresponding to $\approx 22 \text{ mag}/\text{arcsec}^2$.

Comparing the levels of light pollution between countries, the Republic of Singapore presents the most extreme example possible. The city-state island in Southeast Asia with more than 5.7 million inhabitants exhibits the second largest population density worldwide. Consequently, it can be expected that light pollution levels are particularly high. However, the World Atlas demonstrated the country being an unprecedented case with the entire population living under night skies artificially polluted by more than $3000 \mu\text{cd}/\text{m}^2$, the highest level of light-polluted skies as defined by [Falchi et al. \(2016b\)](#). Therefore, the night sky brightness corresponds to a maximum value of $\approx 18.831 \text{ mag}/\text{arcsec}^2$ on the astronomical scale. The threshold was chosen as this value reveals that a night adaption of the human eye is no longer possible, therefore applying to all inhabitants of Singapore. Kuwait and Qatar are following closely with a small percentage of their population (under 5%) experiencing the night sky less polluted. With a particular focus on Europe, Greece, Gibraltar, Malta, Spain and Iceland are among the 20 most light-polluted countries by population with only Iceland having a small number of their population living under natural night skies, considered not to be artificially polluted (zenith values of artificial sky brightness below $14 \mu\text{cd}/\text{m}^2$).

On the contrary, countries comparatively sparsely populated with mostly large areas of no residential settlements at all, e.g., forests, deserts or areas in climatically unfavourable conditions. The Republic of Chad with a population density of only 8.6 inhabitants per square kilometre, is classified as the least light-polluted country with nearly 80% of its population living under a pristine sky with the artificial pollution reaching a maximum value of 1% compared to the natural sky brightness, i.e., an artificial sky brightness of $\leq 1.7 \mu\text{cd}/\text{m}^2$. Unsurprisingly, countries from Central Africa or islands are leading the worldwide ranking, while European countries are missing at the top.

Since population numbers or inhabited areas and, consequently, the amount of light installations or light intensities used are not remaining constant in time, also the levels of light pollution are continuously changing. When studying the development in the near past, [Kyba et al. \(2017\)](#) were able to determine that areas showing illumination by artificial light grew by an average of 2.2% per year over the period 2012-2016, measured against the total number of 9.1% in global increment. The increase of total radiance was quantified to be 1.8% per year, while lit areas have brightened at a rate of 2.2% per year. However, this underlines the current development of this phenomenon being a steadily growing problem. Still, countries registering a complete lighting conversion to well-shielded LEDs showed a decrease in radiance, although this is matter of discussion due to the satellite used for analysis being blind in shorter wavelengths, see Sections [2.6.2](#), [2.6.4](#) and [5.2](#).

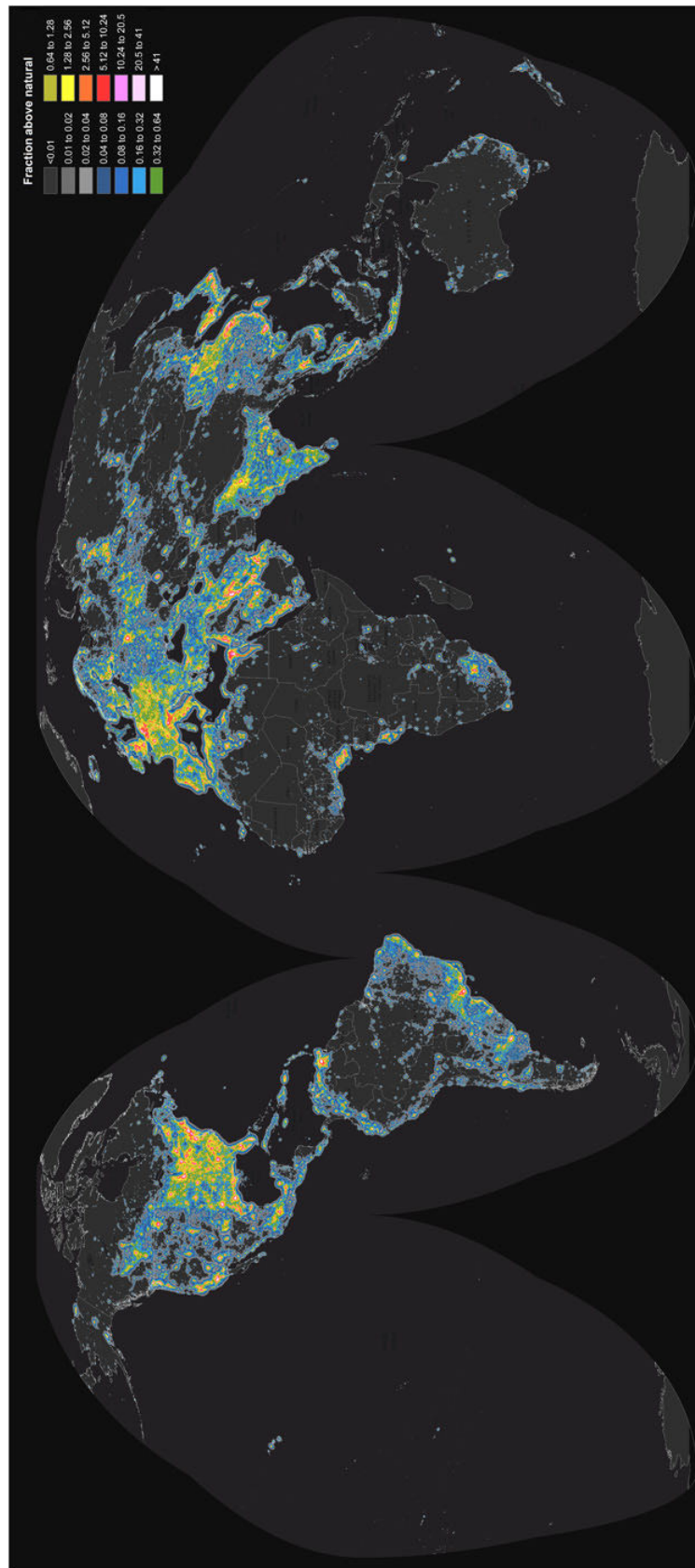


Figure 12 – The 'World Atlas' of light pollution as obtained from [Falchi et al. \(2016b\)](#). The colours indicate the fraction of artificial sky brightness compared to the natural brightness. Reprinted with permission from AAAS.

1.3.2 Special focus on Austria

Figure 13 shows the artificial sky brightness of Austria as obtained from Falchi et al. (2016a,b). Unsurprisingly, Austria follows the global trend of more light polluted areas in urban regions. Especially the state capitals of Austria's federal states demonstrate increased values. As was to be expected, the capital city Vienna is the largest light pollution source. Apart from that, the centre of the country is dominated by the Alps, with large areas only sparsely inhabited, providing some of the least light-polluted areas in Europe.

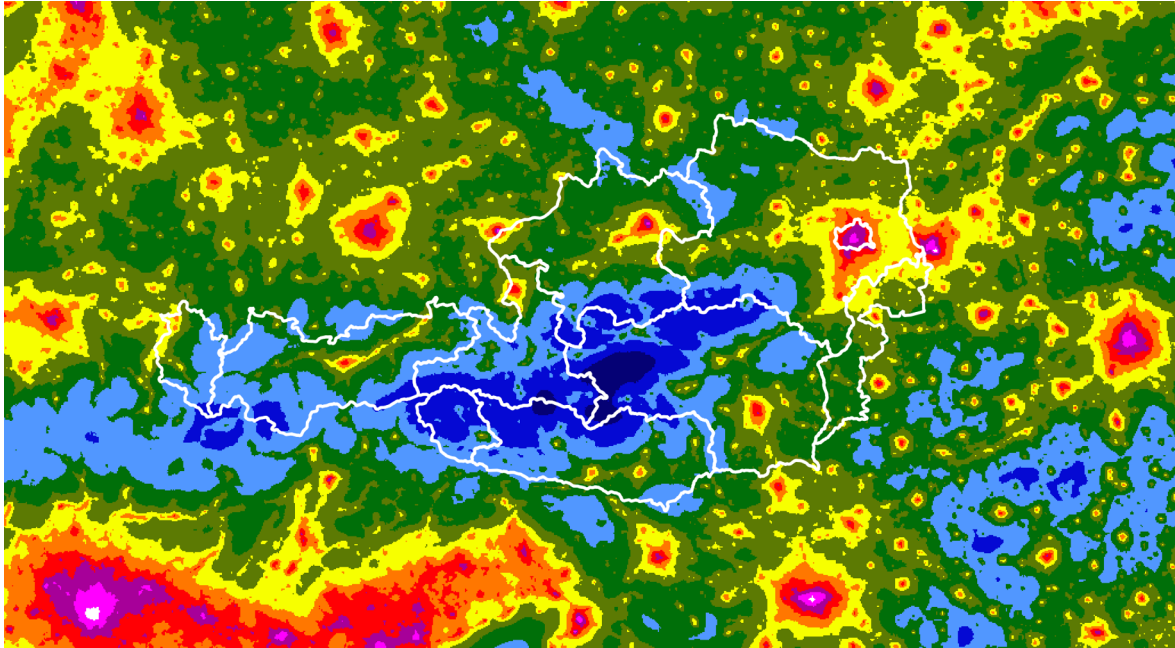


Figure 13 – Map illustrating the artificial night sky brightness of Austria and close surrounding. The borders of the country and the federal states are marked by white lines, the artificial sky brightness follows the same scale as shown in Figure 12. Vienna is located in the Northeast of Austria. The darkest areas in the centre (dark blue coloured) are pursuant to the location of the Alps. The bottom left corner gives a hint of the light pollution in Northern Italy. Created by Stefan Wallner with data obtained from Falchi et al. (2016a,b).

As Table 2 displays, the entirety of Austria's population lives under an at least slightly light-polluted sky. Furthermore, more than ten percent suffer from the highest level of pollution, although this corresponds to only 0.1% of the country's area and can be assigned to the inner regions of urban cities. With more than a third of the populace not able to see the Milky Way on the night sky, Austria provides better conditions compared to the European Union (59.5% with no possibility of seeing the Milky Way) but follows the course of the overall global average (35.9%) quite well.

However, also Austria does not remain untouched by changes in amount of lit areas or intensity over time. Figure 14 evinces the development of total radiation as detected by the VIIRS satellite, see Section 2.6.2, over the years 2013 - 2019. Variations in upwards radiation are clearly visible, although there was a significant increase starting with 2015. Overall, the country recorded an increase in total radiance by 2.53% per year, providing a total growth of 15.5% over the displayed time range. Compared to the global trend, Austria is marginally above the worldwide average. The registered

ASB [$\mu\text{cd}/\text{m}^2$]	FANL [%]	CTSB [$\text{mag}/\text{arcsec}^2$]	Description	Population [%]	Area [%]
≤ 1.7	≤ 1	≥ 21.997	pristine sky	0.0	0.0
> 1.7	> 1	≤ 21.997	unpolluted zenith, slightly polluted towards horizon	100.0	100.0
> 14	> 8	≤ 21.922	pollution reaches zenith	99.9	97.8
> 87	> 50	≤ 21.559	visibility of objects with low intensities are lost	88.7	40.0
> 688	> 404	≤ 20.250	visibility of Milky Way is lost	35.7	1.8
> 3000	> 1765	≤ 18.831	cone stimulation, night adaption not possible	10.3	0.1

Table 2 – ASB = Artificial sky brightness in zenith, FANL = Fraction additional to the natural light, CTSB = corresponding total sky brightness in zenith. (Falchi et al., 2016b)

flattening of the curve after 2017 and the decrease between 2018 and 2019, even if only of small extent, could follow from extensive lighting conversions to well shielded LEDs. Especially the capital city Vienna, which started with the transition in 2017, made huge process. Nevertheless, the data points resulting from 2020 and the years after will enable to give more accurate statements about the impact of LED conversions.

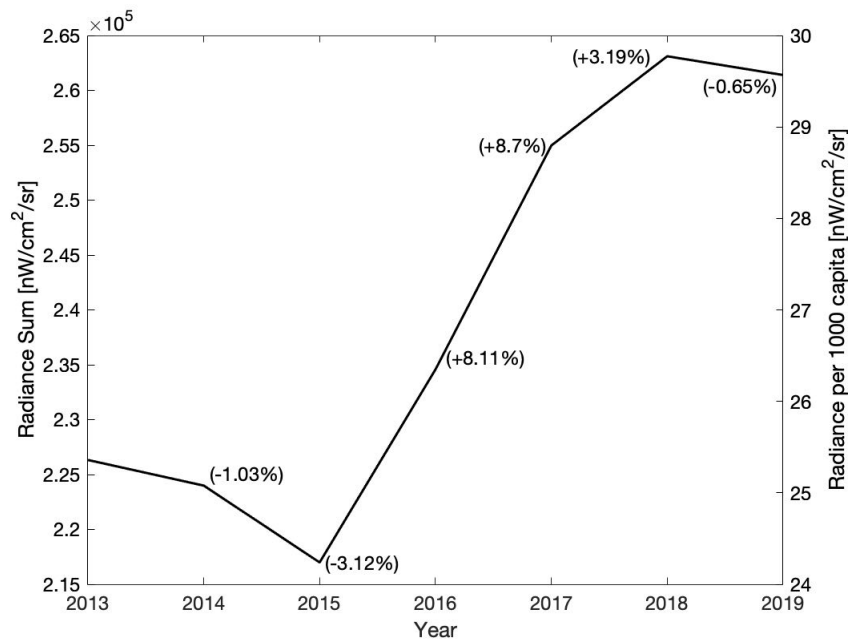


Figure 14 – Total radiance as annual averaged values as detected by the VIIRS satellite for Austria between 2013-2019 compared to the radiance per 1000 capita. Data points were obtained from <http://www.lightpollutionmap.info> by Jurij Stare. They are calculated from averaged VIIRS radiance data vcmcf (VIIRS Nighttime Day/Night Band Composites Version 1) forming an annual average value. The variability of natural light is reduced to a minimum by subtracting a zero point layer (Coefeld et al., 2020). Data shown provide the sum of all pixels and their radiance values with boundaries used from Database of Global Administrative Areas (GADM). The percentage values show the degree of change compared to the year before. Created by Stefan Wallner.

1.4 Potential actions against light pollution

Many people fear that the only potential step towards the preservation of the night sky is to switch off all light sources immediately. Due to the fact that this is closely associated with substantial safety reductions, this is definitely no solution. However, on the contrary, thinking about disturbing glares, over-illumination or misdirection of the light emission may also result to this end. Therefore, the principle of sustainable lighting must be that light should only be installed where it is needed, in the intensity it is needed and only used when it is needed. Those represent also some of the policies as adopted and proposed by the International Dark Sky Association. There are only few countries in the world which adopted laws against the potential increase of light pollution, and usually municipalities who make the decision towards an energy saving LED conversion of public lighting systems are often on their own. The following section aims to show which laws or standards exist, addresses to local governments what should be considered if planning lighting conversions and shows an example how dark areas can be protected in form of official certified 'International Dark Sky Places' as planned in Austria.

1.4.1 Legal situation

1.4.1.1 Austria

Currently, Austria does not have a law regulating light emissions. The emission protection law only includes ordinances against air pollution. However, there are standards which are officially representing the 'state-of-the-art', which unfortunately is an inexact and loose legal concept. Still, under the legal definition of, e.g., Article 12a paragraph 1 Water Protection Act (§12a Abs. 1 WRG), the term characterises that based on fundamental scientific advancements the current state of development of certain processes. Such regulations and generally acknowledged rules of engineering must be maintained at any time to assess the assigned tasks properly and identify and eliminate potential hazards. They are recorded in standards and norms, valid in Austria are the national ÖNORM and international EN (European) or ISO standards.

The standards containing information about public lighting in Austria are:

- ÖNORM EN 13201-2:2016 05 15 Road lighting - Part 2: Performance requirements
- ÖNORM EN 13201-3:2016 05 15 Road lighting - Part 3: Calculation of performance
- ÖNORM EN 13201-4:2016 05 15 Road lighting - Part 4: Methods of measuring lighting performance
- ÖNORM EN 13201-5:2016 05 15 Road lighting - Part 5: Energy performance indicators
- ÖNORM O 1055:2017 09 15 Road lighting - Selection of lighting classes - Rules for the implementation of CEN/TR 13201-1
- ÖNORM O 1051:2019 08 01 Road lighting - Lighting of conflict areas
- ÖNORM EN 12193:2019 06 15 Light and lighting - Sports lighting
- ÖNORM EN 12464-2:2014 05 15 Light and lighting - Lighting of work places - Part 2: Outdoor work places
- ÖNORM O 1052:2016 06 01 Light pollution - Measurement and evaluation

- ÖNORM EN 50110:2014 10 01 Operation of electrical installations - Part 1: General requirements (Part 2-100: National annexes)

Still, even though many standards are available, there is lack of control referable to the regulation of light pollution, especially because EN 13201 standards are only displaying minimum brightness levels and are not referencing suggestions on maximums. Nevertheless, the current government programme 2020 - 2024 includes for the first time that dark places in Austria (as officially recognised by the International Union for Conservation of Nature) shall be protected from light emissions.

1.4.1.2 European Union

[Schroer et al. \(2020\)](#) studied the legal situation comparing European and German laws on a large scale in order to evaluate existing legislatives covering ALAN related statutory provisions and also aiming to point out potential protection gaps. A closer inspection on the applicable case-law of the European Union has shown that content in regard to light emissions is only rarely present, but can be found in three fundamental legal provisions:

- The *EU Nature Protection Framework* contains the i) 'Council Directive 92/43/EEC on the Conservation of natural habitats and of wild fauna and flora' and the ii) 'Council Directive 2009/147/EC on the conservation of wild birds'
- The *Immission Control Law* includes the iii) 'Directive 2009/125/EC of the European Parliament and of the Council of 21 October 2009 establishing a framework for the setting of ecodesign requirements for energy-related products'

Regarding the influence of light emissions, i) and ii) contain protection provisions for either specific species or selected habitats. iii) includes information on light emissions, although mentioning only ecodesign requirements. Across the board, it is concluded that there are three major issues regarding ALAN in European legislatives.

First, the protection is no safeguard for wildlife or environment per se, it only includes two species of certain higher risk, birds due to potential deadly collisions and bats due to the loss of habitat through decreasing wildlife corridor.

Second, to enable the possibility of taking legal measures against a legal entity causing influences on the mentioned species or habitats, a 'significant impact' must exist and recognised.

Third, something that was also applicable to all ÖNORM or EN standards as discussed before, there are no thresholds of light intensities indicating effects on creatures. If there are no certain limits set, mostly an application cannot be defined.

Consequently, as summarised by [Schroer et al. \(2020\)](#) there are significant legislative shortcomings, not only for European laws.

1.4.1.3 Existing laws for prevention measures against light pollution

In Europe, there are various countries which implemented laws or regularities aiming for the containment of light pollution. To gain an overview, they are presented in Table [3](#).

Country	Year	Description
Spain (regional)	1992	The first law aiming to protect the night sky for astronomical observations on Canary Island was implemented in 1988, the 'Sky Law' (31/1988) and approved by the government in 1992. It regulates all potential outdoor lighting installations visible from La Palma to maintain the quality of the night sky. Catalonia and Andalusia followed in 2001 and 2017, respectively.
Italy (regional)	1997	A total of 15 Italian regions implemented regional laws, starting with Veneto in 1997 (L.R. 22/1997).
Czech Republic	2002	Czech Republic adopted a light pollution law (č. 86/2002) regulating lighting sources to be installed well-shielded, limits the amount of light and foresees the implementation of devices capable of dimming or switching off light during the night with exceptions being faint sources below 1500 lumens, temporary or traffic lights. Furthermore, illuminated buildings must be dimmed to at least the half or switched off completely between 11 p.m. and 5 a.m. In addition, sensitive sites enjoy even stronger regulations.
Slovenia	2007	Regulation 4162 displays exact thresholds about the emission of light pollution and sources. For instance, there are limits for illuminated advertising panels, cultural monuments, industrial buildings or airports and a mandatory use of environmental friendly lightings as defined. Also, it is a must for streetlights to be well-shielded.
France	2013	Regulated parameters in the French legislative act (TREP1831126A) are lighting schedules, amount of radiation to the upper hemisphere and luminous flux density depending on usage of light, the necessity of no intrusive light and correlated colour temperature (<3000 K in general and <2400 K in natural areas).
Croatia	2018	Usage of LEDs for streetlights with a maximum CCT of 3000 K and uplight ratio of 0%. For natural protected spaces max. 2200 K. (50301-25 / 05-18-9)

Table 3 – Existing light pollution laws of selected countries. They do not display the entirety of available laws, furthermore the majority providing binding regulations.

1.4.2 Environmentally friendly lighting

Since there are conversions of public lighting systems ongoing, it is important for municipalities to maintain an environmental friendly illumination. The sections above discussed the issues regarding certain parameters of light, like colour temperature or intensity. However, Figure 15 offers a good starting point, what shall be cared about when planning lighting transitions. Among some more recommendations, the most important are:

- **Use of Light Emitting Diodes (LEDs)**

As Sections 1.1.2 and 1.1.3 have shown, LEDs represent the best option for light installations, regarding their efficacy, decrease in maintenance costs or length of service life, up-to-date. For energy saving purposes, they are the right choice.

- **Shielding of lamps**

According to the ÖNORM O 1052, the optimal emission beam angle of a luminaire is below 70°. This can be easily fulfilled with well-shielded LEDs since their light can be optimally pointed to the surfaces to be illuminated. Consequently, there is no loss in energy, since the light intensity can be reduced due to radiating no unnecessary light to the horizontal or upwards. Additionally, this includes illumination directions only from above since every source emitting light upwards from the ground could end in the sky being illuminated instead of a specified object.

- **Environmental friendly light colour**

Sections 1.2.3, 1.2.4 and 1.2.5 illustrated which impacts radiation especially in shorter wavelengths, i.e., blue light, provides for human health, wildlife and environment. Therefore, it is

recommended to use luminaires, emitting no light below the threshold of 500 nm and/or above 680 nm. For LEDs this is fulfilled for colour temperatures between 1800 - 3000 K. For other lighting types with more distributed spectral lines, a reference point constituted by the scotopic to photopic ratio S/P aiming to be below a value of 1.2.

- **Dimming or switching off during late night**

During the night the amount of traffic is usually variable, with less road users late at night. Therefore, if this is the case, light can be dimmed, also according to the standards existing. Focussing on mostly empty crossroads in inhabited areas, such do not have to be illuminated at all or could be equipped with movement sensors, to provide an illumination only when it is really necessary. This is also valid for other types of lightings than streets, like illuminated buildings and facades.

- **Industry and hospitality**

Industrial or hospitality company buildings, often depending on the use of illumination also during night times, should not only install types of lighting according to the points above, also the illumination should be concentrated on opening times solely.

- **Advertisements**

Billboards or advertisements should be characterised depending on their location and the amount of people walking/driving by, when it is necessary to use how much light, to minimise or even stop a permanent operation.

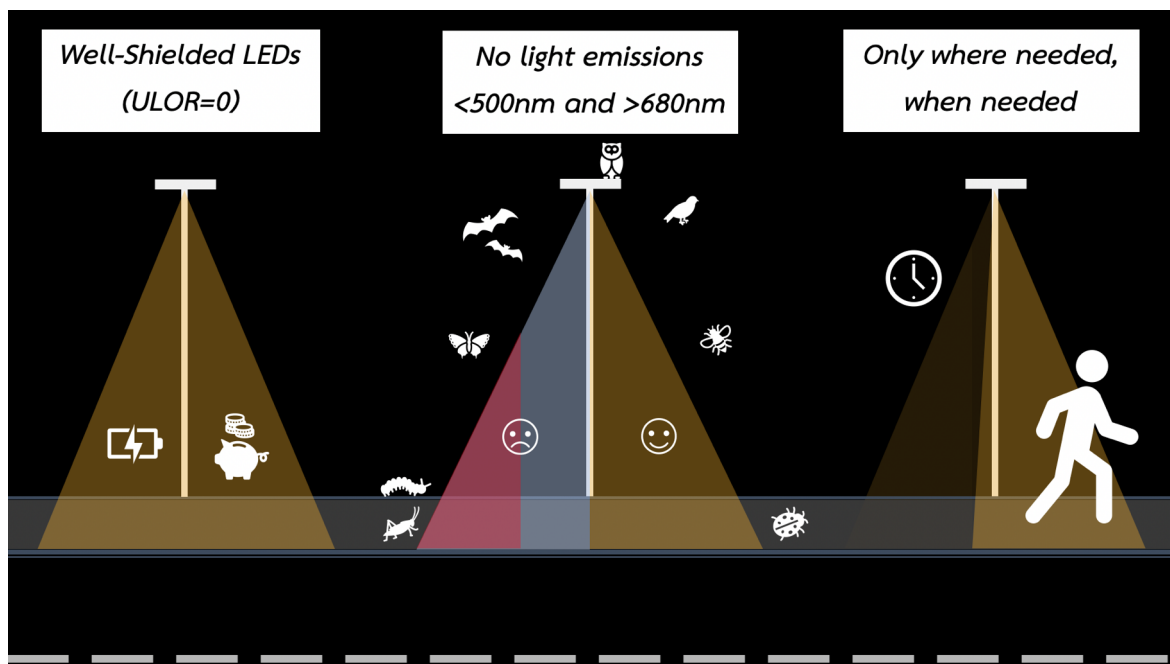


Figure 15 – Most important recommendations to maintain an environmentally friendly system, focussing on streetlights. Created by Stefan Wallner.

An optimum template including all information on the most important concerns and tips for conversions is documented in the 'Austrian Guidelines for Outdoor Lighting' ([Province of Upper Austria, 2019](#)).

1.4.3 Protection of dark sites

In Section 1.3 it was illustrated that light pollution is undergoing a permanent change, mostly with increasing issues due to the amount and intensity of lit areas constantly showing rising numbers. Therefore, it must be of greatest interest to protect those sites still providing a natural or only very low polluted sky. Consequently, there are some global initiatives with the objective of certify such 'dark places' aiming to raise awareness and protect the night sky from further influences. Such projects, as discussed in [Posch et al. \(2017\)](#), include:

- **'International Dark Sky Places'** by the International Dark Sky Association,
- **'Starlight Programme'** by the Starlight Initiative,
- **'Dark Sky Site Designations'** by the Royal Astronomical Society, and
- **'Villes et village étoilés'** by the Association National pour la Protection du Ciel et de l'Environnement Nocturne (ANCPEN).

To discuss fundamentals and requirements of such an initiative, the focus here will be on the 'International Dark Sky Places' (IDSP) programme by the IDA. This certificate was chosen as it is planned to establish the first 'Dark Sky Park' in Austria in the near future.

The IDA bestows an IDSP to natural protected areas and the associated society under various categories. They must fulfil specified requirements and take necessary steps towards a promising protection of the natural dark sky and show exemplary behaviour in the utilisation of outdoor lighting. As defined by the [International Dark Sky Association \(2020\)](#), the different categories are:

- **International Dark Sky Community:** Cities and municipalities, converting public lighting systems to ensure the quality of the night sky not being decreased in the future and strongly engage in public relations to carry out the message of the importance of a dark sky.
- **International Dark Sky Parks:** Areas already exhibiting nature protection status, either public or private, which warranting an environmentally friendly lighting, raising awareness for the general public through public outreach activities.
- **International Dark Sky Reserve:** Large areas with a size of at least 700 km², possessing an exceptional dark core zone and an inhabited peripheral zone. The very low light pollution levels in the core zone must be sustained through actions coming from the peripheral zone.
- **International Dark Sanctuaries:** The darkest and most isolated areas in the world which should be given particular protection.
- **Urban Night Sky Places:** Urban areas, not providing the night sky quality necessary for other categories, but still raise awareness with public relations work.
- **Dark Sky Friendly Developments of Distinction:** Category on a smaller scale than Urban Night Sky Places for single cities, districts or municipalities.

In Austria it is planned, by the initiative of the Principle Government of Upper Austria, to establish the country's very first Dark Sky Park in the near future. The scientific evaluation already began in 2017 and an application shall be submitted by end of 2020. Therefore, to receive an impression of

requirements to be fulfilled by an area and society wanting to become such IDSP, there will be strong focus on the IDA category 'Dark Sky Park'. The following demonstrated guidelines follow the '2018 International Dark Sky Park Guidelines' ([International Dark Sky Association, 2018b](#)).

The key criterion to find out if some natural area is capable of becoming a Dark Sky Park, the minimum night sky brightness mandatory is defined with $21.2 \text{ mag/arcsec}^2$ or 0.4 mcd/m^2 . This threshold is used due to the Milky Way being easily retrievable via naked eye with no significant light pollution sources only being slightly visible at the horizon. The feasibility of the night sky reaching this value must be scientifically proven over a longer period to exclude fluctuations. Additionally, all potential light domes must be recorded.

With the night sky being positively evaluated, the next step is to carry out an accurate census of all public lighting installations inside the specified area. Compiled to a lighting inventory, this shall give hints about the percentage of existing lights following the criteria for outdoor lighting. Such are, among others: all lighting fixtures $>500 \text{ lm}$ must be fully shielded, the colour temperature chosen must not exceed 3000 K ($<25\%$ of light emission below 550 nm or $S/P < 1.3$), illuminated signs must be switched off one hour after local sunset until one hour local sunrise with defined thresholds for intensity, size and colour. At the time of submission of an application, a percentage of 67% of all public outdoor lighting fixtures must follow the guidelines, with a binding confirmation to raise this number to at least 90% after five years and to 100% after ten years.

If discussed qualifications do apply, and with dark sky friendly public outreach activities also started, an application is possible. All local municipalities and also external partners must, as defined in the guidelines, offer their full support of this project. According to the IDA, the time for preparation until a submission is possible is between 2 - 3 years. If a Dark Sky Park designation is positive, an annual report must show the continuous commitment to public outreach and also analyse steadily ongoing measurements of the night sky brightness.

As mentioned, a cooperation between University of Vienna, Provincial Government of Upper Austria and local authorities and clubs prepares an application for Austria's first Dark Sky Place, a potential Dark Sky Park, at the Nature Park Attersee-Traunsee in Upper Austria. The scientific survey regarding measurements of the night sky brightness as well as an analysis of the lighting inventory, can be found in the Appendix.

A wide-angle, fisheye photograph of a night sky. The sky is filled with numerous stars of varying brightness. In the foreground, a dark, silhouetted landscape is visible, including a hillside on the right with some distant lights and a dark shape in the lower left that appears to be a car. The overall scene is dark, with the primary light source being the stars in the sky.

2

MEASURING
LIGHT POLLUTION

2 Measuring Light Pollution

Modern light pollution research is in the good position of having a large number of suitable instruments and devices aiming to characterise and quantify the impact of artificial light at night (ALAN) to the night sky and its environmental impact (Hänel et al., 2018; Levin et al., 2020). However, there still are significant limitations causing problems in observing and measuring either ground-based, i.e., skyglow measurements, and from above, i.e., radiance observations. A more detailed discussion about an outlook for the future will be provided in Section 5.2. This section provides an overview especially of those instruments and measurement techniques used to fulfil all tasks providing the results studied in the publications of Section 4. In addition, to make them objects for comparison, other techniques such as satellites or naked-eye observations were included.

2.1 Naked-eye observations

Unsurprisingly, studying the night sky with the naked eye is the oldest form of observational astronomy. Its great importance in the development of multidisciplinary research becomes apparent considering that the definition of the astronomical magnitude is based on the visibility of stars. In 129 B.C., it was Hipparchus who created a catalogue of stars, grouping them into three classifications according to their brightness: 'brilliant light', 'second degree', or 'faint'. This rough categorisation was later expanded significantly by Claudius Ptolemy of Alexandria in 138 A.D., when he included a catalogue of 1038 stars to his *Almagest*. For the first time, stars were classified in six subgroups. The visibly brightest stars on the night sky were characterised as being of 'first magnitude' whereas the faintest ones, being barely visible to the naked eye, were specified as being of 'sixth magnitude' (Herbig, 1945; Liverington, 2003).

With increasing use of ALAN, in most cases continuously followed by intensifying skyglow, the limiting magnitude decreases due to the brightening of the night sky background. For many years, researchers tried to find an appropriate relationship between limiting magnitude, i.e., the faintest object visible, and night sky brightness. However, especially as absolute values of these parameters diverge significantly, results were often exposed to uncertainties (Garstang, 2000). An approximation for the magnitude limit m_0 often used is

$$\begin{aligned} m_0 &= 0.3834\mu_{\text{sky}} - 1.440 - 2.5 \log F & \text{if } 20 < \mu_{\text{sky}} < 22 \text{ mag arcsec}^{-2} \\ m_0 &= 0.4260\mu_{\text{sky}} - 2.365 - 2.5 \log F & \text{if } 21 < \mu_{\text{sky}} < 25 \text{ mag arcsec}^{-2}, \end{aligned} \quad (21)$$

providing a maximum error of 0.01 or 0.04 mag respectively (Crume, 2014). Here, μ_{sky} is the sky surface brightness and F a field factor, including information about the shape of the target, viewing conditions and observer. The resulting relationship of these parameters is illustrated in Figure 16. The influence of the latter parameter can vary considerably with age or physical state of an observer. Consequently, providing a uniform and generally applicable opportunity of enabling exact characterisations of the limiting magnitude to everyone is impossible, since especially this field factor can have very diverse impacts on the conclusions. Since the approximation introduced in Eq. 21 is valid to dark skies down to $20 \text{ mag arcsec}^{-2}$ only, brighter night sky brightnesses, mostly appearing in or near cities, can further worsen the quality of its outcome.

In order to apply necessary measures enabling also non-professional sky observers, e.g., amateur astronomers, a possibility to analyse the extent of light pollution in one location, John E. Bortle intro-

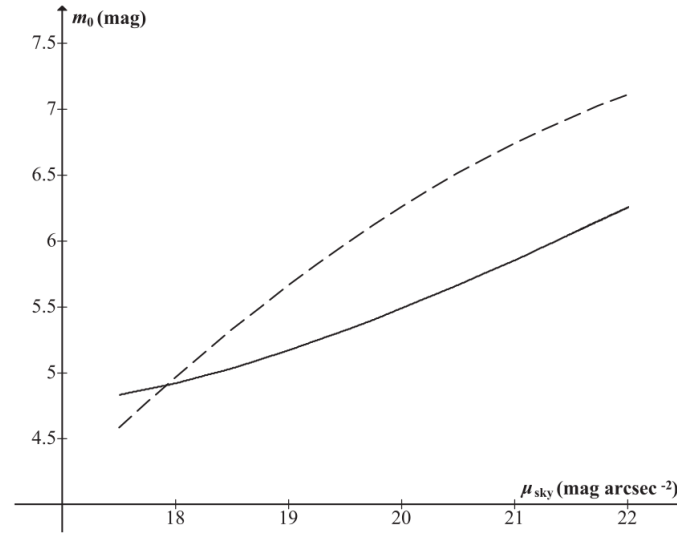


Figure 16 – Relationship between naked eye limiting magnitude m_0 and sky surface brightness μ_{sky} . The solid line is a result of the approximation introduced in Eq. 21 with a field factor of $F = 2$, the dashed line provides results of an older model by Hecht in 1947 (Hecht, 1947). (Crumey, 2014)

duced the so-called 'Bortle scale' (Bortle, 2001). Setting not only the naked eye limiting magnitudes in relation to theoretical 'Sky Quality Meter' measurement results (device and observational technique discussed in Section 2.2), he also described each of his nine newly introduced classes by the visibility of certain objects like star constellations, galaxies or the shape of skyglow itself. To give an example, if M33 is seen directly and the Milky Way also visible in detail, Bortle classes 1–2 can be assumed, being equivalent to a limiting magnitude between 7.1–8.0 mag or a sky brightness between 21.5–21.9 mag arcsec⁻². If on the other hand the Milky Way disappears and can no longer be recognised overhead, the sky can be characterised by Bortle scale 7 at least, being equivalent to a limiting magnitude lower than 5.0 mag and sky brightness brighter than 19.1 mag arcsec⁻². Figure 17 tries to put these parameters into comparison.

Although naked eye observations are of great importance, especially for the public, when conducting surveys about the darkness of the night sky above one location, there are still big uncertainties due to the inevitable dependence on observers. Their physical state and routine can greatly influence the outcomes, providing a variety of conclusions among a number of them. For research purposes, such observations seem suitable only if only coarse resolution data is needed rather than quantitative information. Especially the development of light pollution and skyglow can be detected roughly only, since its increase or decrease is usually creeping. In summary, it can be concluded that a first approximative assessment of the condition of the night sky and the impact of artificial light at night can always be performed via naked eye observations and they play a significant role when transferring the subject to the general public.

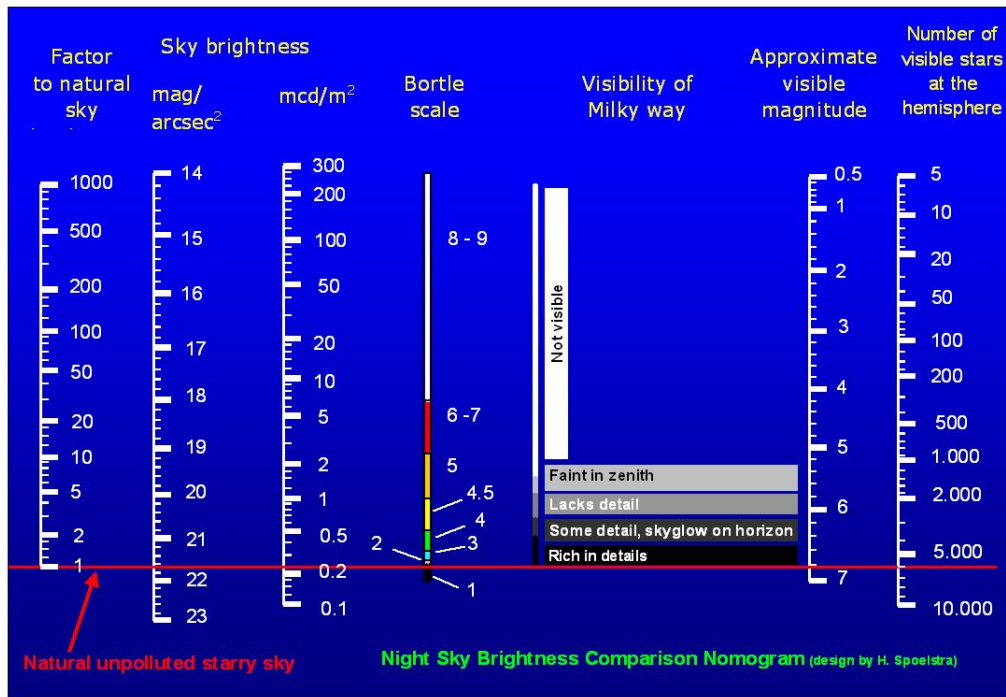


Figure 17 – Comparison of various parameters like sky brightness and limiting magnitude and their relation to the Bortle scale. (Spoelstra, 2009)

2.2 'Sky Quality Meter' and light monitoring networks

The Unihedron 'Sky Quality Meter' (SQM), as shown in Figure 18a, is a hand-sized measurement device, providing an easy opportunity of one-dimensional photometric observations by detecting the brightness of, e.g., the sky's zenith luminosity. Its production was undergone with the background of creating a low cost but still accurate instrument, being used by the wider public. With the first versions being introduced back in 2005 (Cinzano, 2005), the device was updated and improved continuously over the years. Today there are several types of SQMs, varying on the one hand by connection technologies and plugs, being able to connect it to ethernet, or on the other hand if an offline data logger is included. One of the most important modifications the original SQM instrument received was the installation of a lens (renamed 'SQM-L'), resulting in a change of the Full Width Half Maximum (FWHM) of its angular response, decreasing from 60° to 20°. This narrower field of view allows the focus of observations being around the target point, collecting light within a small radius only. Particularly, if paying attention to the zenith, as commonly used due to the fact of being the most characteristic point classifying a night sky, potential light domes around the horizon are not considered directly.

The accuracy of the instruments is at around $\pm 10\%$, which means an uncertainty of 0.1 mag/arcsec². When comparing its spectral response to known photometric bands, as illustrated in Figure 18b, one of the major drawbacks of the device becomes apparent. Compared to B, V and R bands, one can see that the SQM is very insensible in higher wavelengths while also at shorter wavelengths outcomes can still be influenced. Spectral measurements of luminaries, as discussed in Section 2.5, show that this effect can have significant impacts, since, e.g., High Pressure Sodium (HPS) lamps emit large

amount of light in higher wavelengths. Especially, if converting to blue-enlightened Light Emitting Diodes (LEDs), the spectral effectiveness of the device must be taken into account if data provided by SQMs are used for analysis.

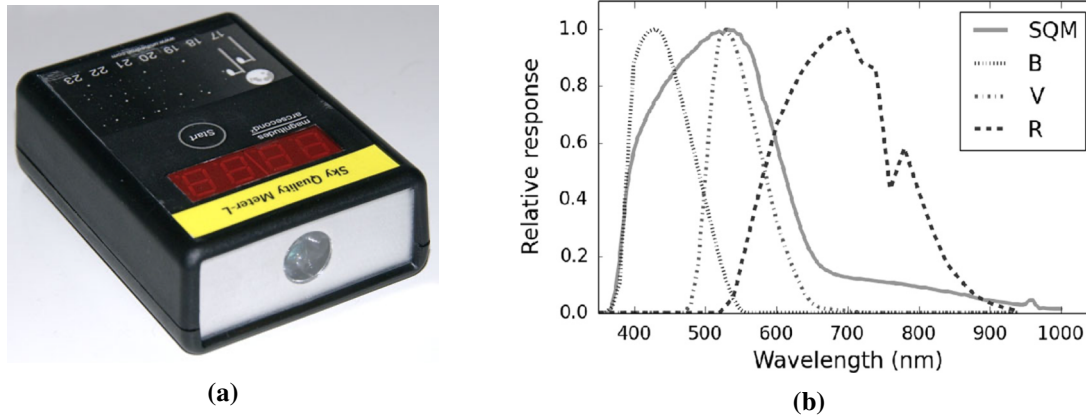


Figure 18 – (a) Aperture of the Unihedron SQM-L device. From Cinzano (2007); (b) Spectral response of the SQM devices. From Aubé et al. (2016). Reprint with permission.

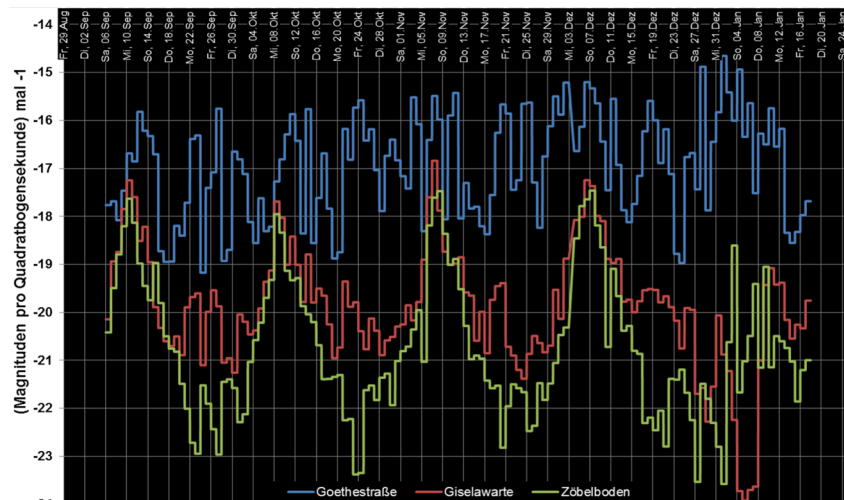


Figure 19 – Night sky brightness data - averaged over each night - in the course of five months at three SQM stations. Goethestraße is located in the provincial capital city Linz (blue line), Giselastraße is suburban (red line) and Zöbelboden is situated in a National Park, therefore rural (green line). The unit of data on the y-axis is $\text{mag arcsec}^{-2} \times (-1)$. Source: Ing. Heribert Kaineder, Amt der oberösterreichischen Landesregierung, Abteilung Umweltschutz

However, Sky Quality Meters are - especially due to being low-priced and still providing data in a satisfactorily accurate precision - the most used devices for characterising light pollution. Because they can work remotely, SQMs are worldwide used to create light monitoring networks and create long-term studies. Currently, Austria has 27 SQM stations installed with the possibility of open-access to data in real time, 24 of them only in the province of Upper Austria (Posch et al. 2018). There the

installation and the first analytics were part of a cooperation between the government of Upper Austria and the Department of Astrophysics Vienna, see (Posch et al. 2017). An example of a short-term evaluation of three SQM stations, Figure 19 demonstrates collected data of five months. Here, to go briefly into detail only, every night is described by a calculated average. The locations chosen are either urban (Goethestraße), suburban (Giselawarte) or rural (Zöbelboden). Their difference in night sky brightness is obvious and in order of magnitudes.

Since the night sky brightness is highly dependent of the lunar illumination, the circalunar rhythm is clearly visible for the rural and suburban sides, whereas it completely loses its shape for the urban location. Consequently, this means that the city of Linz reached a night sky brightness caused by ALAN which is brighter than obtained at full moon. Section 4.4 illustrates a work, carefully discussing the effect of circa-monthly activity caused by moonlight and its influence on results provided by all SQM measurement stations in Upper Austria. The analysis has shown that for sites providing a mean zenithal night sky brightness brighter than $16.5 \text{ mag arcsec}^{-2}$, only due to ALAN, the lunar rhythm vanishes and cannot be seen in the observational data. However, even if being darker in night sky brightness, most of the locations do not show natural rhythms, i.e., only small amount of artificial light can disturb the natural circalunar amplitudes.

By taking a closer look to absolute values, data especially at the rural location seem to even exceed $21.8 \text{ mag arcsec}^{-2}$, mostly being the threshold for skies without any influence of artificial light. However, these results still provide correct data as they are collected in nights with high cloud coverage, even covering natural light coming from stars or the Milky Way.

The analysis of long-term SQM measurements, i.e., couple of months or even years, come with configurable and comprehensive viewing options for the graphical representation, adaptable to respective needs (based on Posch et al. (2018)). Figure 20 illustrates four different display options of two data sets, one originating from an urban site, Linz-Goethestrasse, and one from a rural site, National Park Zoebelboden, both covering the whole year 2018. The analysis results introduced are: (a) Cumulative 'Jellyfish' plots, uncovering accumulations of measured data point over a year by plotting the nocturnal development of the NSB for each night; (b) 'Hourglass' plots, illustrating every night including the nocturnal development of the NSB and length of nights; (c) mean-NSB histograms, showing maxima of and peaks of measured values over the year and (d) circalunar plots, especially indicating nights with new or full moon and therefore showing the lunar cycle and its potential impact to the NSB.

If data covering more years are being analysed, such plots can easily become overloaded. Therefore, a work presented in Section 4.4 tried to investigate if a frequency analysis of the nightly mean zenithal NSB using Fast Fourier Transformation (FFT) leads to suitable results. The conclusion showed that frequencies found in datasets can give hints about the impact of the circalunar periodicity and other seasonal variations. Consequently, the FFT method is a good opportunity of examining long datasets (Puschnig et al. 2020).

To conclude, if trying to achieve an overview about the sky quality at one location as a function of time, an SQM is provided as the right instrument. Still, due to the fact that its measurements are one-dimensional only, there is no way of observing the condition of the whole sky at one time.

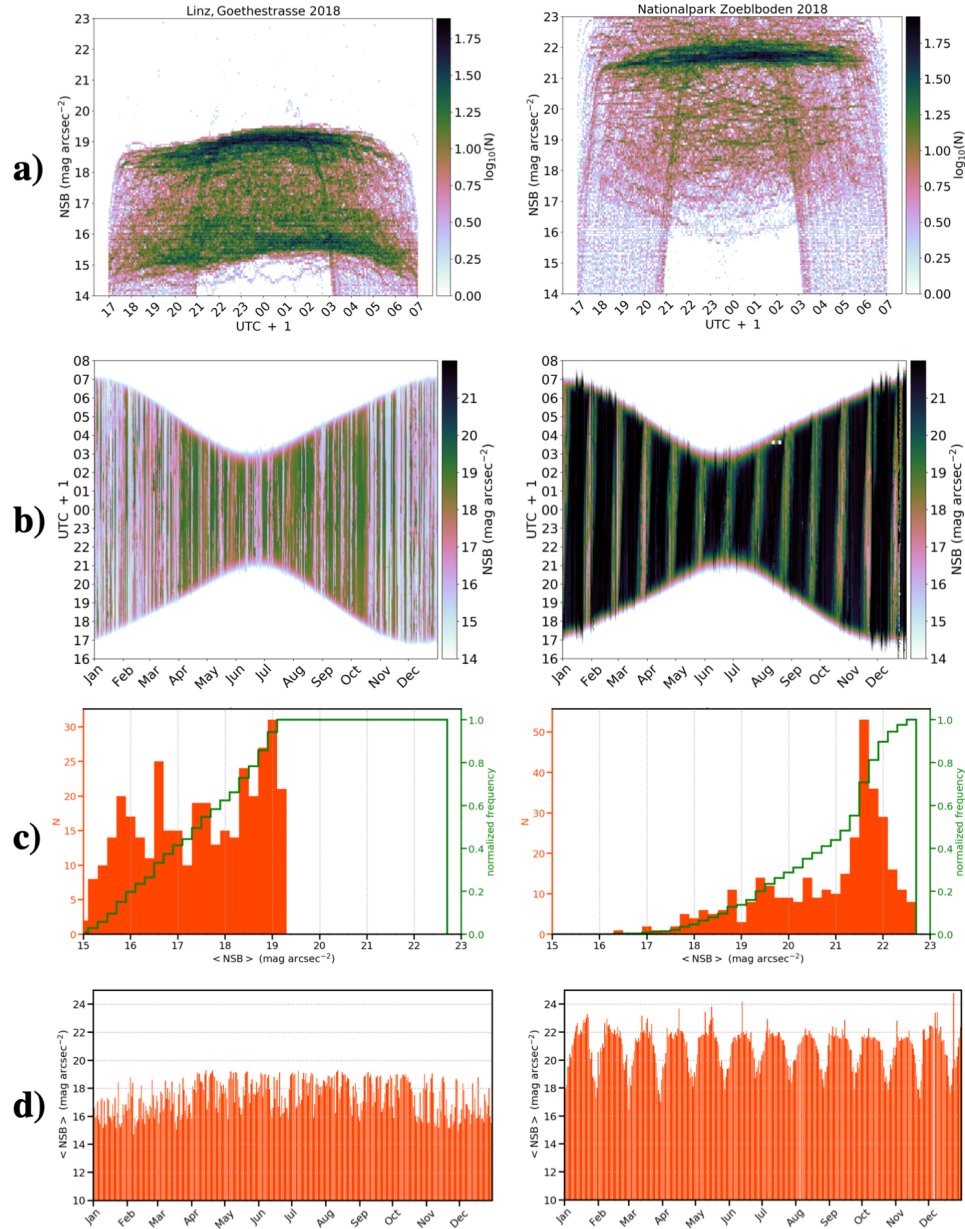


Figure 20 – Potential display options of SQM measurements as captured over the year 2018 on two sites, the left column shows the urban site Linz-Goethestrasse, the right one the rural site National Park Zöbelboden. The plots introduced are (a) 'Jellyfish' plots, (b) 'Hourglass' plots, (c) mean-NSB histograms and (d) circalunar plots (based on [Posch et al. \(2018\)](#)).

2.3 All-sky measurements

All-sky-images are two-dimensional measurements of the entire night sky. Such observations can be obtained via calibrated digital cameras by two different approaches: If equipping the camera with a fisheye lens, the sky as a whole can be captured at one point. Another possibility, using a usual camera lens, is to take multiple images of the sky, capturing it via mosaic imaging. Especially for astronomers, latter option can be of great value due to the possibility of using a CCD camera also (Duriscoe et al., 2007). Both methods do have pros and cons. However, independently of the technique chosen, the aim of all-sky-images is to create a brightness map of the night sky being able to display the skyglow and consequently, the impact of artificial light at night. Furthermore, the sensitivity of digital cameras must be considered, although, their dispersion between types is not very high, see Figure 21.

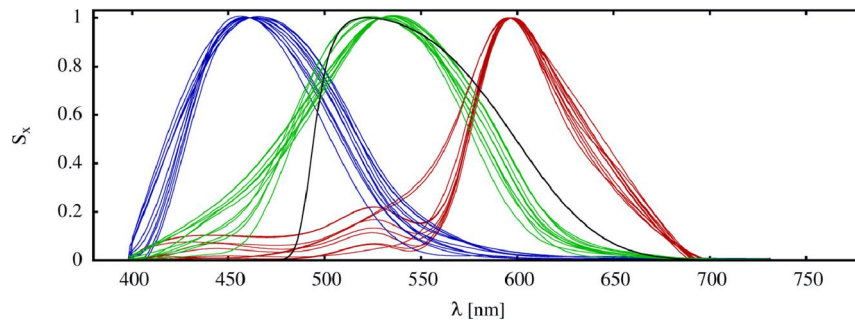


Figure 21 – Spectral sensitivity of commercial DSLR cameras for comparison. The blue, green and red lines show sensitivity curves for various types of DSLR cameras for B, G and R bands, respectively. The V band is shown in comparison (black line). From Kolláth et al. (2020).

Combined with special softwares, all-sky-image raw data processed are turned into matrices which yield exact measurements of the light pollution across the whole sky. Currently, there are two tools available facilitating this: 'DiCaLum' created by Zoltan Kolláth, Eötvös Loránd University, Hungary (Kolláth and Dömény, 2017) and 'Sky Quality Camera', developed by Andrej Mohar from Euromix Ltd., Slovenia (Jechow et al., 2018).

A comparison of both softwares showed that there is only a slight difference detectable, showing a percentage deviation in absolute values of below than ten percent between their results. In particular, compared to any single-point measurement done with an SQM, their analyses enable the possibility of quantifying light domes coming from the horizon, and therefore light emitting sources and their impact to the night sky. Furthermore, by subtracting influences of natural light sources like stars and the Milky Way, data received are even more accurate. Additionally, they enable to see gradients by the subtraction of images, i.e., measured values, from each other or to analyse sectors, i.e., the luminance from zenith to horizon of only chosen azimuths, e.g., light emitting sources.

To give an example of such processed all-sky-images, Figure 22 shows observations of Vienna and the National Park Neusiedler See-Seewinkel (Wallner 2017).

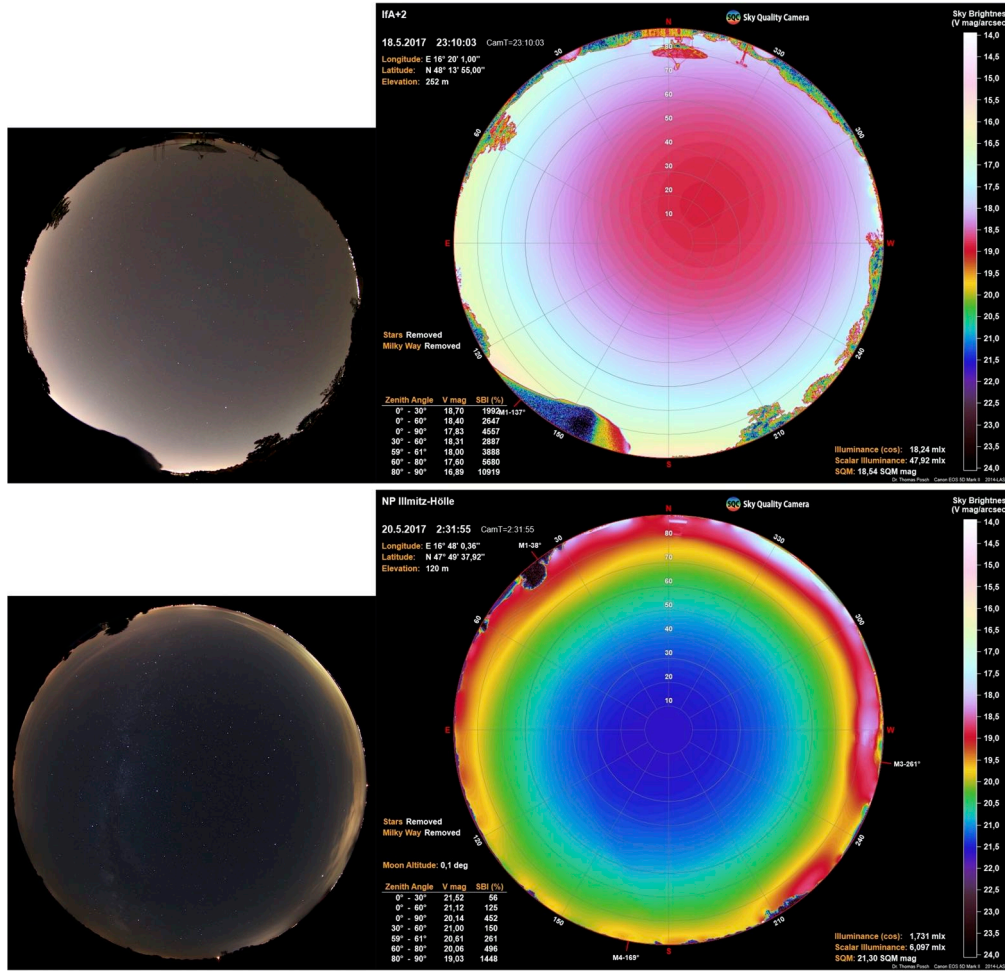


Figure 22 – All-sky-images which show the light pollution at the Department of Astrophysics in Vienna (top) and at the National Park Neusiedler See-Seewinkel in Burgenland (bottom), on the left side the optical images done by a Canon EOS 5D with fisheye lens are shown, on the right side the result of the software "Sky Quality Camera" - taking a look at the scale (white = very bright sky, blue/violet = very dark sky) shows a clear difference between the two locations and underlines that Vienna's night sky is much brighter than at the National Park. From [Wallner \(2017\)](#).

Calculations undertaken are based on the cosine corrected illuminance $E_{v,\cos}$ in the imaging, i.e., horizontal, plane, which is defined as

$$E_{v,\cos} = \int_0^{\frac{\pi}{2}} \int_0^{2\pi} L_{v,\text{sky}}(\theta, \phi) \sin \theta \cos \theta d\phi d\theta, \quad (22)$$

with the assumption of the sky being a hemisphere. Here, θ is the zenith angle, ϕ the azimuth angle and $L_{v,\text{sky}}$ the luminance of the sky. As an example, a typical clear night sky, being not influenced by artificial light, provides a luminance at the zenith of $L_{v,\text{sky},\text{zen}} = 0.25 \text{ mcd/m}^2$. With the approximation of luminance being constant over the whole hemisphere, i.e., $L_{v,\text{sky}}(\theta, \phi) = L_{v,\text{sky},\text{zen}} = \text{const.}$, the horizontal illuminance provides a value of $E_{v,\cos} \approx 0.78 \text{ mlx}$. The illuminance caused by a night sky not affected by light pollution is often approximated with 1 mlx, the calculation founds this to be in order. However, there is the issue that, especially for ecological studies observing the impact on

specific organisms, the 'scalar illuminance' $E_{v,scal,hem}$ describing the total luminous flux incident on a small spherical surface, can be of better fit. Using no cosine correction, it can be defined as

$$E_{v,scal,hem} = \int_0^{\frac{\pi}{2}} \int_0^{2\pi} L_{v,sky}(\theta, \phi) \sin \theta d\phi d\theta, \quad (23)$$

respectively (Jechow et al., 2017).

All technical possibilities show that all-sky-images are a technique of high importance and a valuable input for the light pollution community and therefore frequently used for characterising night skies (Jechow et al., 2016, 2019; Kocifaj et al., 2015). To pre-empt findings discussed in works illustrated in Sections 4.1 and 4.5, all-sky-imagery can also provide input information for modelling approaches (Kocifaj et al., 2019; Wallner et al., 2020). Such linking of photometry and simulations was done before by Kolláth and Kránicz (2014); Kolláth et al. (2016) by the performing of Monte-Carlo simulations, and underlines the need of both investigation concepts. Since meteorological and especially atmospheric parameters are constantly changing, it is impossible to find exact inputs for theoretical simulations for one location and time. Nevertheless, this issue can, for many cases, be avoided if conducting images of sites chosen to be analysed, since images are capturing the conditions at one point. Consequently, if being brought together, theory and practical measurements can lead to significant achievements with an impact in terms of scientific and technological advancement.

2.4 Vertical fisheye observations

The technique of vertical fisheye observations bases on a work presented later in Section 4.3 of this thesis (Wallner, 2019). It uses the same instruments and analysis method as all-sky-images, presented in Section 2.3, though observations differ slightly. Here, the camera equipped with the fisheye lens, is not pointed to the upper hemisphere to capture the night sky, but instead it is focused towards light emitting sources or illuminated surfaces directly. Consequently, the camera is pointed vertically to its original build-up. Without the need of long exposure times, compared to all-sky-images with up to nearly two minutes, images are taken in under a second time due detecting larger luminance values compared to the night sky. It follows that a build-up including a tripod is not necessary, resulting in a quickly performed imaging technique easy to use.

Additionally, the SQC-software is capable of providing information about the correlated colour temperature (CCT). Consequently, light pollution sources like single lamps or illuminated buildings and surroundings can be characterised in greater detail. Furthermore, the lighting efficacy of luminaires can be quantified in particular. Via image subtraction, the gradient of change can be used to find optimal lighting solutions if conducting lamp conversions. Figure 23 illustrates an extract, the analysis of an illuminated surface, from the main work.

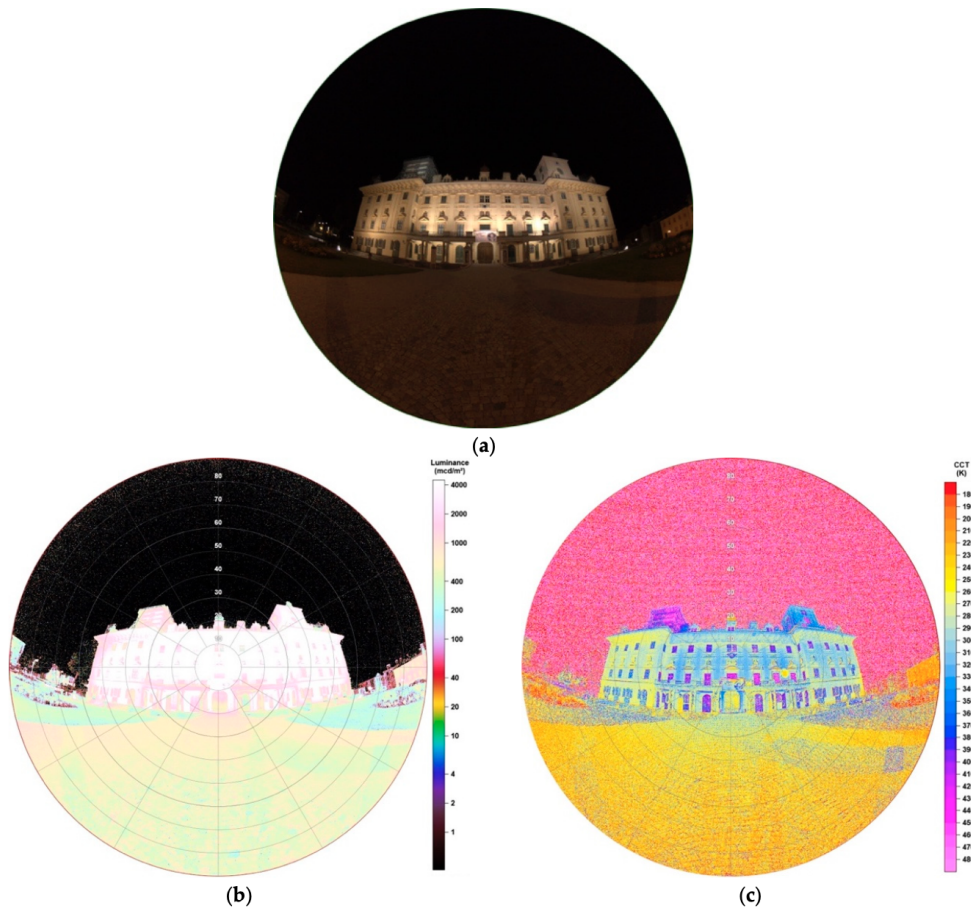


Figure 23 – Vertical fisheye observation and analysis results of the illuminated Castle Esterhazy (Eisenstadt, Austria). (a) shows the raw image as captured, (b) the luminance matrix and (c) the CCT matrix as both provided by the software 'Sky Quality Camera'. From [Wallner \(2019\)](#).

2.5 Spectral measurements

As discussed above in Sections [1.1.2](#), [1.1.3](#) and [1.2](#), the colour temperature of lighting systems used exercise lots of influence regarding impacts on all forms of life and energy sustainability. Very often public databases listing types and numbers of illuminators are missing and private lights as well as advertisements cannot be counted or foreseen. Hence, it is necessary to obtain information about existing situations in towns and cities. Needless to say, all measurement and modelling techniques can help in achieving this, although, spectral observations can characterise the overall picture of light and the amount of emissions in certain wavelength ranges by all light emitting sources. In the case of an extended research searching for city emission functions, which will be discussed later in Section [3](#), the spectral power distribution is together with the total energy output the most important parameter in describing the unique shape of each source.

2.5.1 Influence of various light sources on skyglow

Nearly each spectrometer or spectrograph, if or if not mounted on a telescope, is capable of observing spectra of the sky. This is of great interest, e.g., during sunset being able to detect absorption bands

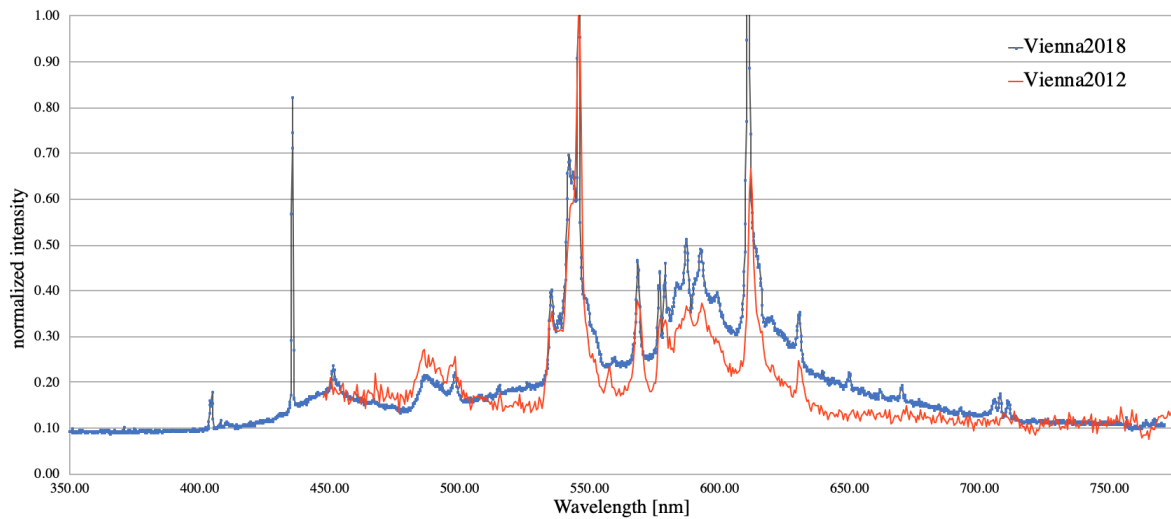


Figure 24 – Spectral power distributions as resulted from measurements collected with the 80 cm Cassegrain telescope at the Vienna University Observatory. Source: J. Puschnig, Argelander-Institut für Astronomie, University of Bonn and F. Binder, Department of Astrophysics, University of Vienna.

due to electronic transitions of molecular oxygen. However, it can also be used to measure the spectral power distribution of skyglow during nighttimes. First, it is important to know, how light source types can influence a city's emission at all. Actually, two components of light yield to impacts on the night sky. On the one hand, there is light travelling directly to the upper hemisphere. This can be a result of lighting fixtures emitting light in an angle of more than 90° , being therefore incompletely shielded or not at all. On the other hand, light can also travel via circuitous routes, being reflected on streets or walls. Logically, the strength of this effect is dependent on the reflectivity of illuminated surfaces. Compared to satellite observations, a variety of instruments can be used and broader wavelength ranges are possible to detect.

Some first information drawn from the spectral observations of skyglow is the possibility of identification of luminaires used in a city. Such conclusions can be deduced by comparing the captured spectral power distribution to ones known from light sources. If a mixture of a variety of sources can be distinguished, also the relative contribution of each can be received. As an example, spectral observations of the skyglow of Vienna in 2012 have shown that at that time 71% of light scattered in the atmosphere originates from fluorescent lamps, 25% from high pressure sodiums lamps and 4% from other sources, including, e.g., high pressure mercury vapour lamps (Puschnig et al., 2014). Figure 24 contrasts one of the spectra obtained in 2012 with a test spectrum collected in 2018. Since LED conversion did not start before 2017 in Vienna, only small deviations are visible. Both spectra show their strongest peaks at 546 nm and an adjacent line at 544 nm which are in fact the ones referring to fluorescent lamps. Peaks at 611 nm are due to a mixture of high pressure sodium lamps. Latter can be clearly identified by looking at sodium lines at 569 nm, 588 nm and 593 nm. However, if discussing occurring changes, one can see that the amount of light emitted in lower wavelengths, up to ~ 540 nm, increased, while decreasing for higher wavelengths. This can be traced back to conversions to blue-richer LEDs. Since luminaires of streets are converted to 4000 K LEDs and only replacing fluorescent lamps with nearly the same colour temperature, the changes must be due to changes of lighting systems of advertisements or illuminated buildings. However, to summarise here, spectral

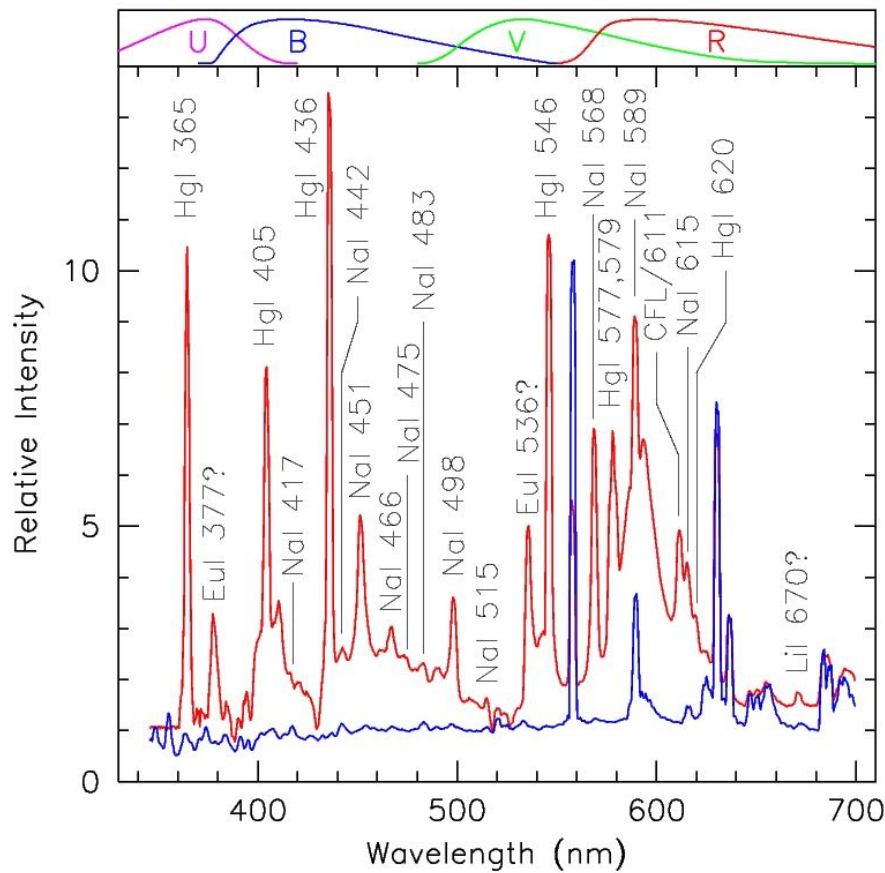


Figure 25 – Comparison between a light polluted night sky at Asiago Astrophysical Observatory, Italy (red line) and the ESO-Paranal, Chile providing a sky nearly without the influence of ALAN (blue line). From [Patat \(2010\)](#).

observations can optimally support observations analysing the development of skyglow during conversions of lighting systems. Figure 25 illustrates the large dispersion in spectral data between a light polluted and a dark sky. It is clearly visible that the influence of ALAN creates large amount of noise leading to problems with astronomical observations.

Furthermore, various types of light sources not only end up in different spectral power distributions but also have significant impacts on the night sky brightness. Due to higher efficacies of luminaires with increased colour temperature and scattering efficiencies of shorter wavelengths, theoretical models have shown that public lighting composed of LEDs with 5000/5100 K lead to a night sky brightness increased by a factor of 8 compared to low pressure sodium lamps and three times brighter than high pressure sodium lamps ([Luginbuhl et al. 2014](#)). The work presented in Section 4.6 discusses this phenomenon as modelled for the megacity of Mexico City. However, this effect is nearly impossible to be observed by measurements since they are demanded to be taken before and after conversions, usually with a time-gap in between too big to assume constant conditions like number and intensity of all lightings, again including advertisements or buildings, installed in a certain place.

2.5.2 Numerical values of spectral impacts

Distance [km]	Clear Sky						Cloudy Sky					
	MSI		ISI		SLI		MSI		ISI		SLI	
	0	30	0	30	0	30	0	30	0	30	0	30
LPS	0.008	0.014	0.241	0.349	0.053	0.078	0.012	0.015	0.317	0.359	0.072	0.081
HPS	0.099	0.113	0.342	0.465	0.188	0.218	0.107	0.114	0.430	0.477	0.210	0.221
Metal Halide	0.663	0.634	0.678	0.651	0.547	0.567	0.647	0.631	0.658	0.648	0.563	0.570
Fluorescent T8	0.403	0.427	0.549	0.594	0.561	0.595	0.417	0.430	0.579	0.598	0.585	0.598
LED 5000 K	0.500	0.533	0.601	0.631	0.598	0.610	0.517	0.536	0.618	0.633	0.608	0.611
LED 4000 K	0.422	0.445	0.555	0.607	0.521	0.550	0.435	0.448	0.591	0.611	0.543	0.553
LED 2700 K	0.261	0.280	0.439	0.516	0.330	0.349	0.271	0.282	0.492	0.524	0.346	0.352
PC Amber	0.034	0.042	0.357	0.540	0.107	0.140	0.039	0.043	0.491	0.558	0.131	0.144
CIE D65	1.000	1.000	1.000	1.000	1.000	1.000	1.000	1.000	1.000	1.000	1.000	1.000

Table 4 – Values for Melatonin Suppression Index *MSI*, Induced Photosynthesis Index *ISI* and Star Light Index *SLI* for directly overhead of an observer, i.e., distance of 0 km, and farer away at 30 km. Cloudy sky values include scattering effects on lower atmospheric scale heights. Extract from [Aubé et al. \(2013\)](#).

Section 1.2 already supplied impressions and examples of impacts on nearly all forms of life on Earth, one may ask if those can be expressed numerically and therefore quantified more precisely. In order to achieve this, [Aubé et al. \(2013\)](#) introduced the possibility of relating certain light sources to three natural processes, namely the melatonin suppression, the photosynthesis and the stellar visibility. The result are indices providing information about the degree of influence, depending solely on the spectral power distribution of the light emitting source. The higher the values are, all ranging from 0 to 1, the more impact can be supposed.

The power spectrum of a light source is related to the melatonin suppression action spectrum $M(\lambda)$ resulting in the Melatonin Suppression Index *MSI*, to the photosynthesis action spectrum $P(\lambda)$ resulting in the Induced Photosynthesis Index *ISI* and to the scotopic spectral sensitivity $V'(\lambda)$ resulting in the Star Light Index *SLI*. The derivations of indices discussed are

$$MSI = \frac{\int_{380\text{nm}}^{730\text{nm}} \Phi_{n,\text{lamp}}(r, \lambda) M(\lambda) d\lambda}{\int_{380\text{nm}}^{730\text{nm}} \Phi_{n,\text{D65}}(r, \lambda) M(\lambda) d\lambda}, \quad (24)$$

$$ISI = \frac{\int_{380\text{nm}}^{730\text{nm}} \Phi_{n,\text{lamp}}(r, \lambda) P(\lambda) d\lambda}{\int_{380\text{nm}}^{730\text{nm}} \Phi_{n,\text{D65}}(r, \lambda) P(\lambda) d\lambda}, \quad (25)$$

$$SLI = \frac{\int_{380\text{nm}}^{730\text{nm}} \Phi_{n,\text{lamp}}(r, \lambda) V'(\lambda) d\lambda}{\int_{380\text{nm}}^{730\text{nm}} \Phi_{n,\text{D65}}(r, \lambda) V'(\lambda) d\lambda}, \quad (26)$$

with $\Phi_n(\lambda)$ being a normalisation leading to a constant lumen spectral power distribution, calculated as

$$\Phi_n(\lambda) = \frac{\Phi(\lambda)}{\int_{380\text{nm}}^{730\text{nm}} \Phi(\lambda)V(\lambda)d\lambda}. \quad (27)$$

Here, $\Phi(\lambda)$ is the unnormalised spectral power distribution of the lamp to be analysed, $V(\lambda)$ is the photopic sensitivity function. As Eq. 24, 25 and 26 illustrate, it is necessary to compare the lamp to a standard spectrum. Since biological evolutions occurring under sunlight were considered as reference, the daylight illuminant CIE D65 was chosen. With a colour temperature of 6500 K it nearly shows the same properties as a midday sun in Northern and Western Europe. Table 4 compares the indices for selected luminaires.

2.6 Satellite observations

Observations on scales at least as big as whole towns or cities can be performed via satellite imagery. Remote nighttime data measuring the radiance of Earth's surface are valuable insights into the global long-term development of light pollution, making statements about potential changes in intensity and distribution. A total of three satellites, two of them still active, provide nighttime images with datasets either freely available - which is not the case for, e.g., JL1-3B and EROS-B - or provide the possibility of automatic georeferencing - which is not the case for, e.g., the International Space Station (ISS).

2.6.1 DMSP-OLS

The first satellite providing usable data was launched in 1992, the Defense Meteorological Satellite Program Operational Linescan System (DMSP-OLS), headed by the U.S. Department of Defense. Operating until 2013, it was the only satellite providing valuable information for light pollution researchers for a long time. Although it impressed through its large wavelength range with the visible telescope being sensitive to radiation between $0.4\mu\text{m}$ - $1.10\mu\text{m}$, main handicaps were a low spatial resolution of 2.7 km and, possibly its biggest disadvantage, having no on-board calibration and thus complicating work on datasets. However, it was possible to quantify and compare light emitting sources and data are still used today in order to analyse the satellite's long-term past observations.

2.6.2 NPP-VIIRS

Currently, one of the two satellites active in investigating artificial light pollution is the Visible Infrared Imaging Radiometer Suite (VIIRS), being an instrument of the Suomi National Polar-Orbiting Partnership (Suomi-NPP) satellite (Changyong et al., 2017). Its main purpose is to produce imagery of clouds, night and terminator scenes. Launched in October 2011, its nadir door opened one month later, providing its first light images (Cao et al., 2014). Due to the existence of 22 spectral bands, including 16 of moderate resolution (M-bands), 5 of imaging resolution and one panchromatic Day and Night-Band (DNB), the electromagnetic spectrum between $0.412\mu\text{m}$ to $12.01\mu\text{m}$ is covered. Latter, the DNB, is the channel used for measuring radiances and reflections on Earth's surface, its spectral coverage ranges from $0.50 - 0.90\mu\text{m}$.

Using four charge-coupled device (CCD) arrays, the band is able to measure night lights and reflected solar or moon lights, providing a huge dynamic range of 45,000,000:1. Consequently, signals as low as quarter moon illumination to brightest daylight can be captured. The scan width of 112.56° entails a swath of 3060 km while the DNB maintains a spatial resolution of 742 m throughout. Providing a revisit time of 12 h, the satellite performs a full global coverage for both solar and lunar illumination. It is necessary to collect calibration data of multiple orbits, due to a large number of scans needed to complete a calibration cycle by time windows being too short to cycle through all aggregation modes. Figure 26 illustrates a composite image of Earth's surface at night, impressively evincing sources of artificial light.



Figure 26 – The 'Black Marble', a composite image as assembled from several VIIRS nighttime observations in 2016. Source: NASA Earth Observatory images by Joshua Stevens, using Suomi NPP VIIRS data from Miguel Román, NASA's Goddard Space Flight Center

2.6.3 Luojia 1-01

LJ 1-01 is a CubeSat operated by the Wuhan University, China and was launched on 2 June, 2018. It was built aiming to acquire high-resolution nighttime imagery and acts as prototype for a future satellite mission including constellation of 60 to 80 units for Earth observation. Fine resolution nighttime images with a spatial resolution of 130 m enable a sensitivity never reached before. Covering a smaller range in wavelengths than the VIIRS, due to its orbit the revisit time is 15 d which could be problematic for short-term analyses. Still, the dynamic range reached by Luojia 1-01 is higher compared to the NPP-VIIRS, providing the possibility of dissolving an even higher range in signal thresholds. The result are finer spatial details of luminaires, i.e., very bright areas, but on the other hand clouds and the moon can influence and lower quality of the images captured. Latter constitutes the need of additional tasks in preprocessing of raw data. However, because Luojia 1-01 lacks of ground-based measurements accurately, the radiometric calibration cannot be conducted as for NPP-VIIRS nighttime imagery, which makes a direct comparison nearly impossible. In any case, the high precision of LJ 1-01 is outstanding and therefore the satellite constitutes to be a valuable tool for future observations of light pollution in high accuracies ([Jiang et al., 2018](#); [Wang et al., 2020](#)).

2.6.4 Comparison

Key specifications of all three mentioned satellites are shown in Table 5. Figure 27 compares images of the city of Wuhan, China as captured over the years by all of those discussed.

	DMSP-OLS	NPP-VIIRS	LJ 1-01
Operator	U.S. Dept. of Defense	NASA/NOAA	Wuhan University
Service life	1992 - 2013	2011 - present	2018 - present
Wavelength range	0.41 - 1.10 μm	0.50 - 0.90 μm	0.48 - 0.80 μm
Orbital altitude	829 km	829 km	645 km
Spatial resolution	2.7 km	742 m	130 m
Swath	~3000 km	~3000 km	~250 km
Revisit time	12 h	12 h	15 d
On-board calibration	No	Yes	Yes

Table 5 – Comparison of specifications of the three satellites performing nighttime imagery: Defense Meteorological Satellite Program Operational Linescan System (DMSP-OLS), Suomi National Polar-Orbiting Partnership Visible Infrared Imaging Radiometer Suite (NPP-VIIRS) and LuoJia 1-01 (LJ 1-01). For given wavelength ranges, only channels/bands useable for nighttime imagery are indicated. (Jiang et al., 2018; Wang et al., 2020)

All satellites presented share one dominating disadvantage which is going to lead to difficulties in the long run of nighttime imagery. Those satellites providing data of high accuracy, i.e., NPP-VIIRS and LJ 1-01, show weaknesses in their spectral sensitivities, being blind to short wavelengths below 480 or 500 nm, respectively. Regarding conversions to LEDs, often providing illumination of high colour temperatures, as discussed above in Sections 1.1.2 and 1.1.3, this issue must not be ignored. Even if cities become brighter, by changing the colour of light emitting sources, existing devices possibly predict a decrease in skyglow. Although, the satellites provide the best opportunity of quantifying global developments, results on the other hand are to be enjoyed with caution. Local measurements and observations on smaller scales seem important to be taken into consideration and therefore are not negligible to permit clear forecasts.

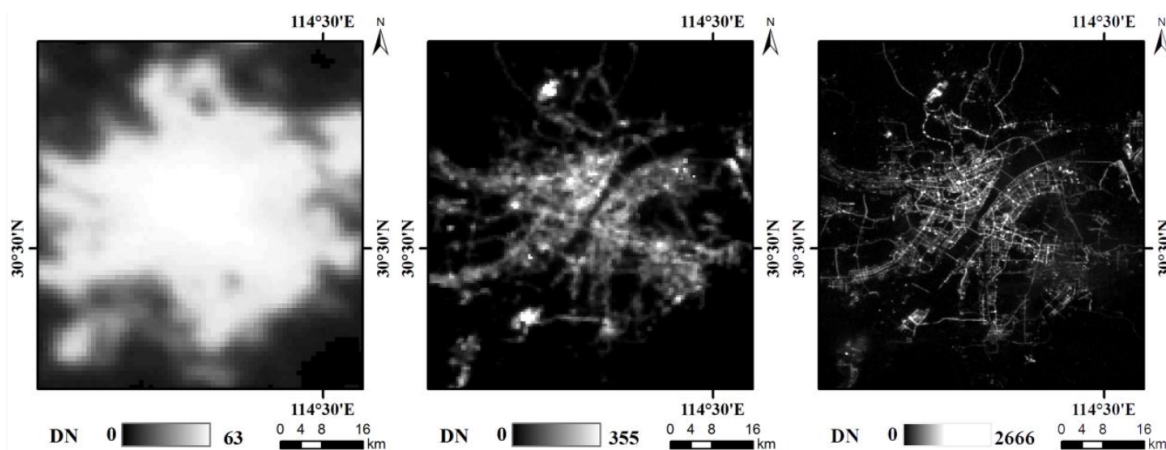
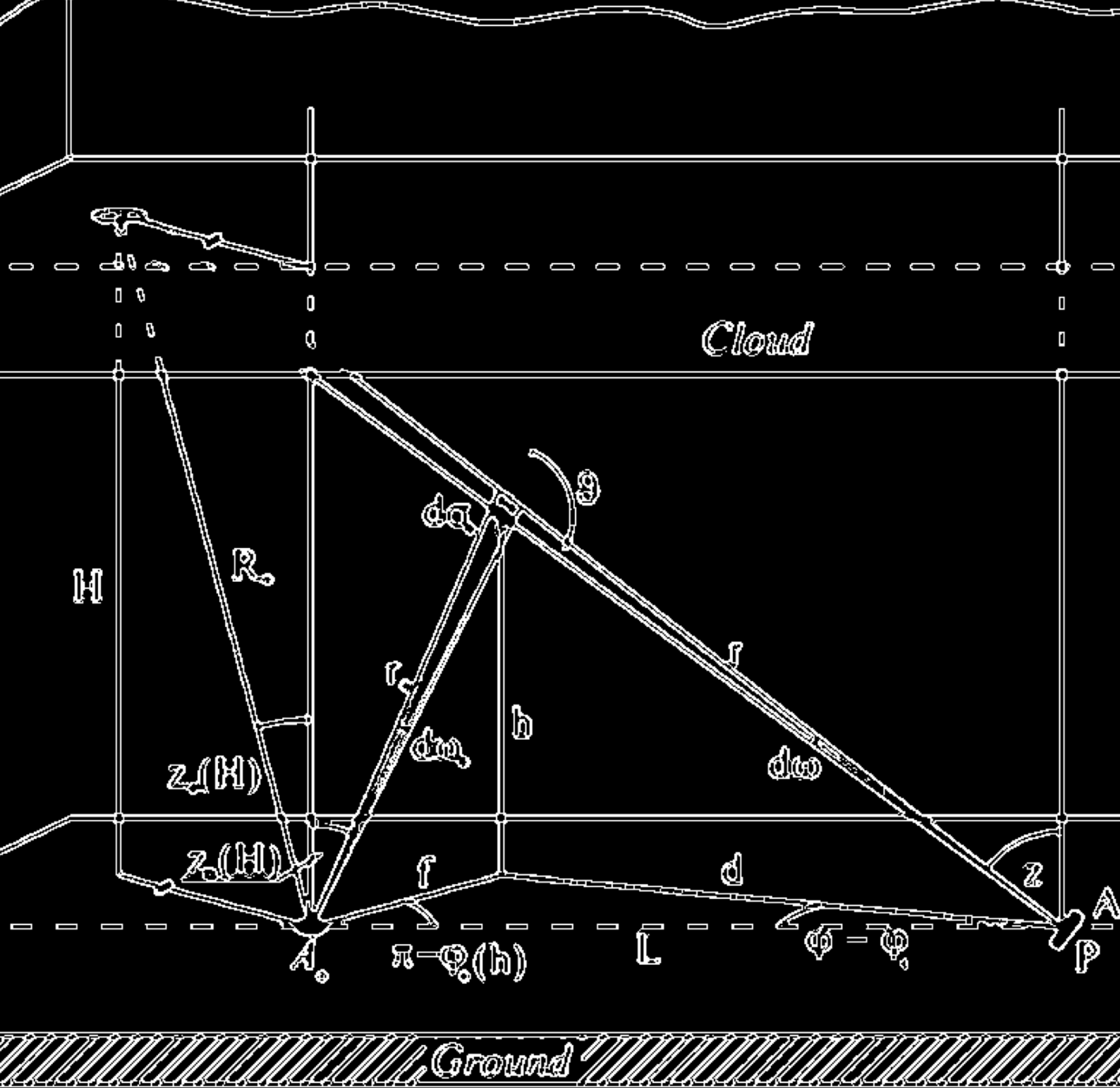


Figure 27 – The city of Wuhan, China as captured by the three satellites discussed. Left: DMSP-OLS in 2013, middle: NPP-VIIRS in 2018, right: LJ 1-01 in 2018. The change in spatial resolutions is significant and clearly visible. (Jiang et al., 2018)



MODELLING
LIGHT POLLUTION

3

3 Modelling Light Pollution

Modelling light pollution, or skyglow, is a matter of high complexity. There are two major factors influencing the behaviour of radiated light and also its result in possible light domes over a city. On the one hand, there is Earth's atmosphere, providing the most volatile part of simulations. Without its existence, there would be no light pollution at all since radiated light to the upper hemisphere would be 'lost' in space. On the other hand, there is the need of having information about the emitted light source itself, which leads to major approximations and assumptions with increased size of investigated areas.

Since especially the atmosphere is variable in very short time scales, while skyglow and light emitting sources are relatively stable over much larger time scales, it is impossible to model certain states of the atmosphere at desired fixed times. The following section gives an overview on the fundamental basics of light pollution modelling and focuses on the most important parameters being used in selected modelling tools.

3.1 Fundamentals of skyglow modelling I - Basic properties of the atmosphere

3.1.1 Aerosols and molecules

With the aim of foreseeing the impacts of light radiated from ground-based sources towards the upper hemisphere, one has to understand the reciprocal action between the emitted electromagnetic light waves with particles in the atmosphere. Molecules and, with a view to light pollution far more important, aerosols distort the original signal and have a significant impact on what is observed in or around a light emitting city. Since, as discussed before, the atmosphere is no stable structure and due to the fact that aerosols are omnipresent with variability in sizes or shapes, they play a key role in skyglow modelling. Past studies include investigations about urban light pollution and the connected role of aerosols also on astronomical observations especially (Joseph et al., 1991).

Following derivations of Horvath (2014), molecules can be approximated as simple dipoles radiating incident light in various directions due to changes of the dipole moment. Consequently, particles like aerosols consisting of various dipoles show a more complex behaviour. Therefore, when introducing a radiative transfer model simulating the encounter of light waves and such atmospheric environment, there is an infinitesimal volume element which contains gas and particles as object of reflection for subsequent evaluation. Figure 28 illustrates such volume element dV being illuminated by a light beam with flux density S . Depending on the composition of the gaseous mixture, light is then scattered into a specific direction as defined by the scattering angle θ and solid angle $d\omega$. This simple design of a single scattering event enables the possibility of defining important parameters and functions for characterisation.

The volume scattering function $\gamma(\theta)$ depicts properties of the volume element's constituents by connecting the incident light beam with the solid scattering angle, resulting in the total flux scattered, given as

$$d^2\phi = S\gamma(\theta)d\omega dv. \quad (28)$$

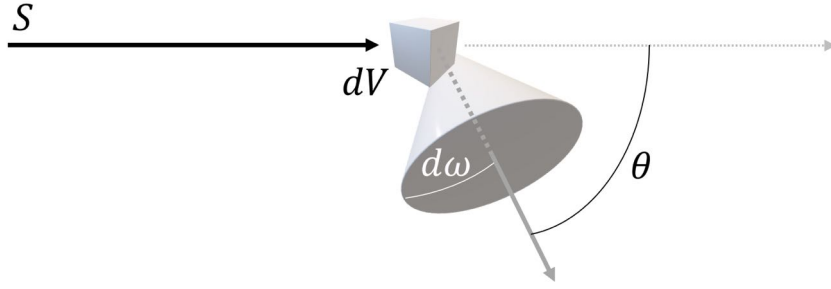


Figure 28 – An incident light beam with flux density S meets a volume element dV containing gas and particles. The light is then scattered into a direction defined by the angle θ in a cone with its opening defined by a solid angle $d\omega$. This concept illustrates the simplest design of a scattering process as occurring in Earth’s atmosphere. Created by Stefan Wallner.

Integrating the flux over all directions results in the total flux, defined as

$$d\phi = S dV \int_{4\pi} \gamma(\theta) d\omega, \quad (29)$$

whereas $\int_{4\pi} \gamma(\theta) d\omega = \sigma_s$ is the scattering coefficient, describing the decrease of light intensity per unit length. Since both parameters are still strongly dependent on the particle number, this issue can be solved via dividing the scattering function by its integral, resulting in the scattering phase function $P(\theta)$, which quantifies the angular distribution of scattered light, as follows

$$P(\theta) = 4\pi \left(\frac{\gamma(\theta)}{\sigma_s} \right). \quad (30)$$

The phase function, being consequently a highly demanded parameter for skyglow modelling, is strongly dependent on the shape of the scattering body, especially its size. In general, it can be applied that with increasing size of particles, either radius or length, the greater is the proportion of light being scattered in forward direction (Bohren and Huffman, 1983). Figure 29 shows the phase functions for different spherical particles varying in size, i.e., in diameter.

Regarding the shape of the scattering body, it cannot be overlooked that there are significant disparities when distinguishing spherical or non-spherical particles. Figure 30 illustrates the development of the optical signal, depending on the scattering coefficient k_{sca}^a and phase function $p(\pi)$ (Kocifaj and Kómar, 2016). As seen from the phase function’s defined solid angle, only backscatter signals were considered, either for spherical particles of different compositions or for the non-spherical particle model U2015 B10, as defined for an irregular cosmic dust particle (Kocifaj et al., 1999), also composed of different materials. Figures 29 and 30 underline the complexity of skyglow modelling, since, it should be stressed here once again, the atmosphere is not stable and highly variable in number and types of particles and aerosols. However, it was shown that if investigating an incident light beam with wavelength comparable to the scatter body, especially low absorbing particles show large contrasts between spherical and non-spherical particles.

At this point only scattering effects were considered, whereas the atmosphere is also causing attenuation of an incident light beam by absorption. Especially the albedo of aerosols can influence the

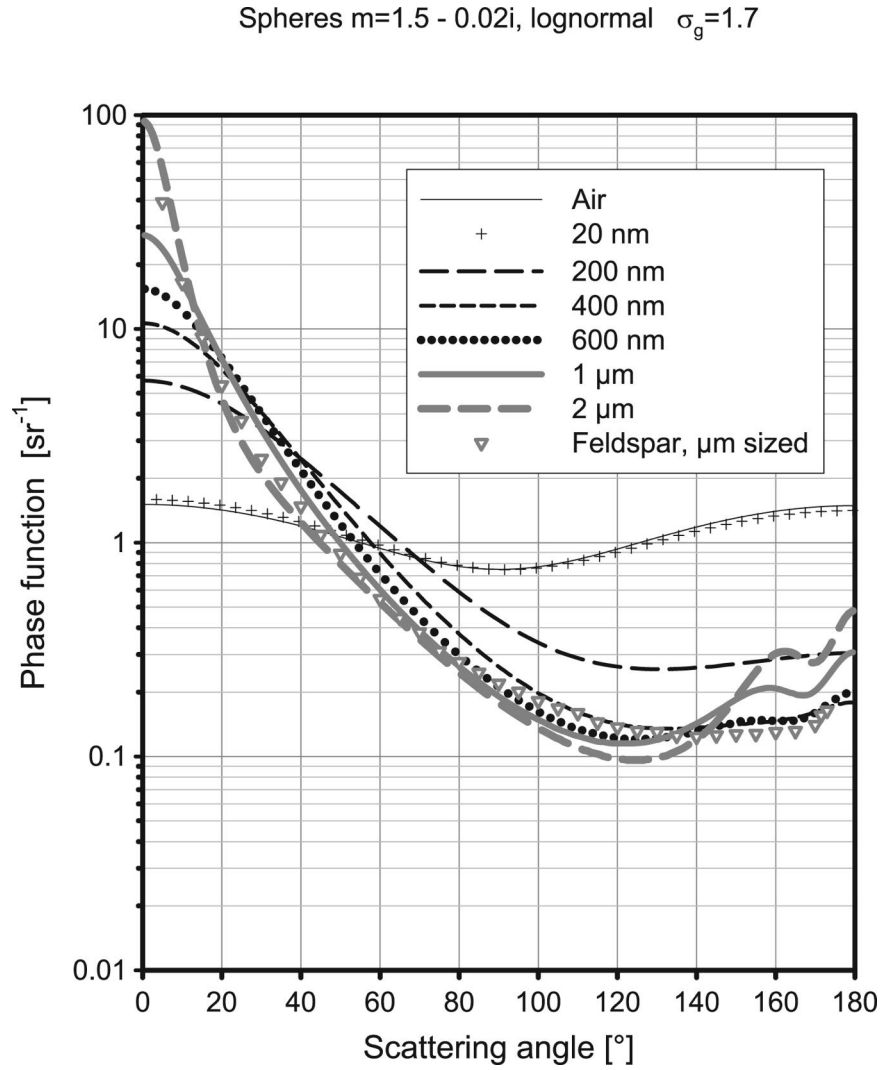


Figure 29 – Various scattering phase functions as computed for spherical particles with different diameters as studied by [Horvath \(2014\)](#). A scattering angle below 90° describes backscattering, an angle of exactly 90° side-scattering and a value higher than 90° forward-scattering. m defines a lognormal size distribution of the particles, σ_g quantifies the geometric standard deviation. The figure shows the power of scattering cross sections, being higher for lower scattering angles. Feldspar is the only particle included having a non-spherical shape.

overall extinction. [Kocifaj and Kómar \(2016\)](#) specifically distinguishes between two cases of skyglow origins. On the one hand, an urban area is characterised by a large number of pollutants. With an observer located inside of the light polluting source, i.e., near to the emitting source, backscattering is dominating skyglow. Considering particles large in their size, scattering becomes less efficient and the absorption is more dominating with increasing diameter, as seen before. Keeping in mind that an urban environment was considered, it follows that such urban particles can work as attenuators for light pollution and lower backscattering intensities. As discussed above this results in the backscatter signal being dominated by non-absorbing particles. On the other hand, the second case study deals with large distances to a light emitting source. Models show that such build up must be treated differently since here near-forward scattering is prevailing. Especially for large non-spherical particles this effect is more intense than for equal-volume spherical particles. In conclusion, skyglow from a city with large distance can be amplified due to the non-spherical particles.

To summarise, the shape, size and composition of scattering bodies play an important role in describing the scattering behaviour of a light wave in the atmosphere. All parameters listed show contributions with different strengths, depending on the position of a light emitting source to an observer, i.e., being located in the near environment or distant. This results not only in the distribution of light over a certain area, the scattering process, but also in an attenuation of an incident light beam and also influences its spectral behaviour ([Kocifaj, 2010](#)).

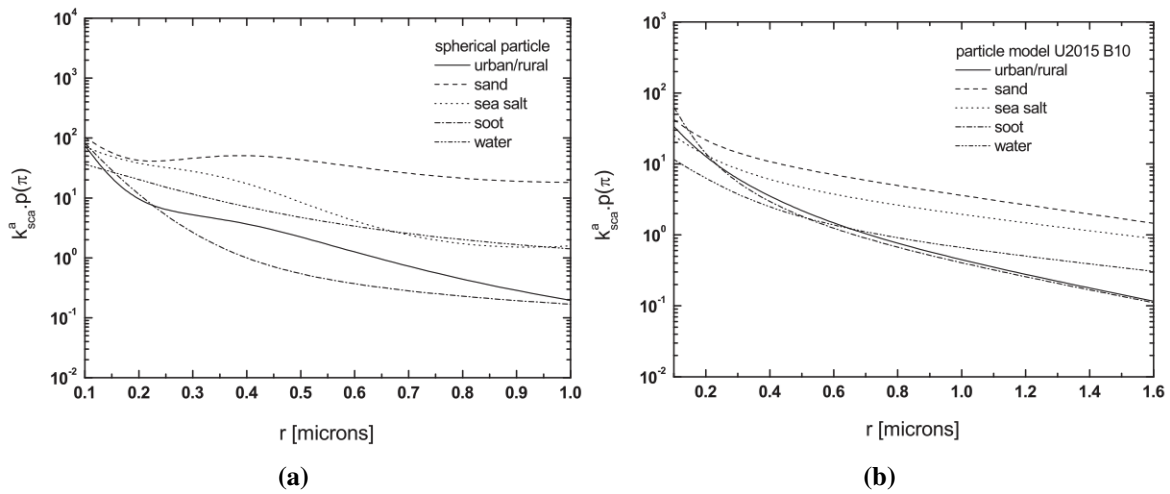


Figure 30 – Development of the scattering coefficient k_{sca}^a and phase function $p(\pi)$ for backscattering signals with particles of different origins as simulated by [Kocifaj and Kómar \(2016\)](#). (a) Assumption of spherical particles with computations provided for a wavelength of $\lambda = 500$ nm.; (b) Assumption particles shaped as the non-spherical model U2015 B10, as defined for an irregular cosmic dust particle. Computations are provided for a wavelength of $\lambda = 800$ nm.

3.1.2 Scattering orders

In general, modelling of the scattering effects committed by a volume sphere in the atmosphere only considers one scattering event, i.e., single scattering, or maximally two events, i.e., double-scattering. Comparing the aerosol optical thickness, it can be assumed that an increase, and following a higher

number of particles present, also enhances the need of assessment of the multiple scattering contribution.

The reason why models usually adhere to a maximum of two scattering events is to reduce computational time, running a simple and fast algorithm while approximating the influence of higher scattering phenomena being neglectable. Aiming to investigate the real impact of higher scattering orders, [Kocifaj \(2018a\)](#) developed an analytical model enabling the calculation of all higher orders. In difference to an experimental approach, such numerical validation solely enables the analysis of single contributions of each scattering order. Figure 31 illustrates results for diffuse irradiance due to the first four scattering orders, either as downwelling irradiance at the ground or upwelling irradiance at the top of the atmosphere. Generally, the plots illustrate higher scattering orders becoming more dominant with increasing distance to a light emitting source. It must be added that this is only applicable for the sky being located opposite the azimuthal position of the light-emitting pixel. Also, spectral distortions are clearly visible. As discussed above, shorter wavelengths show a stronger scattering behaviour for backscatter signals, i.e., first-order scattering (D_1^+) and low scattering angles, larger wavelengths dominate with increasing distance at this point. Considering multiple scattering (D_2^+ , D_3^+ and D_4^+), this effect is lost.

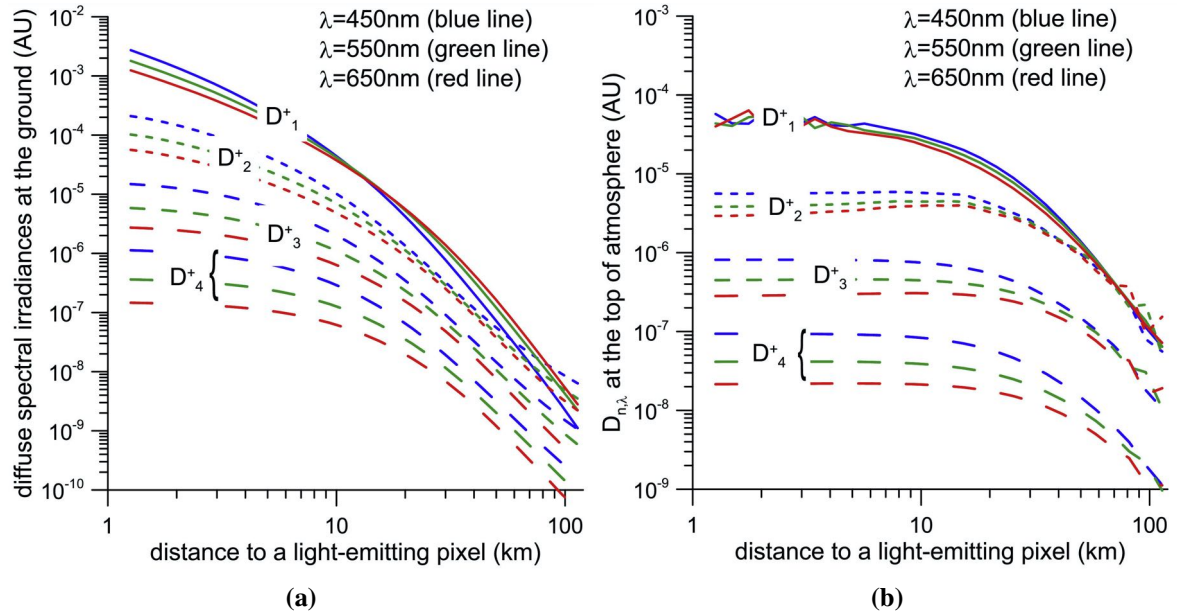


Figure 31 – Results of an analytical provided by [Kocifaj \(2018a\)](#) aiming to calculate the diffuse irradiances due to single and multiple scattering processes: D_1^+ describes a single scattering event, D_2^+ , D_3^+ and D_4^+ characterise the double-, triple- and quadruple scattering processes, respectively. All computational results shown are for three fixed wavelengths, as defined in the figure. **(a)** Results for downwelling irradiances at the ground.; **(b)** Results for upwelling irradiances at the top of the atmosphere.

Although results show that an amplification of diffuse light due to multiple scattering effects at large distances is existent, this effect is hardly noticeable in real conditions. Since values of the brightness of the night sky are several magnitudes smaller than the light dome responsible for, it can be concluded that interferences caused by higher scattering orders can actually be neglected and the consideration

of single scattering solely is an approximation useful for skyglow modelling.

3.1.3 Light pollution vs. air pollution

Air pollution is one of the biggest issues of human kind at this time. Its appearance results in major health issues for humans, suffering of wildlife and species extinctions. Furthermore, Earth's climate is changing due to increased carbon dioxide emissions with gases released from industry and agriculture. Particulate matter PM are small particles in the air which can either originate from natural or artificial sources. The amount of PM₁₀, describing all particles with mass median aerodynamic diameter smaller than 10 microns, is usually a guide quantifying air pollution. Consequently, highly polluted areas are connected to extreme atmospheric conditions and effecting light pollution also.

Until today, this relation was not studied sufficiently, although there were some observations analysed in Upper Austria (Posch et al., 2017) as a result of the light monitoring network providing data from Sky Quality Meter devices, see Section 2.2. Figure 32 illustrates the monthly averaged night sky brightness values for the city of Vöcklabruck (urban) over the year 2016. In addition, also monthly averaged PM₁₀ values are compared. It is clearly visible, that the two curves are following a similar course and therefore seem to have a linear relation.

Figure 33 shows a three dimensional plot, comparing the night sky brightness values as observed in Upper Austria's capital city Linz, its PM₁₀ values and cloud coverage values also. This analysis points out that in dark, cloud free nights the fine dust pollution is low, while in brighter, overcast nights PM₁₀ reaches its maximum.

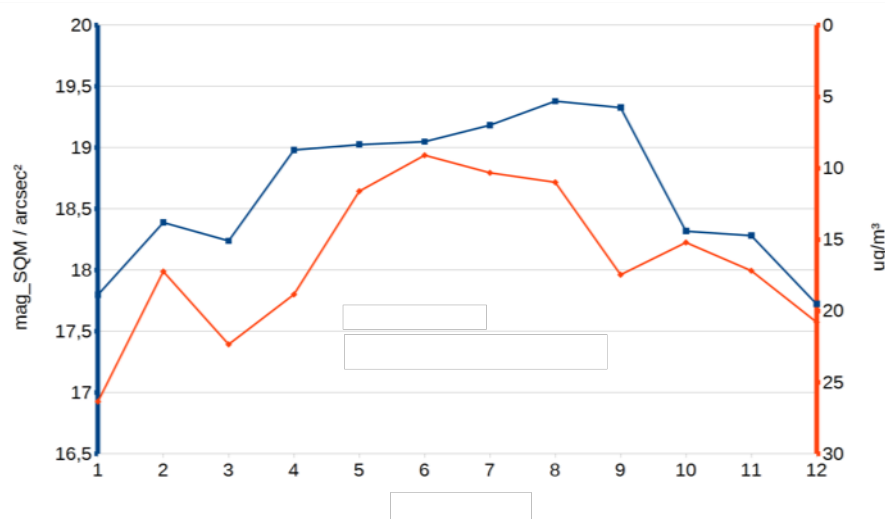


Figure 32 – Comparison of monthly averaged sky brightness values as monitored by the Sky Quality Meter device in Vöcklabruck in Upper Austria (blue) with monthly averaged particular matter PM₁₀ values as observed on the same location (red). (Posch et al., 2017)

The work studied in Section 4.6 bases on the concept of investigating light pollution effects as a result of extreme air pollution conditions.

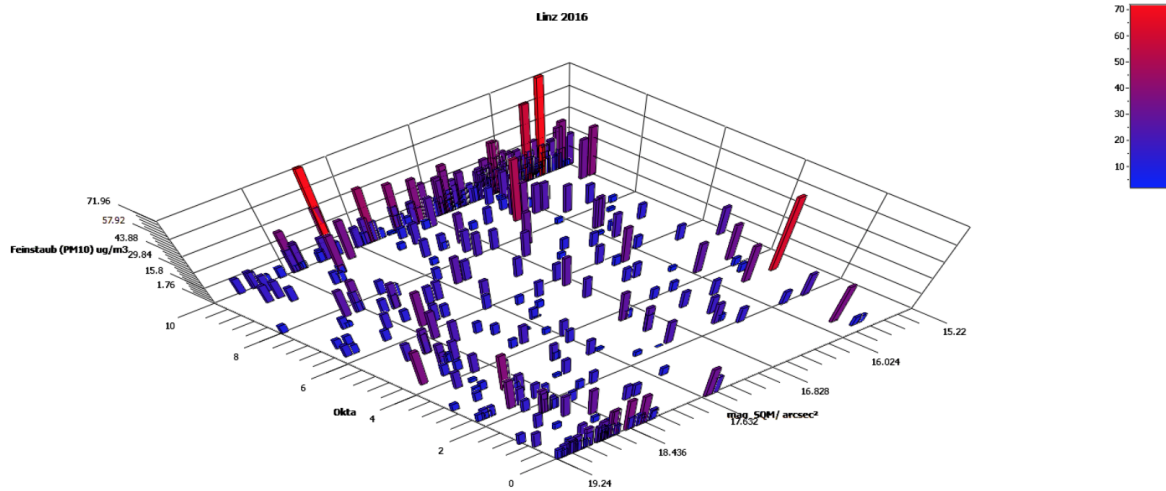


Figure 33 – Coloured scale showing the amount of sky brightness values as observed in Upper Austria’s capital city of Linz by the light monitoring network in comparison with measured particular matter PM_{10} and cloud coverage (Okta). (Posch et al., 2017)

3.2 Fundamentals of skyglow modelling II - The city emission function

The city emission function (CEF) is the most important input one can give when modelling skyglow. Having knowledge about the CEF implies having gathered all necessary information about the entirety of light emitting sources and the appearance of a city. Here it should be mentioned that it is not restricted to real existing ‘cities’, furthermore the term can be used for any defined area acting as light emitting source while there is no influence from outside. Since definition, certain aspects and retrieval of the CEF are differing slightly in various scientific studies (Kocifaj, 2018b; Kolláth et al., 2016; Luginbuhl et al., 2009), a synoptic delineation is proposed as:

The city emission function (CEF) gives clear assertions about a specified area bounded by a closed curve, i.e., the ‘city’ or any defined area, and its luminous intensity distribution resulting by collating radiant intensity functions from all light emitting sources and the radiation behaviour due to topographical impacts on the trajectory of light until it left any possible city surroundings and is radiated into the (upper) atmospheric layers.

While Section 3.1 deals with influences provided by the atmosphere only, the CEF solely depends on the ground-based radiation emitting sources and the structure of their surrounding, e.g., reflecting or blocking surfaces. Having found a suitable description, it is necessary to understand the key elements constituting the CEF. In the following, the fundamental parts are discussed in more detail.

3.2.1 Light emitting sources

The light emitting sources themselves, i.e., (street) lamps, billboards, illuminated buildings or indoor lighting, exercise controlling influence over occurrences to the radiated light waves, since either their installed luminaire or arrangement and set-up define fundamental parameters.

First of all, the CEF of a city is most likely never isotropic, since there is no uniform distribution of light emitting sources over the area. Typically, a city contains 'darker' districts with only low number of installed lightings like parks complexes, water surfaces or even forested areas while 'brighter' districts with denser dispersion of lighting points are indicated as industrial territories, city centres or touristic infrastructure. Consequently, measured skyglow can show discrepancies when, e.g., observations happen either inside of different city parts or from various cardinal points outside (Wallner and Kocifaj, 2019). Another parameter of high importance for assessment is the radiating angle distribution of lighting systems.

As discussed above in sections 1.1.3 and 1.2.1, the type and especially shape of light emitting sources determine the angle of radiation distribution. While street lamps can show enormous differences (Wallner, 2019), advertisements usually emit light normal to the ground's surface and buildings are often illuminated from the ground to high elevation angles. Also indoor lighting does play a role, showing radiation leaving windows above the ground usually parallel to the surface. As shown in Section 3.1, light of various wavelengths show different behaviours when being scattered. Consequently, also the spectral power distribution of the source must be taken into account.

3.2.2 Surface albedo

The more light is radiated downwards, the more important is the aspect of surface reflection. The reflectance of the ground, the so called 'albedo', is decisive for the amount of light reflected. The parameter is described by a dimensionless value, characterising the fraction of light being reflected while the rest is absorbed (Kotthaus et al., 2014). Table 6 gives examples of various surface types and their associated albedo.

Surface type	Albedo	Surface type	Albedo	Surface type	Albedo
Dark soil	0.08-0.13	Asphalt	0.10	Grass	0.13-0.26
Light soil	0.10-0.18	Concrete	0.30	Trees	0.12-0.18
Sand	0.20-0.40	Stone	0.30	Snow	<0.85

Table 6 – Values of various surface albedos as recorded by Shirkey (2008). Discrepancies in values in a certain range can appear due to dry, moist or wet state of a surface type.

As shown in Wallner and Kocifaj (2019), a work presented in detail in Section 4.2, the values for surface albedos, especially for ground types with vegetation periods over a year, seasonal variations are clearly visible. As a consequence, this is also valid for the resulting skyglow, showing fluctuations in measured signals. The most extreme example of a high reflecting surface is snow, reaching albedo values up to 0.85. Figure 34 illustrates observation results of a city near Berlin (Germany) with various meteorological conditions, including a snow covered ground and overcast sky conditions. Results show that the zenith luminance of the overcast sky conditions was amplified by a factor of 33 (29 to 980 mcd/m²) due to fresh snow on the ground solely, underlining the importance of treatment of surface albedo in models, but observations also (Jechow and Hölker, 2019).

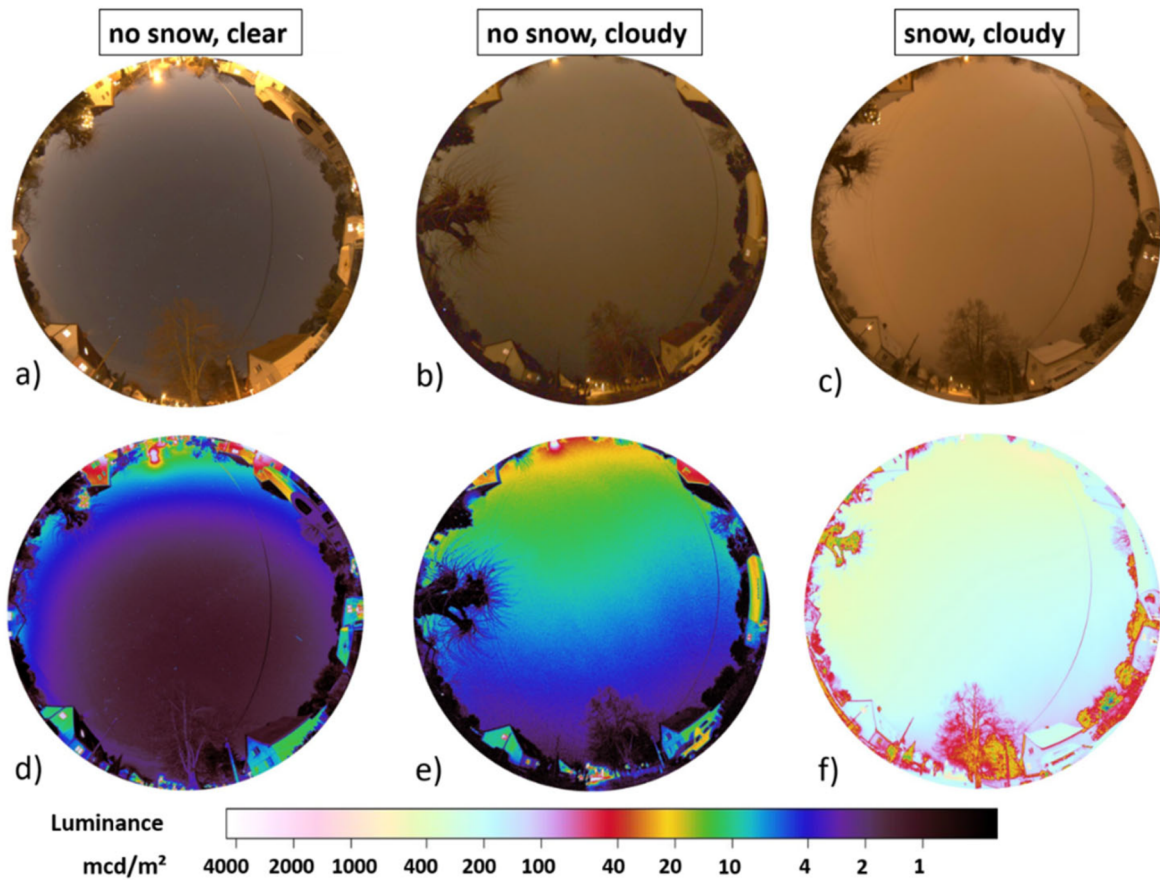


Figure 34 – Photometric data observing the night sky located at Ludwigsfelde, Germany by [Jechow and Hölker \(2019\)](#). Upper images (a - c) show all-sky images, as discussed in Section [2.3](#), with different meteorological conditions as defined in the figure. Lower images (d - f) illustrate the luminance matrix as analysed by 'Sky Quality Camera'. The development of illuminance of the night sky clearly shows the dependence of night sky brightness on surface albedo and cloud conditions.

3.2.3 Topography and blockings

Concentrating on urban environments, buildings commonly not only contribute as light emitting elements, furthermore, they hinder a large number of light waves after being emitted and therefore work as blockings, beside their surfaces working as reflectors. Looking at rural environments, it is usually the complex topography of environment like mountains or hills which can work as attenuators for light. Such blockings usually have a lower surface albedo, resulting in a higher absorption of light. As seen in Section [3.3](#), some models provide the possibility of the inclusion of 'blocking masks' around an observer. However, an overall blocking behaviour of all city structures is nearly impossible to being taken into account for computations.

3.3 Modelling tools

3.3.1 Garstang's model

The first work introducing a model for simulating skyglow and predicting the night sky brightness, was published by [Garstang \(1986\)](#). It is safe to say that all tools which have followed are based on his calculations. Beside the mathematical principles describing the trajectory of a light beam emitted by a city and scattered in the atmosphere in direction of the observer, the specific behaviour of molecular and aerosol scattering were included. The foundation of his theoretical approach is illustrated in Figure 35.

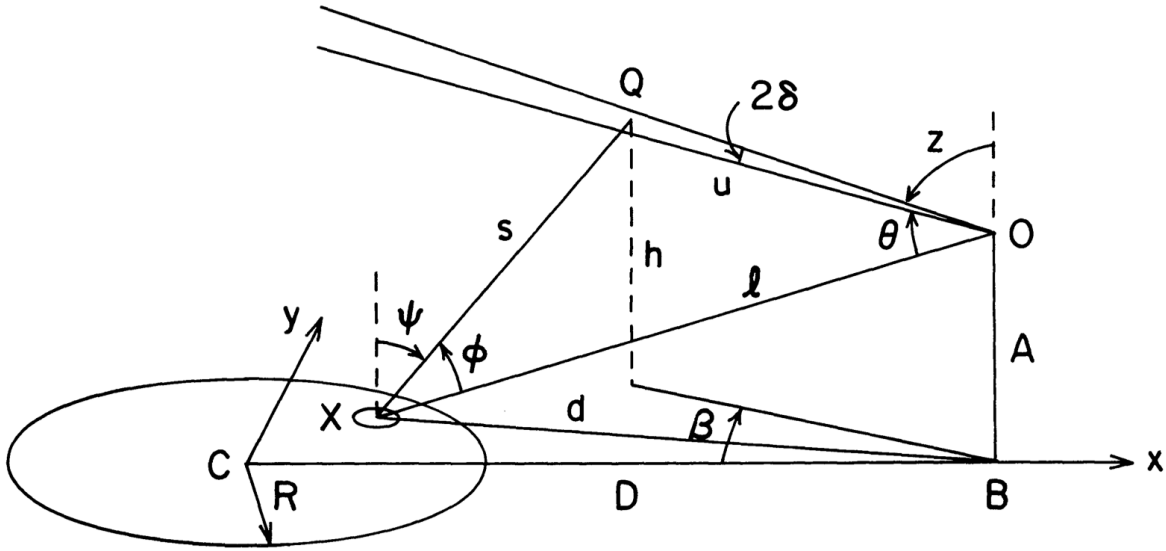


Figure 35 – The basic structure of Garstang's light pollution model, a circular city (C) emitting light upwards to the hemisphere (Q) which is then scattered towards the observer (O). From [Garstang \(1986\)](#) Reprint with permission.

In brief summary, a city with its center C and radius R , situated in the horizontal plane and at height h above sea level is surveyed. The amount of light emitted by this hypothetical source is assumed to be proportional to its population P . Since every city can be described as producing an output L lumens per head of population, the total light output LP is approximated by

$$LP = L_0 P (P/100,000)^{0.1}. \quad (31)$$

Not all light emitted in a city is directed upwards, hence two additional parameters were introduced. F is the fraction of light radiated directly to the upper hemisphere and G is the fraction of light scattered from the surface with a Lambert distribution. The total upward intensity radiated in the direction ψ to the atmosphere at point Q is now described as

$$I_{up} = \frac{LP}{2\pi} [2G(1-F)\cos\psi + 0.554F\psi^4]. \quad (32)$$

After reaching the atmosphere at Q , the light beam is scattered towards the observer O , located at a height A above the horizontal plane of the city and at distance d from the city centre. Assuming an

atmosphere consisting out of molecules and aerosols, these components are described by their particle densities

$$N_{\text{molecules}}(h) = N_m \exp(-c[h + H]), \quad (33)$$

$$N_{\text{aerosols}}(h) = N_a \exp(-ah), \quad (34)$$

with sea level density $N_m = 2.55 \cdot 10^{19} \text{ cm}^{-3}$, constant $c = 0.104 \text{ km}^{-1}$ and aerosol particle density at ground level N_a with reciprocal scale height $a = 0.657 + 0.059 K$. The parameter K can be described as being the optical thickness of the atmosphere, providing a ratio between aerosols and molecules. The model includes an approximate correction for double scattering, although, higher-orders are neglected. To summarise all steps undertaken by Garstang, the basic equation for the calculation of the sky brightness b in lamberts is defined as

$$b = \pi N_m \sigma_R \exp(-cH) \int \int (dx dy / \pi R^2) \int_0^\infty du I_{\text{up}} s^{-2} (\text{EF})_{\text{XQ}} (\text{EF})_{\text{QO}} (\text{DS}) \times [\exp(-ch) 3(l + \cos^2(\theta + \phi)) / (16\pi) + \exp(-ah) 11.11 K f(\theta + \phi)]. \quad (35)$$

Further parameters used are σ_R describing the integrated cross section of a molecular atmosphere, (EF) being the extinction for a certain path, (DS) being the correction for double-scattering, θ the angle through which the light is scattered and following $f(\theta + \phi)$ the scattering function.

As necessary steps, some assumptions and approximations were undertaken in the development of the model. First, there is the critical aspect of presuming the city being a circular area in a horizontal plane and therefore reducing the city emission function to its simplest design. This flat-earth-approximation can be applied without concerns when the distance to the observed city is low, but must be corrected at big distances. [Cinzano et al. \(2000\)](#) amended the model insofar as they included the curved geometry as compelling necessity for satellite observations. Additionally contributing in amplification of a heavily simplified emission function is the rough estimation of total lumen output of the city, distributing the light emission isotropically over the city's area.

Concerning the night sky itself, the derivation used above provides results of the sky brightness if caused by light emitting sources solely. Consequently, the natural background brightness must be explicitly included, being able to evince notable distinctions especially for rural areas with only low impact of ALAN. To do so, an approximate value for the night sky background, depending on zenith angle as well as air mass and including faint stars and airglow, is implied to the model.

However, with the possibility of adopting the model to more realistic cases, i.e., having more than only one isolated light emitting source, also two or more cities can be included to its derivation, although this is linked to the need of large computational capacities and complex solutions. It has shown that even with approximations mentioned before results from calculations can be satisfyingly consistent to observations and a hedge is regarded as being effective if the observer is situated outside of a city or inside of small cities only. Garstang used his model continuously for predicting skyglow around astronomical observatories and prospective sites.

3.3.2 ILLUMINA

ILLUMINA is a theoretical model developed by [Aubé et al. \(2005\)](#). Its original purpose aimed to retrieve the aerosol optical depth value when comparing simulated results to in-situ observations. In order to achieve this goal, artificial skyglow is exhausted, enabling a comparison between the two approaches in the best possible manner during night time. Its basis is the computation of first and second order molecular and aerosol scattering, accounting for spatial heterogeneity in angular geometry of the lighting, in spectral dependence of the source, in the ground spectral reflectance and topography of the surrounding. Consequently, there is an inclusion of complex surface structures, being close to real environmental build-ups. The simulation enables an iterative way of determining the aerosol optical depth via obtaining a best possible theoretical fit by comparing measurements done with a spectrophotometer or by satellite imagery. This is accomplished through focussing on the simulation of light arriving at the device only, making direct simulations of the ground or light sources unfeasible. The basic geometry used, based on cells describing the trajectories of light, is illustrated in Figure 36.

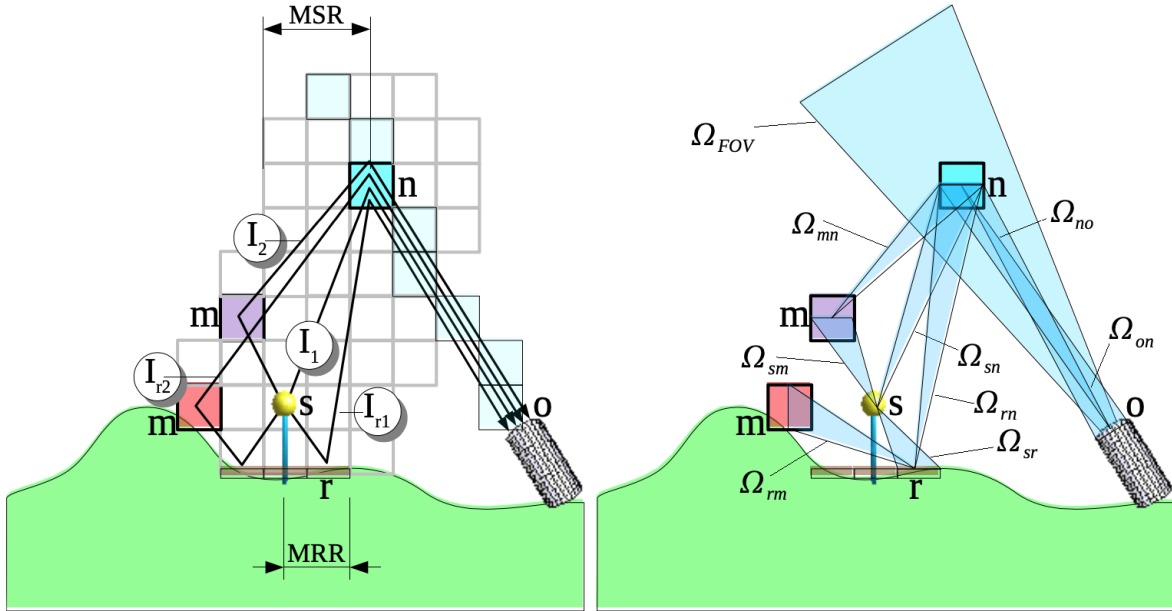


Figure 36 – Modelling geometry of the radiative transfer model as used in *ILLUMINA*. From [Aubé et al. \(2005\)](#). Reprint with permission.

Focussing on the theory, a light source S emits radiation towards a cell n , either directly by light being directed in its direction, or indirectly via scattering in the atmosphere at a first order scattering cell m or due to reflections on the ground. Latter is the impact most severely affected by a complex surface design. The spectral intensity scattered toward the ground-based observer O by the cell n is approximated as

$$I_{no} \approx I_1 + I_{r1} + I_2 + I_{r2}. \quad (36)$$

Here, the inclusion of the first two scattering orders become apparent as I_1 and I_2 are the scattered intensities by either single or second order scattering, I_{r1} and I_{r2} describe the first and second order

scattered intensities after surface reflections. Splitting the parameters of Eq. 36 into their components, other model inputs become clearly visible. Starting with the first order scattering, its derivation is formed as

$$I_1 = L_0 T_{no} E(\theta_{sn}) \Omega_{sn} T_{sn} P_{sn} f(\theta_{sn}, \theta_{no}). \quad (37)$$

Containing information about the physical behaviour of light travelling through the atmosphere, L_0 is the total spectral luminosity emitted by the source, T is the atmospheric transmittance between two cells, $E(\theta_{sn})$ is the averaged emission function for the lighting source in the horizontal with θ_{sn} being the zenith angle of the light path between two cells, Ω_{sn} is the subtended solid angle, here from cell n as seen from the source, P is the probability function of a scattering process happening and f is the normalised scattering phase function. Especially the atmospheric transmittance is dependent of its composition of aerosols and molecules, being described by a weighted transmittance of both. Additionally the occurring extinction is computed via an assumption of exponential decreasing of the uniform concentration vertical profiles defined by scale heights for each. Building on this, the first order scattering after ground reflections is derived as

$$I_{r1} = \frac{L_0 T_{no}}{2\pi} \sum_r E(\theta_{sr}) \Omega_{sr} T_{sr} \rho_r \cos(\theta_{rn} + \epsilon) \Omega_{rn} P_{rn} f(\theta_{rn}, \theta_{no}) T_{rn}, \quad (38)$$

including ρ_r as reflectance of the ground cell and ϵ being the tilt angle of the ground surface. Summing all lighting contributions coming from the ground, also reflectances originated by radii bigger than the horizontal ground cell (maximum reflective radius MRR) are implied to the calculation. Similar to this approach, the second order scattering contributions are derived as sum of a large number of light paths from the source via first order cell m to the scattering cell n . It follows that

$$I_2 = L_0 T_{no} \sum_m (T_{sm} E(\theta_{sm}) \Omega_{sm} P_{sm} f(\theta_{sm}, \theta_{mn}) T_{mn} \Omega_{mn} P_{mn} f(\theta_{mn}, \theta_{no})), \quad (39)$$

$$I_{r2} = \frac{L_0 T_{no}}{2\pi} \sum_r \left(E(\theta_{sr}) \Omega_{sr} T_{sr} \rho_r \sum_m (\cos(\theta_{rm} + \epsilon) \Omega_{rm} P_{rm} f(\theta_{rm}, \theta_{mn}) T_{rm} T_{mn} \Omega_{mn} P_{mn} f(\theta_{mn}, \theta_{no})) \right). \quad (40)$$

The basic equation of the *ILLUMINA* model, describing the total spectral flux arriving at the observer is now given as

$$\Phi_m = \sum_n I_{no} \Omega_{no} \frac{\Omega_{FOV}}{\Omega_{on}}, \quad (41)$$

with the angle Ω_{FOV} being the field of view of the ground-based measuring device.

The model described possesses the advantage of being highly adjustable to unique shapes occurring in real life situations and environment. Due to updates since its introduction, spectral radiant flux maps are created using satellite imagery of the VIIRS Day and Night Band, see Section 2.6.2, ground albedo data from the Moderate Resolution Imaging (MODIS) satellite and light output pattern constructed via an approximate geographical inventory. Its meteorological dependency is limited to clear and overcast sky conditions (Aubé and Simoneau, 2018).

3.3.3 SkyGlow

The 'SkyGlow' or formerly 'MSNsR_{Au}' model was first introduced by Kocifaj (2007, 2008). It illustrates the tool used for calculations resulting in presented works below, in more detail in Sections 4.1, 4.2 and 4.6. This simulation method focusses on providing the possibility of including an unlimited number of ground-based light emitting sources and their spatial distribution. Each can be implemented as real finite-dimensional surface sources with defined spectral and angular radiating properties. Regarding meteorological parameters, the model is capable of performing calculations either for clear sky or completely overcast sky conditions.

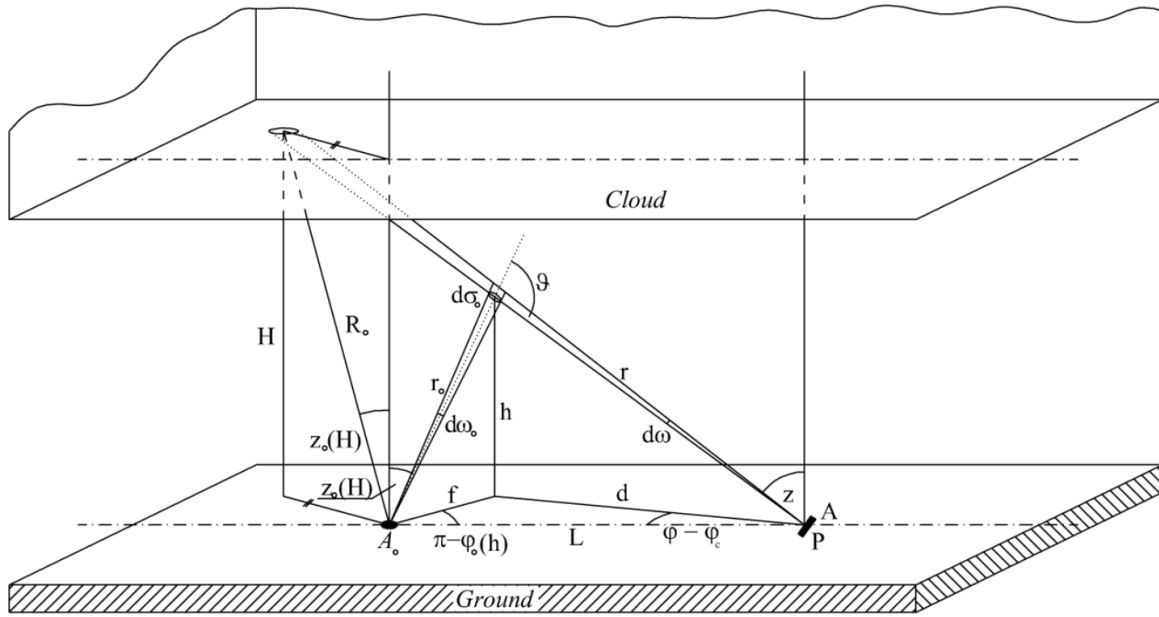


Figure 37 – Modelling geometry as used for computations in *SkyGlow*. Source: Miroslav Kocifaj.

The fundamental basis of the *SkyGlow* tool is illustrated in Figure 37 and can roughly be compared to Garstang's model in Figure 35. It describes a light emitting infinitesimal ground area A_0 , radiating into the upper hemisphere. At a distance of r_0 , the light beam is scattered at a certain altitude h . The radiative flux arriving at the 'scattering point' is described as

$$d\phi_{\lambda,0}(h) = A_0 I_{\lambda}(z_0) \cos(z_0) \frac{d\sigma_0}{r_0^2} t_{\lambda}(h, z_0), \quad (42)$$

simply depending on the intensity $I_{\lambda}(z_0)$ in direction of the zenith angle z_0 and arriving at the elementary surface $d\sigma$ with a transmission coefficient $t_{\lambda}(h, z_0)$. The reason why there is the occurrence of an elementary surface is a consequence of the atmosphere's composition. Due to qualifying aerosols as a mixture of liquid and solid materials, their geometry cannot be accurately described as spherical. Therefore, to have the ability of making the simulation as realistic as possible regarding real particles, the radius of an arbitrarily shaped particle is depicted as radius of a volume equivalent sphere. Consequently, $d\sigma$ can be extended being equal to $r_0^2 d\omega_0$ with the elementary solid angle $d\omega_0 = \sin(z_0) dz_0 d\varphi_0$ only depending on the zenith and azimuth angle φ_0 of the light propagation. Following, its elementary volume is $dv = d\sigma_0 dr_0$.

After reaching the atmosphere, light is scattered towards the observer located at P . The radiant flux which is pointed in its direction is defined as

$$d^2\phi_\lambda^*(h, z, \varphi) = d\phi_{\lambda,0}(h)p_\lambda(\omega_0, \omega')k_{\text{sca},\lambda}(h)dr_0. \quad (43)$$

Here, both $p_\lambda(\omega_0, \omega')$, describing the probability of light coming from ω_0 and being scattered into an angle $\omega' = \frac{A}{r^2}$, and $k_{\text{sca},\lambda}(h)$ being a volume-scattering coefficient, are the key functions for atmospheric optics. They describe the optical properties and therefore the state of the atmosphere. With A being the area of a detector, e.g., a telescope or human eye, z and φ being the zenith and azimuth angle of the sky element as seen from the observer and r the distance between them, the radiant flux arriving at P can be derived as

$$d^2\phi_\lambda(h, z, \varphi) = A_0 I_\lambda(z_0) \cos(z_0) \frac{t_\lambda(h, z_0) t_\lambda(h, z)}{r_0^2} dr k_{\text{sca},\lambda}(h) \left[\frac{A}{4\pi} P_\lambda(\omega_0, \omega') \right] d\omega, \quad (44)$$

with the scattering phase function $P_\lambda(\omega_0, \omega')$. Eq. [42](#), [43](#) and [44](#) build the basis of the model, further derivations show how the angular distribution of the light beam scattered at altitude h behaves. Its definition is as follows

$$\Gamma_\lambda(h, z, \varphi) = \frac{1}{4\pi} [k_{\text{sca},\lambda}^{(M)}(h) P_\lambda^{(M)}(\omega_0, \omega') + k_{\text{sca},\lambda}^{(A)}(h) P_\lambda^{(A)}(\omega_0, \omega')]. \quad (45)$$

It is visible that for all parameters a clear separation between molecules (M) and aerosols (A) is being implemented. Including the possibility of having a great number of light emitting sources, the basic equation for the *SkyGlow* model describes the sum of skyglow impacts caused by N number of sources, the resulting luminance integrated over the finite wavelength range $\langle \lambda_1, \lambda_2 \rangle$ is defined as

$$\begin{aligned} J_V(z, \varphi) = & \frac{1}{\pi H^2} \sum_{i=1}^N \int_{R=0}^{R_i(\varphi'_0)} \int_{\varphi'_0=0}^{2\pi} \cos^4(z_{0,H,i}) B(Q_i, q_i, z_{0,H,i}) \\ & \times \left[\int_{\lambda_1}^{\lambda_2} \rho_\lambda(z_{0,H,i}, z, \vartheta_{H,i}) I_{\lambda,0,i} V_\lambda T_\lambda(H, z, \varphi) d\lambda \right] R dR d\varphi'_0 \\ & + \frac{1}{\cos(z)} \int_{R=0}^{R_i(\varphi'_0)} \int_{\varphi'_0=0}^{2\pi} \int_0^H B(Q_i, q_i, z_{0,H,i}) \frac{\cos^2(z_{0,h,i})}{h^2} \\ & \times \left[\int_{\lambda_1}^{\lambda_2} I_{\lambda,0,i} V_\lambda T_\lambda(h, z, \varphi) \Gamma_\lambda(h, z, \varphi) d\lambda \right] dh dR d\varphi'_0. \end{aligned} \quad (46)$$

h is the height of the cloud base (in the case of overcast sky conditions), the position vector R and the polar angle φ'_0 give information about the location of a radiating element inside the i th light source, B is the function describing the behaviour of radiation emitted by the surface source according to Garstang ([Garstang, 1986](#)), ρ_λ is the spectral reflectance of the cloud layer, $I_{\lambda,0,i}$ is the intensity of the i th light emitting source, V_λ describes the spectral luminous efficiency for an individual observer and T_λ the overall transmission function.

It has shown that the *SkyGlow* model can be applied optimally when conducting real-finite and infinitesimal light sources at clear sky or overcast sky conditions. Despite idealising planar light sources by point-sources, its radiation behaviour is different due to finite-sized entities, bringing potential outcomes nearer to realistic assessments. Due to its high complexity, computational time increases significantly with broad wavelength ranges or large number of light emitting sources, i.e., enlarging

of the integration area. Consequently, there are approaches of simplifying the model while keeping accuracy high. One work presented in Section 4.1 derives a new equation for approximating the influence of distant cities enabling the estimation of errors occurring due to the finite-dimensional system limitation of the theoretical simulation. Another limitation is the necessity of giving mostly unknown atmospheric parameters as input for calculations. Having knowledge about the highly variable atmosphere in total at one time is impossible. However, the work presented in Section 4.5 illustrates how a uniting of observational and theoretical approaches, i.e., digital imaging and theoretical model, can avoid this problem.

3.3.4 Comparison

Although there is quite a large overlap in derivations of the modelling tools presented, there are also a small number of differences between them, leading to slight variations in their results. Especially *ILLUMINA* and *SkyGlow* are sharing a similar structure in their theoretical approach while the outdated Garstang's model forms the basis of both and still is for other concepts. Consequently, as mentioned before, Garstang's model is designed with a large number of approximations and assumptions, allowing a greater margin for errors. Still, it was proven that compared to observations at specific conditions, it demonstrated an outstanding performance for its time. Therefore, it makes sense to take a closer look in comparing both new developed models in more detail, some facts are summarised in Table 7. Still, it makes sense to draw a comparison of significant deviations in all three.

One of the most substantial adjustments occurring across the models is the construction of the light emitting sources. Garstang uses the simplest design of a city emission function, reducing the city's shape to being circular and having an isotropic emission to the upward hemisphere. Since this is realistically seen only the case considering the absence of blockings, e.g., tall buildings or trees, and the fact that smaller cities providing a more concentrated light emission in their centre only, it is no surprise that the model is more effective for those. *ILLUMINA* entails the possibility of forming a complex shaped environment with the installation of light emitting sources in between. Information about the design of the setting and the lights itself are collected in grid cells with a typical resolution of 100 m to 1 km. In this way, results are being strongly affected by the second order scattering behaviour due to reflections appearing on various surfaces. As discussed in Section 3.1, this plays primarily a role at long distances from a city as also seen in simulation results of the model (Aubé and Kocifaj, 2012). *SkyGlow* is based on planar ground sources consisting out of many single pixels without the necessity of being circular. Those contain information about the geometrical position to the observer, total spectral radiant flux emitted upwards and spectral radiant flux with respect to the zenith angle. The number of pixels is basically unlimited, therefore also a large number of light emitting sources can easily be included to the computations.

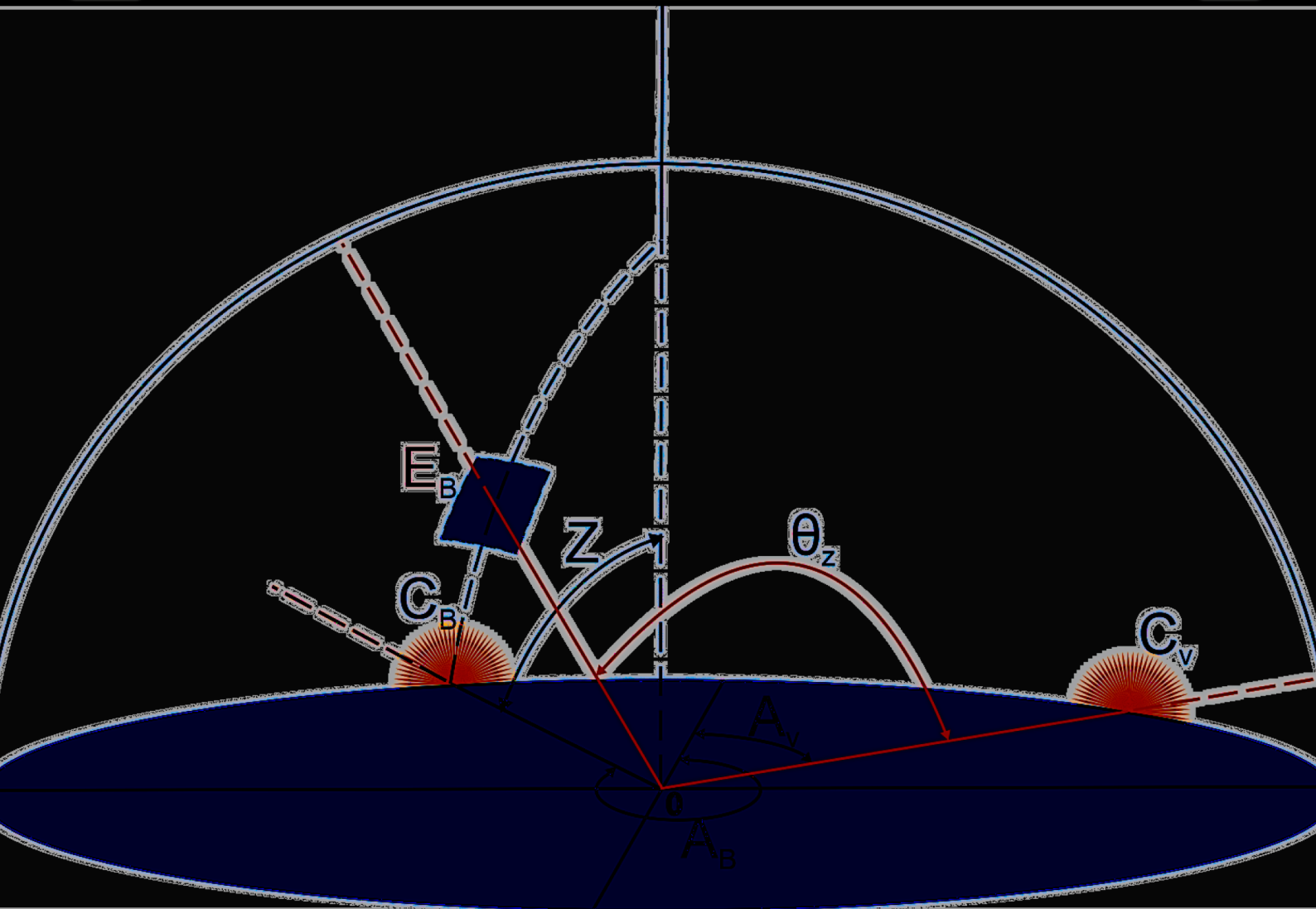
A very important parameter for skyglow modelling, representing an essential part of the emission function, is the total lumen output, describing the total amount of light being produced inside of a city. Such value is not easily or even impossibly available as there is the need of keeping records about all light emitting sources installed, including not only public lighting but also commercial, advertising or private lighting. Unfortunately, to provide reliable results, it is necessary to include this parameter to all skyglow modelling tools and choose its value as realistic as possible. To do so, the theoretical approaches rely on different estimates. Garstang chose an approximation depending on the population number of a city, being derived in Eq. 31. However, his calculation, especially the proportionality factor of 0.1, was chosen as being a best fit solely and therefore showed major discrepancies for various cities over the years. Still, the concept of linking the lumen output to the population

is widely accepted and also adopted by *SkyGlow*. Here, light emitting sources are described via lumen-per-capita method with the numbers of population and lumen-per-capita being changeable. It is especially important at this point to analyse critically weather population-based models provide satisfactory results. The work presented in Section 4.7 shows that theoretical simulations based on the area of artificially lit surfaces could be more advantageous but still has to be discussed for future research (Kocifaj et al., 2020).

	ILLUMINA	SkyGlow
scattering functions	molecules: Rayleigh aerosols: Mie	molecules: Rayleigh aerosols: Henyey-Greenstein
scale heights (standard)	molecules: 8 km, aerosols: 2 km	molecules: 8 km, aerosols: 1.67 km
ground-based sources	complex shape, designed by grid cells	planar, built of many single pixels
max. number of sources	domain size of few hundreds of kilometres	no limit
spectral power distribution	radiant flux map created by satellite imagery	weighted spectrum over all light sources
wavelength range	certain spectral bands, only one wavelength for investigation	integration over the whole visible spectrum (350 - 750 nm) or defined thresholds
scatterer and absorbers	grid cells, computation along light paths	atmospheric voxels
atmosphere	plane-parallel	plane-parallel with a configurable vertical stratification

Table 7 – Summary of fundamental parameters and comparison of their usage in modelling tools.

Focussing on a comparison between *ILLUMINA* and *SkyGlow*, Aubé and Kocifaj (2012) simulated the condition of the night sky at an astronomical observatory with both modelling tools. Results have shown to be similar with resulting values being of the same magnitude. However, there are some discrepancies arising due to the slight varying methodological approaches. As Table 7 shows, there are especially two sources leading to differences in the overall results. First, there is a disparity in aerosol scale heights provoking a slight divergence in scattering behaviour of the atmosphere. Yet, more influential is the dissimilarity of used light-scattering models, i.e., scattering functions. Although both models are in agreement of using Rayleigh scattering function for molecules, the choices of those used for aerosols go apart. While *ILLUMINA* uses the classical Mie phase function, *SkyGlow* applies the Henyey-Greenstein function (Braak et al., 2001), justifying its selection with the non-spherical shapes of aerosol particles. In a different context, i.e., investigations of planetary atmospheres, it has shown that those scattering functions may produce varying results depending on wavelength of observation (Toublanc, 1996) with both showing various strengths. Here, compared to Mie theory, the usage of Henyey-Greenstein in addition to considering single-scattering solely in *SkyGlow*, led to decreased sky brightness values near horizontal altitudes while both models are consistent near the zenith. To give a concluding overview, both *ILLUMINA* and *SkyGlow* are theoretical models providing outstanding performances in modelling skyglow. *SkyGlow* stands out for its highly reduced computational time, the possibility of investigating large domains with high spatial resolution, the inclusion of an unlimited number of light emitting sources and performing computations with a variety of lamp spectra even widely distributed over the examined area. *ILLUMINA* shows a high degree of effectiveness for low and high atmospheric turbidity conditions. Even if being more time consuming, it lays special focus on the second-order scattering effects due to reflections occurring on either surfaces or the light dome, relevant especially to observers at large distances from a city. While both use nearly the same input parameters, their handling is quite different leading to not only varied outcomes but also making them two complementary usable tools.



4

PUBLICATIONS

4 Publications

4.1 'An asymptotic formula for skyglow modelling over a large territory'

Title: *An asymptotic formula for skyglow modelling over a large territory*

Authors: M. Kocifaj, S. Wallner, H. A. Solano-Lamphar

Journal: Monthly Notices of the Royal Astronomical Society (MNRAS)

Status: Published in MNRAS 485, 2214-2224 (2019)

DOI: <https://doi.org/10.1093/mnras/stz520>

Personal contribution: I was responsible for testing the effectiveness and correctness of the new introduced asymptotic formula developed in advance. Therefore, I carried out measurements as discussed in the paper and assumed responsibility for their analysis aiming to apply the results to the theoretical method. Additionally, I was strongly involved in writing of the paper.



An asymptotic formula for skyglow modelling over a large territory

Miroslav Kocifaj,^{1,2★} Stefan Wallner^{1,3} and Hector Antonio Solano-Lamphar⁴

¹ICA, Slovak Academy of Sciences, Dúbravská Road 9, 845 03 Bratislava, Slovakia

²Department of Experimental Physics, Faculty of Mathematics, Physics, and Informatics, Comenius University, Mlynská dolina, 842 48 Bratislava, Slovakia

³Department of Astrophysics, University of Vienna, Türkenschanzstrasse 17, 1180 Vienna, Austria

⁴Cátedras CONACYT, CentroMet, INFOTEC, Avenida San Fernando 37, Toriello Guerra, 14050 Ciudad de México, México

Accepted 2019 February 19. Received 2019 February 19; in original form 2019 January 15

ABSTRACT

An analytical framework to predict skyglow due to distant sources is presented, which can be applied to model sky brightness from the zenith toward the horizon along a vertical plane crossing the hemisphere in the azimuthal position of a light source. Although various powerful algorithms have been developed over the last few decades, the time needed for calculation grows exponentially with increasing size of the modelling domain. This is one of the key issues in skyglow computations, because the numerical accuracy improves only slowly as the modelling domain extends. We treat the problem theoretically, by introducing an analytical formula that is well-suited for light sources located at intermediate and long distances from an observation point and allows tremendous time savings in numerical analyses, while keeping the error at a low level. Field experiments carried out in Eastern Austria provided a unique opportunity to validate the model using real-sky luminance data. The fact that the theoretical model allows the prediction of sky luminance within an acceptable error tolerance is not only in line with the experimental data, but also provides new means of remote characterization of light emissions from artificial sources. The method is particularly attractive for rapid and simple retrieval of the amount of light escaping upwards from the dominant light sources surrounding the observation point. We expect that the method can advance the numerical modelling of skyglow substantially, because it allows real-time computations for very large territories.

Key words: scattering – atmospheric effects – light pollution – methods: analytical – methods: numerical – methods: observational.

1 INTRODUCTION

Excessive glow seen over populated areas is a new previously unidentified threat that has only become very pronounced in the last few decades and is increasing from year to year. The first attempts to model the propagation of artificial light into the nocturnal environment date back to Garstang (Garstang 1986), who computed the night-sky brightness based on the population estimates and assumed lumens per capita. Substantial advances have been achieved by proper treatment of atmospheric optics (Cinzano 2000; Joseph, Kaufman & Mekler 2001) and incorporation of 3D effects as well (Aubé et al. 2005; Kocifaj 2007; 2008; Cinzano & Falchi 2013). Since that time, the numerical prediction of skyglow for a heterogeneous urban area with arbitrarily distributed light-emitting sources has posed no further difficulties (Aubé 2015; Bará, Ribas & Kocifaj 2015; Aubé et al. 2018; Barentine et al. 2018; Kocifaj 2018), except for computer system performance. Currently, the computational time is by far the most important constraint in numerical modelling. It has been shown in numerous cases that even the contribution from a distant source of light to the brightness should be reviewed carefully if its lumen output is large enough (Kocifaj 2011; Aubé & Roby 2014; Falchi et al. 2016; Gaston et al. 2017) or if the light source allows for direct uplight of some percentage (Luginbuhl, Walker & Wainscoat 2009a). For this reason, numerical integration is necessary over a radius large enough around a hypothetical observer. However, the CPU consumption increases at least as a square of the radius, thus imposing an unacceptable burden on computational resources. This might prevent contemporary algorithms from further improvements or extensions, because any new feature implemented in already non-trivial numerical integrators would make the software modules even more complex and computations even more CPU-intensive.

* E-mail: kocifaj@savba.sk

Therefore, significant advances cannot be achieved without major optimization of the present models. This has drawn our attention to new research directed towards development of an efficient method to reduce computational time on the one hand and keep the error margin low on the other hand. The asymptotic formula developed here for clear-sky conditions has been validated experimentally and is useful to astronomers, physicists and engineers who need to model/predict skyglow from many intense distant light sources scattered over a large territory. Unintentionally, a side product of the new theory is that the formula provides a tool for a simple estimate of the total lumen output from a city of interest. We realize this feature is of great value, because the lighting inventory is normally unavailable for whole-city light sources, meaning that the total lumen output is difficult or even impossible to determine directly.

2 SKY RADIANCE AT LARGE DISTANCES FROM A LIGHT-EMITTING SOURCE

The function that is associated with low-order radiance in a plane-parallel atmosphere has the integral form (Kocifaj 2007)

$$J(z) = \frac{B_0}{\mu} \int_0^\infty k_{\text{sca}}(h) \frac{\cos^2 z_0}{h^2} t_1 t_2 \frac{P(\theta)}{4\pi} dh, \quad (1)$$

where z is the observational zenith angle, $\mu = \cos(z)$, B_0 is the radiant intensity (i.e. cosine-weighted radiance) of a light-emitting source, z_0 is the emission zenith angle, h is the altitude above the ground level, and $k_{\text{sca}}(h)$ and $P(\theta)$ are the total volume scattering coefficient at altitude h and the atmospheric phase function, respectively (Kokhanovsky 1998). The function t_1 is the light transmission coefficient at the trajectory from a light source to an atmospheric volume at altitude h . Correspondingly, t_2 is the transmission function for a scattered beam of light travelling from the elementary atmospheric volume to an observer (or equipment) on the ground surface. The emission function of a radiating city is generally unknown, so an isotropic radiator strategy is employed in equation (1) to make the problem solvable. Although this appears superficial compared with what we can potentially expect from a complex urban environment, there are other approximate derivations of the transfer of diffuse city light from a localized source that are based on the assumption of an isotropic radiator and do provide reasonable results (Joseph et al. 2001). An interaction of many divergent urban beams in combination with optical distortion effects due to light-scattering phenomena appears the most likely mechanism for why this approximation still works well. In addition, the global trend in improving illumination systems is directed towards the use of modern street-lighting fixtures with a minimum upper light output ratio (ULOR), which results in significant suppression of direct light emission above the horizontal, so the upward emission function is very much modulated by ground-reflected light. In a model case with ULOR = 10 per cent, the radiant intensity varies only slightly from 0.6–0.8 for almost all directions (Kolláth et al. 2016), except for zenith angles above 80° . However, elevated light emission towards the horizon is efficiently reduced, due to interactions of photons with obscuring objects located near the ground (such as vegetation and buildings, see Luginbuhl et al. 2009b).

This native approach, together with other approximations, is useful in derivation of an analytical formula that is ultimately accurate enough to serve as the basis for modelling the sky radiance from the zenith toward the horizon along a vertical plane crossing the hemisphere in the azimuthal position of a light-emitting city.

Assuming r_1 is the path length from a city to the elementary atmospheric volume and $\mu_0 = \cos(z_0) = h/r_1$, we easily find

$$J(z) \cong \frac{B_0 \bar{k}}{\mu} \int_0^\infty \frac{e^{-kh/\mu_0}}{r_1} \frac{e^{-kh/\mu}}{r_1} \frac{P(\theta)}{4\pi} \mu_0 dr_1 = \frac{I_0 \bar{k}}{\mu} \int_0^\infty \frac{\exp\left\{-kr_1\left(1 + \frac{\bar{\mu}_0}{\mu}\right)\right\}}{r_1^2 + D^2} \frac{P(\theta)}{4\pi} \mu_0 dr_1, \quad (2)$$

where D is the horizontal distance from an observer to the city of interest and I_0 is a ‘specific’ radiance normalized to the city area. I_0 is to characterize the city in terms of a point light source, so its radiometry unit is W sr^{-1} . However, the physical interpretation of I_0 differs from B_0 , which is a product of I_0 and μ_0 . Alternatively, I_0 is measured in candelas in cases in which the spectral response of a measuring device is considered to fit the human visual system. In equation (2), \bar{k} and $\bar{\mu}_0$ are average values in their definition domains. The key difficulty with equation (2) is in the integral form

$$\int_0^\infty \frac{e^{-ax}}{x^2 + D^2} dx. \quad (3)$$

The above integral has an analytical solution in the complex domain. It can be expressed as a function of exponential integrals Ei of complex arguments. However, it is much more convenient to express the formula in the real domain as follows:

$$\int_0^\infty \frac{e^{-ax}}{x^2 + D^2} dx = \frac{1}{D} \left\{ Ci(aD) \sin(aD) + \left[\frac{\pi}{2} - Si(aD) \right] \cos(aD) \right\} = \frac{1}{D} \Psi(aD), \quad (4)$$

where

$$Ci(y) = \gamma + \ln(y) + \sum_{n=1}^\infty \frac{(-1)^n y^{2n}}{2n \cdot (2n)!} = \gamma + \ln(y) - \frac{y^2}{2 \cdot 2!} + \frac{y^4}{4 \cdot 4!} \mp \dots \quad (5)$$

is the cosine integral and

$$Si(y) = \sum_{n=1}^\infty \frac{(-1)^n y^{2n+1}}{(2n+1) \cdot (2n+1)!} = y - \frac{y^3}{3 \cdot 3!} + \frac{y^5}{5 \cdot 5!} \mp \dots \quad (6)$$

2216 *M. Kocifaj, S. Wallner and H. A. Solano-Lamphar*

is the sine integral. The parameter $\gamma = 0.577\dots$ is the Euler–Mascheroni constant. For large values of y , we have

$$Ci(y) = \frac{\sin y}{y} \left(1 - \frac{2!}{y^2} + \frac{4!}{y^4} - \frac{6!}{y^6} \dots \right) - \frac{\cos y}{y} \left(\frac{1}{y} - \frac{3!}{y^3} + \frac{5!}{y^5} - \frac{7!}{y^7} \dots \right) \quad (7)$$

and

$$Si(y) = \frac{\pi}{2} - \frac{\cos y}{y} \left(1 - \frac{2!}{y^2} + \frac{4!}{y^4} - \frac{6!}{y^6} \dots \right) - \frac{\sin y}{y} \left(\frac{1}{y} - \frac{3!}{y^3} + \frac{5!}{y^5} - \frac{7!}{y^7} \dots \right). \quad (8)$$

Our numerical experiments have shown that equation (4) reduces to the simple form of $a^{-1}D^{-2}$ for $aD > 5$. In contrast, for $aD < 1$ we have

$$\frac{1}{D} \left\{ Ci(aD) \sin(aD) + \left[\frac{\pi}{2} - Si(aD) \right] \cos(aD) \right\}_{aD < 1} \cong \left[\frac{\gamma + \ln(aD)}{D} - \frac{a^2}{4} D \right] \sin(aD) + \left[\frac{\pi}{2D} - a \right] \cos(aD). \quad (9)$$

In both cases the error margin is below 5 per cent.

After a bit of manipulation using the derivations above, we have expressed equation (2) as follows:

$$J(z) = \frac{9}{32\pi\mu} I_0 \frac{1}{D} \left\{ Ci(aD) \sin(aD) + \left[\frac{\pi}{2} - Si(aD) \right] \cos(aD) \right\}, \quad (10)$$

where, for a model of an exponential atmosphere with scaleheight \tilde{H} , we have

$$a = \frac{\tilde{\tau}}{\tilde{H}} \left(1 + \frac{\tilde{\mu}_0}{\mu} \right). \quad (11)$$

The atmospheric scaleheight \tilde{H} is the altitude up to which a homogeneous atmosphere would extend. It can be obtained by integrating all of the atmosphere (for gaseous and aerosol components) and replacing the integral by a slab (of thickness \tilde{H}) of constant density. Assuming H_R and H_a are the Rayleigh and aerosol components of the atmospheric scaleheights, we determine \tilde{H} as follows:

$$\tilde{H} = \frac{H_R \tilde{\tau}_R + H_a \tilde{\tau}_a}{\tilde{\tau}_R + \tilde{\tau}_a}. \quad (12)$$

In equation (12), $\tilde{\tau}_R$ and $\tilde{\tau}_a$ are spectrally weighted Rayleigh and aerosol components of the atmospheric optical depth $\tilde{\tau}$, i.e. $\tilde{\tau} = \tilde{\tau}_R + \tilde{\tau}_a$. In principle, \tilde{k} in equation (10) can be obtained using the integral mean value theorem. Assuming the scattering coefficient $k = k_0 \exp\{-r\tilde{\mu}_0/\tilde{H}\}$ is to be averaged along the beam path length (r) from the source of light to the elementary atmospheric volume, we have $\tilde{k} = k_0 \exp\{-\tilde{h}/\tilde{H}\}$, where \tilde{h} is an ‘efficient’ altitude for scattering events, i.e. the altitude at which the density function for scattering events peaks. Although no simple formula for \tilde{h} exists, the numerical runs resulted in an approximate formula $\tilde{h} \approx D\tilde{\tau}/3$. At short distances, $\tilde{h} \ll \tilde{H}$, meaning that $\tilde{k} \cong k_0$. However, the importance of the exponential term increases as the distance from the city approaches large values. By definition, any optical depth τ is the integral of k from the ground to the top of the atmosphere:

$$\tau = \int_0^\infty k(h) dh = k_0 \int_0^\infty e^{-h/\tilde{H}} dh = k_0 \tilde{H}. \quad (13)$$

Therefore $k_0 = \tau/\tilde{H}$. For $\tau = \tilde{\tau}$, it follows that

$$J(z) = I_0 \frac{9}{32\pi} \frac{\tilde{\tau} e^{-D\tilde{\tau}/(3\tilde{H})}}{\mu \tilde{H} D} \left\{ Ci(aD) \sin(aD) + \left[\frac{\pi}{2} - Si(aD) \right] \cos(aD) \right\}. \quad (14)$$

The above formula for sky radiance at distances far away from the city reduces to

$$J(z) = \frac{I_0}{D^2} \frac{9}{32\pi} \frac{e^{-D\tilde{\tau}/(3\tilde{H})}}{\mu + \tilde{\mu}_0}, \quad (15)$$

where $\tilde{\mu}_0$ is a free parameter ranging from 0 to 1. The theoretical approximation to the irradiance at a horizontal surface is then

$$E = 2\pi \int_0^{\pi/2} J(z) \sin z \cos z dz = \frac{9}{16} \frac{I_0}{D^2} e^{-D\tilde{\tau}/(3\tilde{H})} \left[1 + \tilde{\mu}_0 \ln \left(\frac{\tilde{\mu}_0}{1 + \tilde{\mu}_0} \right) \right]. \quad (16)$$

Irradiance on a horizontal surface is determined in W m^{-2} , for sky radiance J in $\text{W m}^{-2} \text{sr}^{-1}$. However, provided $J = J_V$ is the sky luminance (cd m^{-2}), the illuminance E_V (lux) is obtained from equation (16). The last term in square brackets ranges from 0.3 to 1, so the irradiance E ranges from 17–56 per cent of $I_0 e^{-D\tilde{\tau}/(3\tilde{H})}/D^2$.

Basically, I_0 is related to the total radiative flux from a city (W_0). For ‘specific’ radiance I_0 independent of direction, we have

$$W_0 = 2\pi I_0 \int_0^{\pi/2} \sin(z_0) \cos(z_0) dz_0 = \pi I_0. \quad (17)$$

If a city behaves like an isotropic radiator with a constant radiant intensity, the total radiative flux normally increases by a factor of 2. The total radiative flux W_0 (lm) exclusively characterizes the radiation directed upwards. Therefore, W_0 is much smaller than the total lumens installed ($W_0^{\text{installed}}$). For an idealized city with all lights shielded, the sky brightness is typically due to ground reflection, so $W_0 = G \cdot W_0^{\text{installed}}$, where

G is the fraction of light that is isotropically reflected from the ground. It is made clear by combining equations (16) and (17) that irradiance E (W m^{-2}) at distance D from a city producing W_0 Watts upwards is

$$E = \frac{9}{16\pi} \frac{W_0}{D^2} e^{-D\bar{\epsilon}/(3\bar{H})} \left[1 + \bar{\mu}_0 \ln \left(\frac{\bar{\mu}_0}{1 + \bar{\mu}_0} \right) \right]. \quad (18)$$

Correspondingly, illuminance E_V (lux) at distance D from a city producing W_{V0} lumens upwards is

$$E_V = \frac{9}{16\pi} \frac{W_{V0}}{D^2} e^{-D\bar{\epsilon}/(3\bar{H})} \left[1 + \bar{\mu}_0 \ln \left(\frac{\bar{\mu}_0}{1 + \bar{\mu}_0} \right) \right]. \quad (19)$$

Averaging the last term in the square brackets above results in

$$E \approx 0.1 \frac{W_0}{D^2} e^{-D\bar{\epsilon}/(3\bar{H})} \quad (20)$$

and

$$E_V \approx 0.1 \frac{W_{V0}}{D^2} e^{-D\bar{\epsilon}/(3\bar{H})}. \quad (21)$$

For a fully isotropic radiator, the constant factor of 0.1 would reduce by a factor of 2.

In fact, W_{V0} is not an unknown parameter, because, by interpreting equation (17) as the radiative flux upwards, we can easily determine W_{V0} for other conventional models like e.g. Garstang's source (Garstang 1986):

$$W_{V0} = 2\pi \int_0^{\pi/2} I_{\text{up}}(z_0) \sin(z_0) dz_0 = LP [G (1 - F) + F], \quad (22)$$

where the parameters F and G are known as the fraction of light radiated directly into the upward hemisphere and the fraction of the light reflected isotropically from the ground, respectively. In equation (22), I_{up} is the cosine projected luminance, so $\cos(z_0)$ is included implicitly. Note that $\bar{\mu}_0$ is the only new parameter introduced in the theoretical model. Although there is no experience with how $\bar{\mu}_0$ works for many cities, this is by far not the first case in which a new parameter has been introduced to the respective solution. Similarly, as described by Garstang for the parameter F , $\bar{\mu}_0$ should also be retrieved for a city. Among other similarities, $\bar{\mu}_0$ ranges in the same way as F from 0 to 1. Compared with more complex night-sky radiance/luminance models, the above theory is advantageous and easy to use because an extremely low number of input parameters is required.

3 EXPERIMENTAL VALIDATION

To validate our approach, measurements of the sky radiance at different distances from a dominating light-emitting city are necessary. The best way of doing this is to find a well-isolated city with no other emitting sources around and measure the luminance as a function of distance. However, this is hardly possible in Europe, because there are many disturbing light sources. Nevertheless, the theory is to model sky brightness in a plane that crosses the horizon in the azimuthal position of the dominating city. For that specific city, this is the brightest segment of sky, meaning that the contribution from other cities to the sky brightness is generally low if the (angular) separation distance between the observed city and other dominant light sources is large enough.

To receive not only one-dimensional luminance data of the zenith but also two-dimensional all-sky images, we used a digital reflex camera (Canon EOS 5D Mark II) with fisheye lens beside the common Sky Quality Meter (SQM). Combined with special software called 'SKY QUALITY CAMERA' developed by Andrej Mohar from Euromix Ltd., Slovenia, the result is a matrix that yields an exact measurement of the light pollution across the whole sky. With the possibility of subtracting the influence of stars and the Milky Way, the data received are more accurate than any single point measurement done with an SQM. Therefore it was also possible to analyse the luminance variations at different zenith angles and distances to the light-emitting source.

The data were obtained in Eastern Austria in beginning of September 2018 at measuring sites spread at distances of approximately 15–60 km from the city centre of Vienna. The field experiment also includes locations with short distances from a city, to show how the formulae derived earlier work at different distances. Table 1 gives an overview of locations, distances to Vienna and the next bright – for areas far away from Vienna, also dominating – light source, Bratislava. We chose locations in the southeastern direction in Vienna, because in this way a clear separation between the light domes of Vienna and Bratislava was possible. Also, at DM1–DM7 there were no local light sources in the direction of both cities that contribute to their light domes and are only visible clearly separated.

Values of zenith brightness are displayed in Table 2. For better visualization, we have displayed all measuring sites on a map (see Fig. 1). The map also documents that the azimuthal positions of both cities are different enough to permit the use of the theory developed in Section 2.

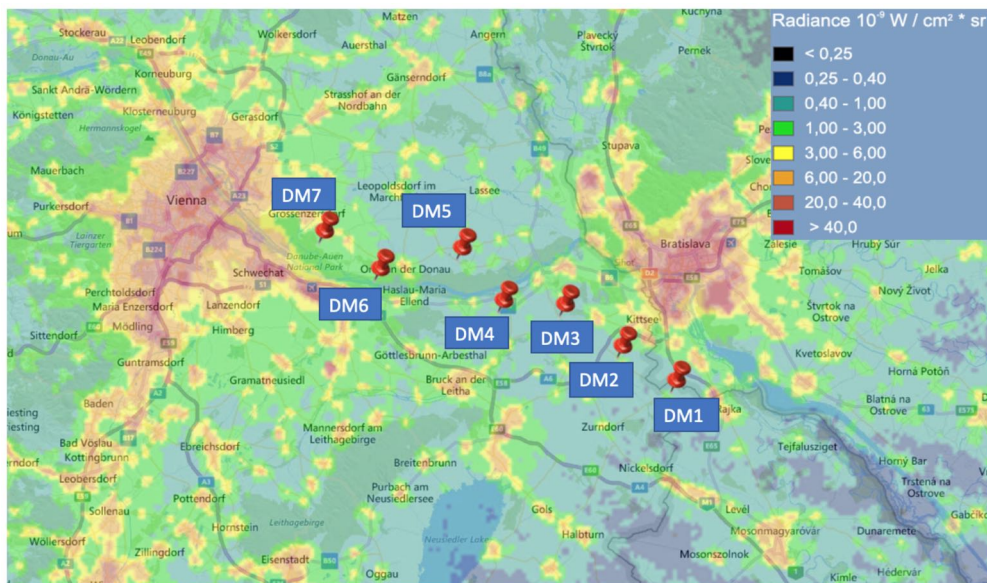
The theoretical model is normally applicable to sources located at intermediate to large distances, so it should be expected that the accuracy of the approximate formula will improve gradually with increasing distance to a city. This is what we have found when applying equation (10) to fit the experimental data (Figs 2 and 3). The luminance is shown as a function of $\mu = \cos z$, where z is the observation zenith angle. For the numerical test, we have used $H_R = 8$ km and $H_a = 1.5$ km, while the aerosol optical depth of 0.12–0.15 was estimated based on the visibility using the improved formula by Wu et al (2014). The parameters I_{V0} and μ_0 (or alternatively W_{V0} and μ_0) were the only unknown inputs to the numerical analysis. They both characterize the emission properties of a city. We have used the method of least-squares

Table 1. Locations and data of measurements performed in Eastern Austria. The local time (CEST) is in the last column. Date format is yyyy-mm-dd.

Identifier	Latitude, longitude (°)	Distance to Vienna city centre (km)	Distance to Bratislava city centre (km)	Date & time
DM1	48.0118, 17.0937	~58	~15	2018-09-05 23:21h
DM2	48.0516, 17.0233	~51	~13	2018-09-05 23:49h
DM3	48.0879, 16.9431	~45	~15	2018-09-06 00:26h
DM4	48.1033, 16.8530	~38	~21	2018-09-06 00:53h
DM5	48.1536, 16.7757	~31	~27	2018-09-06 01:24h
DM6	48.1408, 16.6404	~22	~37	2018-09-06 01:50h
DM7	48.1832, 16.5562	~14	~43	2018-09-06 02:18h

Table 2. Zenith brightness determined from SKY QUALITY CAMERA software and the luminance calculated.

Location	SQM _v (mag)	Luminance (mcd m ⁻²)
DM1	20.46	0.707007
DM2	20.20	0.898305
DM3	20.53	0.662863
DM4	20.72	0.556447
DM5	20.73	0.551345
DM6	20.07	1.012567
DM7	19.37	1.929407

**Figure 1.** Observation points shown with pins and numbered DM1–DM7. The dominant cities are shown: left, Vienna; right, Bratislava. The map shows radiance data from www.lightpollutionmap.info by Jurij Stare.

to determine the luminance patterns that are the best fits to the experimental data. As a result, I_{V0} and μ_0 were found for both cities, Vienna and Bratislava.

Figs 2 and 3 demonstrate that the theoretical model works well and allows for determination of the lumen output upwards from each of the dominant light sources. The only requirement is to take the experimental data at intermediate distances from a city, because the information content is significantly lowered as the distance approaches infinity (compare equations 14 and 15). On the other hand, the formula becomes inaccurate near the city. For the city of Bratislava, the values of $I_{V0} = 2.3 \times 10^7$ (lm sr⁻¹) and $\mu_0 = 0.19$ were extracted from DM6 in Fig. 2. In

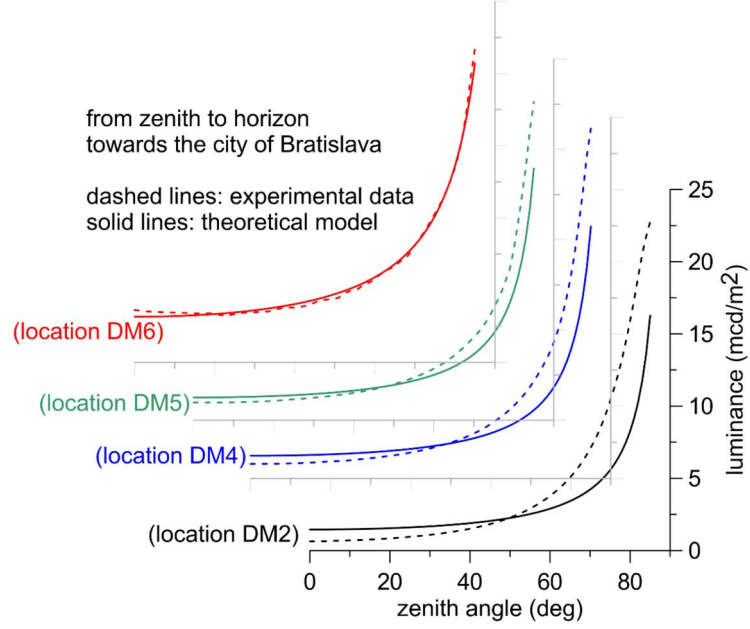


Figure 2. Experimental luminance data (dashed lines) versus theoretical fits (solid lines) for observations made at different places in the neighbourhood of the city of Bratislava. The luminance patterns are always taken from the zenith towards the azimuthal position of the city. The distances (from DM2–DM6) are 13, 21, 27 and 37 km.

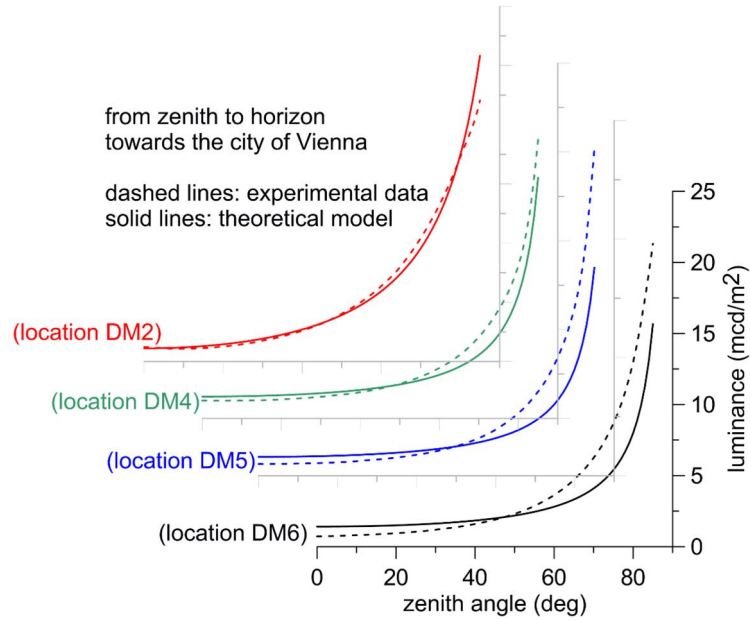


Figure 3. The same as in Fig. 2, but for the city of Vienna. The distances from DM6–DM2 are as follows: 22, 31, 38 and 51 km.

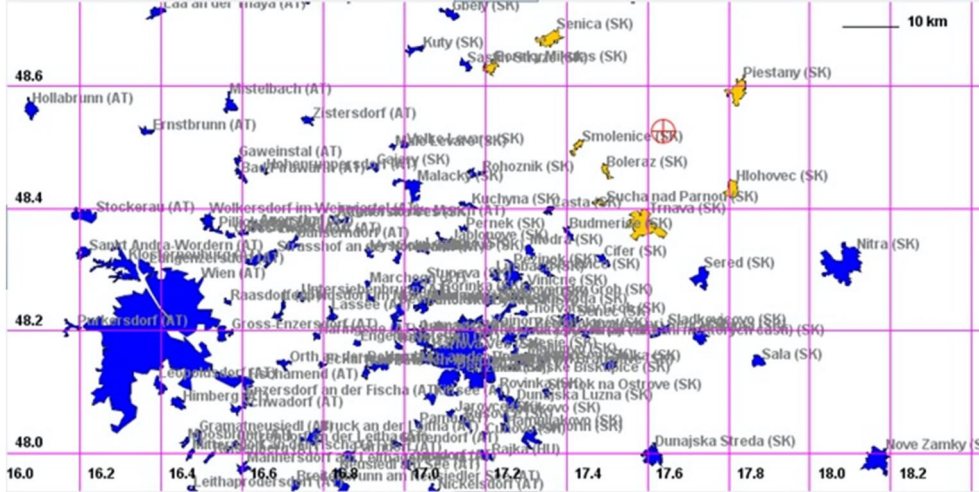


Figure 4. The computational model of Vienna–Bratislava surroundings (model No. 1). The cities and towns included in the computational model are in yellow. The red cross is to indicate the observer's position on the map.

the case of an isotropic radiator, I_{V0} translated to the value of luminous flux $W_{V0} = 1.4 \times 10^8$ (lm). The choice for the observation point DM6 resulted from the requirement to analyse radiance data taken at a distant place. Of all sites, DM6 is at the farthest distance from Bratislava, but still outside the city of Vienna. We have not used the data taken in DM7, as the measuring device was too close to the inner city. The luminance data taken in DM2 were used to characterize the city of Vienna (Fig. 3), while the following parameters were found for Vienna: $I_{V0} = 2.6 \times 10^7$ (lm sr^{-1}), $\mu_0 = 0.13$, i.e. $W_{V0} = 1.6 \times 10^8$ (lm). Strictly theoretically, the higher ratio of distance to city radius implies that the accuracy of the results achieved for Bratislava should be higher than that for Vienna, because the ratio for the city of Bratislava is 6:1 and so slightly exceeds that for the city of Vienna (5:1). The results indicate that Vienna emits only 14 per cent more light to the upward hemisphere compared with Bratislava. Assuming the amount of light escaping upwards is approximately 10–15 per cent of that emitted from all light sources to all directions, we estimate that the total amount of lumens installed in Vienna ($W_{V0}^{\text{installed}}$) varies roughly from 1×10^9 to 1.6×10^9 lm. This also conforms with findings by Puschig, Posch & Uttenhaller (2014), who estimated that the total light output of the city of Vienna due to street lighting is about 1.1 Gigalumens.

4 NUMERICAL VALIDATION AND SOME CONSEQUENCES

The formulae developed in this article are to save the computational time otherwise spent on large-scale modelling for territories with one or both linear dimensions exceeding several tens or hundreds of kilometres. One can expect that cities and towns at large distances from an observer will normally contribute marginally to the sky brightness, because the angular size of each artificially lit area is reduced by the square of its distance. However, the number of cities increases with the square of distance. Both effects show opposite trends, but the intensity also obeys an exponential law in a turbid atmosphere. Therefore, the sky brightness decays more steeply than D^{-2} . For instance, Duriscoe et al. (2018) found that the exponent in the brightness–distance relationship is between -2 and -2.5 at distances up to 300 km, while Aubé (2015) has identified an even steeper decrease with the exponent raised to -3.33 . However, the signals from highly populated cities should not be ignored, even if their distance to an observer is as large as hundreds of kilometres (Cinzano & Falchi 2013).

The numerical experiment on skyglow from many light sources scattered over the metropolitan area of Vienna–Bratislava and its surroundings is demonstrated below. We have started with a small area with a radius of approximately 25 km, as shown in Fig. 4. The model inputs are as follows: spectral bandwidth = 500–520 nm; aerosol optics (optical depth = 0.3, asymmetry parameter = 0.9, single scattering albedo = 0.85); atmospheric model (plane-parallel atmosphere, cloudless conditions, Rayleigh scaleheight = 8 km, aerosol scaleheight = 1.5 km); model of cities/towns (upward light output ratio = 0.1, ground reflectance = 0.1, lumen output expressed as lumens per capita, light source spectrum = HPS). The aerosol optical data under consideration are representative for urban/rural regions, with particles containing a mixture of minerals and other partly absorbing materials (Dubovik et al. 2002; Horvath et al. 2002; Bozzo et al. 2017). Aerosol scaleheight depends on the region and season, and can range from 1–3 km (Husar, Husar & Martin 2000; Wu et al. 2011), but values below 1 km have been also reported by some authors (e.g. Singh & Dey 2012). It is also not rare that H_a from 0.5–4 km is used in aerosol optical studies (Aloysius et al. 2009). The molecular scaleheight is $H_R = 8$ km (in accordance with Waquet et al. 2009). The fraction of light radiated directly into the upward hemisphere is currently low for typical and relatively poor drop-lens cobra-head street lights (Kinze et al. 2017), but

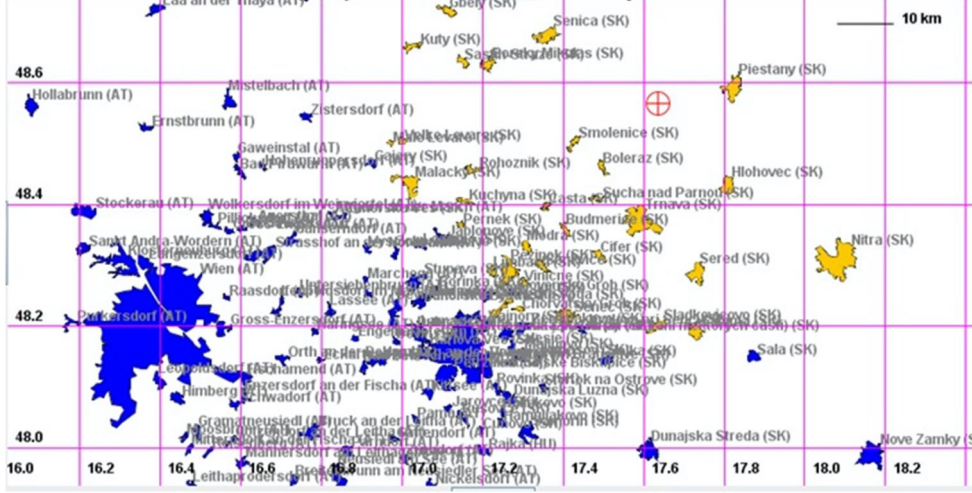


Figure 5. The same as in Fig. 4, but the radius of the artificially lit area around a hypothetical observer is increased to approx. 45 km (model No. 2).

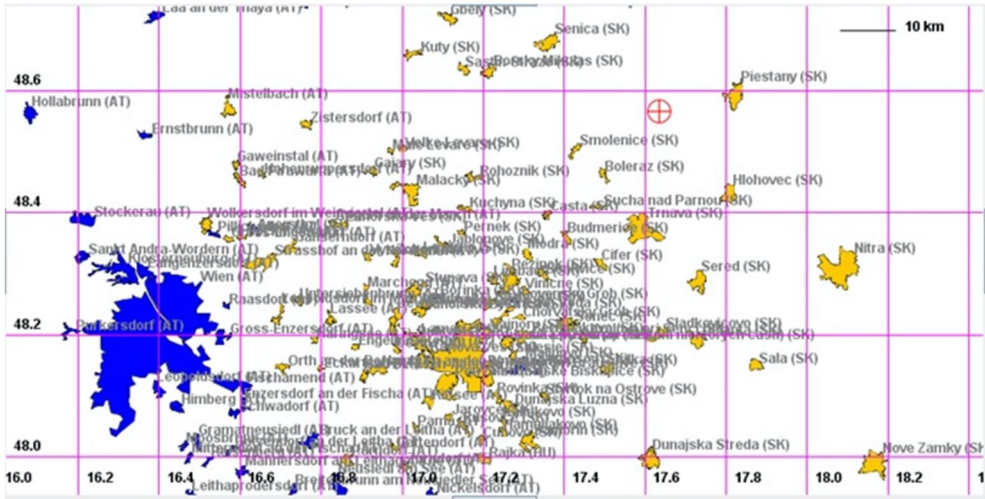


Figure 6. The same as in Fig. 4, but the radius of the artificially lit area around a hypothetical observer is increased to approx. 78 km (model No. 3).

we have used 10 per cent uplight to be consistent with many other skyglow models (e.g. Aubé 2015). The ground reflectance is an average over several types of surface, including asphalt, light and dark soils, deciduous trees and coniferous trees (Shirkey 2008).

The choice for the specific lighting technology (e.g. HPS) plays a minor role in our modelling, since we limit our numerical tests to a narrow-band spectrum and the effects of distant sources are studied relative to the baseline situation No. 1 (see Fig. 4). Although we calculate the absolute values of radiance and irradiance using SKYGLOW SIMULATOR (Kocifaj 2017), we later study the relative influence of distant sources on the zenith radiance $J(0)$ and horizontal irradiance E . First, the theoretical sky radiance in the position of a hypothetical observer (see the red cross in Fig. 4) due to cities and towns in its close surroundings is analysed. The circular area with a maximum radius of about 25 km in Fig. 4 is referred to as model No. 1. We have found that the narrow-band radiance from nearby light sources is approximately $1.2 \text{ nW m}^{-2} \text{ sr}^{-1}$, while the horizontal irradiance is $\approx 30 \text{ nW m}^{-2}$.

By extending the area under evaluation from 25 km to approximately 45 km (model No. 2, Fig. 5), we found that both $J(0)$ and E are refined to $1.5 \text{ nW m}^{-2} \text{ sr}^{-1}$ and 38 nW m^{-2} , respectively. The largest modelling domain has a radius of 78 km (see Fig. 6). In this third

Table 3. The relative radiance and irradiance contributions from cities in different zones compared with the final conditions.

Model No.	Maximum radius (km)	Contribution to zenith radiance (%)	Contribution to horizontal irradiance (%)
1	25	55	53
2	45	68	66
3	78	86	84
3+Vienna	101	100	100
Vienna	distance: 101 km	14	16

run, the zenith radiance and horizontal irradiance have both improved by 25 percent, i.e. $J(0)$ has changed from $1.5 \text{ nW m}^{-2} \text{ sr}^{-1}$ to $1.9 \text{ nW m}^{-2} \text{ sr}^{-1}$, while the previous value of E (38 nW m^{-2}) is now updated to 48 nW m^{-2} . The skyglow effects due to light emissions from the city of Vienna have been analysed separately, showing that Viennese urban and suburban areas contribute to $J(0)$ by $0.3 \text{ nW m}^{-2} \text{ sr}^{-1}$, thus resulting in an approximately 15 per cent increase of zenith radiance from 1.9 to the final value of $2.2 \text{ nW m}^{-2} \text{ sr}^{-1}$. The correction to the horizontal irradiance due to Vienna is $\Delta E = 9 \text{ nW m}^{-2}$, which leads to the final value of $E = 57 \text{ nW m}^{-2}$. To facilitate comparisons, the above results are reported relative to the final conditions as fractions thereof (see Table 3).

The theoretical zenith radiance in the isotropic radiator approximation is derived from equation (15) when adding a weighting factor of $\frac{1}{2}$, i.e.

$$J(0) = \frac{W_0}{D^2} \frac{9}{64\pi^2} \frac{e^{-D\tau/(3\hat{H})}}{1 + \mu_0}. \quad (23)$$

Processing the data taken during the field campaign in Eastern Austria, we have found the total lumen output upwards is $W_{V0} = 1.6 \times 10^8 \text{ lm}$ for the city of Vienna. In addition, the parameter μ_0 is 0.13. Inserting these two values into equation (23) and accepting a ratio of narrow-band (500–520 nm) radiance to luminance of roughly 10^{-4} , we estimated the theoretical zenith radiance $J(0) = 0.3 \text{ nW m}^{-2} \text{ sr}^{-1}$, which is, surprisingly, the same value we have found from numerical integration using SKYGLOW SIMULATOR. This conformity is rather fortuitous, because the approximate formula (23) does not account for some of the input parameters that are used by SKYGLOW SIMULATOR (see e.g. Kocifaj & Kundracik 2016; Barentine et al. 2018). Nevertheless, such a good match lends credence to our approximate model.

It is a bit more difficult to estimate horizontal irradiance, because equation (18) or (19) is only valid for a plane that intersects the upper hemisphere in the azimuthal position of Vienna, so the integration including all azimuths would need an additional workaround. In the limiting case, for very large distances D , equation (19) approaches equation (21). This is why equation (21) can only be used for a rough estimate. In our case, we have found that $E(500\text{--}520 \text{ nm})$ is about $2\text{--}3 \text{ nW m}^{-2}$, which is about 30 percent of the value obtained from numerical integration. Our estimate would improve if using equation (19) in combination with some radiance pattern (e.g. Rayleigh-type, HGPF, NSPF and other-type phase functions, see Sharma 2015). One of the simplest concepts dates back to Tousey & Hulburt (1947), who have applied the separation variables method to express the clear-sky radiance pattern as a product of two functions. The first one (also referred to as the gradation function) depends only on the zenith angle, while the other one (the so-called scattering indicatrix) is ruled by the scattering angle. The optical properties of the atmosphere, such as the transmission coefficient, are included implicitly (see Vida, Foyo-Moreno & Alados-Arboledas 1999). The night-sky brightness $J(z)$ determined from our theory for the principal plane (observer–zenith–centre) can be then used to predict night-sky brightness $J(z, A)$ for azimuth angles (A) other than the azimuth of a light source (A_S):

$$J(z, A) = J(z) S_i(\theta), \quad (24)$$

where the scattering indicatrix $S_i(\theta)$ can be either derived from a scattering phase function (such as HGPF, NSPF, ...) or approximated as suggested by Kittler et al. (2012):

$$S_i(\theta) \propto 1 + c_1 \{e^{d\theta} - e^{d\pi/2}\} + c_2 \cos^2 \theta, \quad (25)$$

where c_1 , c_2 and d are scaling constants. However, the concept of scattering indicatrices is outside the scope of this article. In fact, any approximation is better than truncating the computation before a satisfactory accuracy is achieved. A correction to the irradiance (even if based on equation 21) is not as bad, because, in astronomy, models providing results accurate to within the same order of magnitude are generally considered to be acceptable. Despite the limits of the approximation introduced, the new theory has the potential to offer substantial reward in a significant reduction of central processing unit (CPU) time, while keeping the error margin low.

The CPU time to obtain the sky radiance for an evenly gridded artificially lit surface of the Earth is normally a function of D^2 , so the CPU requirements for running model No. 2 (Fig. 5) are three times stronger than those for model No. 1 (Fig. 4). The CPU consumption grows further when running model No. 3. In that case, the processor time would increase by a factor of 10 relative to the baseline conditions. This is why the approximate formulae allow us to save a significant portion of CPU resources. In addition, the contribution to skyglow from light sources located behind the model boundaries is estimated based on equations (14)–(16), instead of being ignored.

Asymptotic formula for skyglow 2223

Taking into account that W_{0i} and μ_{0i} are to characterize the i th distant source of light (a city or town), we can calculate the radiance as follows:

$$J(z) = J^C(z, D < D_{\text{lim}}) + \frac{9}{64\pi^2} \sum_{i=1}^N \frac{W_{0i} e^{-D_i \tau / (3H)}}{D_i^2 \mu + \mu_{0i}}, \quad (26)$$

where $D_i \geq D_{\text{lim}}$ is the distance between the observer and the i th light source. The radiance J^C denotes numerical integration over all sources within the circular area centred in the observer's position with a maximum radius of D_{lim} . The value of J^C can be obtained from numerical integrators with D_{lim} chosen depending on accuracy and CPU time demands. For instance, the typical modelling domain for the ILLUMINA tool is about $100 \times 100 \text{ km}^2$ (Aubé 2007). A similar radius is considered in SKYGLOW SIMULATOR.

5 CONCLUSIONS

Currently the numerical solvers necessary for modelling the skyglow from artificial sources of light are limited in accuracy, because of various assumptions used in their development and approximations to the physics of light scattering phenomena, partially incomplete or unknown input data and imperfections in modelling the heterogeneity on small and large scales, but also because of finite size of the modelling domain. The latter introduces a systematic error to the computational results, as the numerical integration is only performed for a closed area of e.g. circular, rectangular or any other shape. The computational inaccuracy due to emissions from distant light sources located outside the closed area is largely unknown, but exclusion of these sources definitely has an effect on the systematic underestimation of radiance and irradiance data. Unfortunately, all of the present algorithms and numerical solvers converge to the specified error tolerance only slowly as the size of the closed area increases, and any extension of the modelling domain poses strong requirements on computer power. Distributed and parallel computing can partially tackle the problem; however, the use of large computing clusters to perform routine astronomical skyglow simulations under various conditions in different territories is scarcely practical in a great deal of cases. Note that, for routine modelling purposes, the entire set of calculations usually needs to be repeated, with the aim of simulating the night-sky radiance in various situations: e.g. for various types of lighting technologies, spatial arrangement of light-emitting sources or different atmospheric turbidities.

In this article, we have developed a new analytical formula to compute night-sky brightness from distant light sources under cloudless conditions. The formula permits us to estimate the overall error in radiance/irradiance computations due to numerical modelling being limited to finite-dimensional systems. In other words, the theory models the residual part of numerical integration on an otherwise infinite domain. Our approach to determine the true radiance/luminance is to combine the numerical integration on a finite domain and the approximate formula developed here. This approach reduces computational time and errors significantly. The contribution from distant light sources is a trivial superposition of analytical fits accepting different distances to the sources. Time savings improve with the square of distance or the surface of outermost part of the modelling domain, while all light sources distributed therein are simulated by the last term of equation (26). The field campaign in Eastern Austria has proven that a theoretically predicted sky luminance distribution from the zenith toward the horizon is consistent with what we have determined experimentally. In addition, equations (14) or (15) appear to be ideal tools to retrieve the light output from dominant cities surrounding the observation point.

ACKNOWLEDGEMENTS

This work was supported by the Slovak Research and Development Agency under Project No. APVV-14-0017. Computational work was supported by the Slovak National Grant Agency VEGA (grant No. 2/0016/16).

REFERENCES

- Aloysius M. et al., 2009, *Ann. Geophys.*, 27, 2285
 Aubé M., 2007, in Cipriano M., Jafar J., eds, Proc. of the StarLight Conference 2007, Unesco, La Palma, Spain, p. 351
 Aubé M., 2015, *Phil. Trans. R. Soc.*, B370, 20140117
 Aubé M., Roby J., 2014, *J. Quant. Spectrosc. Radiative Transfer*, 139, 52
 Aubé M., Simoneau A., 2018, *J. Quant. Spectrosc. Radiat. Transf.*, 211, 25
 Aubé M. et al., 2005, in Huang Hung-Lung A. et al., eds, Proc. SPIE 5890, Atmospheric and Environmental Remote Sensing Data Processing and Utilization: Numerical Atmospheric Prediction and Environmental Monitoring, Society of Photo-Optical Instrumentation Engineers, San Diego, California, United States, p. 248
 Barentine J. C. et al., 2018, *J. Quant. Spectrosc. Radiative Transfer*, 212, 10
 Bará S., Ribas S. J., Kocifaj M., 2015, *J. Opt.*, 17, 105607
 Bozzo A. et al., 2017, Tech. Memo. No. 801. ECMWF, Available at: <https://www.ecmwf.int/node/17219>
 Cinzano P., 2000, *Mem. Soc. Astron. It.*, 71, 239
 Cinzano P., Falchi F., 2013, *MNRAS*, 427, 3337
 Dubovik O. et al., 2002, *J. Atmos. Sci.*, 59, 590
 Duriscoe D. M. et al., 2018, *J. Quant. Spectrosc. Radiative Transfer*, 214, 133
 Falchi F. et al., 2016, *Sci. Adv.*, 2, e1600377
 Garstang R. H., 1986, *PASP*, 98, 364
 Gaston K. J. et al., 2017, *Annu. Rev. Ecol. Evol. Syst.*, 48, 49
 Horvath H. et al., 2002, *J. Geophys. Res.*, 107, 4386

2224 *M. Kocifaj, S. Wallner and H. A. Solano-Lamphar*

- Husar R. B., Husar J. D., Martin L., 2000, *Atmos. Environ.*, 29–30, 5067
- Joseph J. H., Kaufman Y. J., Mekler Y., 2001, *Appl. Opt.*, 30, 3047
- Kinzev B. et al., 2017, Technical report, Pacific Northwest National Laboratory. Richland, Washington, p. 38
- Kittler R. et al., 2012, Daylight Science and Daylighting Technology, p. 341
- Kocifaj M., 2007, *Appl. Opt.*, 46, 3013
- Kocifaj M., 2008, *Appl. Opt.*, 47, 792
- Kocifaj M., 2011, *MNRAS*, 415, 3609
- Kocifaj M., 2017, SkyGlow Simulator, <http://skyglow.sav.sk/#simulator> (accessed 2019 January 15)
- Kocifaj M., 2018, *J. Quant. Spectrosc. Radiative Transfer*, 206, 260
- Kocifaj M., Kundracik F., 2016, in Proc. IEEE Lighting Conference of the Visegrad Countries (Lumen V4), IEEE, Karpacz, Poland, p. 16467762
- Kokhanovsky A. A., 1998, *J. Atmos. Sci.*, 55, 314
- Kolláth Z., Dömény A., Kolláth K., Nagy B., 2016, *J. Quant. Spectrosc. Radiative Transfer*, 181, 46
- Luginbuhl C. B., Duriscoe D., Moore C., Richman A., Lockwood W., Davis R., 2009b, *PASP*, 121, 204
- Luginbuhl C. B., Walker C. E., Wainscoat R. J., 2009a, *Phys. Today*, 62, 32
- Puschnig J., Posch T., Uttenthaler S., 2014, *J. Quant. Spectrosc. Radiative Transfer*, 139, 64
- Sharma S. K., 2015, in Kokhanovsky A. A., ed., *Light Scattering Reviews 9*. Springer, Berlin, Heidelberg, p. 53
- Shirkey R. C., 2008, Technical report, ARTL-TR-4645. Army Research Laboratory, White Sands Missile Range, NM, USA
- Singh A., Dey S., 2012, *Atmos. Environ.*, 62, 367
- Tousey R., Hulbert E.O., 1947, *J. Opt. Soc. Am.*, 37, 78
- Vida J., Foyo-Moreno I., Alados-Arboledas L., 1999, *Energy*, 24, 705
- Waquet F., Cairns B., Knobelspiesse K., Chowdhary J., Travis L. D., Schmid B., Mishchenko M. I., 2009, *J. Geophys. Res. Atmos.*, 114, D01206
- Wu D. et al., 2011, *J. Opt. Soc. Korea*, 15, 90
- Wu J. et al., 2014, *J. Geophys. Res. Atmos.*, 119, 13370

This paper has been typeset from a Microsoft Word file prepared by the author.

4.2 'Impacts of surface albedo variations on the night sky brightness – A numerical and experimental analysis'

Title: *Impacts of surface albedo variations on the night sky brightness – A numerical and experimental analysis*

Authors: S. Wallner, M. Kocifaj

Journal: Journal of Quantitative Spectroscopy & Radiative Transfer (JQSRT)

Status: Published in J QUANT SPECTROSC RA 239, 106648 (2019)

DOI: <https://doi.org/10.1016/j.jqsrt.2019.106648>

Personal contribution: M. Kocifaj and myself carried out the idea of this work. As first author, I was responsible for data collection of the light monitoring network and their analysis, adoption of the theoretical model and calculations, and the utilisation of results. Furthermore, I wrote the first version of the paper, and, as correspondent author, was in charge of the submission and revision process.



Contents lists available at ScienceDirect

Journal of Quantitative Spectroscopy & Radiative Transfer

journal homepage: www.elsevier.com/locate/jqsrt

Impacts of surface albedo variations on the night sky brightness – A numerical and experimental analysis

Stefan Wallner^{a,b,*}, Miroslav Kocifaj^{b,c}^a Department of Astrophysics, University of Vienna, Türkenschanzstrasse 17, 1180 Vienna, Austria^b ICA, Slovak Academy of Sciences, Dúbravská Road 9, 845 03 Bratislava, Slovak Republic^c Department of Experimental Physics, Faculty of Mathematics, Physics, and Informatics, Comenius University, Mlynská dolina, 842 48 Bratislava, Slovak Republic

ARTICLE INFO

Article history:

Received 15 July 2019

Revised 12 September 2019

Accepted 12 September 2019

Available online 14 September 2019

Keywords:

Skyglow

Surface albedo

SQM

Simulations

Light pollution

Modeling

ABSTRACT

The aim of this paper is to analyze surface albedo impacts on artificial night sky brightness at zenith. The way in which these parameters correlate with each other is analyzed numerically and then experimentally by Sky Quality Meters (SQMs) in the city of Linz, Austria between 2016 and 2018. Three SQMs are located in city areas that differ in ground type, while other two are installed outside but near the city. To eliminate systematic errors of different SQMs or a missing inter-calibration of all devices, we examine relative change in zenithal brightness instead of its absolute values. However, the ground albedo not only depends on the ground type, but also shows seasonal variation most often driven by vegetation and environmental change. To understand these changes, we use SkyGlow simulator to perform numerical experiments on four different albedo models. The results have proven that seasonal variations are clearly visible as green city parts become darker around autumn and ratios to urban located SQMs increase. We show that there is a major difference in simulation results if either conducting city parts with various surface albedos or using only one averaged value over the whole city. The latter produces worse fit to the observed SQM data, implying that a use of various surface albedos is a need when modeling zenithal brightness in artificially lit areas of a city or town. Also, the seasonal changes of surface albedo cannot be neglected and the parameter itself must be included in the modeling tools.

© 2019 Elsevier Ltd. All rights reserved.

1. Introduction

Ground surfaces differ in albedo which depends not only on natural factors, but also on land use [5]. There are urban parts which are highly populated, green areas with forests, seas and many more types. Furthermore, many of them change over the years, either because of vegetation and meteorological conditions or because of anthropogenic development [19] including construction activities. Therefore, a large heterogeneity of surface albedo values can be observed in nature, especially in urban areas [15,21,24,25]. It should be expected that non-uniform albedo patterns can produce certain types of skyglow distributions. With increasingly expanding artificially lit areas worldwide [26] and tendency to reduce direct light emissions upwards, a need for systematic analysis of the ground albedo impacts on skyglow also increases. For instance, the peak changes to sky brightness can be

observed when e.g. fresh snow is abundant in and around a city [14] or when clouds transit through a monitored part of night sky [8]. Since Garstang's model [6] a number of improvements have been introduced which allow for a high granularity of albedo values or use a direct link to the resolution of satellite products [3]. Also space borne platforms tried to analyze differences of Earth's surfaces when transiting seasons [23] with seeing pronounced effects across temperate regions like US, European or Asian tiles [18] and trying to draw conclusions to the ground albedo [13]. However, the effect of different values of surface albedo, not resulting from meteorological phenomena, has never been analyzed in detail. It also raises the question of how to use this parameter for skyglow predictions in a proper way. This could be particularly important for scientists who are severely limited by light pollution like astronomers, especially when observations are done at city observatories and the skyglow heterogeneity is not only due to light sources itself, but can also result from variability of ground reflected light. Also from ecological point of view the impact of various surface albedo to, e.g., chronobiology, could be of great importance.

* Corresponding author at. University of Vienna, Department of Astrophysics, 1180 Vienna, Austria

E-mail addresses: stefan.wallner@univie.ac.at (S. Wallner), kocifaj@savba.sk (M. Kocifaj).

<https://doi.org/10.1016/j.jqsrt.2019.106648>

0022-4073/© 2019 Elsevier Ltd. All rights reserved.

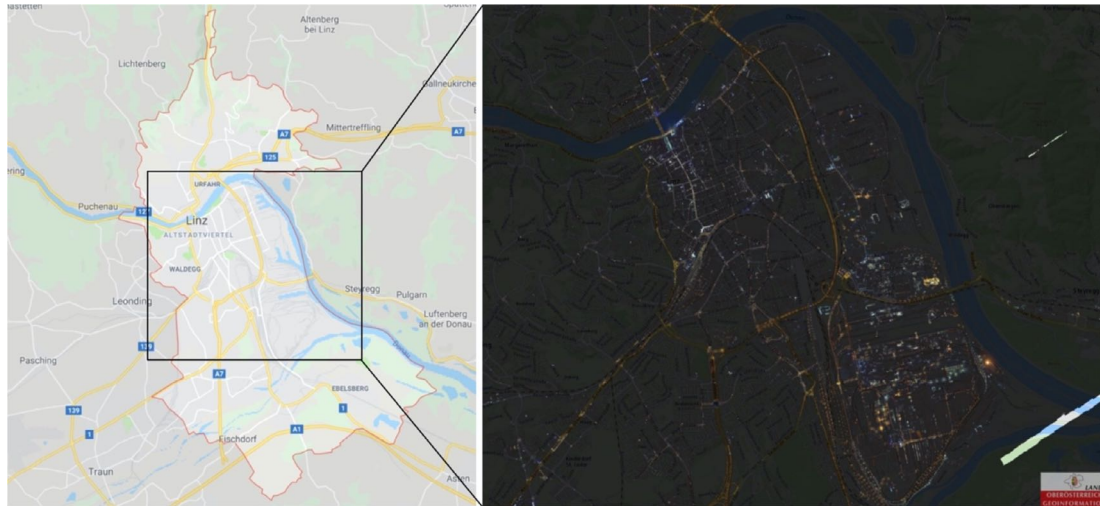


Fig. 1. Left: Street view of Linz and surroundings (by Google Maps); Right: Inner city of Linz as observed by aircraft measurement flights from above [2].

On the one hand, the ground albedo provided on a dense grid can make numerical predictions of sky brightness highly accurate, but computationally inefficient. On the other hand, a use of uniform albedo can produce systematic errors that, however, tend to drop down as the distance to a light source increases. This is because point-source approximation becomes more accurate at large distances. The aim of this work is therefore to answer questions about the importance of surface albedo in skyglow modeling and in proper interpretation of Sky Quality Meter observations (SQM) in a city and its near surroundings. The question on high vs. low granularity of ground albedo data is generally important for arbitrary modeling domain, but it is of special interest to explain some anomalous distributions of zenithal brightness over an urban area including green localities like city parks. We provide results of skyglow simulations which show the impact of changing surface albedo values over a year. This can be fundamental when planning e.g. city districts, observatories or other facilities or scientific measurements which could be affected by light pollution.

2. Data analysis

To obtain an overview of possible changes to the night sky brightness (NSB, also referred to here as zenith brightness, ZB) due to segmented surface albedo values, we chose to analyze the city of Linz, Austria (48.306389, 14.285833), capital city of the county Upper Austria. This location was selected as a light monitoring network [16] exists with Sky Quality Meters (SQMs) based inside and around the city. Also, the city has different types of surfaces as there are urban areas, green parks and the river Danube flowing through. Therefore, the present condition of diverse ground albedos motivated us to analyze their impacts on skyglow. We found that the three SQMs inside the city borders are ideally distributed over mentioned surface types, being capable of comparing simulations to observed data.

Fig. 1 illustrates the city of Linz as seen from above. The center and most urbanized area is located near the mid-eastern borders whereas northern and southern parts are much greener. The Danube matches the eastern city border and divides the urban area in two parts when flowing through the city.

As mentioned before, there are three SQMs stationed in the city. Another two are located in its surroundings, for analysis as later described, being able to compare possible albedo impacts on skyglow also outside the city borders. Detailed positions and short descriptions of all five SQM stations we obtained data from are shown in Table 1. As seen, LGO and LSW are optimal in their locations for this study as the former is situated in the city center and the latter in a green park. LSM is located near the city center, thus it also appears to be of great interest as this SQM can be found near the river bank of the Danube. A map which highlights the observing sites is shown in Fig. 2.

A location-specific advantage in our approach of data analysis is the multiplicity of SQMs in a small area as measurements are usually taken under the same meteorological conditions. The size of the city and the added surroundings can be assumed small compared to the size of 'air mass' (which in meteorological terminology means a body of air having nearly uniform conditions). This benefit simply is not accrued when drawing comparisons of, e.g., skyglow, with instruments installed in different cities or even different countries. Even with properly calibrated SQMs, with big distances in between them it cannot be guaranteed that they operate under the same or at least similar meteorological conditions. This is because the atmospheric turbidity and the nature of air contaminants make observational locations unique also if limiting ourselves to clear sky conditions. Consequently, misinterpretations could result of such inter-comparisons on large scales. Therefore, our approach to compare SQM data harvested in the same site within only a small area makes their comparisons well-reasoned and facilitated.

2.1. Skyglow modeling with SkyGlow tool

2.1.1. Method

Skyglow simulations of Linz were executed using the SkyGlow Simulator [9]. The aim was to see the strength of impacts with varying surface albedos and observing sites.

Model inputs were chosen in analogy with past works before [10,11], i.e., (a) aerosol optics includes: optical depth = 0.3, asymmetry parameter = 0.9, single scattering albedo = 0.85; (b) atmospheric model: plane-parallel atmosphere, cloudless conditions,

Table 1

Description of all SQM stations used for data analysis. The three-lettered identifiers of those located inside the city of Linz start with the letter L.

Identifier	Coordinates (N, E)	Description
LGO	48.305306, 14.308185	Urbanized, city center
LSM	48.305306, 14.282806	Urbanized, at river bank
LSW	48.293435, 14.268312	Mostly urbanized, edge of green area, near stadium
STW	48.288528, 14.353622	Green locality close to city edge
PAS	48.258681, 14.210051	Green locality outside and farer away from city

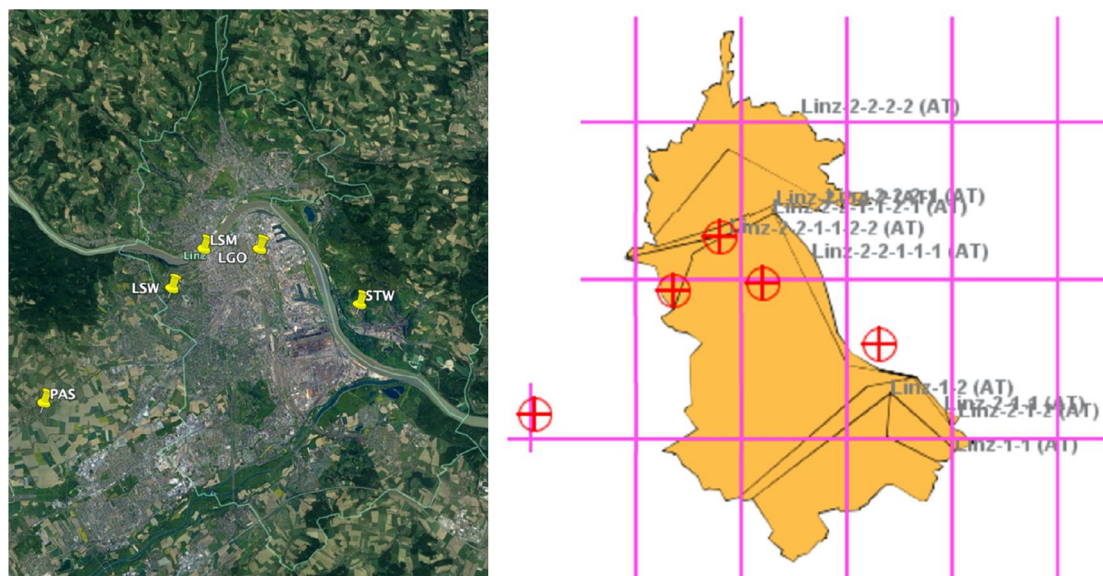


Fig. 2. Left: Distribution of SQM stations; Right: a digitized model for the city of Linz with observing sites highlighted (red circled crosses). The magenta lines describe coordinate system with latitude of 48.35° at the top horizontal, 48.25° at the bottom horizontal, and longitude 14.20° at the left vertical and 14.45° at the right vertical (the separation distance between two grid lines is 0.05°). The image is a bitmap exported from SkyGlow tool, so the labels and other non-described parts generated cannot be controlled, deleted, or modified.

Rayleigh scale height = 8 km, aerosol scale height = 1.5 km; (c) model of city: upward light output ratio = 0.1, lumen output expressed as lumens per capita, light source spectrum = HPS, spectral bandwidth = 500–520 nm. The spectral bandwidth was chosen to also match the peak response wavelength of SQMs with aim to document fundamental features of zenith brightness we can expect under the above conditions. A use of narrow-band modeling and three types of ground surfaces (see the Model A below) is not only to save the computational time significantly, but allows to easily examine our premise that the albedo-induced seasonal variation of zenith brightness has a theoretical foundation. The only parameter we have varied was the ground reflectance. To see effects of differing values, we chose to develop four models for the city of Linz:

- Model A: Linz is divided into different parts, as seen in Fig. 3, which were created to approximately match the real surface types of the city as seen before in Fig. 1. This enables to change ground albedo values for each of the parts generated instead of the whole city.
- Model B: The whole city (i.e. all parts) is specified with the urban ground albedo value only.
- Model C: The whole city is specified with the green ground albedo value only.

- Model D: The city is characterized by only one albedo value resulting of averaging those used in model A with respect to the size of the different areas.

For calculations, we chose the following values as surface albedos: open water = 0.05 [7], green (trees, grass) = 0.12 (see e.g. different grass biomass values in [20]), urban (asphalt, concrete, colored walls) = 0.35 (calculated as an average over different urban materials, see, e.g., [12]). Unlike Bará and Escofet [4] we use spectrally averaged albedo values that are sufficient to validate the hypothesis mentioned above. As it is possible to simulate skyglow for different observing sites, we decided to use five matching the locations of the real SQM stations existing. For Model D, the values mentioned were averaged with respect to the sizes of different city parts as seen in Fig. 3 (Model A). This results in a value for the average = 0.208. The aim of using four different models was to analyze if varying surface albedo values do have a measurable impact on the zenithal night sky brightness and if so how its strength could influence simulations. Other limitations for real life situations, e.g., vegetation, meteorological conditions, etc., were not assumed in the models.

The lumen output is expressed as lumens per capita. Therefore, calculations also include varying numbers of population for different city parts, approximated by the official numbers of inhabitants per statistical districts in 2015 [22]. Consequently, there are, e.g.,

4

S. Wallner and M. Kocijaj / Journal of Quantitative Spectroscopy & Radiative Transfer 239 (2019) 106648

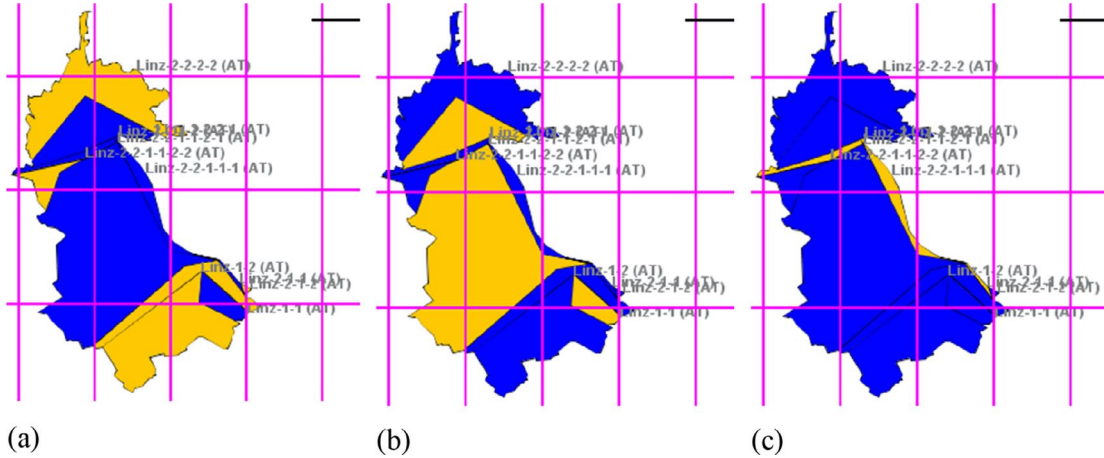


Fig. 3. (a) to (c) show the partitioning of Linz in SkyGlow simulator. The bright yellow-fill parts are to better identify city parts with: (a) high content of green areas, albedo = 0.12; (b) highly urbanized areas, albedo = 0.35; (c) rivers/water surfaces, albedo = 0.05.

Table 2

Results for zenith brightness as calculated by the SkyGlow simulator with an uplight fraction of 0.1. Clear sky ZB is computed for narrow spectral band ranging from 500 to 520 nm. The factors are normalized to the brightest value of model A: $LGO_{modelA} = 7.07 \times 10^{-8} \text{ W/m}^2/\text{sr}$.

Observing site	Zenith brightness (fractions of the LGO in model A)			
	Model A	Model B	Model C	Model D
LSM	0.769	0.832	0.484	0.645
LSW	0.562	0.772	0.431	0.540
LGO	1.000	1.003	0.569	0.741
STW	0.191	0.192	0.149	0.164
PAS	0.034	0.034	0.031	0.032

many more inhabitants, i.e., higher lumen output, for urban areas than for green areas. Water parts were defined with zero inhabitants, hence no emitting light besides reflected light only. Nevertheless, the information on the total lumen output is not necessary for our modeling, because we analyze the relative impacts of ground-albedo on zenith brightness variations. Due to linearity of the radiative transfer model, the value of total lumen output cancels out when zenith brightness at a specific station is evaluated relative to that at another station (see e.g. Table 2 or Figs. 4–6).

2.1.2. Results

The results of simulated ZBs at chosen observing sites are displayed in Table 2. It becomes apparent that there are unneglectable differences in computed values for positions inside the city (LGO, LSW and LSM) depending not only on location but especially on used albedo value(s). The zenith brightness determined for the urban-type surfaces (Model B) differs almost by a factor of 2 from that for green-type surfaces (Model C). As we implied no other light emitting source than Linz it is no surprise that values for localities outside of the city, STW and PAS, are very low and consistent for all models. Since there is certainly other lighting in reality, those results can be considered as a theoretical lower limit.

On closer examination of Models A and D and their results, it shows that the calculated zenithal brightness differ strongly. In fact, only at two locations (LSW, PAS) the results are approaching each other. In other words, letting albedo values vary over a certain range or averaging them over the city results in sometimes large deviations in computed ZB. This effect simply cannot be neglected

when modeling skyglow inside of a dominating light emitting city but could vanish with increasing distance to it.

2.2. Investigation of SQM data

2.2.1. Method

The existing light pollution monitoring network provides an excellent opportunity of analyzing real conditions. SQM data can be obtained online on the website of the government of Upper Austria [1]. Measurements are taken once a minute, the instruments start and end their observations when solar elevation corresponds to -15° . For future analysis, we focus on data obtained for the years 2016–2018.

Since we want to concentrate on clear sky conditions with no snow coverage on the ground, we applied as first step of reducing data to eliminate those received in cloudy nights. Hence, it was necessary to analyze meteorological data as well. Those were made available by the Zentralanstalt für Meteorologie und Geodynamik (ZAMG). In detail data of the semiautomatic weather station located in Linz and visually observed were examined. The latter provided information about the cloud coverage observed three times a day at 7 a.m., 2 p.m. and 7 p.m. The unit to characterize the coverage on the sky is the dimensionless ‘Octa’ with ‘0’ describing no cloud coverage up to ‘8’ fully covered or even ‘9’ if the sky is not visible. To perform the reduction to clear sky data, even with having three measurements a day only, we merely analyzed nights with Octa ≤ 1 at 7 p.m. and at 7 a.m. the next day. If, e.g., only one of these two measurements did not fulfill this requirement, the night was not chosen for further analysis.

A further reduction step was the elimination of data obtained in nights interfered by lunar illuminance. Nights with moon visible for most of the time were also excluded from analysis. In some others, the lunar visibility was only partly given. In these cases, data before moon rose or after it set at the horizon were used. Subsequently, the number of nights available was very restricted with having 48 nights in total, 18 of them from 2016, 9 from 2017 to 21 from 2018.

It should be accepted that the measurements are scarcely free of errors. For instance, magnitude values could sometimes exceed 22 in a clear night, some data can be taken during early twilight with a too strong influence by sunlight, or magnitude values can

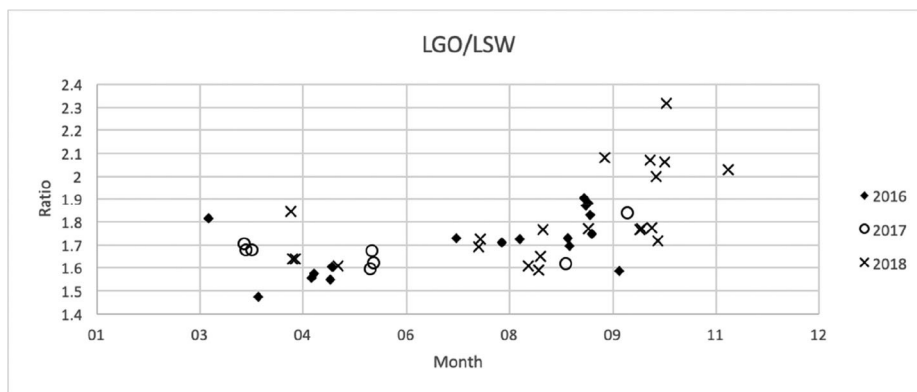


Fig. 4. The plot shows the ratios of SQM values (night averages) collected for the stations LGO and LSW. The experiment has been conducted from 2016 to 2018 with the method described in Section 2.2.1.

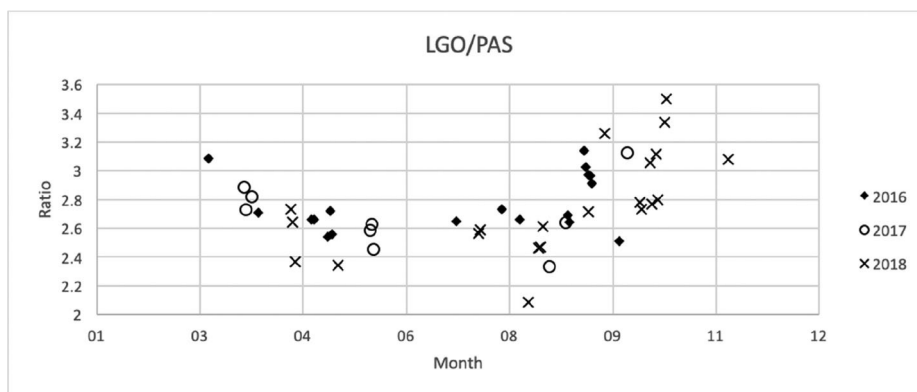


Fig. 5. The same as in Fig. 4, but for the stations LGO and PAS.

appear smaller than 18.0. These values are interpreted as lower and upper thresholds, so all other out of the range specified are eliminated. We chose these values as minimum/maximum since other studies show that the night time averaged SQM values of these stations lie within this range during their maxima in comparable conditions [16,17]. For being able to compare all stations with each other, logged values of all five SQMs at one time had to be available. If one instrument was out of service for a whole night, only this one was excluded, e.g., LSM in summer 2017.

In conclusion, with the reduction steps executed, the amount of data nights during a night is variable, even in two consecutive following nights. A summary of all nights used for analysis and the amount of data points for each of them is shown in Appendix A. The table clearly shows how the nights are distributed over the years, especially in which months. Unsurprisingly, as meteorological conditions are not as needed, there is almost no useable data in winter months. After this workflow, the SQM values left for each night were averaged.

2.2.2. Results

The best way to demonstrate the effect of different surface albedos on skyglow is to interpret the relative change of the zenith brightness (ZB) over the whole city. Therefore, we calculated ZB ratios for any combination of two stations as many advantages go

along with this. With this method, we avoid effects such as, e.g., temperature responses of SQMs. Even if inter-calibration of the measuring devices is missing, the SQMs provide consistent information on the relative change of ZB as our analysis is based on the ratios, more precisely in their change. These ratios remain stable even if determined from improperly calibrated SQMs. Consequently, unknown coefficients of proportionality of different SQMs are eliminated when using ratios as described.

Unsurprisingly, the optical signals measured by the SQMs differ as, e.g., LGO is located in the city center and thus always brighter than stations located in green areas. The values between LGO and LSW, see Fig. 4, differ up to the factor of 2.4, between LGO and PAS, see Fig. 5, up to 3.6. However, it is quite surprising that there is a factor of up to 1.7 between the ratios for LGO and LSM, shown in Fig. 6, which are two stations very near to each other, but with last one located near the river bank.

The behavioral trend caused by vegetation over the year is clearly visible. Later in a year, around autumn, ratios between bright to darker observing sites increase until winter, and decrease when reaching months around summer after spring. This effect can be explained by changes of the surface albedo in green areas as trees are losing their leafs and less reflectivity of the ground takes over. Just as well apparent is this impact inside of the city of Linz. LSW, located in a green area (park) follows this trend if comparing

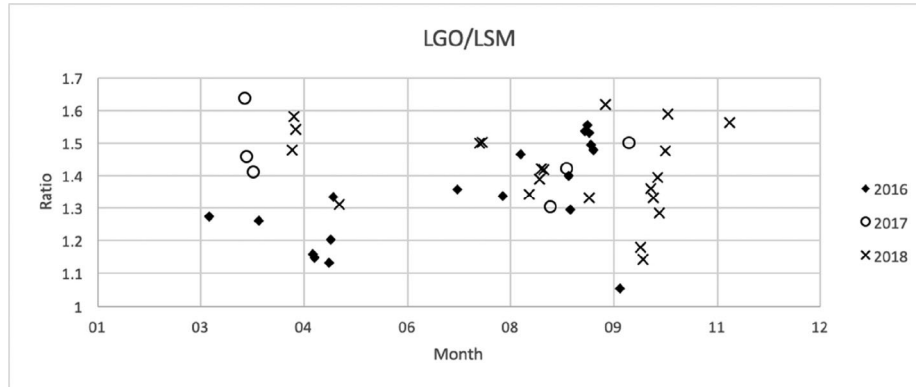


Fig. 6. The same as in Fig. 4, but for the stations LGO and LSM.

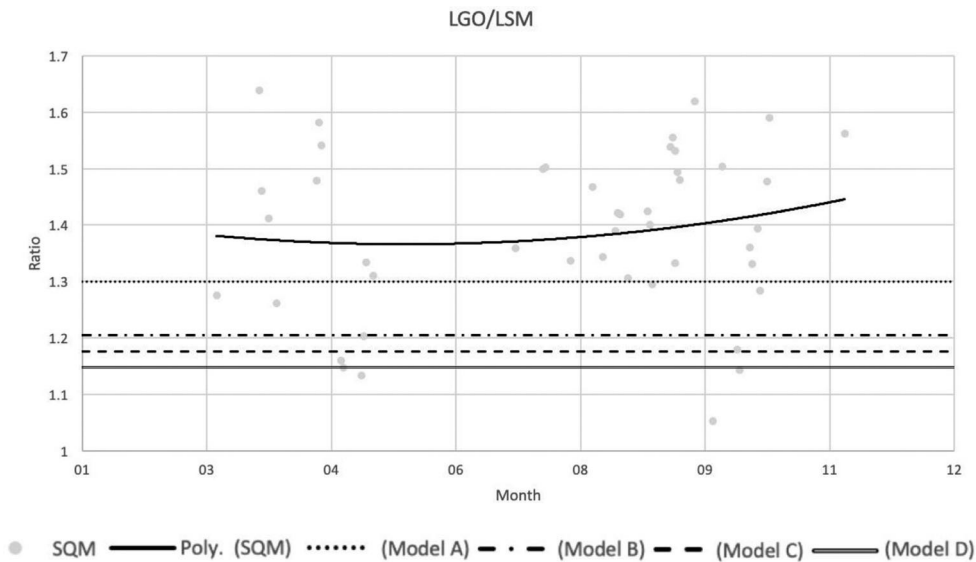


Fig. 7. Comparison between ratios of LGO and LSM as calculated by SkyGlow tool to real SQM values (gray dots). The strength of the polygonal fit of SQM values (solid line) is $R^2 = 0.01798$.

against LGO or LSM. The difference in surface albedo between LGO and LSM is marginal only, therefore their ratios remain nearly constant over the year. Other resulting plots then described ones are illustrated in Appendix B. Most of our resulting plots show a relationship of ratios which follow a 2nd polynomial order. Like discussed before this is a result of vegetation, especially when comparing green to urban areas. Figs. 7–9 also give statistical values to see the strength of such polygonal fits. As there is more scattering in SQM data when comparing the two stations inside the city, the fit is stronger applicable when comparing the urban SQM (LGO) to the one in green area (LSW), although still inside of the city borders.

3. Comparison between modelled and real data

Figs. 7–9 illustrate comparisons between ratios of zenith brightness, modelled (chapter 2.1) and observed (chapter 2.2.). The two

stations located outside of the city, STW and PAS, cannot be included in this comparison as other light emitting sources than Linz were not included. The main purpose of this work was to see theoretical impacts of seasonal changes of ground albedo on ZB inside the city only.

When comparing the conducted data sets, it raises the question, which of our assumed models describes the real observed values the best. However, it must be clear that simulations are time independent while changes in surface albedos change ratios of SQM data. In any case, the aim is to roughly see the impact of either having various albedo values over the city as approximated from satellite images, like illustrated from Google Earth in Fig. 2, or having only one averaged value.

Results show that model A with different surface albedos chosen is the best one describing the SQM values obtained over the three years for all three stations. This gets underlined when looking at the polygonal fit of the data set. In most cases, model D

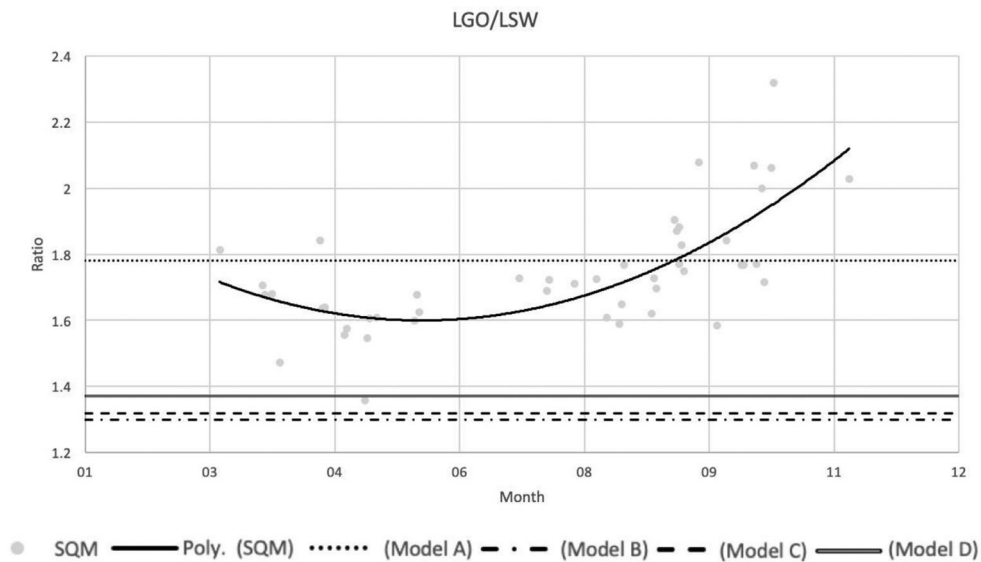


Fig. 8. Comparison between ratios of LGO and LSW as calculated by SkyGlow tool to real SQM values (gray dots). The strength of the polygonal fit of SQM values (solid line) is $R^2 = 0.50958$.

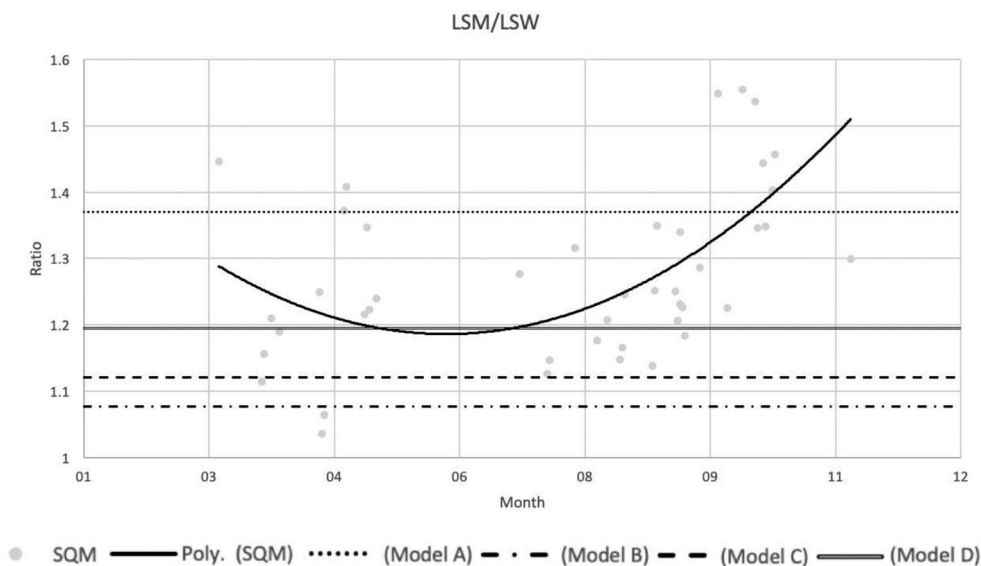


Fig. 9. Comparison between ratios of LSM and LSW as calculated by SkyGlow tool to real SQM values (gray dots). The strength of the polygonal fit of SQM values (solid line) is $R^2 = 0.29282$.

for uniformly reflecting city highly differs from observed values. Also, a strong difference to model A has been found. This result shows that there is a high impact if using surface albedos either distributed or averaged.

As model D is not fitting SQM data well, there is a strong indication for future skyglow simulations of not using an averaged surface albedo but to part the analyzed city into different areas with

respect to their ground types. Of course, it is not surprising that latter method is more accurate, but the strength astonishes. We expect that with increasing distance to a dominating light source this effect becomes negligible, as, e.g., PAS underlines this when comparing the two models.

The results of our comparison clearly illustrate that if simulating light pollution effects of a city to the ZB on long terms, chang-

ing surface albedos over a year must be included as only one static model is not sufficient. The albedo segmentation becomes more significant with higher fractions of non-urban city parts, i.e., especially green ones. The higher the percentage of green parts the more impacts can be expected when simulating ZB inside and outside a city or town.

4. Conclusions

Currently direct emissions upwards are intentionally reduced through modernization of street lighting, e.g., by conversion from traditional cobra-head products to well shielded lamps. As a consequence, importance of ground albedo effects in skyglow modeling constantly increases and questions arose on what granularity of ground-albedo data is necessary to make numerical modeling accurate within a specified error tolerance. For instance, a too dense data grid may appear useless if the accuracy of night sky brightness computations improves only marginally and the relative change of ZB will remain below detection limit. On the other hand, replacing the whole-city surfaces by a uniformly reflecting area can be very rough approximation when modeling skyglow inside the city or at its edges. To verify albedo impacts on skyglow, we have analyzed SQM data recorded systematically in the city of Linz, Austria, which has surfaces of different types such as areas densely covered by houses and other buildings or green areas (e.g. city parks). The different-typed areas clumped together represent an ideal scenario for identifying the night sky brightness changes when transitioning from a green area to other (non-green) area. In addition, we can also expect that reflectance of a green part will change over a year because leafs of deciduous trees change colors in autumn and grass and trees are developing in spring, thus implying seasonal variation of ground albedo.

The ground albedo impacts on zenith brightness have been analyzed numerically and then experimentally for the light monitoring network in the city of Linz. The numerical modeling was motivated by a need for better understanding of NSB changes due to simulated albedo distributions which then helped in making decisions for further experimental work. To associate the NSB changes more strongly to ground albedo variation, we evaluated the ratios of SQM values and their change over time in different city areas (while avoiding winter season due to potential snow cover).

We have shown that surface albedo changes during a year, especially in green parts. In autumn the leaf fall makes green city parts darker. Ratios of urban to green located SQMs confirm this trend.

The major differences in computed results have been found when using either various albedo values for parts of a city or using only one averaged albedo value over the whole city. A use of average albedo for the city of Linz does not provide accurate predictions of ZB inside urban area, while simulations are way closer to the experimental SQM data if different surface albedos are considered.

The changes of night sky brightness due to ground albedo heterogeneity we have explored can theoretically have several consequences to skyglow research. For instance, it could be expected that albedo of green parks show a seasonal behavior and this effect can be used to verify the theories and hypotheses we postulated before. The results obtained legitimize a further research on different configurations of light-reflecting surfaces and different city models. We especially need to address the questions on: (a) what is the minimum size of a compact area to make NSB changes detectable at short, intermediate or even larger distances, (b) what are typical NSB errors due to surface albedo obtained as a weighted average over city areas, and (c) what is the amplitude of these effects for different direct upright scenarios. The results

of this paper shall be motivation for further studies, especially to compare data from other cities with different observing conditions.

Acknowledgements

The authors want to dedicate this work to our beloved colleague Thomas Posch, who had been a connector between our institutions for many years.

This work was supported by the University of Vienna and the Slovak Research and Development Agency under the contract No. APVV-18-0014. The authors want to thank the provincial government of Upper Austria for their cooperation and efforts relating to the light monitoring network and public release of data. We especially want to thank Heribert Kaineder and Martin Waslmeier.

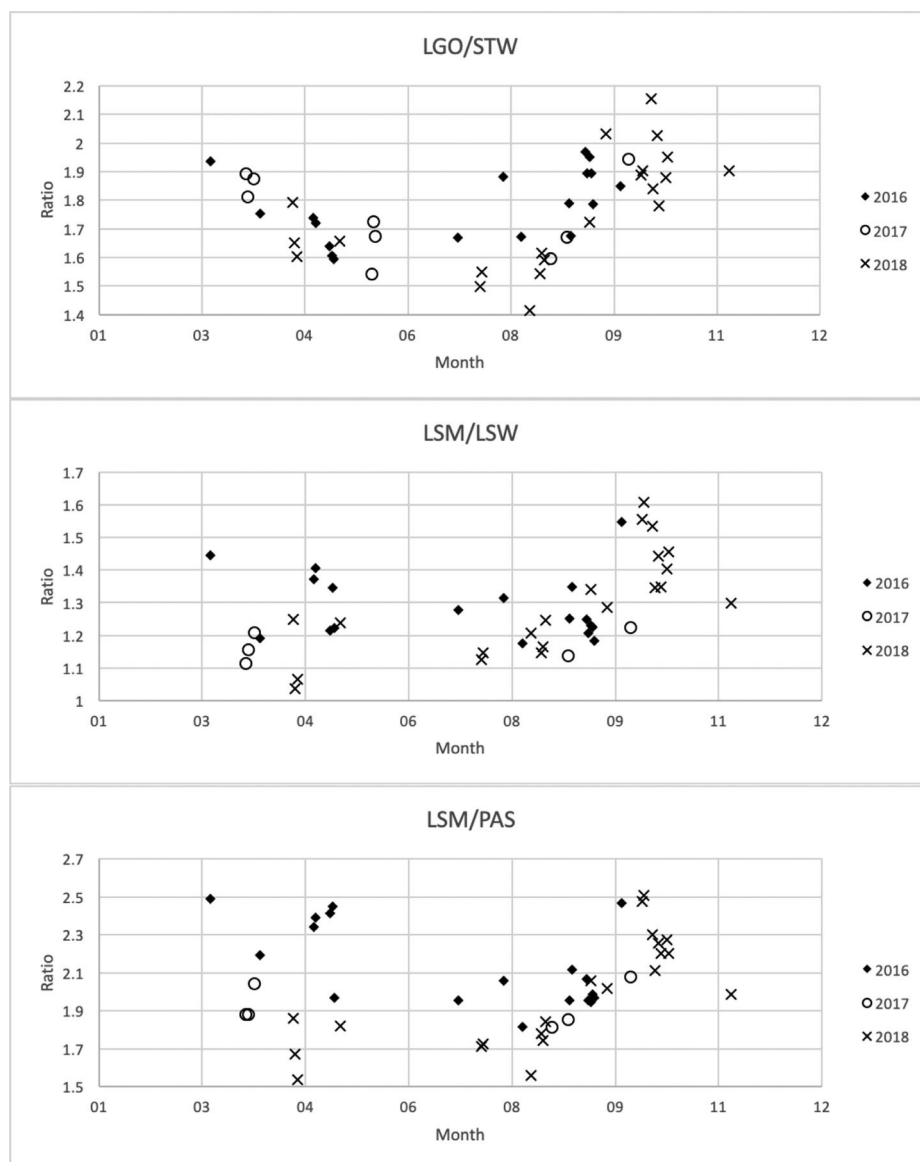
Appendix A

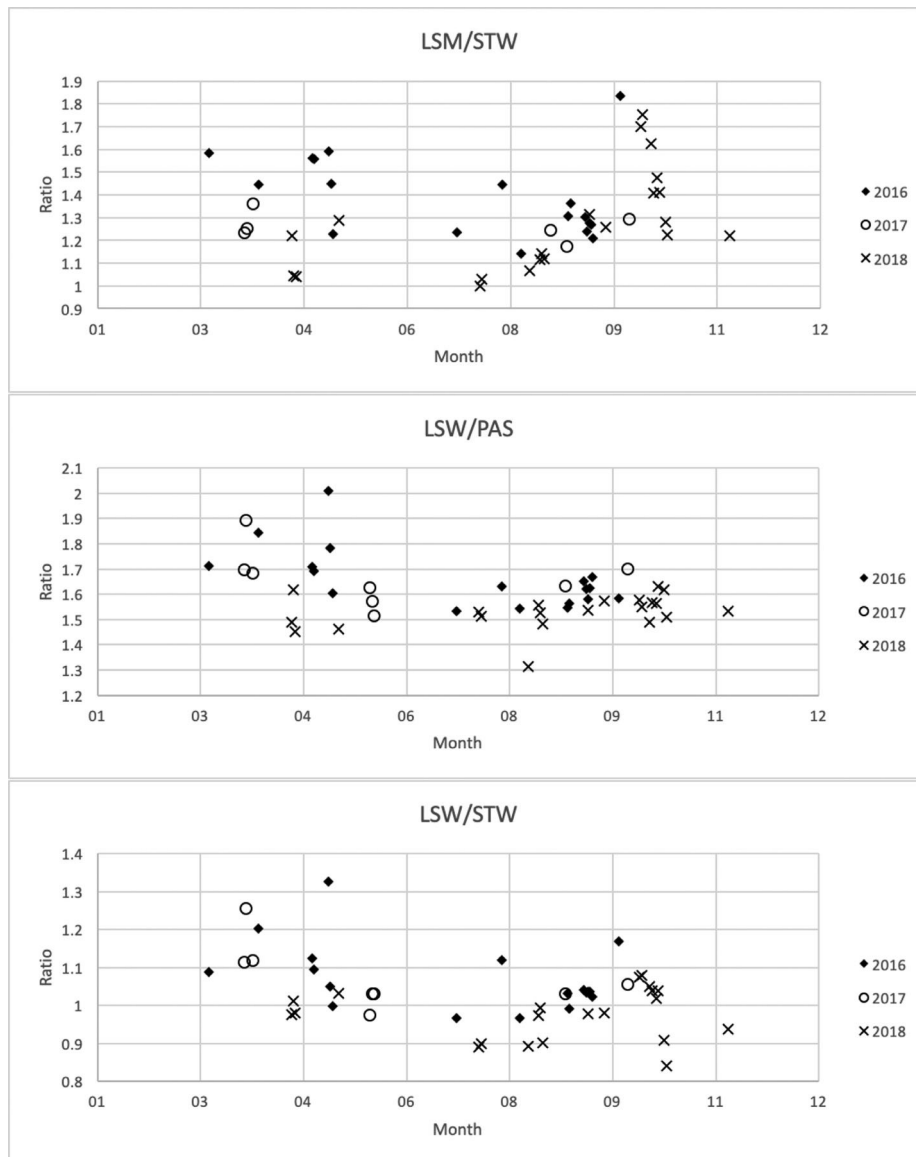
Summary of all nights used for analysis and amount of data points

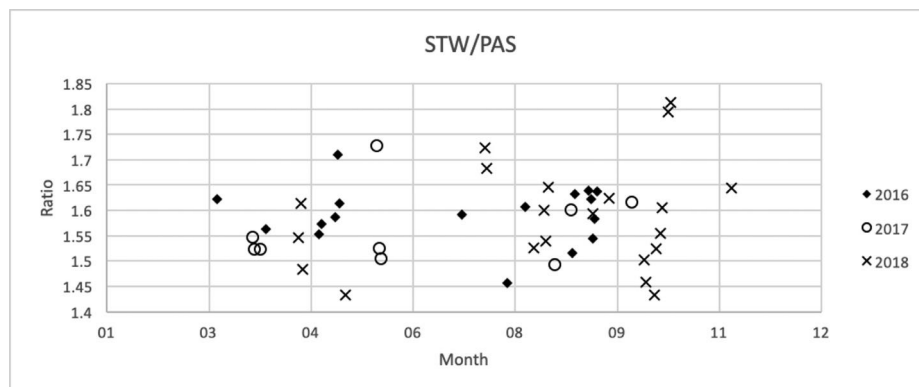
Night (dd.mm.yy)	Amount of data points	Comments
09.03.16	10.03.16	436
02.04.16	03.04.16	505
28.04.16	29.04.16	286
29.04.16	30.04.16	347
06.05.16	07.05.16	399
07.05.16	08.05.16	324
08.05.16	09.05.16	287
07.07.16	08.07.16	218
29.07.16	30.07.16	200
07.08.16	08.08.16	244
30.08.16	31.08.16	323
31.08.16	01.09.16	478
07.09.16	08.09.16	329
08.09.16	09.09.16	278
09.09.16	10.09.16	231
10.09.16	11.09.16	197
11.09.16	12.09.16	159
24.09.16	25.09.16	314
26.03.17	27.03.17	175
27.03.17	28.03.17	355
30.03.17	31.03.17	331
26.05.17	27.05.17	207
27.05.17	28.05.17	243
28.05.17	29.05.17	158
21.08.17	22.08.17	416
29.08.17	30.08.17	247
28.09.17	29.09.17	249
18.04.18	19.04.18	301
19.04.18	20.04.18	237
20.04.18	21.04.18	163
11.05.18	12.05.18	373
18.07.18	19.07.18	137
19.07.18	20.07.18	120
11.08.18	12.08.18	357
16.08.18	17.08.18	230
17.08.18	18.08.18	231
18.08.18	19.08.18	133
09.09.18	10.09.18	486
17.09.18	18.09.18	245
04.10.18	05.10.18	396
05.10.18	06.10.18	438
09.10.18	10.10.18	481
10.10.18	11.10.18	584
12.10.18	13.10.18	565
13.10.18	14.10.18	506
16.10.18	17.10.18	287
17.10.18	18.10.18	186
16.11.18	17.11.18	333

Appendix B

Resulting plots from the SQM analysis as described in chapter 2.2.1







References

- [1] Amt der oberösterreichischen Landesregierung, Abteilung Umweltschutz, <https://www.land-oberoesterreich.gv.at/159659.htm> (Accessed 20 May 2019).
- [2] Amt der oberösterreichischen Landesregierung, Abteilung Umweltschutz, Lichtmesskampagne Zentralraum Oberösterreich - Erfassung des abgestrahlten Lichts mit einem nächtlichen Überflug - Aircraft data acquisition report FUB Cessna 207T, 2015, Technical report, https://www.land-oberoesterreich.gv.at/Mediendateien/Formulare/Dokumente%20UWD%20Abt_US/us_strahlen_Endbericht_Lichtkataster_20151126_Linz_Final.pdf (Accessed 27 August 2019).
- [3] Aubé M, Kociřaj M. Using two light-pollution models to investigate artificial sky radiances at Canary Islands observatories. *Mon. Not. R. Astron. Soc.* 2012;422:819–30.
- [4] Bará S, Escofet J. On lamps, walls, and eyes: the spectral radiance field and the evaluation of light pollution indoors. *J. Quant. Spectrosc. Radiat. Transf.* 2018;205:267–77.
- [5] Bonan GB. Effects of land use on the climate of the United States. *Clim. Change* 1997;37:449–86.
- [6] Garstang RH. Model for artificial night-sky illumination. *Publ. Astron. Soc. Pac.* 1986;98:364–75.
- [7] Herman BM, Browning R, Rabinoff R. The change in Earth-atmosphere albedo and radiational equilibrium temperatures due to stratospheric pollution. *J. Appl. Meteorol.* 1976;15:1057–67.
- [8] Jechow A, Kyba CCM, Höcker F. Beyond All-Sky: assessing ecological light pollution using multi-spectral full-sphere fisheye lens imaging. *J. Imaging* 2019;5(4):46.
- [9] Kociřaj M. 2017, SkyGlow Simulator, <http://skyglow.sav.sk/#simulator> (Accessed 15 March 2019).
- [10] Kociřaj M, Solano-Lamphar HA. Angular emission function of a city and sky-glow modeling: a critical perspective. *Astronom. Soc. Pac.* 2016;128:124001.
- [11] Kociřaj M, Wallner S, Solano-Lamphar HA. An asymptotic formula for skyglow modeling over a large territory. *Mon. Not. R. Astron. Soc.* 2019;485(2):2214–24.
- [12] Kotthaus S, Smith TEL, Wooster MJ, Grimmond CSB. Derivation of an urban materials spectral library through emittance and reflectance spectroscopy. *ISPRS J. Photogr. Remote Sensing* 2014;94:194–212.
- [13] Levin N. The impact of seasonal changes on observed nighttime brightness from 2014 to 2015 monthly VIIRS DNB composites. *Remote Sens. Environ.* 2017;193:150–64.
- [14] Levin N, Zhang Q. A global analysis of factors controlling VIIRS nighttime light levels from densely populated areas. *Remote Sens. Environ.* 2017;190:366–82.
- [15] Liu Y, et al. Evaluation of the VIIRS BRDF, Albedo and NBAR products suite and an assessment of continuity with the long term MODIS record. *Remote Sens. Environ.* 2017;201:256–74.
- [16] Posch T, Binder F, Puschnig J. Systematic measurements of the night sky brightness at 26 locations in Eastern Austria. *JQSRT* 2018;211:144–65.
- [17] Puschnig J, Wallner S, & Posch T. Unpublished results, Circalunar variations of the night sky brightness - An FFT perspective on the impact of light pollution.
- [18] Román MO, et al. NASA's Black Marble nighttime lights product suite. *Remote Sens. Environ.* 2018;210:113–43.
- [19] Sagan C, Toon OB, Pollack JB. Anthropogenic albedo changes and the Earth's climate. *Science* 1979;206:1363–8.
- [20] Samimi C, Kraus T. Biomass estimation using Landsat-TM and -ETM+, towards a regional model for Southern Africa? *Geol.* 2004;59:177–87.
- [21] Shirkey RC. 2008, An Army Illumination Model (AAIM), Army Research Laboratory, ARL-TR-4645, 15, <https://apps.dtic.mil/dtic/tr/fulltext/u2/a493692.pdf>.
- [22] Stadtregierung Linz, Linz in Zahlen, https://www.linz.at/zahlen/010_Stadtgebiet/ (Accessed 7 June 2019).
- [23] Xie Y, Weng Q, Fu P. Temporal variations of artificial nighttime lights and their implications for urbanization in the conterminous United States, 2013–2017. *Remote Sens. Environ.* 2019;225:160–74.
- [24] Zhuosen W, et al. Monitoring land surface albedo and vegetation dynamics using high spatial and temporal resolution synthetic time series from Landsat and the MODIS BRDF/NBAR/albedo product. *Int. J. Appl. Earth Obs. Geoinf.* 2017;59:104–17.
- [25] Zhang G, et al. Time Series High-Resolution Land Surface Albedo Estimation Based on the Ensemble Kalman Filter Algorithm. *Remote Sens.* 2019;11:753.
- [26] Falchi F, et al. The new world atlas of artificial night sky brightness. *Sci. Adv.* 2016;2(6):e1600377.

4.3 'Usage of Vertical Fisheye-Images to Quantify Urban Light Pollution on Small Scales and the Impact of LED Conversion'

Title: *Usage of Vertical Fisheye-Images to Quantify Urban Light Pollution on Small Scales and the Impact of LED Conversion*

Author: S. Wallner

Journal: Journal of Imaging

Status: Published in **J IMAGING 5(11), 86 (2019)**

DOI: <https://doi.org/10.3390/jimaging5110086>

Personal contribution: As single author of this paper, I developed the idea of using the measurement instruments commonly used of all-sky imagery in a different way, by tilting the fisheye camera to a 'vertical' plane and capture single light sources. Consequently, I executed the observational work, analysis. Furthermore, I was solely responsible for the content of the paper, and the submission and revision process.

Article

Usage of Vertical Fisheye-Images to Quantify Urban Light Pollution on Small Scales and the Impact of LED Conversion

Stefan Wallner ^{1,2}

¹ Department of Astrophysics, University of Vienna, Türkenschanzstrasse 17, 1180 Vienna, Austria; stefan.wallner@univie.ac.at

² ICA, Slovak Academy of Sciences, Dúbravská cesta 9, 84503 Bratislava, Slovak Republic

Received: 28 October 2019; Accepted: 14 November 2019; Published: 18 November 2019



Abstract: The aim of this work was to develop an easy and quick technique for characterizing various lighting situations, that is, single lamps or illuminated signs and to quantify impacts on small scales like streets, buildings and near areas. The method uses a DSLR-camera equipped with fisheye-lens and the software Sky Quality Camera, both commonly used as part of night sky imagery in the light pollution community, to obtain information about luminance and correlated colour temperature. As a difference to its usual build-up, observed light emitting sources were captured by pointing the camera towards analysed objects, that is, images were taken via vertical plane imaging with very short exposure times under one second. Results have proven that this technique provides a practical way to quantify the lighting efficacy in a certain place or area, as a quantitative analysis of the direct emission towards the observer and the illumination on surroundings, that is, street surfaces, sidewalks and buildings, was performed. When conducting lamp conversions, the method can be used to characterize the gradient of change and could be a useful tool for municipalities to find the optimal lighting solution. The paper shows examples of different lighting situations like single lamps of different types, also containing various luminaires, illuminated billboards or buildings and impacts of the lighting transition to LEDs in the city of Eisenstadt, Austria. The horizontal fisheye method is interdisciplinary applicable, for example, being suitable for lighting management, to sustainability and energy saving purposes.

Keywords: light pollution; digital imaging; lighting quality; LED; colour temperature; all-sky; CCT; fisheye

1. Introduction

For many years, the amount of artificial light at night has increased worldwide and so has light pollution. Observations show that 83% of the world's population live under a light-polluted sky [1] and that there still is a growth of artificially lit areas on Earth by 2.2% per year [2]. This results in an impact noticeable not only for astronomers by losing visibility with increasing night sky brightness [3,4], but furthermore, artificial light interferes with ecosystems on our planet. Nature and environment are affected negatively as they suffer from skyglow over cities [5–8]. Even aquatic ecosystems suffer from light pollution as observed [9,10]. However, also impacts on human health cannot be neglected, as sleep deprivation is only one among many issues found [11–13]. In past scientific works, one can find suggestions on an environmentally friendly usage of artificial light, while still providing possibilities of energy savings. Consequently, there shall be a focus for global change in the 21st century [14–16]. One chance is by changing current existing and mostly outdated lighting situation systems in cities from inefficient lamps of past generations (High pressure sodium, Low pressure sodium, etc.) to Light Emitting Diodes (LEDs). With a higher efficiency, they provide the possibilities of controlling colour

temperatures or being able to dim during night-time, to only name a few. However, their use—not only in public but also indoor light and luminous screens of TVs, laptops and smartphones—can become dangerous if using a great deal of light in short wavelengths (blue) which has even more negative effects on human health or the environment [9,13,17]. A lot of cities worldwide changed their street lighting to LEDs already and the impacts of those changes were observed [18,19] or modelled [20].

The most commonly used measurement technique for quantifying light pollution are ‘Sky Quality Meters’ (SQMs) [21,22], giving the opportunity of one-dimensional photometric measurements by detecting the brightness of the sky’s zenith luminosity. Sometimes, if various devices are available, they are grouped together to form light monitoring networks [23,24]. Other methods involve all-sky images, which provide two-dimensional images of the night sky [25–30], satellite data, especially to quantify the development of light pollution on global scales [1,2,4,31] or theoretical simulations to calculate the behaviour of light in our atmosphere [32–34]. All methods do have pros and cons [35]. In general, impacts of entire cities or districts were analysed to see, for example, a gradient in skyglow.

The aim of this work is to find an easy and quick method by using a currently used technique in light pollution communities, the all-sky method, for quality analysis on small scales. This includes either single lamps of different types or the impact of artificial light on objects as houses, buildings or streets. This should help characterizing lighting situations easily on a low time scale.

2. Materials and Methods

2.1. Location

To observe on the one hand various examples of lighting situations and lamps and on the other hand the impact of a LED conversion, the city of Eisenstadt, Austria (N 47°50′46.93″, E 16°31′40.66″) was chosen. The capital city of the Austrian municipality Burgenland is home to total of 14,000 inhabitants. In 2018, the local government decided to undergo a transition of the existing public street lighting system, from mostly High Pressure Sodium Lamps (HPS) to more modern and energy saving LEDs. The conversion started in mid 2018 and was finished in April 2019. More than 2400 lamps were changed to LEDs, only few HPS lamps were maintained in the inner city for historical reasons. As chosen by the municipal authorities, the colour temperature for all LEDs is 3000 K, being also fully shielded with ULOR = 0 (Uplight Output Ratio), that is, no light emitted to the upper hemisphere.

With having changed most of the public street lighting, there still exists a variety of lamps distributed over the city. Especially when observing areas not controlled by the local authorities, for example, schools or parking spaces, lamp types can differ significantly from those changed. Some of them will be replaced in the future, for some there are no plans of being exchanged so far. The great number of lighting situations, especially light sources not affected by the LED conversion, makes the city of Eisenstadt an optimal example of capturing various points of reference.

2.2. Instruments & Images

Images were taken by a digital single-lens reflex camera (Canon EOS 5D Mark II) with fisheye-lens. This method is more commonly used for obtaining all-sky images of the night sky to analyse its brightness, the impact of cloudy sky conditions or the identification of light domes close to the horizon from light emitting sources [25–30]. Because neither of these are important parameters for the purpose of this work, the camera was not pointed onto the sky but rather in vertical directions. This approach was used before [28], here it is used inside of a city observing not traces on the sky but to quantify impacts of single lamps, illuminances of buildings, advertisements and impacts on streets. Hence, this method is used on a far smaller scale being able to characterize single light pollution sources and impacts on surroundings.

Various types of images were taken: (i) images of six different lamp types, (ii) images of two illuminated buildings, (iii) images of two luminous advertisements, (iv) images of a street before and after the LED conversion. As some of the images were captured before and some after the transition of

public street lighting, they were obtained between July 2018 and October 2019. The image captions each include the exact recording dates. The ISO of 1600 and focal ratio of $f/3.5$ remained constant for all images. However, because of the very bright light emitting sources, exposure times can be kept very short, under one second per image. Therefore, a tripod is not absolutely necessary. All images were taken under clear sky conditions. Lamps and other emitting sources were always centred as best as possible.

Since further analysis steps shall also provide correlated colour temperatures (CCT) of each lighting situation, also spectra of lamps—see Section 3.1—were obtained, creating the possibility of comparing software results to spectra measured. In this regard, the spectrometer Mavospec Base by Gossen (Nuremberg, Germany) was used. However, this instrument is only used to allow a comparison and is in principal not part of the measurement technique described in this work.

2.3. Software & Analysis Method

To analyse all images in detail, there is the need of a software which is able to give luminance and CCT data as output. One which is capable of doing so is “Sky Quality Camera” (SQC) developed by Andrej Mohar from Euromix d.o.o. (Ljubljana, Slovenia). The primary goals of this software are to process all-sky images of the night sky to quantify the impact of artificial light at night and to identify certain light emitting sources close to the horizon. The software is therefore a common tool in light pollution communities and used continuously when analysing all-sky images. Furthermore, like mentioned above, SQC was also used for horizontal fisheye-images before, but as a difference, not in an urban environment or quantitatively [25–30].

Important settings of the software being used for this work are—no subtraction of brightest stars or Milky Way (since no sky is observed), altitude of sky border is 0 degrees (to allow the full field of view being analysed), clear sky (no automatic detection of possible clouds).

At this point must be mentioned that exact data values, like mcd/m^2 for luminance or Kelvin for CCT, can be obtained interactively by the user, meaning that when moving the mouse over the resulting images, values for certain positions, for example, the lamp’s head, are displayed. If no further explanation is included, this is how some values, also possibly beyond the illustrated scales, were read.

The approach of this work, to use luminance and CCT analyses for single light emitting sources shall be a new method to obtain information not only about the sources itself but to compare different systems for a possible conversion, especially LEDs. Analysing the gradient of luminance and CCT temperature will also be observed by subtraction of SQC images [29]. This shows the development of these parameters in an optimal way. The subtraction is a tool provided by the software, images must be aligned to each other before a subtraction is performed. Alignment can be performed in the software via manual rotation in three axes.

As exposure times are very short, signal to noise ratio rapidly decreases for dark areas. This means in effect, that this technique cannot be used to quantify impacts on the night sky. Although, a certain glare caused by the light emitting sources possibly pointing towards the sky can be observed.

The used camera is calibrated to the software.

3. Results of Various Lighting Systems

3.1. Lamps

Hereafter, six examples of different lamp types are displayed and analysed. Every lamp was also photographed during daytime to receive an impression of its shape. Furthermore, the spectrum was collected like described in Section 2.2. The fisheye image which is analysed by SQC software is also shown with the resulting outcomes.

3.1.1. HPS Lamp

The High Pressure Sodium (HPS) lamp, like captured in Figure 1a, was the method of choice for public street lighting for many years. Not only Eisenstadt but for many cities around the globe it used to

be or still is the most ubiquitous type. In the near past, with the development of LEDs, doubts raised on it, especially its low luminous efficacy. The spectrum of the lamp, visible in Figure 1b, shows the typical peak of the sodium D-line at 589 nm, the visible result is a golden-orange light. The colour temperature measured was 2037 K. The lighting situation captured, seen in Figure 2a shows a typical street lighting situation in Eisenstadt before its change. The image was taken midway between two HPS lamps.

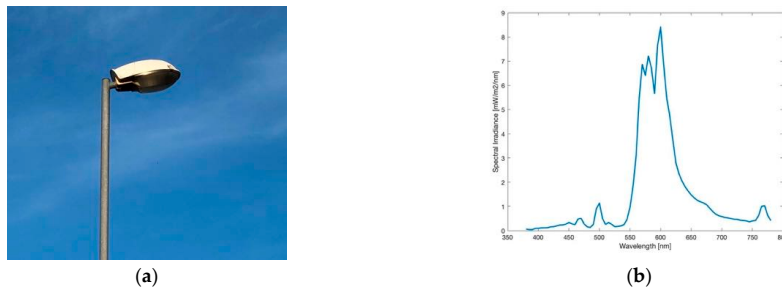


Figure 1. (a) Image of the High Pressure Sodium (HPS) lamp during daytime; (b) Spectrum of lamp observed.

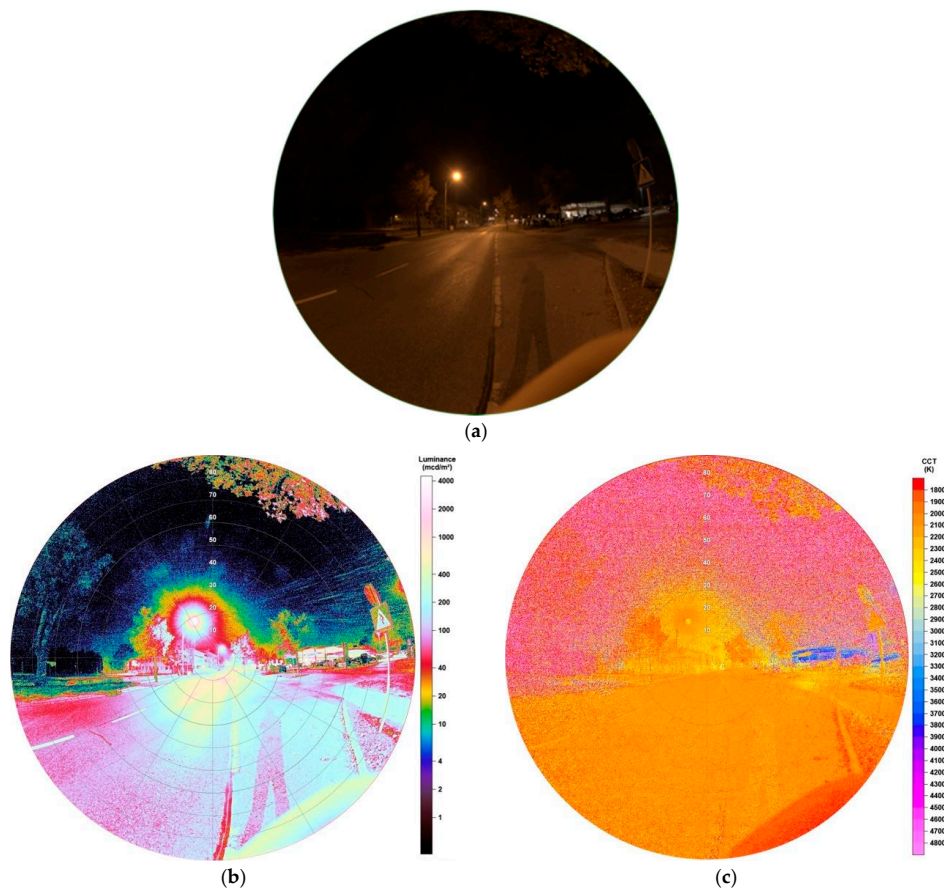


Figure 2. (a) Image of HPS lamp during night-time taken with fisheye lens for detailed analysis (date: 10.10.2018, 23:54 h; exposure time: 0.2 s); (b) Luminance matrix of image (a) as displayed by Sky Quality Camera (SQC); (c) Colour correlated temperature (CCT) matrix of image (a) as displayed by SQC.

Luminance data of the resulting image, provided by the SQC software, are shown in Figure 2b. Values at the HPS lamp's head reach numbers up to 7250 mcd/m^2 , on the street between 100 (at observer) and 2200 mcd/m^2 (under lamp). It occurs, when looking at nearby standing trees, that the lamp, as typical for HPS lamps, does not show full cut-off behaviour by far. There is high amount of emission to the sides, also visible at the building in the background. A comparison to another HPS lights inside different shaped lamps is described later in Sections 3.1.3 and 3.1.5. The resulting image also shows structures on the night sky, looking like ice pillars. As this was definitely not possible as temperatures were way too high, it seems this is an effect of saturation and low signal to noise on the night sky. However, as we do not want to analyse the night sky, this error can be neglected.

Figure 2c shows the correlated colour temperature matrix for the image. On the illuminated street, CCT analysis displays values between 1800–2200 K which matches the measurement of the lamp. For the lamp's light emitting head SQC shows higher values up to 2300 K. This can be explained by a saturation happening by its high luminosity. It can be concluded that the CCT analysis can only be applied to illuminated surfaces and glare around the light, as latter can be seen in the luminance data and still carries information about the colour temperature as seen in the CCT data.

3.1.2. LED Lamp

Since mid 2019, more than 2400 Light-Emitting Diodes replace HPS lamps for the public street lighting in Eisenstadt. LEDs do carry a lot of advantages, being cheaper in the maintenance, having the highest luminous efficacy on the market (up to 350 lm/W as theoretical maximum), for the first time being able to dim single lamps and generate colour temperatures as wished. This in its turn means, that LEDs can also be reason of danger for the environment as, for example, over-illumination is produced more easily. Furthermore, as more light is emitted at lower wavelengths, that is, blue light, has negative effects on animals, nature and humans as discussed above. Figure 3a shows the type of head now distributed over the whole city. The spectrum, shown in Figure 3b, definitely matches LED-like spectra with a colour temperature of 3201 K measured. The image taken for analysis is shown in Figure 4a.

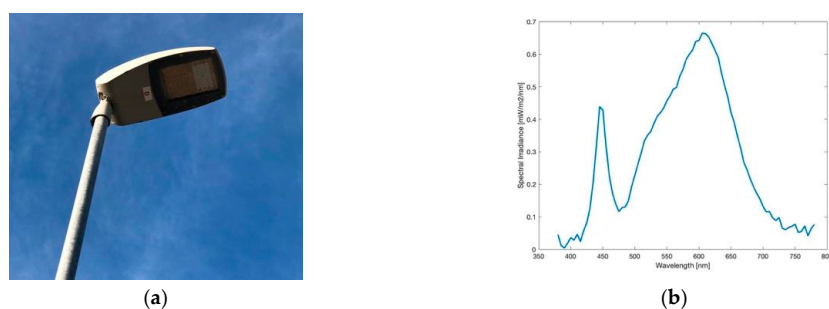


Figure 3. (a) Image of the light emitting diode (LED) lamp during daytime; (b) Spectrum of lamp observed.

All LEDs installed are full cut-off, meaning that there is no emission to the upper hemisphere. This is underlined by the luminance matrix in Figure 4b. Higher luminance values only appear on the street, the sidewalk and a small area surrounding the lamp. The building standing right to the lamp is only illuminated very weakly. In the image taken, Figure 4a, it is only slightly visible. The building displays luminance values up to a maximum of 70 mcd/m^2 , the sidewalk between $90\text{--}600 \text{ mcd/m}^2$ (observer to below lamp) and the lamp's head up to 2256 mcd/m^2 . Furthermore, a tree, which can be seen at the upper right edge of the image, appears only to be slightly illuminated as an impact of reflection on the street. The ratio of illuminance of the street between lamp and observer seems to be more uniform compared to the HPS lamp.

The CCT data, illustrated in Figure 4c, show great distribution. The street and sidewalk show values between 2600–3000 K, the green area (grass) on the right to the lamp between 2700–3200 K, the building between 2800–3300 K. The red stroke in the centre of the image shows a person wearing a

red uniform. It seems that for the LED lamp, due to its lower luminance values, a mixing in colour temperatures is happening between the light and illuminated surfaces, that is, that effects caused by the wavelength-dependent surface albedo cause the colour temperature of the illuminated ground to be lower than the lamp's light itself. Subsequently, the CCT analysis is able to display, how strongly this mixing is happening depending on the strength of illuminance. With increasing luminance of lamps, see, for example, the HPS-lamp in Figure 2c, also the mixing effects decreases as surface albedo effects play less role. When comparing a LED with higher luminance (see later in Section 3.1.4) the colour of the lamp is dominating also on the ground.

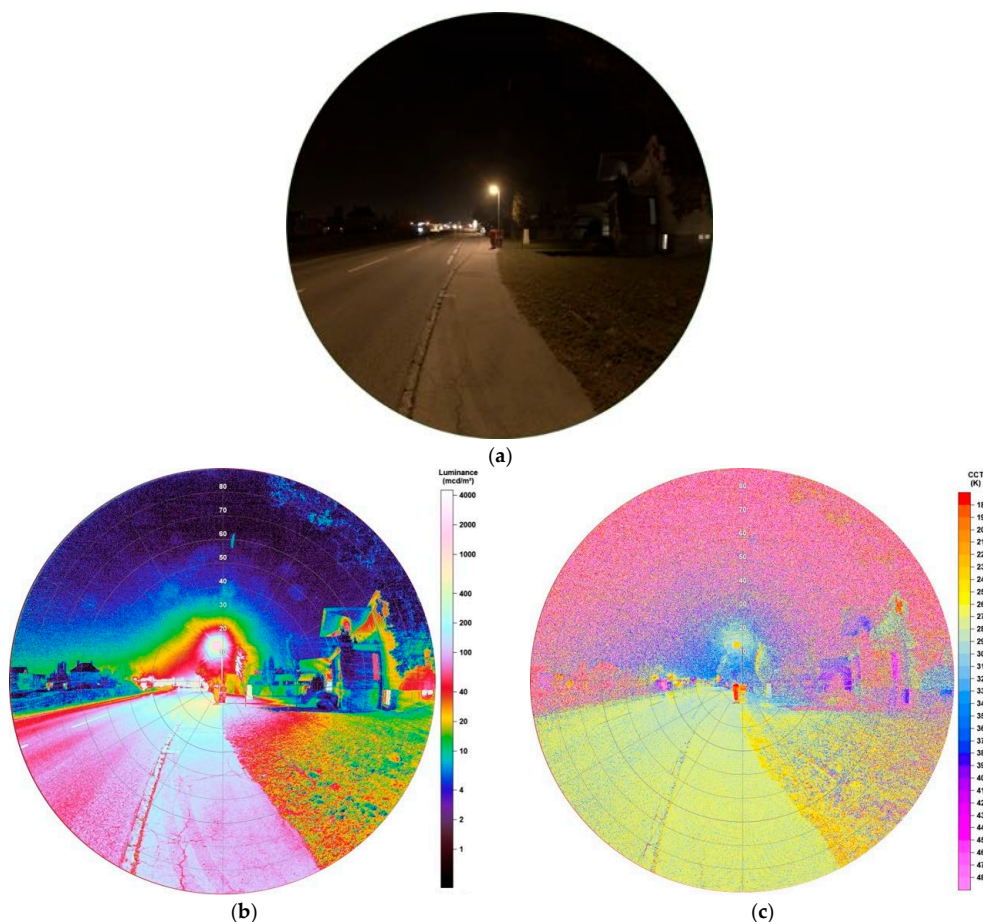


Figure 4. (a) Image of LED lamp during night-time taken with fisheye lens for detailed analysis (date: 10.10.2018, 22:57 h; exposure time: 0.6 s); (b) Luminance matrix of image (a) as displayed by SQC; (c) CCT matrix of image (a) as displayed by SQC.

3.1.3. Ball Light

In the city, this type of lamp, as pictured in Figure 5a, was frequently used for illumination around buildings, parking areas and pedestrian zones. Today only a few of them are left. With a colour temperature of 1856 K, as measured by the spectrometer, its spectrum, illustrated in Figure 5b, shows a dominant peak in the orange wavelengths and can be described as HPS-like, comparing to Figure 1b. The slight difference to the HPS spectrum seen before, can be explained by a frosted glass film around the ball light. The biggest disadvantage of a ball light is the emission of light to all angles and therefore wasting energy especially by emitting to the upper hemisphere as can be seen in Figure 6a. As the

mounting is affixed at the bottom it can be assumed that there is even more light emitted upwards than downwards. An advantage of this lamp is the colour temperature, which only includes a neglectable peak at lower wavelengths at 500 nm.

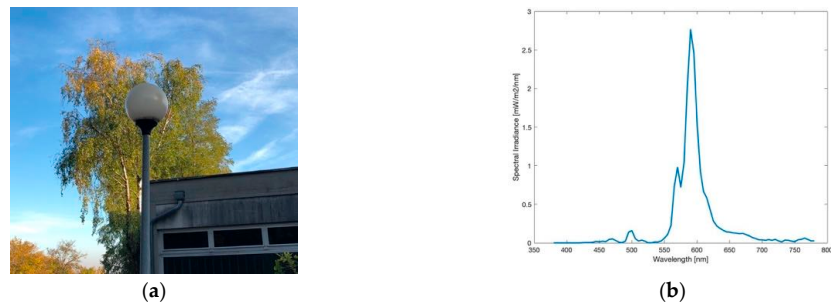


Figure 5. (a) Image of the ball light during daytime; (b) Spectrum of lamp observed.

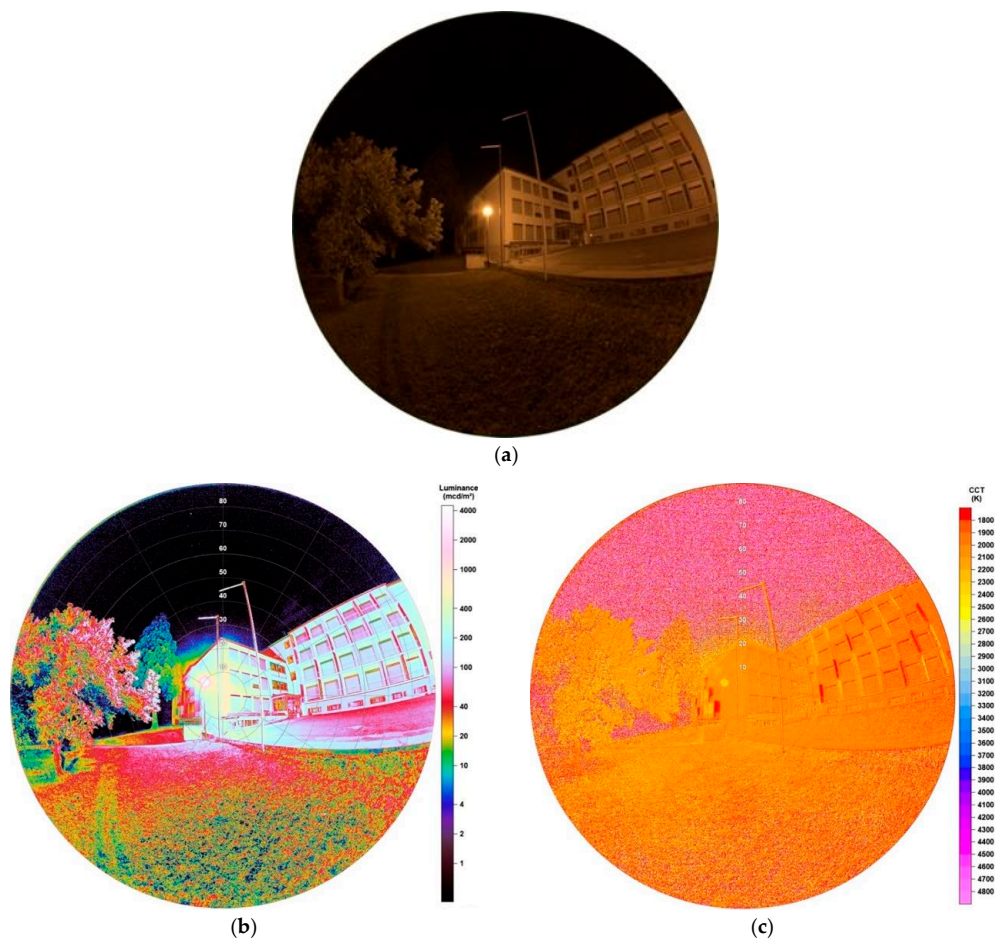


Figure 6. (a) Image of ball light during night-time taken with fisheye lens for detailed analysis (date: 29.07.2019, 23:15 h; exposure time: 0.4 s); (b) Luminance matrix of image (a) as displayed by SQC; (c) CCT matrix of image (a) as displayed by SQC.

Results of performed analysis, be it the luminance or the CCT data, underline the features of the ball light discussed before. Figure 6b shows that high luminance values are not only found on the footpath or parking area but also up to the building's top. This confirms the fact of light emission to all angles. Values at the lamp's head rise to around 3500 mcd/m^2 , whereas the footpath under the lamp is lower illuminated ($<540 \text{ mcd/m}^2$) than the building right behind the lamp ($<750 \text{ mcd/m}^2$). Also, it is of great concern that the tree, standing left to the lamp, also is illuminated very strongly, showing values up to 200 mcd/m^2 .

The correlated colour temperature, displayed in Figure 6c, differs slightly from the spectrometer's value. SQC shows a CCT of around 2000 K for all illuminated surfaces. When displaying averaged CCT values in areas depending on the angles from the image centre, between 0° and 30° the result is 2049 K, whereas between 0° and 90° (whole image) shows nearly no difference with 2031 K. Consequently, this is again strengthening the nearly uniform emission to all angles. Results, especially the colour temperature, give evidence that the ball light contains a HPS lamp.

3.1.4. Tube Lamp

At first view, one might be led to believe the tube lamp, captured in Figure 7a, seems to emit light like a fluorescent tube. However, Figure 8a shows that the emission only occurs at the top of the pipe shaped light. This type is not widely spread and only a few are used for a car park. Its spectrum, illustrated in Figure 7b, confirms that this lamp contains a LED with a colour temperature of 2921 K. Comparing its appearance to the new LED street lighting, for example, displayed in Figure 4a, this becomes even clearer. Although, the emission of light only happens at the top of the lamp, it raises the question, if the type of construction of this lamp is necessary. There is the possibility that it was originally designed for fluorescent tubes, which would increase the apex angle of emission compared to a LED located only at the top extremely.

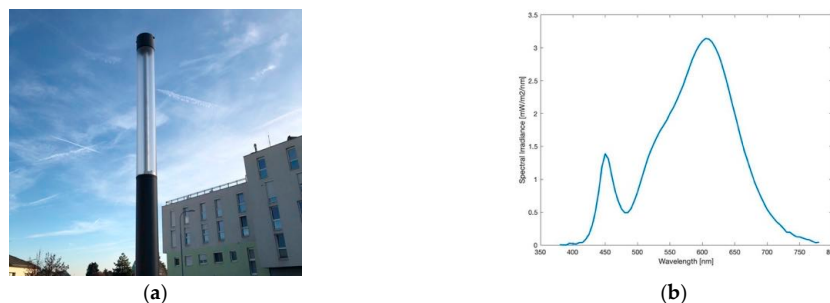


Figure 7. (a) Image of the tube lamp during daytime; (b) Spectrum of lamp observed.

Luminance data, see Figure 8b, illustrate that emission of light is not only pointed to the lower hemisphere as the tree standing behind the lamp is fully illuminated. Values at the lamp's top appear to be higher, up to 4200 mcd/m^2 , than the ball light in Figure 8a, the area close to the lamp ($\sim 2 \text{ m}$ around it) between $1000\text{--}1500 \text{ mcd/m}^2$.

Other light emitting sources can be observed in the background, like a billboard left of the lamp. This is clearly visible when examining the CCT analysis in Figure 8c, as there are different colour temperatures. Compared to the HPS lamp, also here SQC displays a colour temperature of $\sim 2300 \text{ K}$ for the lamp itself, which is far from its real value. Its glare around the lamp's head, which can be seen in the luminance data, gives more realistic values between $2850\text{--}3100 \text{ K}$. In conclusion, the CCT analysis provides the possibility of a separation of different light sources, also displaying the impact of each. This effect is not possible when only observing the luminance matrix.

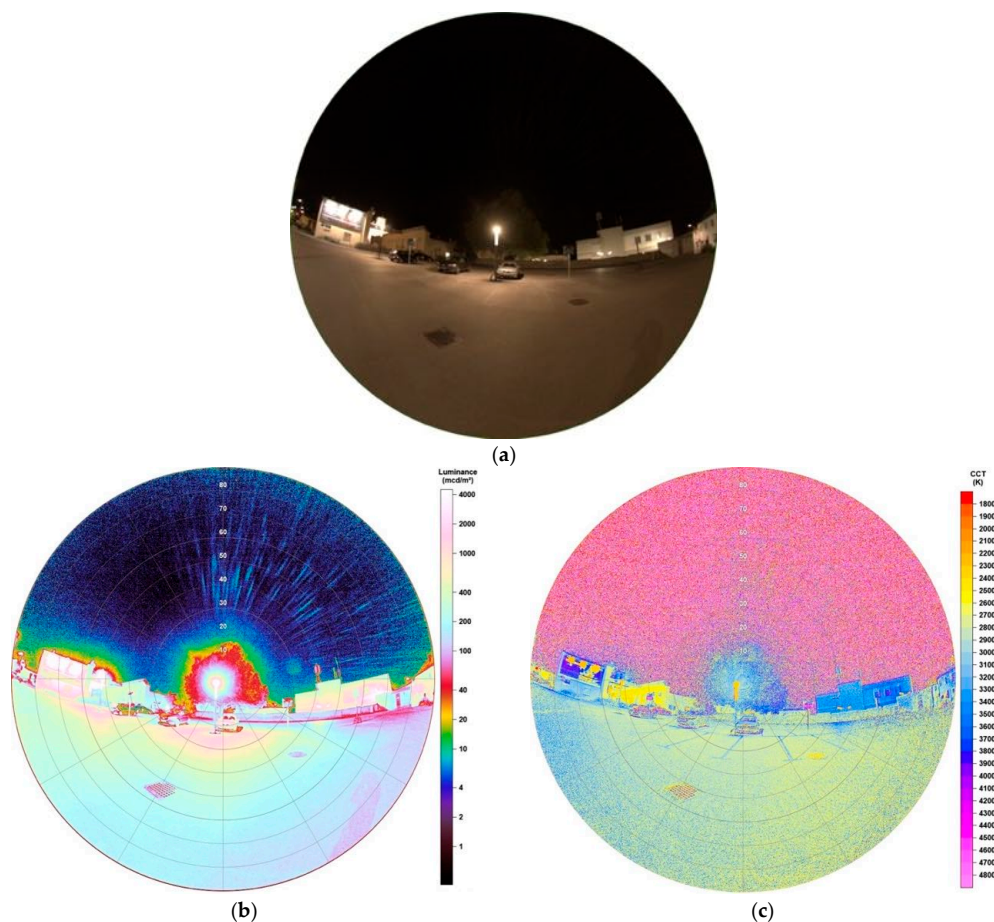


Figure 8. (a) Image of tube lamp during night-time taken with fisheye lens for detailed analysis (date: 29.07.2019, 23:23 h; exposure time: 0.3 s); (b) Luminance matrix of image (a) as displayed by SQC; (c) CCT matrix of image (a) as displayed by SQC.

3.1.5. Lantern

Around 70 lanterns, like pictured in Figure 9a, were not affected by the conversion to LEDs in Eisenstadt. They are located in the inner city, illuminating the pedestrian zone and will be maintained for historical reasons. Its spectrum, illustrated in Figure 9b, appears to be the same as obtained from the ball light in Figure 5b. Also, the measured colour temperature, 1896 K, underlines this. Consequently, the lanterns also include HPS lamps. Figure 10a shows the lighting situation at the pedestrian area, when looking to the left of the centred lamp, a great number of other lanterns are visible.

As expected, based on the lamp's shape, the luminance data, displayed in Figure 10b, show that also the lantern enlightens in nearly all angles as buildings in the near surrounding appear to be strongly illuminated. Showing values around $13,500 \text{ mcd/m}^2$, the lantern is more luminous than the ball light. This also has an impact on the wall behind the lamp, having luminance values up to 3500 mcd/m^2 . In comparison to the HPS lamp used on the street, the luminance data show a more uniform distribution of the illumination to all sides, whereas in Figure 2b some objects on the sides of the street, like a tree on the left side of the image, only display lower luminance values. Consequently, the light emission of the HPS lamp measured is more orientated to lower angles than observed here.

The CCT analysis in Figure 10c illustrates the same pattern as the engulfing glare of the ball light in Figure 6c. CCT values of the illuminated surfaces are distributed between 1800–2200 K.

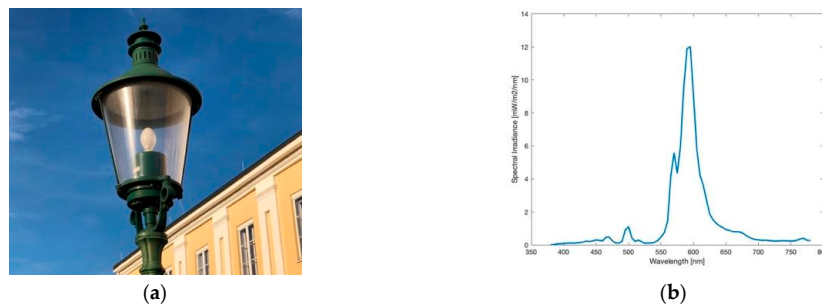


Figure 9. (a) Image of the lantern during daytime; (b) Spectrum of lamp observed.

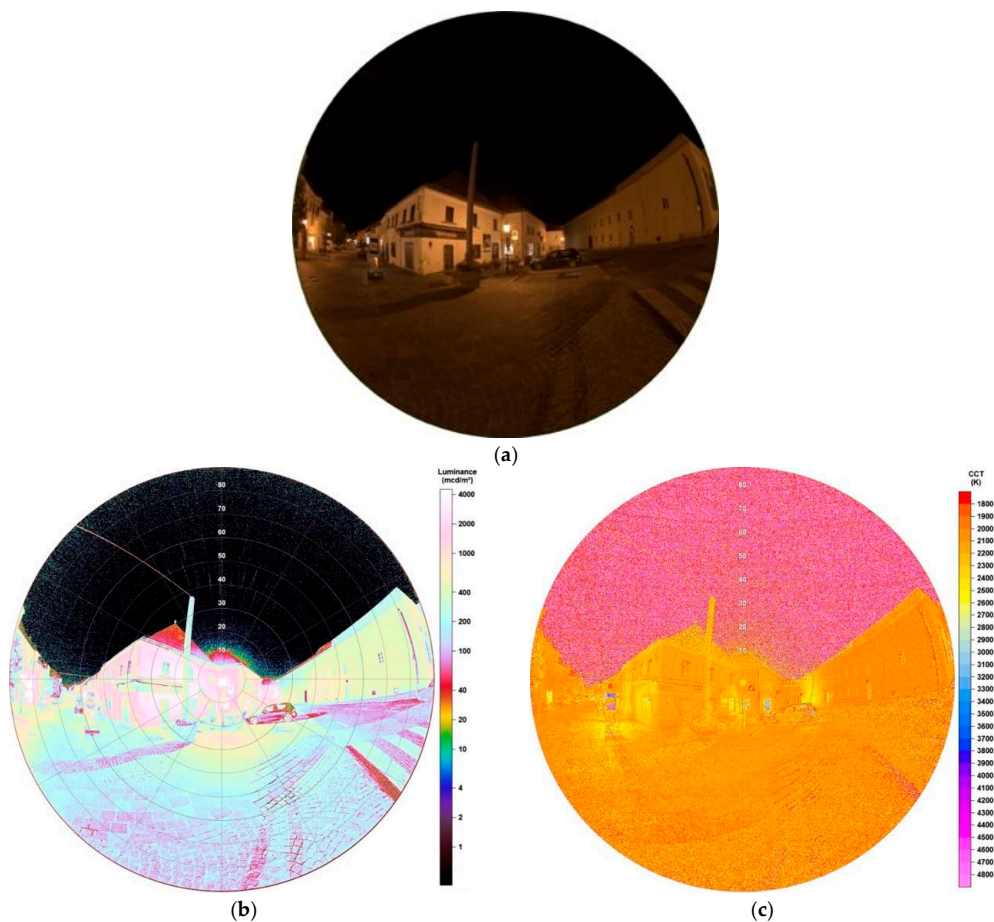


Figure 10. (a) Image of lantern during night-time taken with fisheye lens for detailed analysis (date: 29.07.2019, 23:29 h; exposure time: 0.1 s); (b) Luminance matrix of image (a) as displayed by SQC; (c) CCT matrix of image (a) as displayed by SQC.

3.1.6. Ring-Shaped Lamp

The ring-shaped lamp, captured in Figure 11a, appears to emit no light to the upper hemisphere due to its shape. The measured spectrum, visible in Figure 11b, matches a fluorescent lamp with an obtained colour temperature of 3660 K. There are only few of those installed in the city of Eisenstadt, the one observed here is part of a parking area, as seen in Figure 12a.

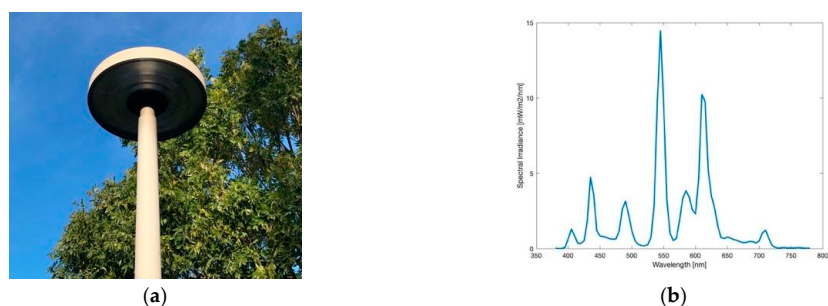


Figure 11. (a) Image of the ring-shaped light during daytime; (b) Spectrum of lamp observed.

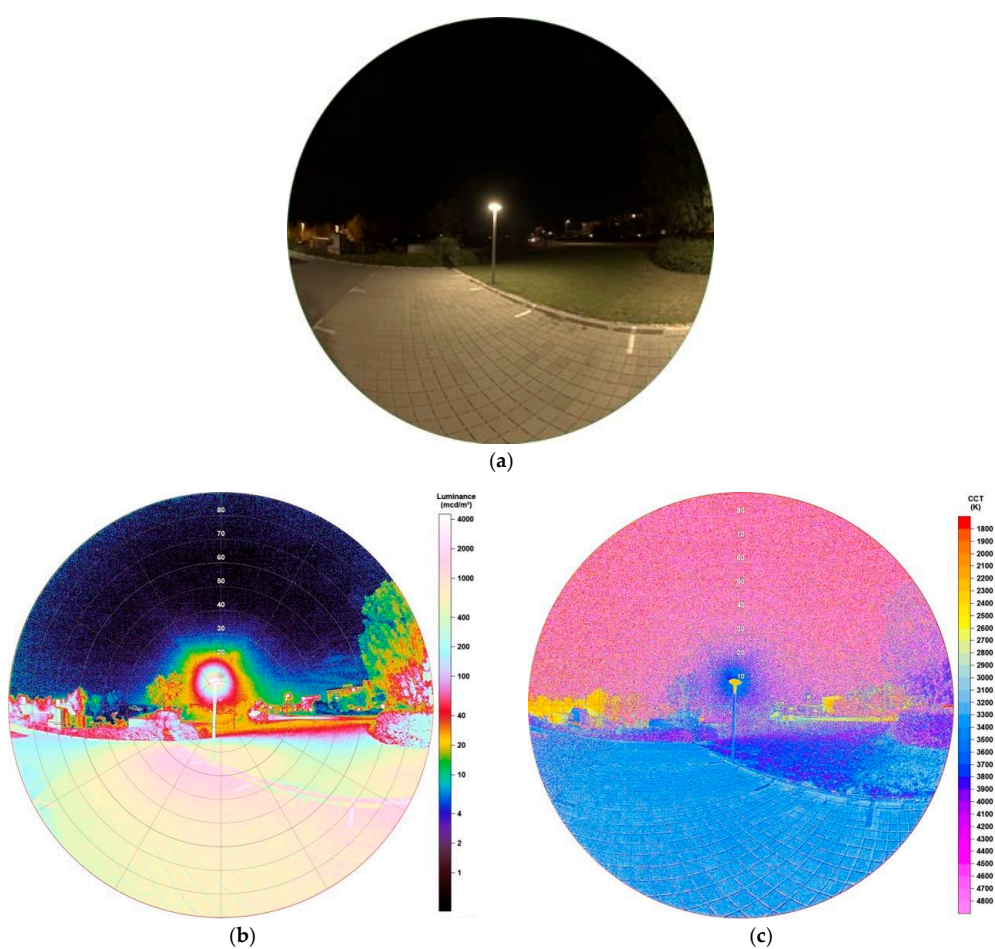


Figure 12. (a) Image of ring-shaped lamp during night-time taken with fisheye lens for detailed analysis (date: 24.10.2019, 20:52 h; exposure time: 0.3 s); (b) Luminance matrix of image (a) as displayed by SQC; (c) CCT matrix of image (a) as displayed by SQC.

Figure 12b shows the luminance matrix of the analysed image and gives indications about the cut-off behaviour of this lamp type, especially when looking at the tree standing right next to the lamp. Here it must be mentioned, that it is illuminated by a second ring-shaped lamp, which is not visible in this image. Still, a clearly observable gradient in luminance values is displayed, as the bottom of the

tree shows values up to 290 mcd/m² and the top up to 28 mcd/m². Consequently, there is a factor of 10 in luminance between the bottom and the top of the tree. The lamp's head displays up to 4400 mcd/m².

Also, CCT data, as seen in Figure 12c, can be used to discuss this behaviour. The colour temperature of the lamps glare shows values between 3400–3800 K. Through mixing with colour temperatures of surfaces, the parking area shows values around 3000–3400 K, 3500–3600 K where white lines mark the parking spaces, 3600–3900 K at the grassed area. Green leaves of the tree show values up to 4500 K. Here, also the tree must be discussed in more detail as values of the lamps colour temperature are only visible on the tree up to the height of the lamp, the upper part of the tree shows in general much higher values.

Comparing to the full cut-off LED lamp in Section 3.1.2, results of luminance and CCT matrices show that emission of light is also concentrated to the lower hemisphere, whereas here emission appear to be 90° as values on the tree standing near the lamp(s) strongly decrease above the lamp's height. By definition of the Illumination Engineering Society (IES), full cut-off LED are predestined to emit no light at or above horizontal, that is, 90° above nadir and limited to <10% intensity at or above 80°.

3.2. Buildings

In the following subsection, there are observations of bigger scaled impacts of grouped lamps, still small compared to whole cities. Two examples of illuminated buildings were captured, first a Market Hall and then Castle Esterházy, a touristic magnet of Eisenstadt. In the former case, the Market Hall is not illuminated every night, that is, there was no continuous periodicity found, whereas the Castle is illuminated throughout a year. Missing local laws regulating the brightness of building facades, there is no continuity in illuminated surfaces in the city. However, the second example, Castle Esterhazy, appears to be the brightest illuminated building in Eisenstadt.

3.2.1. Lower Luminance—Market Hall

Figure 13a shows the lighting situation in front of the Market Hall. The much stronger illuminated Castle Esterházy is located in the near surrounding but has no dominant impact on the imaged Market Hall. To prove this, also the castle was captured on the right edge of the image. Illumination of the Market Hall is executed by lamps installed on the ground emitting light upwards towards the wall. The wall is painted with bright yellow and orange colours, which is going to show impacts on the analyses as shown later.

Luminance data, as illustrated in Figure 13b, show great distributions as some parameters must be considered. At first, it becomes clear that the observation angle plays an important role. When looking at the pillars, which are directly illuminated by lamps from the ground, luminance values increase with increasing distance to the image centre, which has a passage as significant feature. The two pillars around this passage both show values between 3500–3650 mcd/m², the second pillar left of the passage 3850–4000 mcd/m², right 3700–3800 mcd/m², the third left 4250–4450 mcd/m², right 4000–4100 mcd/m², to give only few examples. The seventh pillar left of the passage, which marks the last one, even shows values between 6200–6350 mcd/m². This effect can be easily explained as bigger observation angles are overlying impacts of lighting situations with more than one light emitting source. Subsequently, for the analysis of buildings and streets with different distributed light sources standing near each other, this must be considered. Below, in Section 4, the impact on a street will be observed but as a subtraction is being chosen for analysis, the whole image can be used to find out valuable and reliable information as subtraction is also performed at overlying illuminances at the edges. The ground, approximately one meter ahead of the wall, is nearly evenly illuminated with luminance values between 250–300 mcd/m², values in front of the observer (approx. 5 m from the Market Hall) still display around 70 mcd/m². This shows huge impact of lamps even if emitting light only upwards due to reflection and over-illumination.

CCT data, as displayed in Figure 13c, show a great variety of colour temperatures. Like mentioned before, one reason is the yellowish painted wall which mixes with the colour of the light. It appears that strong illuminated surfaces, like above lamps, show values of 2300 K, not strong illuminated

surfaces, where the wall's colour is visible, between 2600–2650 K. Also, values >3000 K appear at windows and doors which are not illuminated, the passage even displays values >5500 K as a blue billboard is located inside.

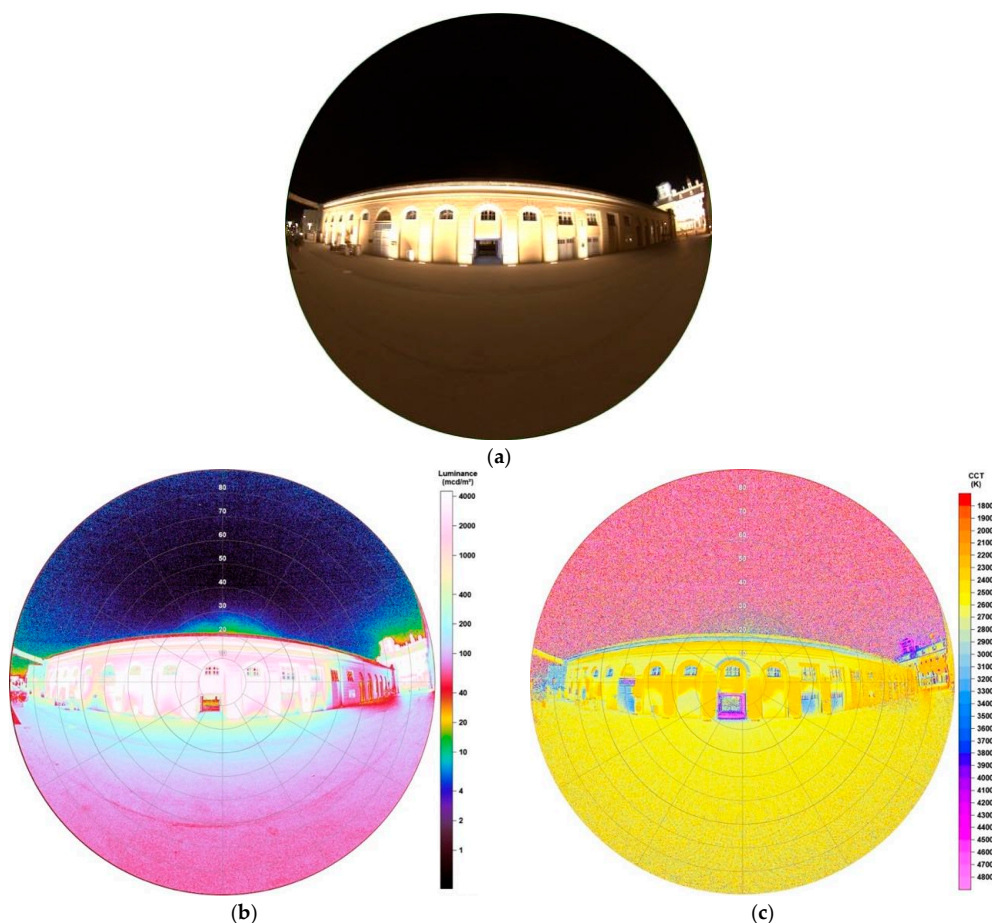


Figure 13. (a) Image of the illuminated Market Hall during night-time, taken with fisheye lens for detailed analysis (date: 29.07.2019, 23:24 h; exposure time: 0.4 s); (b) Luminance matrix as displayed by SQC; (c) CCT matrix as displayed by SQC.

3.2.2. Higher Luminance—Castle Esterházy

Castle Esterházy marks the landmark of Eisenstadt and therefore appears to be the most touristic visited place in the city. Its outer façade is illuminated every night, throughout a year, playing a big role on the light dome existing above the city. Since its illumination is very strong, Figure 14a shows the image taken at an exposure time of only 1/30 s. The size of this manifest shows one of the great advantages of fisheye lenses, having no problems to capture the whole building while standing very near. The image here was taken at ~15 m distance to the main entrance. The sources of its illumination are various—there are lamps installed on the outside of the balcony enlightening the facade upwards, there are lamps around the main entrance illuminating from the ceiling downwards, there is an illuminated billboard above the main entrance, there are two headlamps located in front of the castle enlightening the left and right parts of the castle and there are two very strong headlamps located on the neighbouring building illuminating the two towers from a distance of approximately 50 m. In conclusion, there is a great number of sources, causing the castle to be strongly illuminated.

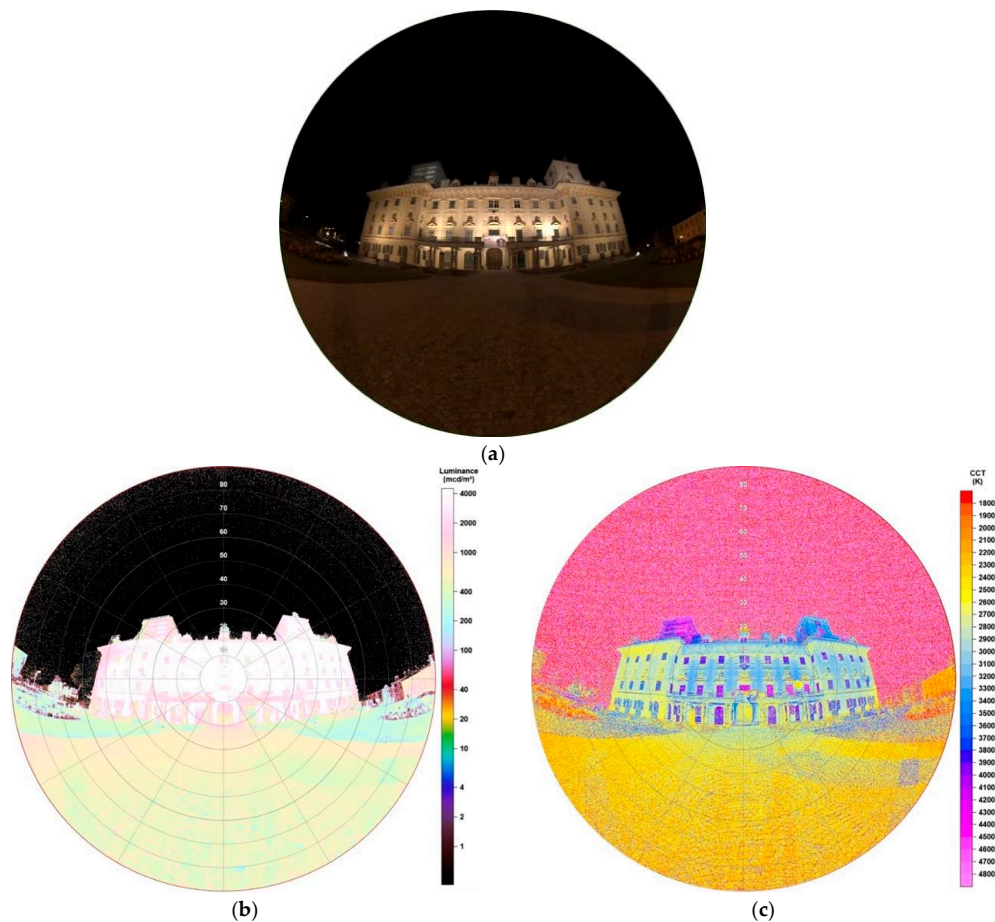


Figure 14. (a) Image of the illuminated Castle Esterházy during night-time, taken with fisheye lens for detailed analysis (date: 29.07.2019, 23:25 h; exposure time: 1/30 s); (b) Luminance matrix as displayed by SQC; (c) CCT matrix as displayed by SQC.

By looking at the luminance data of Figure 14b some can suggest nearly continuous luminance values over the building. Detailed analysis shows the opposite, as the scale provided by the software, is now by far too low. This is underlined when displaying the following: the right edge of the castle shows values 1000–2500 mcd/m², the left part 3000–20,000 mcd/m², the centre part 6000–48,000 mcd/m², the right part 5000–8000 mcd/m², the right edge 1000–4000 mcd/m², the right tower 4800–5800 mcd/m² and the advertisement above the main entrance <44,000 mcd/m². The results show that no uniformity in illumination is existing and, for example, the left part of the castle is stronger enlightened than the right part. All values were analysed on the building's surfaces, not on windows, doors or passages. The left tower was restructured as a scaffold is visible. Therefore, the left tower cannot be analysed. As light emitting sources, that is, the lamps, are clearly separated from each other, there is no overlying in illuminations like seen in Section 3.2.1. The data also show great impacts on the ground in the surrounding of the castle, having 350–500 mcd/m² on the grassed areas in front or between 2000 mcd/m² on the footpath in front of the main entrance to around 320 mcd/m² at the observer.

As envisaged, the CCT data, displayed in Figure 14c, also show that the lamps used for illumination of the castle also differ in types and colour temperatures. Again, it must be considered, that mixtures in colour temperatures through the yellowish coloured wall are resulting. The centre part of the castle shows nearly a uniform distribution of values between 3000–3200 K, the left part between 2500–3000 K,

the right part 2700–3300 K and the right tower 3100–3600 K. Comparing the different parts of the building again shows that no uniformity in illumination is existing.

3.3. Billboards and Signs

This section describes analyses of illuminated signs in the city. The first one is an illuminated logo lettering, the second one a LED video wall. Both are enlightened throughout a year in Eisenstadt.

3.3.1. Monochromatic Sign

As Figure 15a displays, the sign is a monochromatic logo lettering of a local market. It is installed beside one of the most frequented roads of the city. Its observed spectrum, shown in Figure 15b, underlines its monochromatic behaviour. The lettering captured here has a reddish colour, whereas the market also owns another lettering greenish coloured. Latter one is located around the corner on another side of the market but impacts are still visible on the left side of the image.

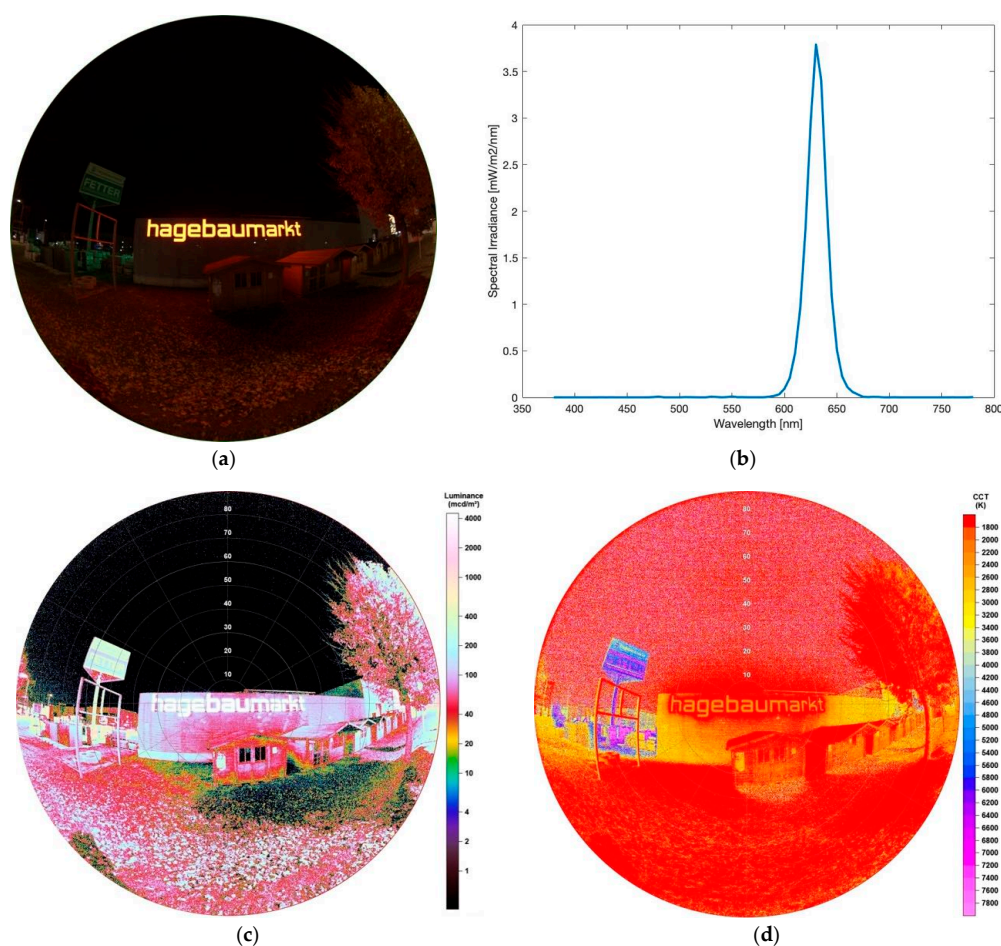


Figure 15. (a) Image of the illuminated monochromatic billboard during night-time, taken with fisheye lens for detailed analysis (date: 24.10.2019, 21:20 h; exposure time: 0.1 s); (b) Spectrum of billboard observed; (c) Luminance matrix as displayed by SQC; (d) CCT matrix as displayed by SQC. Please note a higher CCT scale up to 7800 K.

The luminance matrix obtained by SQC software, visible in Figure 15b, shows values of the sign between 13,500–15,500 mcd/m². The ground in front of the sign seems to be only slightly illuminated,

displaying $<20 \text{ mcd/m}^2$, reflections higher up, for example, at the second left wooden cottage in front of the sign $<170 \text{ mcd/m}^2$. The ground in front of the cottages almost is not illuminated due to being shadowed by them. The tree on the right edge of the image shows an interesting result, as the side looking towards the sign is lower enlightened than the side pointing towards the street and being illuminated by a LED lamp there.

CCT data underline latter discussed result, as, like seen in Figure 15c, the tree also shows a different colour temperature on the side looking to the street ($\sim 2400 \text{ K}$) than to the sign (1500 K). The illuminated letters show a uniform colour temperature of 2300 K whereas the glare of 1500 K . As latter displays the found 1500 K also very uniformly, it seems that the lower end of scale still seems to be too high as values could also distribute below. CCT data from the ground show that even if there is nearly no luminance at all, as mentioned before due to shadow of the wooden cottages, there are still effects of the illuminated sign as values are around 1500 K again.

3.3.2. LED Video Wall

As a second example of enlightened street advertisements, a LED video wall was captured. In total, three images of different displays were taken to also see the impact of different visual displays with different colour temperatures. Figure 16a–c show luminance matrices of the different advertisements 1–3, Figure 16d–f the related CCT analyses of advertisements 1–3.

Results clearly show different impacts on the surrounding if watching different displays. Advertisement 1, Figure 16a,d,g, seems to have the biggest impact as its glare leaves marks in front of the night sky. When observing the area of 0° to 13° around the centre of the image (where billboard is located), luminance values spread between $7000\text{--}14,000 \text{ mcd/m}^2$ and CCT values between $2200\text{--}5400 \text{ K}$. These big differences are not surprising as they are strongly dependent from colour of background and used letters on the display. Advertisement 2, Figure 16b,e,h, shows luminance values in the mentioned area between $5000\text{--}13,500 \text{ mcd/m}^2$ and colour temperatures between $2400\text{--}7600 \text{ K}$, advertisement 3, Figure 16c,f,i, $1500\text{--}11,000 \text{ mcd/m}^2$ and $1900\text{--}7000 \text{ K}$.

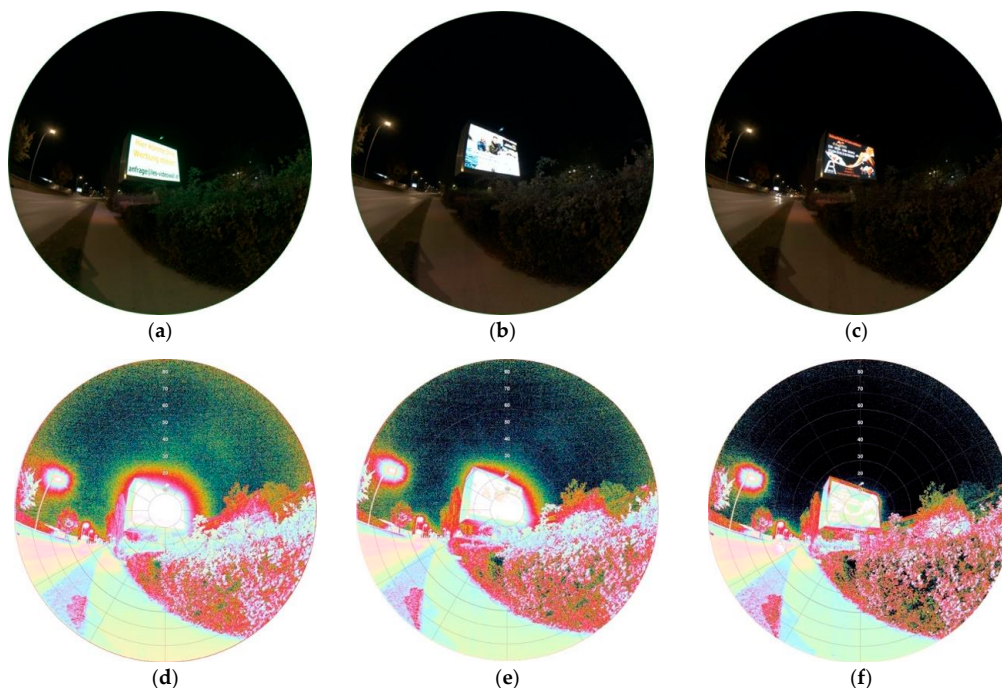


Figure 16. Cont.

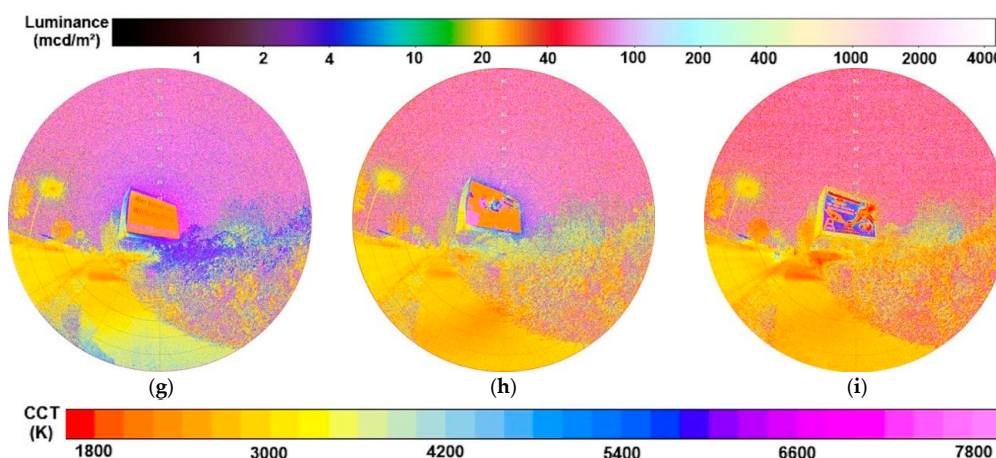


Figure 16. Raw versions and SQC products of images of a LED video wall, all taken on 24.10.2019, 21:09 h with different advertisements: (a–c) show the raw images captured, (d) and (g) show luminance and CCT values of advertisement 1, (e) and (h) of advertisement 2, (f) and (i) of advertisement 3. Please note a higher CCT scale up to 7800 K.

4. Results of LED Lighting Transition Analysis

To analyse impacts of the LED conversion performed in Eisenstadt, ‘overview’ images before and after the transition were captured from a high-rise building. The images show a street and its lighting situation being able to see impacts also on nearby buildings, plants and sidewalks. Later the images get subtracted, a tool which is implemented in the SQC software, to show changes in more detail.

4.1. Observations before LED Conversion

The image taken before LED transition started in Eisenstadt, was obtained in July 2018. It is displayed in Figure 17a. Here one must say, that moon was $\sim 12^\circ$ above the horizon, being 91.6% illuminated. Meteorological conditions were the reason why later images, after that lunar cycle, were not possible, as conversion started directly after. Consequently, the moon will play a role on the night sky in both luminance and CCT data but not on the lighting situation of the street or its analysed surrounding, as the high-rise building was blocking any moonlight. The moon was located behind the building (viewing direction to the west) and only sparsely above the horizon.

Figure 17b shows the luminance matrix and on the left edge there are higher luminance values on the sky visible, which are now a result of the moon. However, also light domes from light emitting sources farer away are apparent. Still, coming back to the lighting situation of the street, it becomes clear that, unsurprisingly, the highest luminance values, beside the lamps themselves, appear to be directly below the lamps. Two lamps are located in front of the observer, the street’s surface below both showing values between 1000–1200 mcd/m^2 , the surface midway between 80–160 mcd/m^2 . Furthermore, looking at the lamp to the right, there is also an impact on the thuja plants below the lamp’s head, being illuminated up to 2000 mcd/m^2 . Despite being ‘protected’ by those thuja plants, the building located in the centre image, shows great impact too, being illuminated up to the top. The highest luminance values displayed on the house’s wall are 45 mcd/m^2 . Compared to Section 3.1.1, this situation again shows the emission of the HPS lamp to also angles of the upper hemisphere.

Unsurprisingly, CCT data, illustrated in Figure 17c, show the street being dominated by the HPS lamp having nearly uniform values between 2000–2100 K. The house also shows values between 1900–2300 K, underlining the impact of light coming from the street. Looking at thuja between the lamps, there is a great distribution of CCT data, which is a result of low illumination. Still, also the thuja near the lamp to the right are dominated by values around 2000–2400 K.

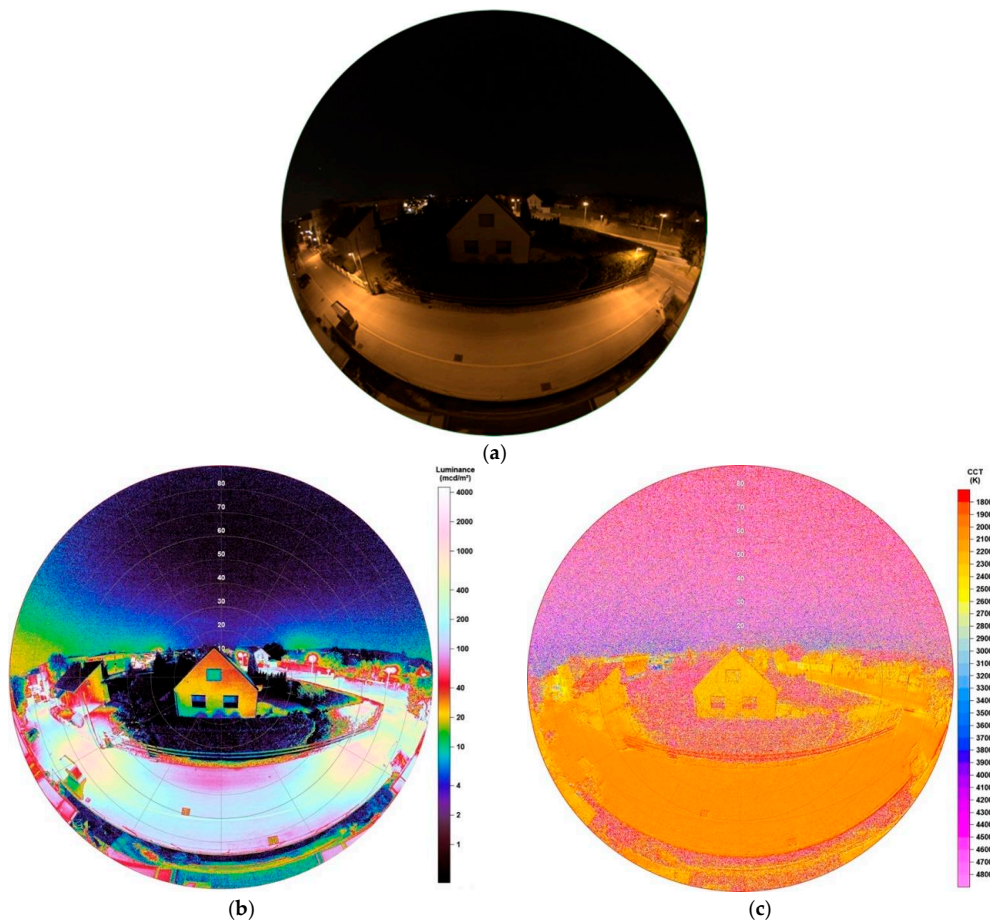


Figure 17. (a) Image of illuminated street and building during night-time before conversion to full cut-off-LEDs, taken with fisheye lens for detailed analysis (date: 30.07.2018, 23:22 h; exposure time: 0.5 s); (b) Luminance matrix as displayed by SQC; (c) CCT matrix as displayed by SQC.

4.2. Observations after LED Conversion

Figure 18a shows the pictured lighting situation after the LED conversion was finished in July 2019. Being taken with the same exposure times, one can clearly see major differences, as, for example, the building in the image centre appears to be lower illuminated and impacts on the night sky, that is, light domes from various city parts, seems to have darkened.

Luminance data, illustrated in Figure 18b, underline these impacts. Values under the lamps now display 350–600 mcd/m², midway of the lamps 30–130 mcd/m². Still, there is also an impact on the thuja, caused by the lamp to the right, of <1300 mcd/m². Also, the building again appears to be illuminated but much lower than seen before, with values around 18 mcd/m² at the top and 2–5 mcd/m² at the bottom.

The resulting CCT data, shown in Figure 18c, displays the street being engulfed in a new colour with values between 2700–3100 K. The house now shows great distribution in CCT values and it is not possible to see a threshold of values on its surface. However, at the top it seems that values spread between 2400–3400 K, whereas at the bottom at much higher ones.

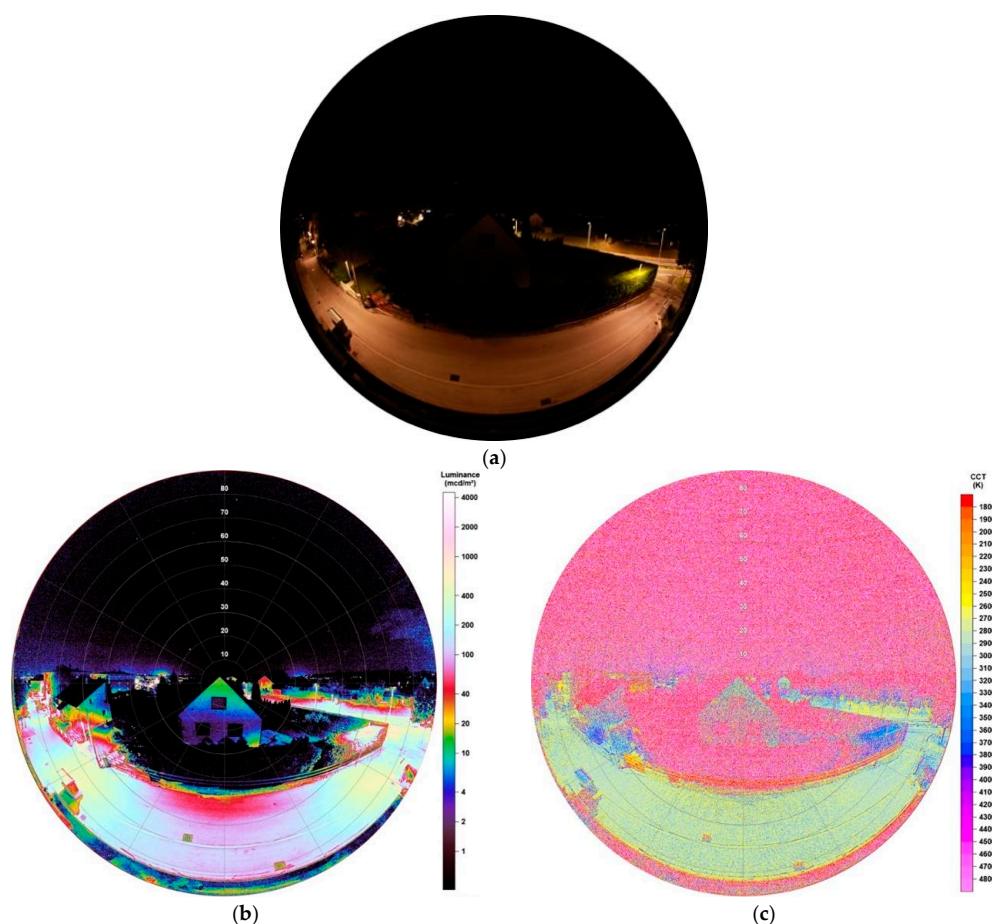


Figure 18. (a) Image of illuminated street and building during night-time after conversion to full cut-off-LEDs, taken with fisheye lens for detailed analysis (date: 02.07.2019, 02:03 h; exposure time: 0.5 s); (b) Luminance matrix as displayed by SQC; (c) CCT matrix as displayed by SQC.

4.3. Comparison and Subtraction

Figure 19 shows an optimal way of comparison between the lighting situations before and after the LED conversion. Subtracting the image before the transition from the image after transition shows how values changed in respect to the current condition.

In Figure 19a,b, one can see the change in luminance data in two different scales. In first, with lower scale, it is clearly visible that at most surface areas luminance has decreased (green coloured), only few, especially the sidewalks, have increased. Decreasing values on the left of the night sky again show impact of the moon, being on the sky at the image captured before the transition.

To quantify areas with higher impacts in more detail, also a higher scale was chosen. Results show that on the street, luminance decreased stronger below lamps, on the wall of the building in the image centre, the thuja and even at other city parts visible on the right side of the image. Increased luminance can be observed at sidewalks and small street parts. Both can be explained by the full cut-off behaviour of the new installed LED lamps. Luminance values under lamps on the street show a decrease of up to 770 mcd/m^2 , midway between the lamps up to 50 mcd/m^2 . The house in the centre of the image shows a decrease of 35 mcd/m^2 on the top and between $10\text{--}15 \text{ mcd/m}^2$ in the centre. The sidewalk is analysed by an increase between 40 to 120 mcd/m^2 .

CCT data, shown in Figure 19c, confirm the expectations as colour temperature appears to be increasing with the transition. Comparing to Sections 3.1.1 and 3.1.2, changes in CCT must be around 1000 K, which is underlined in the SQC result. A stronger increase is shown at areas which are lower illuminated after the change in lighting system.

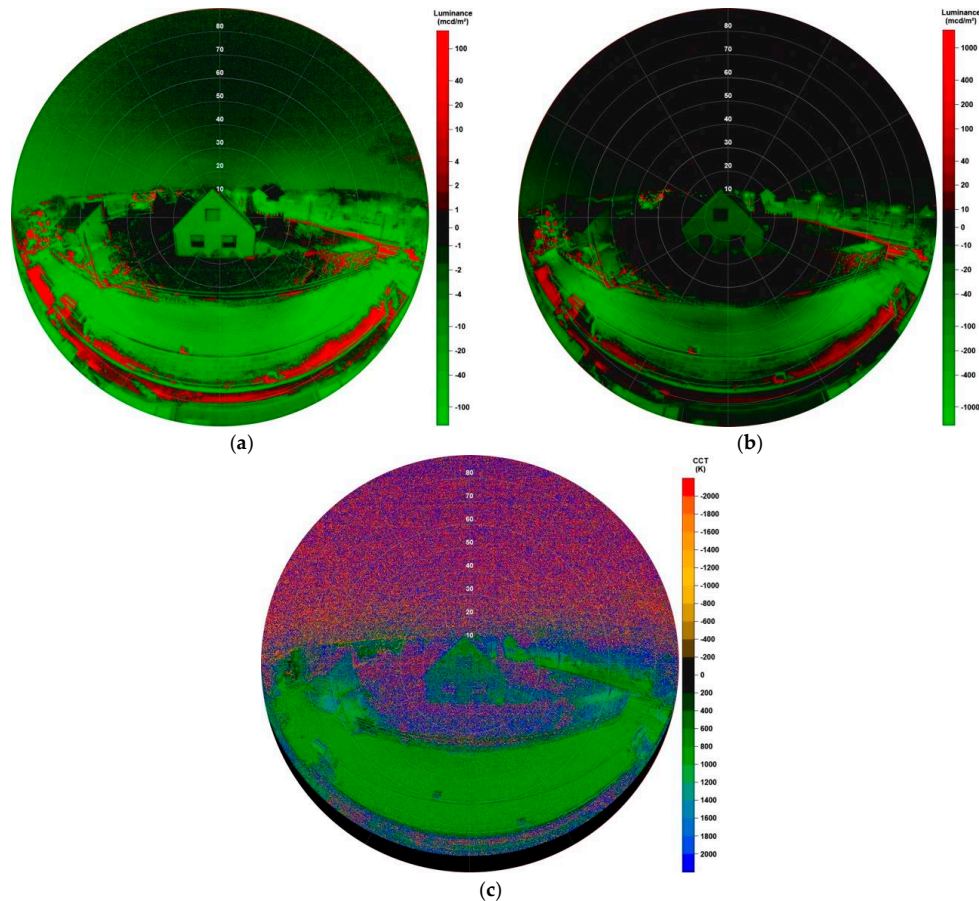


Figure 19. Subtraction of image after transition and image before transition, showing the differences in luminance and CCT. (a) Shows luminance comparison with lower scale; (b) shows luminance comparison with higher scale; (c) shows CCT comparison. Calculation was image after transition (Figure 18) minus image before transition (Figure 17).

Table 1 shows resulting values of the subtraction for luminance and CCT at different areas depending on the angle from the image centre. As both lamps located in front of the observer are located at around $\sim 60^\circ$ from the image centre, also the area $59^\circ\text{--}61^\circ$ was included.

Table 1. Development of luminance [mcd/m^2] and colour temperature [K] values for different zenith angles as analysed from the subtraction of images as seen in Figure 19 by SQC software.

Angle from Image Centre	$\Delta\text{mcd}/\text{m}^2$	ΔCCT (K)
$0^\circ\text{--}30^\circ$	−10.97	+767
$0^\circ\text{--}60^\circ$	−17.89	+759
$0^\circ\text{--}90^\circ$	−28.81	+779
$30^\circ\text{--}60^\circ$	−20.43	+765
$59^\circ\text{--}61^\circ$	−56.77	+835

5. Discussion

The results obtained showed that vertical fisheye imaging and analyses performed via Sky Quality Camera software can provide lot of valuable information about light emitting sources and their impacts on surroundings. Especially the wide-angle characterization enabled the possibility of examining various luminaires in different lighting settings. Moreover, due to the wide field optics, there was also the opportunity of analysing facades, particularly of buildings greater than the field of view if using a ‘normal,’ that is, non-fisheye, camera lens while standing near to keep the signal high. SQC is capable of obtaining luminance or CCT values interactively, allowing local studies with respect to uniformity of illuminance or identifying extreme values, easily, as also studied in the past [36]. Furthermore, the technique is able to perform quantitative analyses of not only the emission of light sources but especially their direct emission towards the observer. The analysis of a video wall has shown that the impact on its surrounding depends on the display content and can vary strongly by one and the same LED billboard. Especially luminance data illustrate that it is the dominant colour of the advertisement’s background which specifies the strength of illuminance on the sidewalk, street and so forth. Therefore, if needed to characterize such video walls, it is necessary observing the ad showing measurably the strongest luminance values. After the transition from mostly HPS lamps to LEDs in Eisenstadt, it was possible to analyse the impacts of this change at one location. Subtracting images taken before and after the conversion provides a great possibility of comparison and to quantify impacts of old versus new light sources on surroundings. As expected, higher colour temperatures, an increase of around 800 K from HPS lamp to LEDs and mostly lower luminance values, a decrease of up to 770 mcd/m^2 , were the result of the analysis.

There are limitations to the analysis as high luminance values, that is, values mostly above 4000 mcd/m^2 , can be followed by a saturation of the image, visible in Figures 8 and 10. Especially heads of lamps seem to show different CCT values than their glare or illuminated surfaces, which are more realistic compared to spectrometer measurements. Consequently, this must be considered if trying to find the colour temperature of a lamp. If obtaining colour temperatures of illuminated surfaces, one must take into account that a mixing of colour temperatures of either the emitted light or the painted surfaces occurs. Subsequently, the CCT of an illuminated surface is rarely in exact accordance with the light coming from the lamp. As SQC is generally designed for imaging the night sky, the luminance scale’s thresholds applied to the images can be too low, especially when capturing illuminated signs or buildings. Hence, differentiating of luminance values above 4000 mcd/m^2 is not possible by only looking at the resulting matrices. It may well be the case if using the interactive software as, when moving the mouse over the image, values above this threshold are still displayed.

The paper shows results of only few usages of vertical fisheye images as they can be used in more multifaceted ways for further study, for example, lamp dimming in different intensities or the impact of different heights of lamp heads. These are only two examples of far more ideas, how the technique can be used in future works. It is interdisciplinary applicable, as it can be used to quantify impacts of artificial light at night, especially single light emitting sources for studies in ecology, sustainability, lighting management and far more. All images analysed were taken under clear sky conditions to avoid external influences and being able to concentrate on impacts on the ground. Still, it is of great interest for future works to investigate the method described in this work also under different meteorological conditions. It could be expected that, for example, foggy conditions are followed by major impacts on luminance data, whereas an overcast sky on CCT data, as generally seen on night sky imagery [26].

6. Conclusions

There were various examples of light emitting sources, illuminated objects and lighting situations being analysed with the Sky Quality Camera software via vertical plane imaging. Luminance matrices give the possibility of receiving an impression on the luminosity of light emitting sources and their illuminated surroundings. CCT analyses can not only distinguish but also quantify impacts of different light emitting sources, also when being grouped together. Examples of three different shaped lamps,

all containing HPS bulbs, were identified having various impacts on nearby buildings, streets and so forth, depending only on their emission angle. Both luminance and CCT data are able to illustrate the uniformity of illumination of an area around lamps, for example, streets, sidewalks or car parks or on buildings. Furthermore, both can characterize if new installed LEDs or other lamp types are full cut-off or still emitting light to parts of the upper hemisphere.

The technique of using a fisheye lens appears to have both pros and cons. On the one hand, it is easily possible to capture very big buildings on one image without being far away from them and possibly losing signal. Furthermore, its build-up is a commonly used method in the light pollution community, generally imaging the night sky on all-sky images. Therefore, if characterizing single sources, this build-up must not be changed and can be used with much smaller exposure times and even without a tripod. A disadvantage at light emitting sources with a great number of lights and short distance to each other, there is an increasing overlying in illuminances when moving away from the image centre.

In conclusion, the results show that the method of vertical plane imaging and analyses performed via the SQC software is an easy and quick way to obtain information about lighting situations on small scales like the characterization of single lamps or illuminated signs and impacts on streets, buildings and other surroundings. With this method, it is possible to investigate illuminated places, not exclusively urban environments and collect information about possibilities of improvements of lamps installed.

Funding: Open Access Funding provided by the University of Vienna.

Acknowledgments: The author wants to dedicate this work to his beloved colleague Thomas Posch. Also, he wants to thank everybody, who was involved in developing this paper, especially Andreas Jechow.

Conflicts of Interest: The author declares no conflict of interest.

References

1. Falchi, F.; Cinzano, P.; Duriscoe, D.; Kyba, C.C.M.; Elvidge, C.D.; Baugh, K.; Portnov, B.A.; Rybnikova, N.A.; Furgoni, R. The new world atlas of artificial night sky brightness. *Sci. Adv.* **2016**, *2*, e1600377. [[CrossRef](#)]
2. Kyba, C.C.M.; Kuester, T.; Sanchez de Miguel, A.; Baugh, K.; Jechow, A.; Hölker, F.; Bennie, J.; Elvidge, C.D.; Gaston, K.J.; Guanter, L. Artificially lit surface of Earth at night increasing in radiance and extent. *Sci. Adv.* **2017**, *3*, e1701528. [[CrossRef](#)] [[PubMed](#)]
3. Wesolowski, M. Impact of light pollution on the visibility of astronomical objects in medium-sized cities in Central Europe on the example of the city of Rzeszów, Poland. *J. Astrophys. Astr.* **2019**, *40*, 20. [[CrossRef](#)]
4. Cinzano, P.; Falchi, F.; Elvidge, C.D. Naked-eye star visibility and limiting magnitude mapped from DMSP-OLS satellite data. *Mon. Not. R. Astron. Soc.* **2001**, *323*, 34–46. [[CrossRef](#)]
5. Dominiononi, D. The effects of light pollution on biological rhythms of birds: An integrated, mechanistic perspective. *J. Ornithol.* **2015**, *156*, 409–418. [[CrossRef](#)]
6. Bennie, J.; Duffy, J.; Davies, T.; Correa-Cano, M.; Gaston, K. Global trends in exposure to light pollution in natural terrestrial ecosystems. *Remote. Sens.* **2015**, *7*, 2715–2730. [[CrossRef](#)]
7. Bennie, J.; Davies, T.; Inger, R.; Gaston, K. Mapping artificial lightscapes for ecological studies. *Methods Ecol. Evol.* **2014**, *5*, 534–540. [[CrossRef](#)]
8. Gaston, K.J.; Bennie, J.; Davies, T.W.; Hopkins, J. The ecological impacts of night-time light pollution: A mechanistic appraisal. *Biol. Rev.* **2013**, *88*, 912–927. [[CrossRef](#)]
9. Grubisic, M.; van Grunsven, R.H.A.; Manfrin, A.; Monaghan, M.T.; Hölker, F. A transition to white LED increases ecological impacts of nocturnal illumination on aquatic primary producers in a lowland agricultural drainage ditch. *Environ. Pollut.* **2018**, *240*, 630–638. [[CrossRef](#)]
10. Brüning, A.; Hölker, F.; Franke, S.; Kleiner, W.; Kloas, W. Impact of different colours of artificial light at night on melatonin rhythm and gene expression of gonadotropins in European perch. *Sci. Total. Environ.* **2016**, *543*, 214–222. [[CrossRef](#)]
11. Rybnikova, N.A.; Portnov, B.A. Outdoor light and breast cancer incidence: A comparative analysis of DMSP and VIIRS-DNB satel- lite data. *Int. J. Remote. Sens.* **2016**, *38*, 5952–5961. [[CrossRef](#)]

12. Stevens, R.G.; Zhu, Y. Electric light, particularly at night, disrupts human circadian rhythmicity: Is that a problem? *Philos. Trans. R. Soc. B* **2015**, *370*, 20140120. [CrossRef] [PubMed]
13. Haim, A.; Zubidat, A.E. LED light between Nobel Prize and cancer risk factor. *Chronobiol. Int.* **2015**, *32*, 725–727. [CrossRef] [PubMed]
14. Davies, T.W.; Smyth, T. Why artificial light at night should be a focus for global change research in the 21st century. *Glob. Chang. Biol.* **2018**, *24*, 872–882. [CrossRef] [PubMed]
15. Falchi, F.; Cinzano, P.; Elvidge, C.D.; Keith, D.M.; Haim, A. Limiting the impact of light pollution on human health, environment and stellar visibility. *J. Environ. Manag.* **2011**, *92*, 2714–2722. [CrossRef]
16. Hölker, F.; Moss, T.; Griefahn, B.; Kloas, W.; Voigt, C.C.; Henckel, D.; Hänel, A.; Kappeler, P.M.; Völker, S.; Schwöpe, A.; et al. The Dark Side of Light: A Transdisciplinary Research Agenda for Light Pollution Policy. *Ecol. Soc.* **2010**, *15*, 13. [CrossRef]
17. Cajochen, C.; Frey, S.; Anders, D.; Späti, J.; Bues, M.; Pross, A.; Mager, R.; Wirz-Justice, A.; Stefani, O. Evening exposure to a light-emitting diodes (LED)-backlit computer screen affects circadian physiology and cognitive performance. *J. Appl. Physiol.* **2011**, *110*, 1432–1438. [CrossRef]
18. Barentine, J.C.; Walker, C.E.; Kocifaj, M.; Kundracik, F.; Juan, A.; Kanemoto, J.; Monrad, C.K. Skyglow changes over Tucson, Arizona, resulting from a municipal LED street lighting conversion. *J. Quant. Spectrosc. Radiat. Transf.* **2018**, *212*, 10–23. [CrossRef]
19. Baddiley, C. Light pollution modelling and measurements at Malvern hills AONB, of county conversion to blue rich LEDs. *J. Quant. Spectrosc. Radiat. Transf.* **2018**, *219*, 142–173. [CrossRef]
20. Aubé, M.; Simoneau, A.; Wainscoat, R.; Nelson, L. Modelling the effects of phosphor converted LED lighting to the night sky of the Haleakala Observatory, Hawaii. *Mon. Not. R. Astron. Soc.* **2018**, *478*, 1776–1783. [CrossRef]
21. Unihedron Home Page. Available online: <http://unihedron.com> (accessed on 8 November 2019).
22. Cinzano, P. *Night Sky Photometry with Sky Quality Meter, First Draft*; ISTIL Internal Report n 9, v.1.4; ISTIL: Thiene, Italy, 2005; Available online: http://unihedron.com/projects/darksky/sqmreport_v1p4.pdf (accessed on 18 November 2019).
23. Posch, T.; Binder, F.; Puschign, J. Systematic measurements of the night sky brightness at 26 locations in Eastern Austria. *J. Quant. Spectrosc. Radiat. Transf.* **2018**, *211*, 144–165. [CrossRef]
24. Bertolo, A.; Binotto, R.; Ortolani, S.; Sapienza, S. Measurements of Night Sky Brightness in the Veneto Region of Italy: Sky Quality Meter Network Results and Differential Photometry by Digital Single Lens Reflex. *J. Imaging* **2019**, *5*, 56. [CrossRef]
25. Jechow, A.; Hölker, F.; Kolláth, Z.; Gessner, M.O.; Kyba, C.C.M. Evaluating the summer night sky brightness at a research field site on Lake Stechlin in northeastern Germany. *J. Quant. Spectrosc. Radiat. Transf.* **2016**, *181*, 24–32. [CrossRef]
26. Jechow, A.; Kolláth, Z.; Ribas, S.J.; Spoelstra, H.; Hölker, F.; Kyba, C.C.M. Imaging and mapping the impact of clouds on skyglow with all-sky photometry. *Sci. Rep.* **2017**, *7*, 6741. [CrossRef]
27. Jechow, A.; Ribas, S.J.; Canal-Domingo, R.; Hölker, F.; Kolláth, Z.; Kyba, C.C.M. Tracking the dynamics of skyglow with differential photometry using a digital camera with fisheye lens. *J. Quant. Spectrosc. Radiat. Transf.* **2018**, *209*, 212–223. [CrossRef]
28. Jechow, A.; Kyba, C.C.M.; Hölker, F. Beyond All-Sky: Assessing Ecological Light Pollution Using Multi-Spectral Full-Sphere Fisheye Lens Imaging. *J. Imaging* **2019**, *5*, 46. [CrossRef]
29. Jechow, A.; Hölker, F.; Kyba, C.C.M. Using all-sky differential photometry to investigate how nocturnal clouds darken the night sky in rural areas. *Sci. Rep.* **2019**, *9*, 1391. [CrossRef]
30. Jechow, A. Observing the Impact of WWF Earth Hour on Urban Light Pollution: A Case Study in Berlin 2018 Using Differential Photometry. *Sustainability* **2019**, *11*, 750. [CrossRef]
31. Duriscoe, D.M.; Anderson, S.J.; Luginbuhl, C.B.; Baugh, K.E. A simplified model of all-sky artificial sky glow derived from VIIRS Day/Night band data. *J. Quant. Spectrosc. Radiat. Transf.* **2018**, *214*, 133–145. [CrossRef]
32. Kocifaj, M. Light-pollution model for cloudy and cloudless night skies with ground-based light sources. *Appl. Opt.* **2007**, *46*, 3013–3022. [CrossRef]
33. Aubé, M.; Franchomme-Fosse, L.; Robert-Staehler, P.; Houle, V. Light pollution modelling and detection in a heterogeneous environment: Toward a night-time aerosol optical depth retrieval method. *Proc. SPIE* **2005**, *5890*, 248–256.
34. Kocifaj, M.; Wallner, S.; Solano-Lamphar, H.A. An asymptotic formula for skyglow modelling over a large territory. *Mon. Not. R. Astron. Soc.* **2019**, *485*, 2214–2224. [CrossRef]

J. Imaging **2019**, *5*, 86

24 of 24

35. Hänel, A.; Posch, T.; Ribas, S.J.; Aubé, M.; Duriscoe, D.; Jechow, A.; Kolláth, Z.; Lolkema, D.E.; Moore, C.; Schmidt, N.; et al. Measuring night sky brightness: Methods and challenges. *J. Quant. Spectrosc. Radiat. Transf.* **2018**, *205*, 278–290. [[CrossRef](#)]
36. Gălăţanu, C.D.; Gherasim, I.; Beu, D.; Lucache, D.D. Luminance Field of the Façades: From Aggressive to Attractive Lighting. In Proceedings of the 2018 IEEE International Conference on Environment and Electrical Engineering and 2018 IEEE Industrial and Commercial Power Systems Europe (EEEIC / I&CPS Europe), Palermo, Italy, 12–15 June 2018; p. 8494624.



© 2019 by the author. Licensee MDPI, Basel, Switzerland. This article is an open access article distributed under the terms and conditions of the Creative Commons Attribution (CC BY) license (<http://creativecommons.org/licenses/by/4.0/>).

4.4 'Circalunar variations of the night sky brightness – an FFT perspective on the impact of light pollution'

Title: *Circalunar variations of the night sky brightness – an FFT perspective on the impact of light pollution*

Authors: J. Puschnig, S. Wallner, T. Posch

Journal: Monthly Notices of the Royal Astronomical Society (MNRAS)

Status: Published in MNRAS 492, 2622-2637 (2020)

DOI: <https://doi.org/10.1093/mnras/stz3514>

Personal contribution: The idea for this paper was developed by J. Puschnig and T. Posch. My contribution was the simulation of the moon calculation model as discussed in the paper and its analysis, wrote parts of the paper and helped with the analysis of the FFT data by investigating resulting frequencies. Additionally, I was deeply involved in the revision process of the work.



Circalunar variations of the night sky brightness – an FFT perspective on the impact of light pollution

Johannes Pusch¹,¹★ Stefan Wallner^{2,3} and Thomas Posch²

¹Argelander-Institut für Astronomie, Universität Bonn, Auf dem Hügel 71, D-53121 Bonn, Germany

²Institut für Astrophysik, Universität Wien, Türkenschanzstraße 17, A-1180 Wien, Austria

³ICA, Slovak Academy of Sciences, Dubravská cesta 9, 84503 Bratislava, Slovak Republic

Accepted 2019 December 11. Received 2019 December 10; in original form 2019 August 12

ABSTRACT

Circa-monthly activity conducted by moonlight is observed in many species on Earth. Given the vast amount of artificial light at night (ALAN) that pollutes large areas around the globe, the synchronization to the circalunar cycle is often strongly perturbed. Using 2-yr data from a network of 23 photometers (Sky Quality Meters; SQM) in Austria (latitude $\sim 48^\circ$), we quantify how light pollution impacts the recognition of the circalunar periodicity. We do so via frequency analysis of nightly mean sky brightnesses using Fast Fourier Transforms. A very tight linear relation between the mean zenithal night sky brightness (NSB) given in $\text{mags}_{\text{SQM}} \text{ arcsec}^{-2}$ and the amplitude of the circalunar signal is found, indicating that for sites with a mean zenithal NSB brighter than $16.5 \text{ mags}_{\text{SQM}} \text{ arcsec}^{-2}$ the lunar rhythm practically vanishes. This finding implies that the circalunar rhythm is still detectable (within the broad bandpass of the SQM) at most places around the globe, but its amplitude against the light polluted sky is strongly reduced. We find that the circalunar contrast in zenith is reduced compared to ALAN-free sites by factors of $\frac{1}{9}$ in the state capital of Linz ($\sim 200\,000$ inhabitants) and $\frac{1}{3}$ in small towns, e.g. Freistadt and Mattighofen, with less than 10 000 inhabitants. Only two of our sites, both situated in national parks (Bodinggraben and Zöblboden), show natural circalunar amplitudes. At our urban sites, we further detect a strong seasonal signal that is linked to the amplification of anthropogenic skyglow during the winter months due to climatological conditions.

Key words: instrumentation: photometers – light pollution – methods: data analysis – methods: observational – techniques: photometric – Moon.

1 INTRODUCTION

1.1 Impact of moonlight on animals, plants, and humans

The Moon's synodic period of 29.5 d is its orbital time around the Earth required to show the exact same lunar phase, i.e. the time span between two consecutive full moons. The corresponding circalunar oscillation of the Moon's illumination impacts many types of life on Earth, in particular in the context of reproduction cycles. Scientific work on this topic dates back to the early 20th century (e.g. Fox & Gardiner 1924) and it was likely already recognized by fishermen in the antiquity – due to practical implications – that the size of (edible) gonads of sea urchins varies over the lunar month (Raible, Takekata & Tessmar-Raible 2017).

Later studies revealed that also predator–prey interactions change with moon phase and illumination (Clarke 1983; Shimose, Yokawa & Tachihara 2013), giving advantages to either side, depending

on the context. More recently, Fallows, Fallows & Hammerschlag (2016) studied interactions between white sharks (*Carcharodon carcharias*) and Cape fur seals (*Arctocephalus pusillus pusillus*). They found that the shark attack frequency and seal capture success were significantly higher at sunrise during periods of low lunar illumination. In other species, the lunar cycle may control activity (Kolb 1992), foraging, habitat use, and communication. See Kronfeld-Schor et al. (2013) for a recent review on those topics. And for the golden rabbitfish (*Siganus guttatus*), Takemura et al. (2006) found a direct influence of moonlight intensity on changes in melatonin production.

Some animals are driven by the Moon in their orientation (Papi & Pardi 1963; Frisch 1994), in particular Dacke et al. (2011) found that dung beetles (*carabaeus lamarcki*) use the polarization pattern around the Moon as a compass for maintaining their travel direction.

Bünning & Moser (1969) studied how different types of plants react on moonlight. They revealed that plants may undergo leaf movements such that the intensity of lunar illumination is reduced and disturbing effects caused by moonlight are eliminated. It was further shown that illumination by moonlight may even promote

* E-mail: johannes.pusch@uni-bonn.de

flowering, e.g. Ben-Attia et al. (2016) found flowering patterns in the cactus *Cereus peruvianus* with a period of ~ 29.5 d and a correlation between moon phase and number and proportion of flowers in bloom. In aquatic systems, Zantke et al. (2013) first established that the marine worm *Platynereis dumerilii* possesses an endogenous circalunar clock and Last et al. (2016) was one of the first to search for impacts on aquatic ecosystems and especially noticed a vertical migration of zooplankton which takes place in winter when the Moon is above the horizon at the Arctic, fjord, or other sea areas.

Besides animals and plants, the impact of moonlight on humans is still under debate, see e.g. Zimecki (2006) for a review. However, many authors find evidence that women of reproductive age do follow the circalunar rhythm (Reinberg, Smolensky & Touitou 2016), especially the ovulation seems to accumulate around new moon (Law 1986).

What about the effect of lunar illumination on human sleep? On one hand, Cajochen et al. (2013) find that at full moon the electroencephalogram delta activity during the deep sleep phase is 30 per cent decreased and that the sleep duration is reduced by 20 min, but on the other hand, Cordi et al. (2014) find no such significant effects depending on lunar cycle. However, Cajochen et al. (2014) pointed out that the volunteers tested by Cordi et al. (2014) were not synchronized with respect to their own natural sleep timing, which may have led to low signal to noise in their result.

Given the plethora of studies about how moonlight impacts various species on Earth, our work on how artificial light at night (ALAN) impacts the recognizability of the lunar cycle, seems to be a timely matter, as ALAN thus presumably perturbs those species in manifold ways (reproduction, predator–prey interaction, activity, orientation, and so forth) as well.

1.2 Moonlight versus light pollution

Given the fact that ALAN is ever increasing on a global scale (Kyba et al. 2015), effects of artificial light on organisms and ecosystems have gained increasingly more attention in recent years (Hölker et al. 2010; Gaston, Visser & Hölker 2015; Manfrin et al. 2017). It has become clear that ALAN indeed has multifaceted consequences for flora and fauna, see e.g. Schroer & Hölker (2016) for a review.

However, despite the fact that the influence of moonlight on beings on our planet is well documented (see previous section), and that ALAN's impact on various organisms and ecosystems have been demonstrated by many authors, to date no studies were performed to investigate ALAN's impact on processes that rely on synchronization with moonlight. The reason for this knowledge gap is that the community is lacking a quantification of the strength of the circalunar rhythm in dependence of the level of light pollution (Davies et al. 2013). With this work, we aim to provide such a quantification, i.e. a simple empirical relation between the mean night sky brightness (NSB) and the amplitude of the circalunar rhythm, allowing the knowledge gap to be filled in the near future.

2 LOCATIONS AND METHODS OF OUR MEASUREMENTS

This paper is primarily based on zenithal NSB measurements taken with Sky Quality Meters (model SQM-LE). These are photodiode-based devices with an optical element on the front that narrows down the field of view to a Gaussian-like cone with a full width at half-maximum of $\sim 20^\circ$. Its effective bandpass ranges from approximately 400–650 nm (see Fig. 1). Technical characterization

and testing was done by Cinzano (2005) and details about the absolute radiometric calibration are found in Bará, Tapia & Zamorano (2019).

Our SQM measurements have been carried out in the Austrian county of Upper Austria at 23 sites, distributed over the whole area of this county and ranging from its capital city Linz – which has very bright skies – to very remote locations such as Krippenstein on the Dachstein plateau (~ 2000 m above sea level). See Table 1 for station codes and geographic coordinates. Measurements are taken in an automated way, with SQM devices located in weather-proof housings. The network of SQMs is run by the provincial government of Upper Austria. Starting with six devices in 2014, it has grown to 23 SQMs by 2016. A detailed description of the individual sites, their exact locations and light pollution levels are found in Posch, Binder & Puschnig (2018).

Measurements are taken every minute, thus a huge amount of data is generated every night. However, the present data analysis is based on the *mean* nocturnal NSBs ($\langle \text{NSB} \rangle$) and is restricted to data obtained during the years 2016–2017. For each night and SQM site, we calculate $\langle \text{NSB} \rangle$ as arithmetic means of the minute-by-minute SQM readings for each night. The data series is further constrained for solar elevations below -15° , in the same way as described by Posch et al. (2018). The contribution of scattered sunlight to the NSB is negligible below this altitude. Our $\langle \text{NSB} \rangle$ measurements range from 17.3 to 21.0 $\text{mag}_{\text{SQM}} \text{arcsec}^{-2}$.

We stress that we do not apply any further filtering, i.e. data obtained when the sky was cloudy are included.

3 SYNTHETIC MODELS OF GROUND ILLUMINATION BY THE MOON AND TOTAL ZENITHAL NIGHT SKY BRIGHTNESS

In order to study ALAN's impact on the lunar rhythm, we first want to understand the amplitude of the *naturally* occurring oscillation of moonlight at our sites, i.e. without any contribution of anthropogenic light at night. We do so using two models. The first one, describing the lunar variation of *ground illumination* in units of *lux* and the second one, describing the naturally occurring variation of zenithal NSB in units of $\text{mag}_{\text{SQM}} \text{arcsec}^{-2}$, which may be approximately converted to luminance in units of cd m^{-2} (Bará 2016; Bará 2017), using equation (1). Despite the fact that this formula is widely used to estimate luminances from SQM magnitudes, it was originally derived by Garstang (1986) for Johnson V-band magnitudes, and is thus just an approximation.

$$\text{Luminance} [\text{cd/m}^2] = 10.8 \times 10^4 \times 10^{(-0.4 \times [\text{mag arcsec}^{-2}])} \quad (1)$$

3.1 Simplified model of ground illumination by the Moon

3.1.1 General solution for all possible values

To obtain insight into the contribution of moonlight to the total ground illumination, we make use of the moonlight model by Seidelmann (1992). The model does not take into account contributions of the skyglow, stars, or airglow and thus depend only on two parameters: the mean altitude of the Moon ($0-90^\circ$, where 90° is the zenith) and the Moon's phase angle ($0-180^\circ$, where 180° is full moon). Note that the parallax value is neglected due to its very small contribution. We show the whole parameter space covered by the model in Fig. 2.

Unsurprisingly, the amount of ground illuminance is highest when the full moon can be observed in the zenith. It is recognized

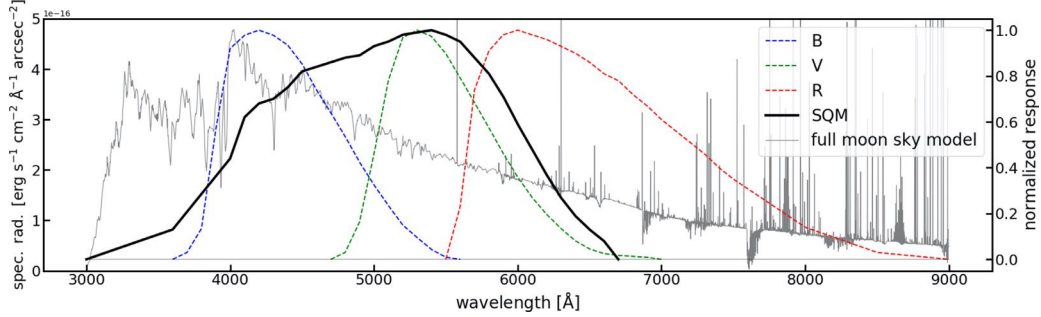


Figure 1. Skycalc radiance model for the zenith with the full moon at 45° altitude. Transmission curves of the SQM and Bessel B , V , R filters are overplotted.

Table 1. Basic information of the 23 SQM locations in Upper Austria, categorized into urban, intermediate, and rural sites, as done in Posch et al. (2018).

Code	Name	Latitude N	Longitude E	Elevation (m) (above sea level)
<i>Urban</i>				
LSM	Linz, Schlossmuseum	N 48 18 19	E 14 16 58	287
LGO	Linz, Göthestraße	N 48 18 19	E 14 18 30	259
LSW	Linz, Sternwarte	N 48 17 36	E 14 16 6	336
STY	Steyr	N 48 2 57	E 14 26 32	307
STW	Steyregg-Weih	N 48 17 19	E 14 21 13	331
TRA	Traun	N 48 14 8	E 14 15 11	269
WEL	Wels, Rathaus	N 48 9 23	E 14 1 29	317
<i>Intermediate</i>				
BRA	Braunau	N 48 15 40	E 13 2 41	351
GRI	Grieskirchen	N 48 14 4	E 13 49 33	336
FRE	Freistadt	N 48 30 33	E 14 30 7	512
MAT	Mattighofen	N 48 5 50	E 13 9 6	454
PAS	Pasching	N 48 15 31	E 14 12 36	292
VOE	Vöcklabruck	N 48 0 21	E 13 38 43	434
<i>Rural</i>				
BOD	Nationalpark Bodinggraben	N 47 47 31	E 14 23 38	641
FEU	Feuerkogel	N 47 48 57	E 13 43 15	1628
GIS	Giselawarte	N 48 23 3	E 14 15 11	902
GRU	Grünbach	N 48 31 50	E 14 34 30	918
KID	Kirchschlag-Davidschlag	N 48 26 31	E 14 16 26	813
KRI	Krippenstein	N 47 31 23	E 13 41 36	2067
LOS	Losenstein, Hohe Dirn	N 47 54 22	E 14 24 40	982
MUN	Münzkirchen	N 48 28 45	E 13 33 29	486
ULI	Ulrichsberg, Schöneben	N 48 42 20	E 13 56 44	935
ZOE	Nationalpark Zöbloden	N 47 50 18	E 14 26 28	899

that with increasing phase angle and altitude the illumination does not increase linear, but rather exponential, owed to the fact that the transmittance of the atmosphere is proportional to $e^{-\frac{\tau}{\cos(z)}}$, with τ being the optical depth and z the zenith distance. Some values which underline this can be found in Table 2. In fact, for zenithal positions, there is a factor ~ 8.4 in ground illumination between full and half moon. The large difference is caused by *coherent backscattering* or *opposition surge* (Hapke, Nelson & Smythe 1998). In this phenomenon, portions of waves travelling along same paths but in opposite directions, interfere constructively with each other, causing a peak at zero phase (full moon).

In case of full moon, the illuminance varies by a factor of ~ 166 between zenithal and horizontal positions. Please note that horizontal position, i.e. altitude of zero degrees, is valid for the centre of the lunar disc. Hence, a slight ground illumination is

visible and not zero. The resulting values can be considered as theoretical only, since every other possible light emitting source is neglected, even stars or the Milky Way are not taken into account. However, the model shows how the lunar position and its phase angle are associated with the consequential ground illumination.

3.1.2 Application of the illuminance model to one of our sites

We now apply the model to one of our sites, namely VOE. To do so, we first calculate for the years 2016–2017 the altitude and phase of the Moon at *midnight* and then derive the corresponding illuminance through the model. The result is shown in Fig. 3. A strong seasonal variation is recognized in the model, mainly caused by the changing altitude of the ecliptic (and thus the Moon) between summer and

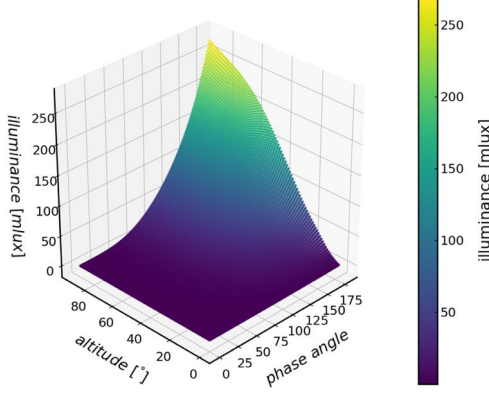


Figure 2. Results of the illuminance model as developed by Seidelmann (1992) for all phase angles and altitudes of the Moon.

Table 2. Resulting values of the theoretical Moon model for half and full moons. ALT is the lunar altitude, PA is the lunar phase angle, and G_{ILL} is the ground illumination caused only by moonlight.

ALT (°)	PA (°)	G_{ILL} (mlux)
0	90	0.192
0	180	1.622
45	90	19.474
45	180	164.059
90	90	31.949
90	180	269.153

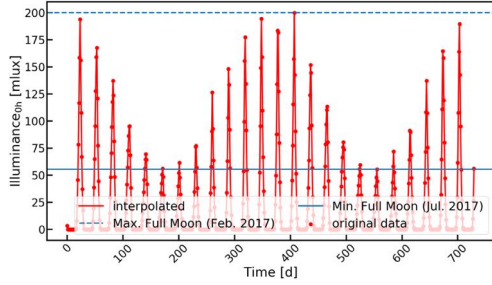


Figure 3. Ground illuminance (the Moon's contribution to it) evaluated for the location of Vöcklabruck, Upper Austria, over the years 2016–2017. The high-frequency lunar cycle is modulated with a seasonal variation caused by the seasonal change of the Moon's altitude.

winter, leading to a natural variation of the moon illuminance by a factor of ~ 3.6 (peak-to-peak for full moon).

3.2 Zenithal night sky model for the SQM band

3.2.1 The Cerro Paranal Advanced Sky Model

Using the *Cerro Paranal Advanced Sky Model* (Skycalc), we are able to compare our zenithal SQM measurements to a synthetic

Impact of light pollution on the lunar rhythm 2625

sky model that is cloud free and takes into account several sources of light such as scattered moonlight, starlight, molecular emission of the lower atmosphere, and the airglow (upper atmosphere).

Skycalc was published by Noll et al. (2012) and Jones et al. (2013), as part of an Austrian in-kind contribution to the European Southern Observatory (ESO), e.g. ESO's exposure time calculator is based on it. Skycalc's current version (2.0.4) also comes with a PYTHON-based command line interface.¹ However, the model used for our study is based on Skycalc 1.4.4, which was available through a web interface only. The main input parameters are zenith distance (or airmass) of the observation, precipitable water vapour (PWV), and monthly averaged solar flux. For the moon radiance component, the separation of Sun and Moon as seen from Earth, the Moon-target separation, moon altitude over horizon, and the Moon–Earth distance are needed.

We have decided to make some simplifications, allowing us to evaluate the model on a two-dimensional parameter grid with vectors of (Sun–Moon separation, moon altitude) only. This is reasonable in our case, because the measurement devices we are using, the SQMs of type SQM-LE, are equipped with a front lens that narrows down the field of view to a roughly 20° wide cone, pointed towards zenith. Hence, we only need to consider zenithal NSB. The two input parameters Moon-target separation and moon altitude can thus be simplified to one parameter, with the former one being the moon zenith distance. We have further decided to evaluate the model for a fixed PWV value of 5 mm, a monthly averaged solar flux of 130sfu and for a fixed mean Moon–Earth distance. These simplifications have practically no influence on our results, since ALAN's contribution to our SQM measurements is magnitudes larger than the natural variation caused by phenomena such as PWV or solar flux. However, variations due to moon phase and height are fully treated by our gridded model evaluation for the zenith. Since the natural, cloudless sky brightness changes smoothly, a grid spacing of one degree in both parameters (Sun–Moon separation, moon altitude) was found to be sufficient.

The result is a synthetic (cloud-free) night sky spectrum for the target location in units of $\text{photons s}^{-1} \text{m}^{-2} \mu\text{m}^{-1} \text{arcsec}^{-2}$, i.e. spectral radiance. We first convert to $\text{erg s}^{-1} \text{cm}^{-2} \text{\AA}^{-1} \text{arcsec}^{-2}$ and then multiply with the SQM transmission curve as published in Cinzano (2005) and shown in Fig. 1, together with transmission curves of Bessel *BVR* filters. The radiance within the SQM band is then calculated via integration over the wavelength axis. Using a zero-point (ZP) of -12.92 (Puschnig et al., in preparation), we finally convert to $\text{mag}_{\text{SQM}} \text{arcsec}^{-2}$ via equation (2).

$$\begin{aligned} \text{NSB} [\text{mag}_{\text{SQM}} \text{arcsec}^{-2}] \\ = -2.5 \times \log_{10}(\text{radiance} [\text{erg s}^{-1} \text{cm}^{-2} \text{arcsec}^{-2}]) + \text{ZP} \end{aligned} \quad (2)$$

Note that equation (2) results to a modelled zenithal sky brightness of $21.87 \text{ mag}_{\text{SQM}} \text{arcsec}^{-2}$ for new moon, which is in agreement with SQM observations of remote, rural sites (Posch et al. 2018; Bará et al. 2019; Bertolo et al. 2019). We further stress that the exact absolute value is not critical for the scientific results of the paper.

¹<https://www.eso.org/observing/etc/doc/skycalc/helpskycalccli.html>

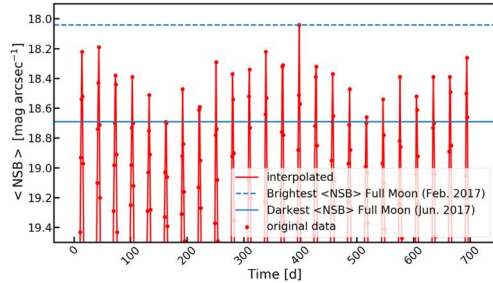


Figure 4. Skycalc sky model for the zenith, evaluated for one of our sites (VOE) for the years 2016–2017. The y-axis was limited to show only the bright peaks around full moon. Beside the circa-monthly oscillation, a seasonal variation is recognized, caused by changing altitude of the Moon between summer and winter.

3.2.2 Application of the Cerro Paranal Advanced Sky Model to one of our sites

Analogous to Section 3.1.2, we now evaluate the Skycalc model for one of our sites (VOE) that we use as a proxy for our network. We do so for the years 2016–2017. However, in this case we calculate for each night the mean NSB ($\langle \text{NSB} \rangle$) rather than just the value at midnight. The result is shown in Fig. 4. As for the illuminance model, a strong seasonal variation is recognized, that is mainly caused by the changing altitude of the Moon. However, the relative change between brightest and darkest $\langle \text{NSB} \rangle$ (18.04 versus 18.69 $\text{mag}_{\text{SQM}} \text{arcsec}^{-2}$) corresponds to a (linear scale) factor of 1.8 only, which is half the amplitude that is seen in the illuminance model. The main reason for this discrepancy lies in the fact that we evaluate the illuminance model at midnight only, i.e. at the point of maximum illumination, whereas for Skycalc we calculate the nightly means within dark-time limits. Given the fact that summer nights are shorter, the relative contribution of the full moon to the zenithal $\langle \text{NSB} \rangle$ is thus higher in summer than in winter and the dynamic range of the seasonal variation shrinks in that case.

4 DATA ANALYSIS

4.1 Fourier analysis

Using our 2-yr data of nightly mean $\langle \text{NSB} \rangle$ values, we aim to reveal the amplitude of the circalunar periodicity (and other periodic signals that might exist). Numerous implementations of discrete Fourier transforms exist, but probably the most common one is the Fast Fourier Transform (FFT), which we also use for the analysis of our SQM data. In particular, we apply the FFT algorithm as implemented in NUMPY (Van Der Walt, Colbert & Varoquaux 2011), the fundamental package for scientific computing with PYTHON. In the following, we describe some general properties of the FFT and highlight common obstacles of the method and how we treat them.

4.1.1 Which unit to choose?

The SQM delivers data in units of $\text{mag}_{\text{SQM}} \text{arcsec}^{-2}$. However, conversions into linear units are available, see equation (1). Thus, we investigate how well the amplitude of periodic variations such as the circalunar cycle caused by varying moon phases or the seasonal rhythm, that is driven by variations of the moon zenith distances

Table 3. We test the influence of single and double gaps on the ability to recover signal amplitudes from synthetic sky model data. The gap fraction in per cent is given in *column 1* and the recovered amplitudes of the circalunar and the seasonal variation are shown in *columns 2 and 3* for the single gap case, and *columns 5 and 6* for the double gap test. FFT Noise is given in *columns 4 and 7*. The unit for all measurements is $\text{mag}_{\text{SQM}} \text{arcsec}^{-2}$.

GF (1)	Single gap			Double gap		
	A (2)	S (3)	N (4)	A (5)	S (6)	N (7)
0	1.508	0.073	0.006	1.508	0.073	0.006
1	1.489	0.077	0.008	1.488	0.075	0.009
5	1.415	0.078	0.013	1.438	0.083	0.011
7.5	1.397	0.070	0.012	1.403	0.078	0.014
10	1.356	0.081	0.012	1.349	0.075	0.015
20	1.217	0.072	0.014	1.205	0.074	0.015
30	1.037	0.060	0.015	1.067	0.067	0.015
50	0.754	0.036	0.013	0.765	0.010	0.015

between summer and winter, are recovered in frequency space after application of the FFT in dependence of the data input unit.

For a linear input, the increase in zenithal NSB from new moon to full moon starts very shallow, almost unrecognizable. Then, few days before full moon, the increase accelerates to finally form a sharp peak in the (time, $\langle \text{NSB} \rangle$) plane (see Fig. A3). On the contrary, in logarithmic units such as $\text{mag}_{\text{SQM}} \text{arcsec}^{-2}$ the phase of the shallow increase is more pronounced (stretched in time) and the later steep increase somewhat compressed. Thus, the apparent course in the (time, $\langle \text{NSB} \rangle$) plane is rather smooth compared to linear units (see Fig. A2).

Since the FFT of a signal that is spread out in time delivers a compact result in frequency space and vice versa, logarithmic units such as $\text{mag}_{\text{SQM}} \text{arcsec}^{-2}$ are preferred, because the smoother course leads to a better definition of the circalunar cycle in frequency space, i.e. a single peak.

4.1.2 The role of gaps in $\langle \text{NSB} \rangle$ measurements

Gaps in SQM data series can occur due to several reasons, be it hardware or software failures or even meteorological conditions. In this section, we investigate how gaps in the time series affect the ability of the FFT algorithm to correctly reproduce amplitudes of time-dependent variations. We do so by introducing single and double gaps of varying lengths into our synthetic sky model. The recovered amplitudes of the circalunar and seasonal rhythm are then evaluated against the gap fraction, i.e. the fraction of data points on the equal-distant input time grid without measurement.

We stress that under all circumstances gaps should not be left as such, but replaced with some form of interpolation or reasonable value. We made tests using linear, quadratic, and cubic spline interpolations, as well as using the mean of the remaining data as fill value. We find that the latter one is the most robust and preferred method. Although cubic spline interpolation gives *slightly* better results for small gaps, i.e. when the gaps size is much smaller than the periodicity of the desired signal, it can cause unforeseen results for larger gaps.

Our results are summarized in Table 3, which shows that the single- and double-gap tests give very similar results: gap fractions of 1 per cent, 5 per cent, 7.5 per cent, and 10 per cent recover the amplitude of the circalunar variation (A) at levels of 99 per cent, 92–95 per cent, 91 per cent, and 87–88 per cent, respectively. Even

gap fractions of 20 per cent recover 75–77 per cent of the true amplitude.

The seasonal variation (S) is less affected, because of its longer periodic time. It can be accurately derived even for gap fractions of 20 per cent.

However, as described by Munteanu et al. (2016), for even larger periods of missing data, one should consider to perform spectral analysis using other algorithms such as the *Z transform* or the *Lomb–Scargle algorithm*. They might be able to reproduce the amplitude for cases where gaps make up more than 50 per cent of the time series.

Additionally, the presence of gaps in the time series leads to an increase of ‘frequency noise’ in the amplitude spectrum, limiting the chance to detect low-amplitude variations at certain frequencies. As shown in Table 3, the noise roughly doubles between 0 and 5 per cent gap fractions, but stays almost constant from thereon.

4.1.3 Importance of the length of the data series for FFTs

The length of a time series as well as its sampling rate are of importance for FFT studies, because they define the frequency resolution in the final amplitude spectrum.

Our sampling rate f_s is one measurement per night or $f_s = 1 \text{ d}^{-1}$. The distance δt between two data points is $\delta t = \frac{1}{f_s} = 1 \text{ d}$. The final frequency range is thus limited to the interval $[-\frac{f_s}{2}; +\frac{f_s}{2}]$, i.e. $-0.5 \dots 0.5 \text{ d}^{-1}$. The highest measurable frequency is 0.5 d^{-1} or 2 d periodic time. The number of discrete points N in the final frequency domain equals the number in time domain. Thus, the distance $\delta \nu$ in frequency space is $\delta \nu = \frac{f_s}{N}$, which shows that the frequency resolution is controlled by the sampling rate f_s and the length of the time series N . Since our sampling rate is fixed, the number of data points is the main quantity that drives the frequency resolution in our final amplitude spectrum.

For example, if we wanted to *detect* the frequency of the lunar synodic month (without prior knowledge), with an accuracy of 0.5 d, we would need at least 1711 data points, equivalent to 4.68 yr at a sampling rate of one measurement per night.

However, with prior knowledge of the period – in our case 29.5 d for the synodic month – one can adjust the time axis such that the final discrete amplitude spectrum covers the corresponding frequency, i.e. $\frac{1}{29.5} = 0.0339 \text{ d}^{-1}$. This is achieved by limiting the data points such that no discontinuities occur at the edges of the time series, i.e. spectral leakage (see next paragraph) is eliminated. That way, even time series of only 1 yr recover the amplitude on levels better than 90 per cent.

4.1.4 Avoiding spectral leakage

The ability of the FFT algorithm (and any other discrete Fourier transforms) to recover amplitudes is limited due to the fact that the duration of the observation is finite. This means that the input signal is factual a product with a rectangular window. The discrete spectrum of any finite signal is thus spread out over multiple frequency components and the amplitude is not fully recovered anymore. This behaviour is called *spectral leakage*.

However, the effect may be reduced by (1) avoiding discontinuities of the input signal or (2) gradually decreasing the amplitude of the signal towards the edges of the measurement series. The first method requires prior knowledge of the periodic time and phase of the signal of interest (which in most applications is not fulfilled). The latter case can be achieved by multiplying the input time series

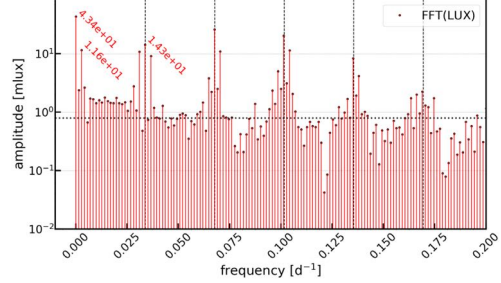


Figure 5. FFT amplitude spectrum of the illuminance model as described in Section 3.1. The shown frequency range is limited to values between 0 and 0.2. Note that the unit of the y-axis is milli-lux. Labelled amplitudes (from left to right) correspond to the mean of all input data, the seasonal variation, and the circalunar cycle.

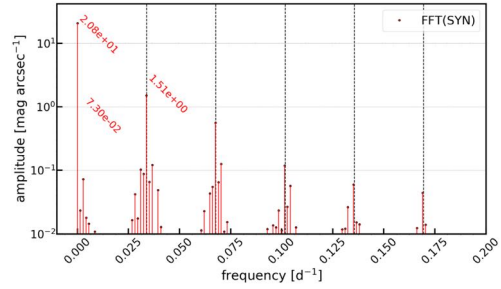


Figure 6. FFT amplitude spectrum of the Skycalc sky model as described in Section 3.2. The shown frequency range is limited to values between 0 and 0.2. Labelled amplitudes (from left to right) correspond to the mean $\langle \text{NSB} \rangle$ of the input data, the seasonal variation, and the circalunar cycle.

with a window function, e.g. a Hanning window, before the FFT is applied.

Since the periodicity of the synodic month is known, we could test both scenarios using sinusoidal and our synthetic sky time series as input. Although the application of a Hanning window improved amplitude recovery in cases where discontinuities occurred at the edges, we find that a continuous input time series (e.g. from first new moon 2016 to last new moon in 2017) gives best results with only negligible amounts of spectral leakage and amplitude recovery at levels better than 95 per cent. Thus, for our main science case, i.e. studying the circalunar rhythm, a continuous time series as input for the FFT is recommended and all our FFT analysis was performed using data from new moon 2016 January 9 to new moon 2017 December 18 only.

5 RESULTS

5.1 FFT analysis of the illuminance and Skycalc models

As a reference for our measurement sites, we perform an FFT analysis of our model data using the considerations from Section 4.1. To do so, for the Skycalc model we first calculate the nightly averages, i.e. $\langle \text{NSB} \rangle$, as described in Section 2. The resulting FFT amplitude spectra are shown in Figs 5 and 6.

An analysis of both models reveals significantly strong amplitudes at the frequency of $\frac{1}{29.5} = 0.0339 \text{ d}^{-1}$, i.e. the fundamental of the circalunar rhythm. Also its harmonics are identified at multiples of that frequency. However, the noise level in the illuminance model is higher because of its peak-like input (see Section 4.1.1).

We also note that the zero-frequency amplitude is not comparable between the models. While for the Skycalc model, the zero frequency is in fact a representation of the mean $\langle \text{NSB} \rangle$, this is not true for the illuminance model, because for the FFT analysis all input data with illuminance levels of 0 lux is considered as gaps and are thus filled with the mean in order to improve recognition of the circalunar rhythm as explained in Section 4.1.2.

It is also recognized that the seasonal variation seen in the amplitude spectrum of the illuminance model is stronger than in the Skycalc model. This is caused because we only consider midnight values for the illuminance model, while for the Skycalc model nightly averages are calculated. Hence, the contribution of the peak NSB at midnight is smoothed out in time due to averaging, while it is fully captured for midnight data. The averaging effect is even stronger in winter when the Moon's contribution to the zenithal $\langle \text{NSB} \rangle$ is highest, because then the nights are longer. The seasonal signal is thus equalized throughout the year.

5.2 Identifying the synodical month in the $\langle \text{NSB} \rangle$ data and quantifying its amplitude

From our SQM data, we first calculate the nightly averages, i.e. $\langle \text{NSB} \rangle$, as described in Section 2 and then perform an FFT analysis using the considerations from Section 4.1. That way, we can clearly detect the circalunar rhythm at all our sites (see Table 4), be it rural or urban. However, the amplitude decreases from 1.55 to $0.33 \text{ mags}_{\text{SQM}} \text{ arcsec}^{-2}$, corresponding to a factor of 3 on a linear scale, from the darkest to the brightest sites. A comparison between amplitude spectra of a typical urban and rural site is shown in Fig. 7.

It is also recognized that at rural sites, harmonics of the main variation at a frequency 0.0339 d^{-1} can be identified up to third order. In contrast, at urban sites, they perish in frequency noise, which increases with light pollution. In fact, the FFT noise roughly shows a bimodal distribution between rural and urban sites, as seen in Fig. 8. This is, because day-to-day variations are more pronounced at urban, light-polluted sites due to backscattering of ALAN at clouds (Kyba et al. 2011, 2012; Puschnig, Posch & Uttenthaler 2014a; Puschnig et al. 2014b; Aubé et al. 2016). Thus, the observed NSB typically jumps between two preferred values; see e.g. Posch et al. 2018, figs A1a, A1b, and 7). Since the noise as calculated here is dominated by high frequencies, i.e. roughly 64 per cent of the frequencies correspond to periodic times of equal or less than 5 d, the same bimodality is seen here.

Another interesting feature seen in Fig. 8 is that the scatter of the noise level increases along the $\langle \text{NSB} \rangle$ axis, i.e. darker sites show larger variance in the noise. The cause of this trend might be explained by findings of Kocifaj & Solano Lamphar (2014), who showed that the amplification factor due to clouds decreases with increasing city size and thus the level of light pollution.

5.3 Relation between the circalunar amplitude and zenithal $\langle \text{NSB} \rangle$ for mid-latitudes

Previous observations have already qualitatively shown, that the circalunar rhythm steadily fades away with an increasing level of anthropogenic light at night. Using our FFT analysis, we can now quantify how ALAN affects the lunar cycle's degree of recognition.

Table 4. Summary of recognized features in the FFT amplitude spectrum for 23 SQM stations and the synthetic sky model (SYN). *Column 1* is the station code, *columns 2 and 3*, the average night sky brightness from the peak at zero frequency in units of $10^{-5} \text{ W m}^{-2} \text{ sr}^{-1} \text{ } \mu\text{m}^{-1}$ and $\text{mags}_{\text{SQM}} \text{ arcsec}^{-2}$, respectively. The amplitude of the circalunar cycle in $\text{mags}_{\text{SQM}} \text{ arcsec}^{-2}$ is shown in *column 4* and the circalunar contrast CLC, i.e. the amplitude expressed in per cent of $\langle \text{NSB} \rangle$, is found in *column 5*. The amplitude of the seasonal variation (bright winters, dark summers in units of $\text{mags}_{\text{SQM}} \text{ arcsec}^{-2}$ is given in *column 6* and the noise in $\text{mags}_{\text{SQM}} \text{ arcsec}^{-2}$ in the last column.

COD (1)	$\langle \text{NSB} \rangle_{\text{w}}$ (2)	$\langle \text{NSB} \rangle_{\text{mag}}$ (3)	A (4)	CLC (5)	S (6)	N (7)
LGO	18.25	17.31	0.34	36.8	0.73	0.071
LSM	15.32	17.51	0.33	34.3	0.77	0.070
WEL	12.74	17.70	0.36	39.3	0.86	0.067
LSW	12.39	17.73	0.41	45.9	0.58	0.069
STW	10.31	17.93	0.45	50.0	0.49	0.069
TRA	8.90	18.09	0.46	52.8	0.55	0.061
STY	7.54	18.27	0.50	58.5	0.69	0.068
PAS	6.33	18.46	0.53	62.9	0.57	0.054
BRA	5.88	18.54	0.66	83.7	0.67	0.057
GRI	5.56	18.60	0.57	69.0	0.92	0.057
VOE	5.56	18.62	0.64	82.0	0.74	0.060
FRE	5.56	18.60	0.71	92.3	0.76	0.070
MAT	3.67	19.05	0.83	114.8	0.65	0.062
MUN	1.91	19.76	1.10	175.4	0.56	0.047
GIS	1.44	20.07	1.02	155.9	0.06	0.050
ULI	1.38	20.13	1.16	191.1	0.50	0.057
KID	1.12	20.37	1.19	204.8	0.09	0.040
GRU	1.07	20.39	1.34	243.6	0.38	0.036
FEU	0.84	20.66	1.22	207.6	0.07	0.057
LOS	0.83	20.86	1.30	243.6	0.01	0.059
KRI	0.73	20.81	1.16	191.1	0.07	0.049
ZOE	0.70	21.01	1.55	324.6	0.10	0.056
BOD	0.62	21.04	1.51	301.8	0.10	0.064
SYN	0.73	20.81	1.51	301.8	0.08	0.004

We do so by plotting the mean NSB, given by the amplitude at zero frequency, against the amplitude of the circalunar rhythm. The result is shown in the left-hand panel of Fig. 9. A linear fit (see equation 3) is found to be appropriate, with a scatter of only $0.062 \text{ mags}_{\text{SQM}} \text{ arcsec}^{-2}$. Extrapolation leads us to an $\langle \text{NSB} \rangle$ level of $16.5 \text{ mags}_{\text{SQM}} \text{ arcsec}^{-2}$, the level at which the circalunar rhythm practically vanishes (at zenith) and is indistinguishable from the polluted night sky.

$$A = 0.322 \langle \text{NSB} \rangle - 5.324 \quad (3)$$

We may also convert the amplitudes in linear units, e.g. to luminance (see equation 1), and then express the amplitude of the circalunar cycle as multiple of $\langle \text{NSB} \rangle$, which we denote as *circalunar contrast* (CLC). As shown in the right-hand panel of Fig. 9, the contrast between the average $\langle \text{NSB} \rangle$ level and the darkening/brightening due to new/full moon ranges between 30 and 300 per cent for our urban and rural sites, respectively.

5.4 Searching for other than lunar frequencies in the $\langle \text{NSB} \rangle$ data

As seen in Sections 3 and 5.1, a naturally occurring seasonal variation caused by the changing height of the ecliptic (and thus the Moon) is expected. In our measurements, however, for the darkest, rural stations (FEU, KRI, LOS, ZOE, BOD), we do not recover any such seasonal variation at a significant level (compare Table A1).

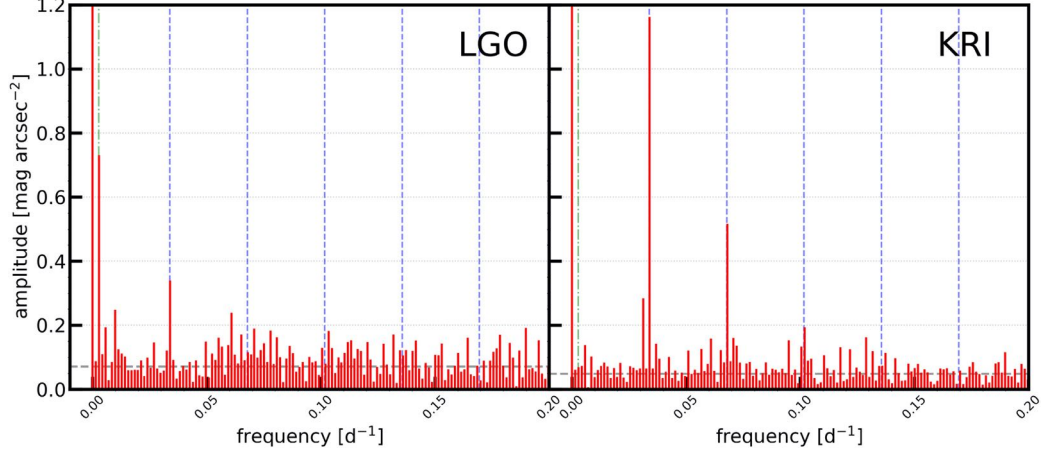


Figure 7. FFT amplitude spectrum of an urban (LGO) and rural (KRI) site. The shown frequency range is limited to values between 0 and 0.2 and the amplitude range is cut at $1.2 \text{ mag}_{\text{SQM}} \text{ arcsec}^{-2}$ in order to focus on amplitudes in the given frequency range, but excluding the peak at zero, i.e. the mean NSB.

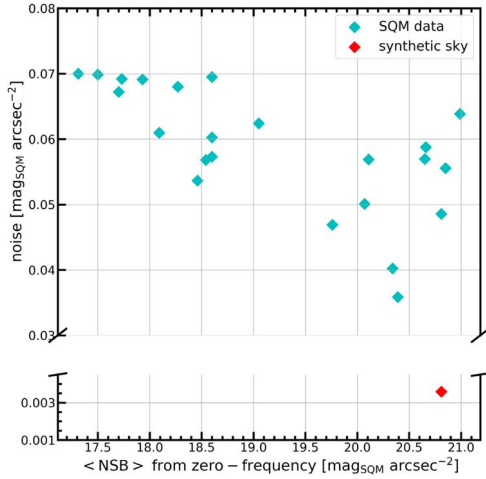


Figure 8. FFT noise increases with the level of light pollution.

This is mainly because our $\langle \text{NSB} \rangle$ data include overcast skies that weaken the amplitude of the signal in an unforeseeable way, and given the fact that we cover only 2 yr, the signal easily vanishes.

On the other side, we do detect a very strong seasonal variation at all urban and also at most intermediate stations (compare Table A1). However, the amplitude of that signal is too large to be caused by the Moon. This oscillation might be the result of climatological effects that enhance ALAN during winters, i.e. combined effects of increased surface albedo and lower vegetation state (Wallner & Kocifaj 2019). The observed seasonal variation might also be related to the aerosol optical depth (AOD). As demonstrated by Aubé (2015), the zenith radiance can increase several tens of times when optical depth is significantly lowered. However, disentangling the contribution of the several effects (surface albedo, vegetation,

AOD) is beyond the scope of this paper and would require ancillary data products.

At urban sites (LGO, LSM, WEL, LSW, STY, PAS, BRA, GRI, VOE, MAT), we further detect a significant ($>3\sigma$) signal with a periodic time of ~ 100 d. The cause of this roughly quarterly variation is unclear and was not reported previously. In our Table A1, we denote it as *unknown*.

We also search for weekly variations that might be associated with an increased human night-time activity on weekends. Although we do see at our urban stations amplitudes on the order of 0.15–0.20 $\text{mag}_{\text{SQM}} \text{ arcsec}^{-2}$, these are not significant ($<3\sigma$). Furthermore, its frequency is very close to that of the third lunar harmonic.

6 DISCUSSION AND CONCLUSION

Prior to a discussion of possible limitations of our method and implications of our findings in a wider context, we first compare our results to those of Bará (2016), who performed an SQM-based FFT analysis of 14 Galician stations using a 1-yr data set. Bará (2016) has previously defined the *moonlight factor* (y) as the ratio of *power densities* between the fundamental circalunar frequency and the zero frequency. Note that they used double-sided power density spectra, while we use single-sided amplitude spectra. The power spectra of Bará (2016) thus show negative and positive frequency components $k > 0$ with heights of $\frac{A_k^2}{4}$ compared to our amplitudes (A) in Table 4 and at a height of A_0^2 for the zero-frequency component ($\langle \text{NSB} \rangle_{\text{mag}}$). They reported ranges for the moonlight factor between $0.2\text{--}0.3 \times 10^{-3}$ for urban sites, $1.5\text{--}2.4 \times 10^{-3}$ for dark rural sites, and values in-between for intermediate regions. A compilation of the moonlight factor calculated for our sites is shown in Table 5. We find that the moonlight factor derived through our FFT methodology and data is almost a factor of 2 lower than those reported in Bará (2016). Although it is expected that the Moon's impact on zenithal NSBs in Galicia is stronger than in Upper Austria, because the Galician network's geographic latitude is lower by $\sim 5^\circ$ and thus the ecliptic and Moon closer to zenith, a factor of 2 seems to be relatively high. We argue that the relatively large difference is mainly caused because Bará (2016) takes into

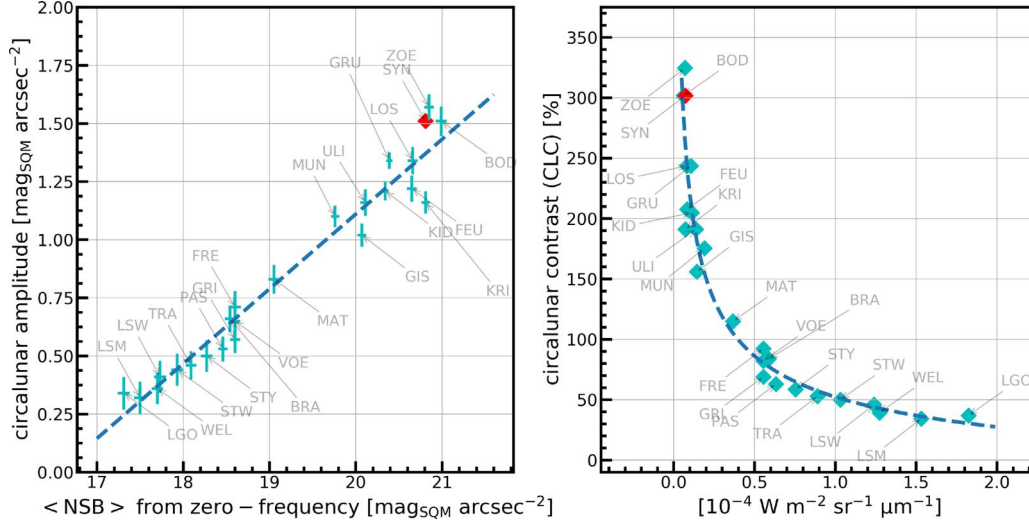


Figure 9. *Left-hand panel:* Relation between the circalunar amplitude and zenithal $\langle \text{NSB} \rangle$ for mid-latitudes ($\sim 48^\circ$). Individual points denote amplitudes derived through FFT analysis, with $\pm 1\sigma$ errors found from the noise in the FFT amplitude spectra. The data are in good agreement with a linear relation with a scatter of only $0.06 \text{ mag}_{\text{SQM}} \text{ arcsec}^{-2}$. The red point denotes amplitude and $\langle \text{NSB} \rangle$ for our synthetic Skycalc sky model. *Right-hand panel:* The same relation as shown in the left-hand panel, but converted to luminance using equation (1) and normalized to the moonless, zenithal luminance of the synthetic sky model, i.e. the contrast of the Moon's luminance at zenith against skyglow.

Table 5. Station codes and zero-frequency $\langle \text{NSB} \rangle$ in units of $\text{mag}_{\text{SQM}} \text{ arcsec}^{-2}$ are shown in columns 1 and 2. Calculations of the moonlight factor (y) as defined in Bará (2016) are given in column 3.

COD (1)	$\langle \text{NSB} \rangle$ (2)	$y \times 10^3$ (3)
<i>Urban</i>		
LGO	17.31	0.10
LSM	17.51	0.09
WEL	17.7	0.10
LSW	17.73	0.13
STW	17.93	0.16
TRA	18.09	0.16
STY	18.27	0.19
<i>Intermediate</i>		
PAS	18.46	0.21
BRA	18.54	0.32
GRI	18.6	0.23
VOE	18.62	0.30
FRE	18.6	0.36
MAT	19.05	0.47
<i>Rural</i>		
MUN	19.76	0.77
GIS	20.07	0.65
ULI	20.13	0.83
KID	20.37	0.85
GRU	20.39	1.08
FEU	20.66	0.87
LOS	20.86	0.97
KRI	20.81	0.78
ZOE	21.01	1.36
BOD	21.04	1.29
SYN	20.81	1.32

account NSB measurements obtained at midnight only rather than averaging over dark time hours as we do. As a result – in analogy to the explanation in Section 5.1 – for nightly averages peak values that occur at midnight are smoothed in time, which is also the reason why we do not capture the seasonal variation (compare Fig. 10). On the other hand, averaging over dark times has the advantage of providing a better definition and thus less scatter of the amplitudes over several months, because a single nightly measurement may easily be affected by short-term perturbations such as cloud cover, which may impact NSB measurements in a complex way: considering that backscattering of moonlight on scattered clouds (in zenith) exists in analogy to previous findings of Kyba et al. (2011, 2012) and Puschnig et al. (2014a, b), clouds may enhance the zenithal NSB on the one hand, but it may also lower the zenithal NSB on the other hand, e.g. for fully overcast skies, similar to previous findings of Posch, Binder & Puschnig (2018) and Jechow, Hölker & Kyba (2019).

However, recognition of the circalunar amplitude as performed by Bará (2016) is affected by spectral leakage that lowers the amplitude (compared to our approach) due to smearing out of the signal over multiple frequencies, as explained in Section 4.1.4. Additionally, Bará (2016) uses only 1-yr of input data, leading to lower frequency resolution and thus even more leakage, as explained in Section 4.1.3.

We conclude that a combination of these effects causes the factor 2 discrepancy, but we stress that the linear relation in Fig. 9, its intercept mainly, would not change by a factor 2 for geographic locations similar to those of the Galician network. This is shown in the following.

In principle, it is expected that the relation in Fig. 9 shifts towards lower circalunar amplitudes for geographic latitudes north of 48° and towards higher amplitudes otherwise. In order to assess how much the relation's intercept may shift, we perform FFT analysis

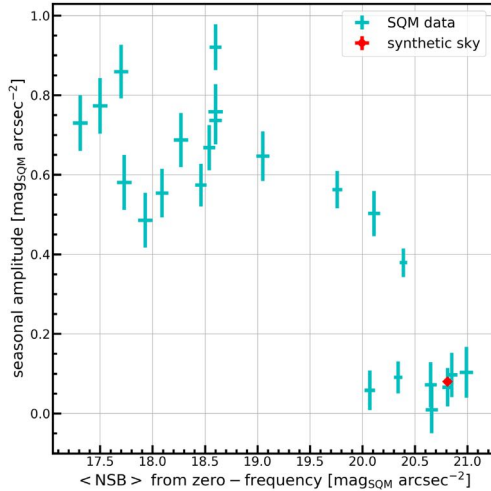


Figure 10. The amplitude of the seasonal oscillation against $\langle \text{NSB} \rangle$, both derived through FFT analysis of nightly $\langle \text{NSB} \rangle$ values. Each point corresponds to one of our SQM stations, with error bars indicating the $\pm 1\sigma$ errors found from the noise in the FFT amplitude spectrum. The red point shows the location of our synthetic Skycalc sky model, indicating that for our SQM network the amplitude of the naturally occurring seasonal variation due to the Moon (its seasonal change of altitude) has an amplitude of less than $0.1 \text{ mag}_{\text{SQM}} \text{ arcsec}^{-2}$, which is too low to be detectable within the frequency noise as we see in our FFT amplitude spectra. Thus, no clear trend or relation is identified. The strong seasonal amplitudes seen at urban sites are thus caused by other seasonal effects such as changing albedo or vegetation state between winter and summer (Puschign et al., in preparation).

of 2-yr Skycalc models calculated for different latitudes. For the first test, we choose a latitude of $N 36^\circ$ (e.g. Gibraltar). The derived amplitude of the circalunar cycle is $1.61 \text{ mag}_{\text{SQM}} \text{ arcsec}^{-2}$, which is only $\sim 0.1 \text{ mag}_{\text{SQM}} \text{ arcsec}^{-2}$ higher than for the synthetic models calculated for our network. For the second test, we choose a latitude of $N 60^\circ$ (e.g. slightly north of Stockholm). However, we caution that for latitudes above 51.5° , during summer there are no dark times with the Sun being more than 15° below the horizon. As a result, gaps in the input data limit the recoverability of the circalunar amplitude, as explained in Section 4.1.2. In that case, we thus find an amplitude of $1.02 \text{ mag}_{\text{SQM}} \text{ arcsec}^{-2}$ only, which is mainly due to the large summer gaps accounting for roughly 25 per cent of the input data. From these tests, we conclude that our relation between the circalunar amplitude and $\langle \text{NSB} \rangle$ is at least valid for latitudes between $\sim 40^\circ$ – 50° .

Our linear relation between zenithal $\langle \text{NSB} \rangle$ and the circalunar amplitude in Fig. 9 implies that the circa-monthly variation of moonlight is still traceable over large areas, not only in Upper Austria, but also in many other countries (compare light pollution atlas by Falchi et al. 2016). The circalunar rhythm is thus expected to practically vanish due to ALAN only in the innermost parts of major cities where the zenithal NSB may exceed $16.5 \text{ mag}_{\text{SQM}} \text{ arcsec}^{-2}$. However, at the same time, it is recognized that the contribution of the Moon to the total zenithal NSB (i.e. contrast) is largely reduced due to ALAN, namely by a factor of $\sim \frac{1}{9}$ for urban areas (e.g. Linz with $\sim 200\,000$ inhabitants), a factor of $\sim \frac{1}{3}$ for small towns with less than 10 000 inhabitants (e.g. Freistadt or Mattighofen) and

Impact of light pollution on the lunar rhythm 2631

still up to $\sim \frac{1}{2}$ for one of our rural stations (e.g. Münzkirchen, a village with less than 2600 inhabitants). Only two of our sites, both situated in national parks (Bodinggraben and Zöblboden), show natural circalunar amplitudes.

Finally, we discuss implications of the SQM's spectral bandpass that covers a range of ~ 300 – 680 nm . Although this is very close to the so-called *photosynthetically active radiation*, i.e. the spectral range between 400–700 nm to which photosynthetic organisms are sensitive, we caution that within that spectral range, chlorophyll – the most abundant plant pigment – has a sensitivity curve that is very different from the SQM's sensitivity curve shown in Fig. 1. Rather than being mostly sensitive to green photons, chlorophyll is mostly sensitive to red and blue photons. The exact degradation of the circalunar rhythm as recognized by photosynthetic organisms may thus be different from what we observe using SQMs. However, other species such as e.g. ocean fish, that have maximum spectral sensitivities between 500 and 550 nm (Marshall 2017) may recognize the degradation of the circalunar cycle exactly as described in our paper. How they are affected by a decreased amplitude of the circa-monthly signal is yet to be shown in future (chrono)biological studies.

7 SUMMARY

We studied the circalunar periodicity via FFT analysis of nighttime averages of zenithal NSB measurements obtained during the years 2016 and 2017 through a network of 23 SQMs located in Upper Austria at a latitude of $\sim 48^\circ$. Models of the sky (Noll et al. 2012; Jones et al. 2013) and the Moon (Seidelmann 1992) were used as a reference of ideal conditions and to develop an optimal methodology for the recognition of the circalunar periodicity. The following conclusions are drawn from our study:

- (i) A tight linear relation between $\langle \text{NSB} \rangle$ given in $\text{mag}_{\text{SQM}} \text{ arcsec}^{-2}$ and the circalunar amplitude is found (see Fig. 9). This relation indicates that for sites with $\langle \text{NSB} \rangle$ brighter than $16.5 \text{ mag}_{\text{SQM}} \text{ arcsec}^{-2}$, the lunar rhythm practically vanishes. This finding implies that the circalunar rhythm is still detectable (within the broad bandpass of the SQM) at most places around the globe.
- (ii) However, the circalunar contrast in zenith is largely reduced compared to ALAN-free sites. In the state capital of Linz ($\sim 200\,000$ inhabitants), the Moon's contribution to zenithal $\langle \text{NSB} \rangle$ is reduced by a factor of $\frac{1}{9}$. For small towns (e.g. Freistadt or Mattighofen) with less than 10 000 inhabitants, we find that the circalunar contrast in zenith is lowered by a factor of $\frac{1}{3}$ due to ALAN and even at one of our rural sites, Münzkirchen, a village with less than 2600 inhabitants, the circalunar zenithal contrast is reduced to a level of $\frac{1}{2}$ compared to ALAN-free conditions.
- (iii) Only two of our sites, both situated in national parks (Bodinggraben and Zöblboden), show natural circalunar amplitudes.
- (iv) At our urban sites, we further detect a strong seasonal signal that is linked to the amplification of anthropogenic skyglow during the winter months due to combined effects of enhanced albedo (due to snow) and a lower vegetation state (Puschign et al., in preparation).
- (v) At urban sites, we further detect a significant ($>3\sigma$) signal with a periodic time of $\sim 100 \text{ d}$. The cause of this roughly quarterly variation is unclear and was not reported previously.

ACKNOWLEDGEMENTS

We dedicate this work to Thomas Posch, our most valued colleague, mentor, and dearest friend, who passed away during the develop-

ment phase of this manuscript. This paper would have never been written without Thomas, as it was him who first introduced Johannes and Stefan to this stunning field of research many years ago. He will be missed by us, not only because of his expertise and keen mind, but also because of his cordiality.

We acknowledge support by the provincial government of Upper Austria, in particular we thank Heribert Kaineder and Martin Waslmaier for their dedication and tireless efforts to establish a network of SQMs in Upper Austria, and share the data with the public.

We are grateful to the referee for his/her constructive input.

This research further made use of SCIPY (Jones et al. 2001) and NUMPY (Van Der Walt et al. 2011), two PYTHON packages that make life as a scientist easier.

REFERENCES

- Aubé M., 2015, *Phil. Trans. R. Soc. B*, 370, 20140117
- Aubé M., Kocifaj M., Zamorano J., Lamphar H. S., de Miguel A. S., 2016, *J. Quant. Spectrosc. Radiat. Transfer*, 181, 11
- Bará S., 2016, *R. Soc. Open Sci.*, 3, 160541
- Bará S., 2017, *Int. J. Sustainable Light*, 19, 104
- Bará S., Tapia C. E., Zamorano J., 2019, *Sensors*, 19, 1336
- Ben-Atia M., Reinberg A., Smolensky M. H., Gadacha W., Khedaier A., Sani M., Toutou Y., Boughammi N. G., 2016, *Chronobiol. Int.* 33, 419
- Bertolo A., Binotto R., Ortolani S., Sapienza S., 2019, *J. Imaging*, 5, 56
- Bünning E., Moser I., 1969, *Proc. Natl. Acad. Sci. U.S.A.*, 62, 1018
- Cajochen C., Altanay-Ekici S., Münch M., Frey S., Knoblauch V., Wirz-Justice A., 2013, *Curr. Biol.* 23, 1485
- Cajochen C., Altanay-Ekici S., Münch M., Frey S., Knoblauch V., Wirz-Justice A., 2014, *Curr. Biol.*, 24, R795
- Cinzano P., 2005, Technical report, Night Sky Photometry with Sky Quality Meter, Istituto di Scienza e Tecnologia dell'Inquinamento Luminoso, Thiene, Italy
- Clarke J. A., 1983, *Behav. Ecol. Sociobiol.*, 13, 205
- Cordi M. et al., 2014, *Curr. Biol.*, 24, R549
- Dacke M., Byrne M. J., Baird E., Scholtz C. H., Warrant E. J., 2011, *Phil. Trans. R. Soc. B*, 366, 697
- Davies T. W., Bennie J., Inger R., Gaston K. J., 2013, *Sci. Rep.*, 3, 1722
- Falchi F. et al., 2016, *Sci. Adv.*, 2, E1600377
- Fallows C., Fallows M., Hammerschlag N., 2016, *Environ. Biol. Fishes*, 99, 805
- Fox H. M., Gardiner J. S., 1924, *Proc. R. Soc. London. B*, 95, 523
- Frisch K. v., 1994, *The Dance Language and Orientation of Bees*. Harvard University Press, Cambridge, MA
- Garstang R. H., 1986, *PASP*, 98, 364
- Gaston K. J., Visser M. E., Hölker F., 2015, *Phil. Trans. R. Soc. B*, 370, 20140133
- Hapke B., Nelson R., Smythe W., 1998, *Icarus*, 133, 89
- Hölker F., Wolter C., Perkin E. K., Tockner K., 2010, *Trends Ecol. Evol.*, 25, 681
- Jechow A., Hölker F., Kyba C. C. M., 2019, *Sci. Rep.*, 9, 1391
- Jones A., Noll S., Kausch W., Szyszka C., Kimeswenger S., 2013, *A&A*, 560, A91
- Jones E. et al., 2001, SciPy: Open source scientific tools for Python, <http://www.scipy.org/>
- Kocifaj M., Solano Lamphar H. A., 2014, *MNRAS*, 443, 3665
- Kolb H. H., 1992, *J. Zool.*, 228, 661
- Kronfeld-Schor N., Daominoni D., De la Iglesia H., Levy O., Herzog E. D., Dayan T., Helfrich-Forster C., 2013, *Proc. R. Soc. B*, 280, 20123088
- Kyba C. C. M., Ruhtz T., Fischer J., Hölker F., 2011, *PLoS One*, 6, 1
- Kyba C. C. M., Ruhtz T., Fischer J., Hölker F., 2012, *MNRAS*, 425, 701
- Kyba C. C. M. et al., 2015, *Sci. Rep.*, 5, 8409
- Last K. S., Hobbs L., Berge J., Brierley A. S., Finlo C., 2016, *Curr. Biol.*, 26, 244
- Law S. P., 1986, *Acta Obstet. Gynecol. Scand.*, 65, 45
- Manfrin A. et al., 2017, *Front. Environ. Sci.*, 5, 61
- Marshall J., 2017, *Curr. Biol.*, 27, R494
- Munteanu C., Negrea C., Echim M., Mursula K., 2016, *Ann. Geophys.*, 34, 437
- Noll S., Kausch W., Barden M., Jones A. M., Szyszka C., Kimeswenger S., Vinther J., 2012, *A&A*, 543, A92
- Papi F., Pardi L., 1963, *Biol. Bull.*, 124, 97
- Posch T., Binder F., Puschnig J., 2018, *J. Quant. Spectrosc. Radiat. Transfer*, 211, 144
- Puschnig J., Posch T., Uttenthaler S., 2014a, *J. Quant. Spectrosc. Radiat. Transfer*, 139, 64
- Puschnig J., Schwöpe A., Posch T., Schwarz R., 2014b, *J. Quant. Spectrosc. Radiat. Transfer*, 139, 76
- Raible F., Takekata H., Tessmar-Raible K., 2017, *Front. Neurol.*, 8, 189
- Reinberg A., Smolensky M. H., Toutou Y., 2016, *Chronobiol. Int.*, 33, 465
- Schroer S., Hölker F., 2016, *Impact of Lighting on Flora and Fauna*. Springer International Publishing, Cham, Switzerland, p. 1
- Seidelmann P. K., 1992, *Explanatory Supplement to the Astronomical Almanac*. University Science Books, Mill Valley, California
- Shimose T., Yokawa K., Tachihara K., 2013, *Bull. Mar. Sci.*, 89, 759
- Takemura A., Ueda S., Hiyakawa N., Nikaido Y., 2006, *J. Pineal Res.*, 40, 236
- Van Der Walt S., Colbert S. C., Varoquaux G., 2011, *Comput. Sci. Eng.*, 13, 22
- Wallner S., Kocifaj M., 2019, *J. Quant. Spectrosc. Radiat. Transfer*, 239, 106648
- Zantke J. et al., 2013, *Cell Rep.*, 5, 99
- Zimecki M., 2006, *Postepy Hig Med Dosw. (Online)*, 60, 1

APPENDIX A

Impact of light pollution on the lunar rhythm 2633

Table A1. Summary of significant ($\frac{S}{N} > 3$) peaks in the FFT amplitude spectra. No windowing function was applied, instead we truncated the input time series at the edges in order to avoid discontinuities with respect to the lunar synodic month. That way, the circalunar amplitude could be recovered with highest accuracy. However, other amplitudes such as the one attributed to the seasonal variation are only lower limits in most cases. We found that the application of a Hanning window leads to an increase of the seasonal amplitude between 0.05 and 0.1 mags_{QM} arcsec⁻².

COD (1)	ν (2)	T (3)	A (4)	S/N (5)	Note (6)	COD (1)	ν (2)	T (3)	A (4)	S/N (5)	Note (6)
LGO	0.00e+00	inf	17.31	244.0	Mean	BRA	0.00e+00	inf	18.54	326.3	Mean
LGO	2.82e-03	353.0	0.73	10.3	Seasonal	BRA	2.82e-03	354.0	0.67	11.8	Seasonal
LGO	9.92e-03	100.9	0.24	3.4	Unknown	BRA	5.65e-03	177.0	0.18	3.2	Seasonal (1st harm.)
LGO	3.40e-02	29.4	0.34	4.7	Circalunar	BRA	9.89e-03	101.1	0.19	3.3	Unknown
LGO	6.09e-02	16.4	0.24	3.3		BRA	3.39e-02	29.5	0.66	11.7	Circalunar
						BRA	6.07e-02	16.5	0.17	3.1	
LSM	0.00e+00	inf	17.51	250.6	Mean	BRA	6.78e-02	14.8	0.30	5.3	Circalunar (1st harm.)
LSM	2.82e-03	354.0	0.77	11.1	Seasonal	BRA	7.06e-02	14.2	0.19	3.3	
LSM	5.65e-03	177.0	0.24	3.4	Seasonal (1st harm.)	BRA	7.77e-02	12.9	0.19	3.3	
LSM	9.89e-03	101.1	0.24	3.5	Unknown	BRA	1.03e-01	9.7	0.17	3.0	Circalunar (2nd harm.)
LSM	3.39e-02	29.5	0.33	4.8	Circalunar						
LSM	6.07e-02	16.5	0.24	3.4		FRE	0.00e+00	inf	18.60	267.6	Mean
						FRE	2.82e-03	354.0	0.76	10.9	Seasonal
WEL	0.00e+00	inf	17.70	263.2	Mean	FRE	3.39e-02	29.5	0.71	10.2	Circalunar
WEL	2.82e-03	354.0	0.86	12.8	Seasonal	FRE	6.78e-02	14.8	0.27	3.9	Circalunar (1st harm.)
WEL	5.65e-03	177.0	0.22	3.3	Seasonal (1st harm.)	FRE	7.06e-02	14.2	0.23	3.3	
WEL	9.89e-03	101.1	0.21	3.1	Unknown						
WEL	3.39e-02	29.5	0.36	5.4	Circalunar	GRI	0.00e+00	inf	18.60	324.6	Mean
WEL	6.07e-02	16.5	0.21	3.1		GRI	1.42e-03	706.0	0.18	3.1	
						GRI	2.83e-03	353.0	0.92	16.1	Seasonal
LSW	0.00e+00	inf	17.73	256.2	Mean	GRI	5.67e-03	176.5	0.20	3.5	Seasonal (1st harm.)
LSW	2.82e-03	354.0	0.58	8.4	Seasonal	GRI	9.92e-03	100.9	0.19	3.2	Unknown
LSW	9.89e-03	101.1	0.24	3.5	Unknown	GRI	2.69e-02	37.2	0.17	3.0	
LSW	3.39e-02	29.5	0.41	6.0	Circalunar	GRI	3.40e-02	29.4	0.57	10.0	Circalunar
LSW	6.07e-02	16.5	0.23	3.3		GRI	6.09e-02	16.4	0.18	3.2	
LSW	7.06e-02	14.2	0.21	3.1		GRI	6.80e-02	14.7	0.27	4.7	Circalunar (1st harm.)
						GRI	1.03e-01	9.7	0.17	3.0	Circalunar (2nd harm.)
STW	0.00e+00	inf	17.93	259.4	Mean	VOE	0.00e+00	inf	18.62	309.0	Mean
STW	2.82e-03	353.0	0.49	7.0	Seasonal	VOE	2.82e-03	354.0	0.74	12.2	Seasonal
STW	3.40e-02	29.4	0.45	6.5	Circalunar	VOE	9.89e-03	101.1	0.20	3.3	Unknown
STW	6.09e-02	16.4	0.23	3.3		VOE	2.12e-02	47.2	0.18	3.0	
STW	7.08e-02	14.1	0.24	3.5		VOE	3.39e-02	29.5	0.64	10.6	Circalunar
						VOE	6.78e-02	14.8	0.32	5.3	Circalunar (1st harm.)
TRA	0.00e+00	inf	18.09	296.7	Mean	VOE	7.06e-02	14.2	0.23	3.8	
TRA	2.82e-03	354.0	0.55	9.1	Seasonal	VOE	7.77e-02	12.9	0.24	3.9	
TRA	3.39e-02	29.5	0.46	7.5	Circalunar	VOE	1.03e-01	9.7	0.18	3.0	Circalunar (2nd harm.)
TRA	6.07e-02	16.5	0.20	3.3		MAT	0.00e+00	inf	19.05	305.3	Mean
TRA	6.78e-02	14.8	0.21	3.4	Circalunar (1st harm.)	MAT	2.83e-03	353.0	0.65	10.4	Seasonal
TRA	7.06e-02	14.2	0.21	3.5		MAT	9.92e-03	100.9	0.25	3.9	Unknown
						MAT	3.40e-02	29.4	0.83	13.3	Circalunar
STY	0.00e+00	inf	18.27	268.6	Mean	MAT	6.52e-02	15.3	0.24	3.9	
STY	2.82e-03	354.0	0.69	10.1	Seasonal	MAT	6.80e-02	14.7	0.32	5.1	Circalunar (1st harm.)
STY	9.89e-03	101.1	0.23	3.3	Unknown	MAT	7.08e-02	14.1	0.22	3.6	
STY	3.39e-02	29.5	0.50	7.4	Circalunar	MAT	7.79e-02	12.8	0.23	3.8	
STY	6.07e-02	16.5	0.21	3.1		MAT	1.78e-01	5.6	0.19	3.1	
STY	6.78e-02	14.8	0.23	3.5	Circalunar (1st harm.)						
STY	7.06e-02	14.2	0.21	3.1		MUN	0.00e+00	inf	19.76	421.4	Mean
STY	7.77e-02	12.9	0.24	3.6		MUN	2.82e-03	354.0	0.56	12.0	Seasonal
						MUN	3.39e-02	29.5	1.10	23.4	Circalunar
PAS	0.00e+00	inf	18.46	344.1	Mean	MUN	3.67e-02	27.2	0.14	3.0	
PAS	2.82e-03	354.0	0.57	10.7	Seasonal	MUN	6.50e-02	15.4	0.16	3.5	
PAS	5.65e-03	177.0	0.16	3.0	Seasonal (1st harm.)	MUN	6.78e-02	14.8	0.45	9.6	Circalunar (1st harm.)
PAS	9.89e-03	101.1	0.17	3.2	Unknown	MUN	7.06e-02	14.2	0.24	5.1	
PAS	3.39e-02	29.5	0.53	9.9	Circalunar	MUN	1.02e-01	9.8	0.19	4.1	Circalunar (2nd harm.)
PAS	6.07e-02	16.5	0.17	3.2							
PAS	6.50e-02	15.4	0.17	3.1							
PAS	6.78e-02	14.8	0.24	4.5	Circalunar (1st harm.)						
PAS	7.06e-02	14.2	0.18	3.4							

2634 *J. Puschnig, S. Wallner and T. Posch*

Table A1 – continued

COD (1)	ν (2)	T (3)	A (4)	S/N (5)	Note (6)	COD (1)	ν (2)	T (3)	A (4)	S/N (5)	Note (6)
GIS	0.00e+00	inf	20.07	400.5	Mean	FEU	0.00e+00	inf	20.66	362.6	Mean
GIS	1.42e-03	706.0	0.21	4.2		FEU	3.11e-02	32.2	0.20	3.5	
GIS	5.67e-03	176.5	0.18	3.6	Seasonal (1st harm.)	FEU	3.39e-02	29.5	1.22	21.5	Circularunar
GIS	7.08e-03	141.2	0.21	4.1		FEU	3.67e-02	27.2	0.19	3.4	
GIS	8.50e-03	117.7	0.23	4.7		FEU	6.78e-02	14.8	0.60	10.5	Circularunar (1st harm.)
GIS	1.13e-02	88.2	0.16	3.3		FEU	7.06e-02	14.2	0.23	4.0	
GIS	1.27e-02	78.4	0.18	3.7		FEU	1.02e-01	9.8	0.24	4.2	Circularunar (2nd harm.)
GIS	1.42e-02	70.6	0.18	3.6		FEU	1.24e-01	8.0	0.19	3.3	
GIS	1.56e-02	64.2	0.18	3.7							
GIS	1.84e-02	54.3	0.17	3.3		KRI	0.00e+00	inf	20.81	428.6	Mean
GIS	2.55e-02	39.2	0.18	3.6		KRI	3.12e-02	32.1	0.28	5.8	
GIS	3.12e-02	32.1	0.18	3.6		KRI	3.40e-02	29.4	1.16	23.9	Circularunar
GIS	3.40e-02	29.4	1.02	20.3	Circularunar	KRI	6.09e-02	16.4	0.16	3.2	
GIS	6.80e-02	14.7	0.47	9.4	Circularunar (1st harm.)	KRI	6.80e-02	14.7	0.51	10.6	Circularunar (1st harm.)
GIS	7.08e-02	14.1	0.30	6.0		KRI	7.08e-02	14.1	0.16	3.2	
GIS	1.02e-01	9.8	0.19	3.7	Circularunar (2nd harm.)	KRI	9.49e-02	10.5	0.15	3.1	
						KRI	1.02e-01	9.8	0.19	3.9	Circularunar (2nd harm.)
						KRI	1.29e-01	7.8	0.16	3.3	
ULI	0.00e+00	inf	20.13	353.8	Mean						
ULI	2.83e-03	353.0	0.50	8.8	Seasonal						
ULI	8.50e-03	117.7	0.19	3.3		LOS	0.00e+00	inf	20.86	355.1	Mean
ULI	1.13e-02	88.2	0.18	3.1		LOS	1.27e-02	78.7	0.20	3.4	
ULI	1.56e-02	64.2	0.21	3.7		LOS	2.40e-02	41.6	0.21	3.5	
ULI	2.12e-02	47.1	0.25	4.3		LOS	3.11e-02	32.2	0.24	4.0	
ULI	2.83e-02	35.3	0.18	3.1		LOS	3.39e-02	29.5	1.30	22.0	Circularunar
ULI	3.12e-02	32.1	0.29	5.2		LOS	3.67e-02	27.2	0.20	3.5	
ULI	3.40e-02	29.4	1.16	20.4	Circularunar	LOS	6.78e-02	14.8	0.56	9.5	Circularunar (1st harm.)
ULI	3.97e-02	25.2	0.21	3.8		LOS	7.06e-02	14.2	0.31	5.2	
ULI	6.52e-02	15.3	0.19	3.4							
ULI	6.66e-02	15.0	0.18	3.1		ZOE	0.00e+00	inf	21.01	378.2	Mean
ULI	6.80e-02	14.7	0.45	7.9	Circularunar (1st harm.)	ZOE	1.55e-02	64.4	0.17	3.1	
ULI	7.08e-02	14.1	0.20	3.5		ZOE	1.98e-02	50.6	0.25	4.5	
						ZOE	3.39e-02	29.5	1.55	28.0	Circularunar
						ZOE	3.67e-02	27.2	0.39	7.1	
KID	0.00e+00	inf	20.37	506.3	Mean	ZOE	3.81e-02	26.2	0.20	3.7	
KID	7.06e-03	141.6	0.14	3.6		ZOE	3.95e-02	25.3	0.19	3.5	
KID	9.89e-03	101.1	0.14	3.5	Unknown	ZOE	6.78e-02	14.8	0.62	11.2	Circularunar (1st harm.)
KID	1.27e-02	78.7	0.14	3.5		ZOE	7.06e-02	14.2	0.28	5.1	
KID	1.55e-02	64.4	0.14	3.4							
KID	1.84e-02	54.5	0.13	3.3		BOD	0.00e+00	inf	21.04	329.6	Mean
KID	2.54e-02	39.3	0.17	4.3		BOD	5.62e-03	178.0	0.20	3.1	
KID	3.11e-02	32.2	0.14	3.4		BOD	9.36e-03	106.8	0.23	3.5	
KID	3.39e-02	29.5	1.19	29.6	Circularunar	BOD	2.81e-02	35.6	0.20	3.1	
KID	3.67e-02	27.2	0.20	5.0		BOD	3.18e-02	31.4	0.23	3.6	
KID	6.50e-02	15.4	0.12	3.1		BOD	3.37e-02	29.7	1.51	23.6	Circularunar
KID	6.78e-02	14.8	0.52	13.0	Circularunar (1st harm.)	BOD	3.56e-02	28.1	0.48	7.6	
KID	7.06e-02	14.2	0.25	6.3		BOD	3.93e-02	25.4	0.34	5.3	
KID	1.02e-01	9.8	0.20	4.9	Circularunar (2nd harm.)	BOD	6.74e-02	14.8	0.56	8.7	Circularunar (1st harm.)
KID	1.34e-01	7.5	0.12	3.0	Circularunar (3rd harm.)	BOD	6.93e-02	14.4	0.29	4.5	
GRU	0.00e+00	inf	20.39	568.6	Mean	BOD	7.49e-02	13.3	0.20	3.1	
GRU	2.83e-03	353.0	0.38	10.6	Seasonal	BOD	9.74e-02	10.3	0.23	3.6	
GRU	3.12e-02	32.1	0.17	4.6		BOD	1.01e-01	9.9	0.20	3.1	Circularunar (2nd harm.)
GRU	3.26e-02	30.7	0.13	3.6							
GRU	3.40e-02	29.4	1.34	37.3	Circularunar						
GRU	3.68e-02	27.2	0.28	7.7							
GRU	6.52e-02	15.3	0.19	5.3							
GRU	6.80e-02	14.7	0.53	14.8	Circularunar (1st harm.)						
GRU	7.08e-02	14.1	0.23	6.4							
GRU	1.02e-01	9.8	0.15	4.1	Circularunar (2nd harm.)						
GRU	1.05e-01	9.5	0.11	3.1							

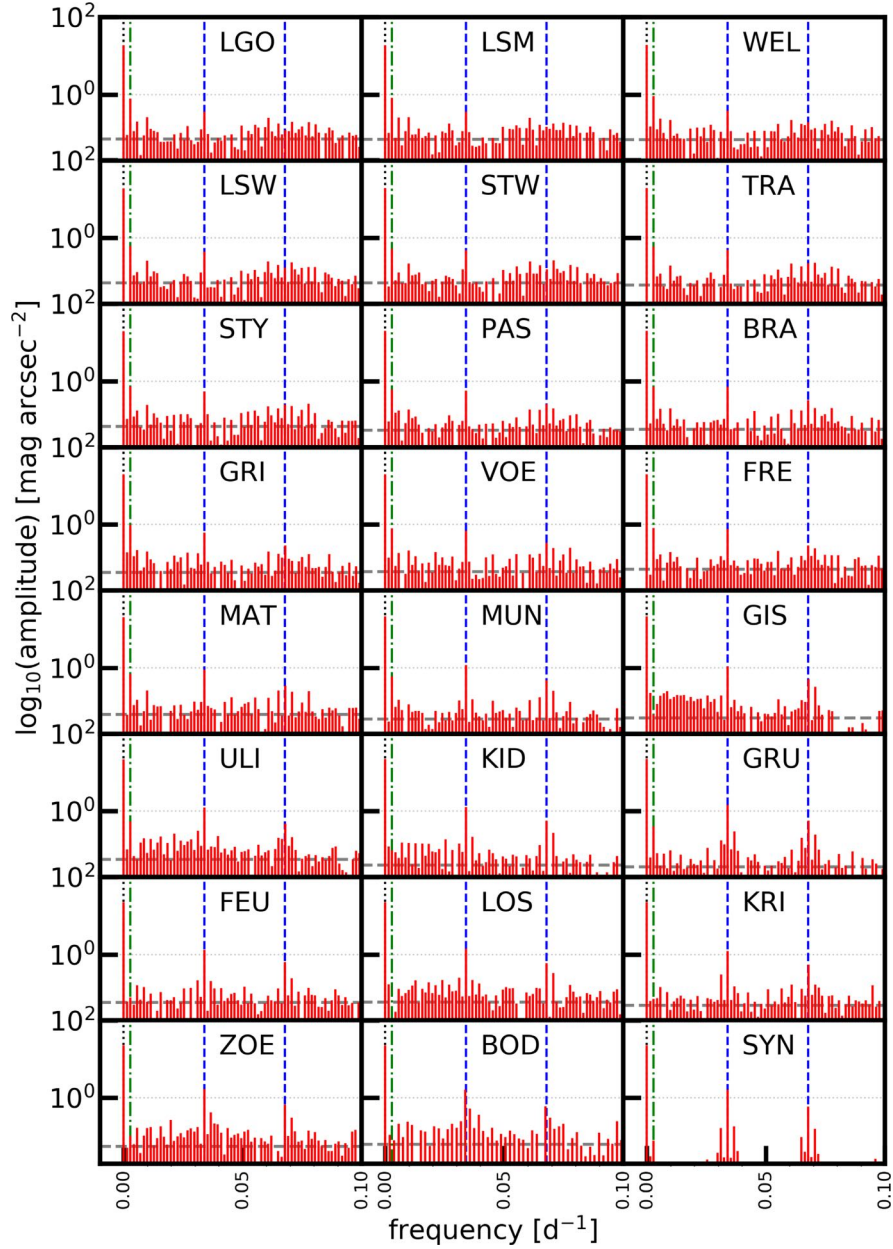


Figure A1. The panels show cutouts of the FFT amplitude spectra ranging from 0 to 0.1 d^{-1} for 23 locations in Upper Austria, sorted by increasing $\langle \text{NSB} \rangle$ values, i.e. decreasing light pollution. The amplitude spectra were obtained from a 2 yr long data set (2016–2017) of nightly $\langle \text{NSB} \rangle$ values. For comparison, an amplitude spectrum of a cloud-free synthetic sky model as described in Section 3.2 is shown in the bottom right panel (SYN). The peak at zero frequency, i.e. $\langle \text{NSB} \rangle$, is indicated by a black dotted line, the seasonal variation $\frac{1}{365} \text{ d}^{-1}$ is marked with a green dash-dotted line, the expected lunar synodic frequency of $\frac{1}{29.5} \text{ d}^{-1}$ and its first harmonic are marked with blue, dashed lines and the mean noise level is shown as horizontal dashed line.

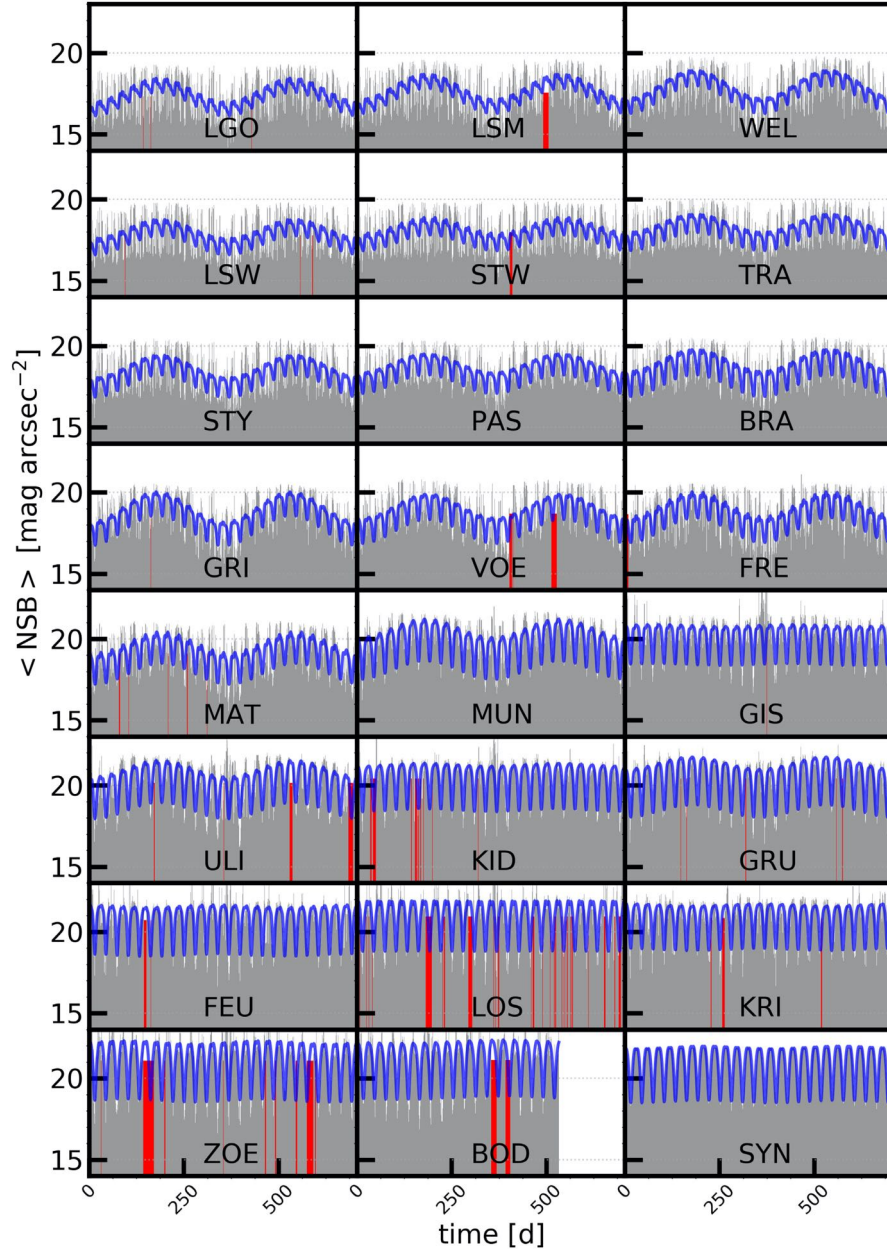


Figure A2. The grey shaded areas in the panels show $\langle \text{NSB} \rangle$ time series for 2016 and 2017 obtained from 23 SQM stations in Upper Austria and from a cloud-free synthetic sky model (SYN) as described in Section 3.2. On top of that, the result of an inverse FFT (iFFT) of identified frequency components is shown as blue line. The iFFT frequencies correspond to the mean brightness level, the circalunar rhythm plus its first two harmonics as well as a yearly cycle, i.e. bright winters and dark summers. This cycle is driven by an increase of overcast skies during the winter months and an amplification of light pollution by clouds. Data gaps that were set to the mean $\langle \text{NSB} \rangle$ value are marked in red.

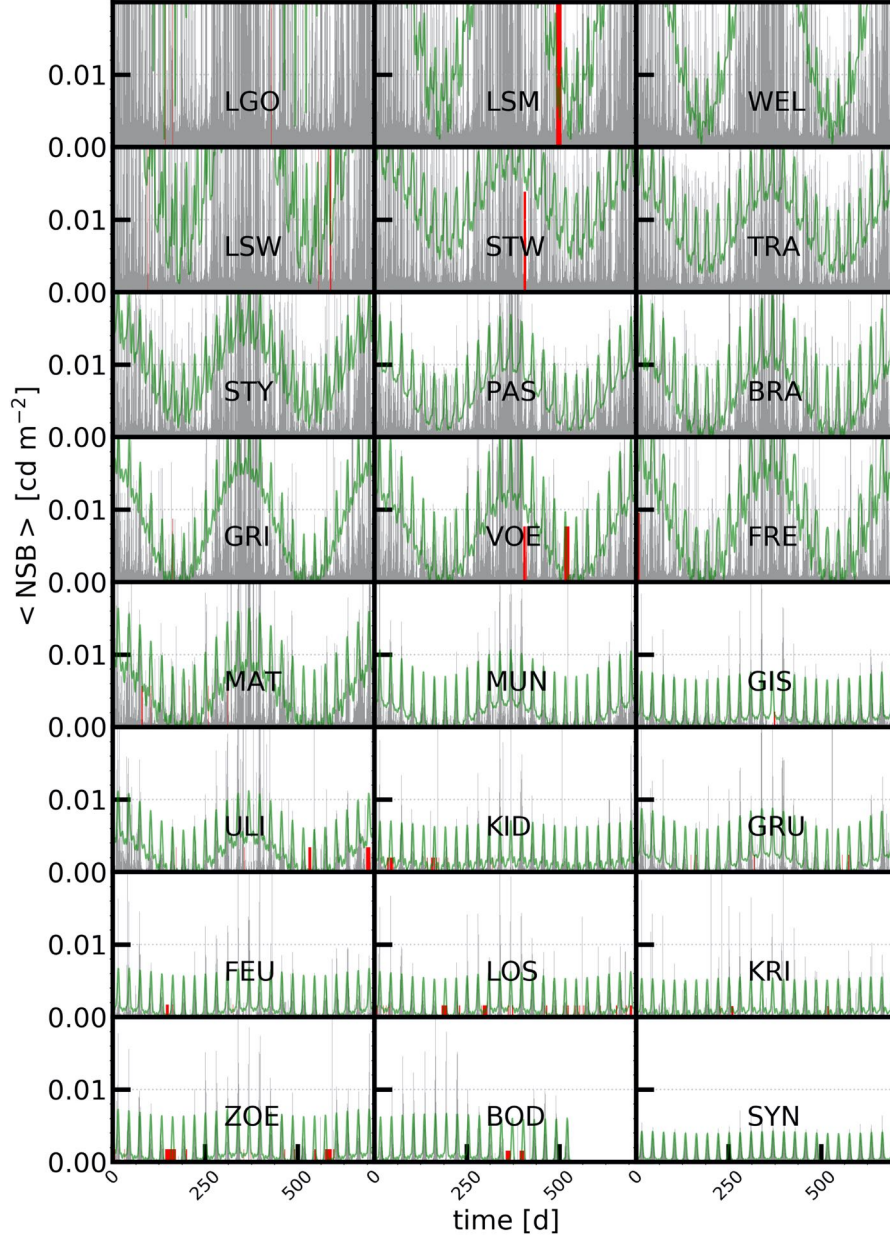


Figure A3. The grey shaded areas in the panels show $\langle \text{NSB} \rangle$ time series for 2016 and 2017 obtained from 23 SQM stations in Upper Austria and from a cloud-free synthetic sky model (SYN) as described in Section 3.2. On top of that, the result of an inverse FFT (iFFT) of identified frequency components is shown as blue line. The iFFT frequencies correspond to the mean brightness level, the circalunar rhythm plus its first two harmonics as well as a yearly cycle, i.e. bright winters and dark summers. This cycle is driven by an increase of overcast skies during the winter months and an amplification of light pollution by clouds. Data gaps that were set to the mean $\langle \text{NSB} \rangle$ value are marked in red.

This paper has been typeset from a \LaTeX file prepared by the author.

4.5 'Night sky imaging as potential tool for characterization of total lumen output from small and medium-sized cities'

Title: *Night-sky imaging as a potential tool for characterization of total lumen output from small and medium-sized cities*

Authors: S. Wallner¹, M. Kocifaj¹, L. Komar, H. A. Solano-Lamphar

Journal: Monthly Notices of the Royal Astronomical Society (MNRAS)

Status: Published in MNRAS 494, 5008-5017 (2020)

DOI: <https://doi.org/10.1093/mnras/staa925>

Personal contribution: My contribution in this paper was the execution of measurements, the analysis via suitable software, and the adoption of the theoretical model as discussed to those observations. As co-first author, I was responsible for data collection and input as provided from all authors involved, wrote the majority of the paper and, also as correspondent author, accountable for the submission and revision process.

¹Co-first authorship



Night-sky imaging as a potential tool for characterization of total lumen output from small and medium-sized cities

S. Wallner^{1,2★†}, M. Kocifaj^{2,3★†}, L. Komar² and H. A. Solano-Lamphar^{2,4}

¹Department of Astrophysics, University of Vienna, Türkenschanzstrasse 17, 1180 Vienna, Austria

²ICA, Slovak Academy of Sciences, Dúbravská Road 9, 845 03 Bratislava, Slovak Republic

³Department of Experimental Physics, Faculty of Mathematics, Physics, and Informatics, Comenius University, Mlynská dolina, 842 48 Bratislava, Slovak Republic

⁴Cátedras CONACYT, CentroMet, INFOTEC, Avenida San Fernando 37, Toriello Guerra, 14050 Ciudad de México, México

Accepted 2020 March 30. Received 2020 March 30; in original form 2020 February 16

ABSTRACT

In this article, the asymptotic formula developed in past work and applied to predict skyglow due to distant sources was evolved, with the objective of characterizing small and medium-sized cities in the observer's surroundings. To enable this, a combination of theoretical computations and in situ measurements is needed, aiming to distinguish between dominant and smaller light-emitting sources, with the latter usually being camouflaged when measuring the night sky. Furthermore, for numerical modelling of skyglow, few of the most important parameters, specifically the amount of total lumens installed and radiated to the upward hemisphere, can be derived. Astronomical observatories, in particular, can profit from this concept, since they are usually situated far away from large cities but can still be surrounded by smaller villages and towns. We present a detailed description of how theoretical computations are combined with all-sky photometry in order to obtain the properties mentioned. Results are compared with satellite data, showing that, regarding approximations undertaken for processing, they are comparable, underlining the functionality of our approach. The idea of including in situ observations enables us to quantify the impact of small and medium-sized cities globally and independent of location, as long as measurements were conducted outside light domes. In addition, the presented work may be of major interest to the light-pollution community if conducting long-term observations of cities, since the quality of commonly used satellite data is going to decrease in the future, due to blindness in short wavelengths and upcoming conversions of public lighting systems to blue-enlightened LEDs.

Key words: scattering – atmospheric effects – light pollution – methods: observational – software: simulations.

1 INTRODUCTION

Light pollution has become a global issue, due to its increasingly dominant and diverse effects on nature and living organisms. Over the past decade, awareness of artificial light propagating into the nocturnal environment has increased (Luginbuhl et al. 2009; Aubé 2015; Kocifaj 2018). Today, one can study the impact of various lighting situations, e.g. street lighting, on skyglow under different conditions (Kinzey et al. 2017), with further focus on various influences, such as the spectral composition of light emission (Luginbuhl et al. 2014) and its development over time (Kyba et al. 2017), the directionality of urban beams (Solano-Lamphar 2018) or the relative contribution of a variety of sources (Bará et al. 2019). Furthermore, past works have shown that meteorological phenomena like clouds can change skyglow levels significantly (Jechow et al. 2017), having an even greater impact on urban ecosystems (Kyba et al. 2011). Beside wildlife, artificial light at night can specifically exert influence on human health in terms of circadian clocks and photoperiodism (Gaston et al. 2013), but, in addition, can also induce a physiological response in wild plants (Bennie et al. 2016), with unknown potentially negative impacts on their phenology or growth

* E-mail: stefan.wallner@univie.ac.at (SW); kocifaj@savba.sk (MK)

† Co-first authorship: the two authors have contributed equally to the article.

Lumen output in night-sky imaging 5009

form, to name only a few examples out of the many existing. Moreover, daily observational astronomical work suffers, since light sources on the ground are impairing the visibility of our night skies and thus faint objects become barely visible. The prediction of skyglow variation in different territories is therefore of great importance from a nature conservation and human health perspective.

Among light-source spectral power distributions and their optical distortion due to light scattering and absorption phenomena in the atmospheric environment, the total light output of a city is a key element in all skyglow modelling tools. The amount of light radiated towards the upper hemisphere is critical to evaluate the resulting impacts from skyglow on living organisms, due to providing a variety of sensitivities and threshold levels in their perception of light intensities (see e.g. Perkin et al. 2011). Although satellite data can provide information on upward directed light, the large amount escaping the urban area in other directions and at other angles is largely unknown. Therefore, the light output contributing to skyglow is difficult, or rather impossible, to infer solely from satellite observations. Some estimates are possible using information on the total power consumption. As an example, Joseph et al. (1991) inferred the light output from street lighting of Tel Aviv based on the average power consumption of the luminaires used and evaluated the upward light intensity in photons per second. Light-output appraisal was also performed in a similar way for the city of Vienna, taking into account the total power consumption of the city's street lighting system (Puschig, Posch & Uttenthaler 2014). However, this approach can only provide approximate values for total lumen outputs, while contributions coming from other light sources, e.g. vehicles, residential lighting, wall-mounted security lighting or the floodlights used in sports stadiums, are excluded from such derivations (even if they are likely equally important). In most cases, the number of total lumens installed is only known for a small number of cities, due to having a publicly unavailable or incomplete inventory of light sources. Consequently, there is a strong need for the development of an efficient technique to quantify the lumen output, which is applicable to many cities and independent of whether official statistics for public illumination are available or not. Duriscoe, Luginbuhl and Elvidge (2014) used satellite data obtained by the *Suomi-NPP* Visible Infrared Imaging Radiometer (VIIRS) as inputs to compute the frequently used Garstang (1986) model, in order to predict the total lumens of outdoor lighting from an anthropogenic sky luminance observed at locations on the ground. A new approximate formula simulating the night-sky brightness at intermediate and larger distances from light sources has been derived only recently (Kocifaj, Wallner and Solano-Lamphar 2019) and is used here to characterize light emissions in terms of total lumen outputs. The formula appeared useful, not only to estimate the amount of light escaping from dominant cities but also to save significant computational resources when modelling skyglow over a large territory. A retrieval method based on the aforementioned formula is preferred, primarily because the detection technique is performed rapidly, the experimental equipment is low-priced and there is no requirement for satellite data. However, use of the formula for mid-sized cities remains largely unexamined. The method introduced here requires measurements of the sky brightness (whatever unit is selected, i.e. radiometric for radiance or photometric for luminance) along a vertical plane crossing the hemisphere in the azimuthal position of a city. Such data are usually difficult to interpret if acquired toward a medium-sized (satellite) city, due to the optical signal potentially being compounded by the superposition of light emission from both the small or medium-sized city and a dominant city in its vicinity. The key issue behind the new technique is whether the contribution from these smaller cities/towns can be displayed individually, with the aim of assessing their total output emission in lumens or Watts. Astronomical observatories, in particular, are usually located far away from large cities to keep their influence on sky brightness low. Still, smaller light-emitting sources, like villages or towns, can be situated around them and possibly evolve to increase their impact on skyglow. Consequently, it is of great importance for observatories to characterize small and medium-sized cities and distinguish their long-term development independent of other dominating or larger light sources. This article addresses the above question and reports that success may be achieved with the proper combination of in situ optical measurements, theoretical analysis and numerical modelling. The theoretical model we have developed in 2019 is designed to simulate both radiometric and photometric variables (see the discussion below and equation 16 in Kocifaj et al. 2019). In the present study, the data recorded comprise night-sky luminance, but we also use the more common term 'brightness' or the radiometric term 'radiance' wherever it is needed.

2 SKY LUMINANCE AT LARGE DISTANCES FROM A LIGHT SOURCE

It has been shown by Kocifaj et al. (2019) that night-sky luminance due to a ground-based light source (city or town) can be approximated for intermediate and/or long distances D by the formula

$$J(z) = I_0 \frac{9}{32\pi} \frac{\tilde{\tau} e^{-D\tilde{\tau}/(3\tilde{H})}}{\mu \tilde{H} D} \left\{ Ci(aD) \sin(aD) + \left[\frac{\pi}{2} - Si(aD) \right] \cos(aD) \right\}, \quad (1)$$

where z is the observational zenith angle, $\mu = \cos(z)$, I_0 the luminance of a city normalized to its area, i.e. the city interpreted as a point light source (I_0 is measured in cd or lm sr^{-1}). The functions $Si(x)$ and $Ci(x)$ introduced above are sine and cosine integrals, respectively (Press et al. 2007). The argument x is the product of distance D and parameter a , with

$$a = \frac{\tilde{\tau}}{\tilde{H}} \left(1 + \frac{\tilde{\mu}_0}{\mu} \right), \quad (2)$$

where μ_0 is the mean effective cosine of the emission angle (see section 2 of Kocifaj et al. 2019) and \tilde{H} is the altitude up to which a homogeneous atmosphere would extend. Here we assume that \tilde{H} is composed of the weighed contributions of molecular and aerosol constituents, i.e.

$$\tilde{H} = \frac{H_R \tilde{\tau}_R + H_a \tilde{\tau}_a}{\tilde{\tau}_R + \tilde{\tau}_a}, \quad (3)$$

5010 *S. Wallner et al.*

where $\tilde{\tau}_R$ and $\tilde{\tau}_a$ are the Rayleigh and aerosol components of the total optical depth of a cloudless atmosphere except for ozone or water-vapour absorption bands, i.e. $\tilde{\tau} = \tilde{\tau}_R + \tilde{\tau}_a$ (Utrillas et al. 2000). Here, H_R and H_a are the Rayleigh and aerosol components of the atmospheric scaleheights. Aerosol scaleheight typically ranges from 1–3 km (Wu et al. 2011), while $H_R = 8$ km is a commonly accepted value in many studies (see e.g. Waquet et al. 2009). The emission function for a city, i.e. the luminous intensity emitted by that city, is generally unknown, so an isotropic-like radiator appears to be a useful zero-order approximation, resulting in the following formula:

$$J(z) = W_0 \frac{9}{64\pi^2} \frac{\tilde{\tau} e^{-D\tilde{\tau}/(3\tilde{H})}}{\mu \tilde{H} D} \left\{ Ci(aD) \sin(aD) + \left[\frac{\pi}{2} - Si(aD) \right] \cos(aD) \right\}, \quad (4)$$

where W_0 (lm) is the total amount of lumens directed above the horizontal; consequently, it is obtained as a superposition of both direct emission upwards and isotropic reflection from the ground. If the entirety of light approaching the sky is due only to diffuse reflection from the ground, then $W_0 = G \cdot W_0^{\text{installed}}$, where G is the diffuse reflectance and $W_0^{\text{installed}}$ is the total lumen output from all light sources in the city.

A potential error in $J(z)$ can result from imperfections of the approximate theoretical model, or from uncertainty in some key parameters, such as W_0 and μ_0 , which are notoriously unknown. The optical thickness $\tilde{\tau}$ and/or scaleheight \tilde{H} can be either measured or inferred by indirect methods. Nevertheless, these parameters are only known with limited accuracy, because the aerosol content is highly variable in time and can change significantly with the point of observation. Such variability links to atmospheric processes, including their dynamics, chemistry, humidity, turbulence, etc. The correct procedure to treat the errors in $J(z)$ is to combine the errors of particular variables in quadrature, i.e.

$$\Delta J(z) = \sqrt{\left(\frac{\partial J}{\partial W_0} \Delta W_0 \right)^2 + \left(\frac{\partial J}{\partial \tilde{\tau}} \Delta \tilde{\tau} \right)^2 + \left(\frac{\partial J}{\partial \tilde{H}} \Delta \tilde{H} \right)^2 + \left(\frac{\partial J}{\partial \mu_0} \Delta \mu_0 \right)^2}. \quad (5)$$

After a bit of manipulation, we obtain

$$\left(\frac{\Delta J}{J} \right)^2 = \left(\frac{\Delta W_0}{W_0} \right)^2 + \left(\frac{\Delta \tilde{\tau}}{\tilde{\tau}} \right)^2 \left[\left(1 - \frac{\tilde{\tau} D}{3\tilde{H}} \right) + \eta(aD) \right]^2 + \left(\frac{\Delta \tilde{H}}{\tilde{H}} \right)^2 \left[\left(\frac{\tilde{\tau} D}{3\tilde{H}} - 1 \right) - \eta(aD) \right]^2 + \left(\frac{\Delta \mu_0}{\mu_0} \right)^2 \left[\frac{\eta(aD) \mu_0 \tilde{\tau} D}{aD \mu \tilde{H}} \right]^2. \quad (6)$$

Here,

$$\eta(x) = x \frac{Ci(x) \cos x - \left[\frac{\pi}{2} - Si(x) \right] \sin x}{Ci(x) \sin x + \left[\frac{\pi}{2} - Si(x) \right] \cos x} \quad (7)$$

is valid for an arbitrary x . For large values of x , the function of $\eta(x)$ approaches asymptotically to -1 , so ΔJ_V relative to the theoretical luminance J_V , as derived equivalently to equation (6), would read

$$\left(\frac{\Delta J_V}{J_V} \right)_{aD>5} \cong \sqrt{\left(\frac{\Delta W_0}{W_0} \right)^2 + \left(\frac{\tilde{\tau} D}{3\tilde{H}} \right)^2 \left[\left(\frac{\Delta \tilde{\tau}}{\tilde{\tau}} \right)^2 + \left(\frac{\Delta \tilde{H}}{\tilde{H}} \right)^2 \right] + \left(\frac{\Delta \mu_0}{\mu_0} \right)^2 \left(\frac{\mu_0}{\mu + \mu_0} \right)^2}. \quad (8)$$

The above formula is applicable to sky luminance observed from intermediate or large distances (for $aD > 5$). Normally, the main goal is to estimate the error of luminous flux W_0 , using the experimental data of sky luminance (J_V). The upper threshold for the error of W_0 , analogously to equation (8), is defined as

$$\frac{\Delta W_0}{W_0} = \sqrt{\left(\frac{\Delta J_V}{J_V} \right)_{aD>5}^2 + \left(\frac{\tilde{\tau} D}{3\tilde{H}} \right)^2 \left[\left(\frac{\Delta \tilde{\tau}}{\tilde{\tau}} \right)^2 + \left(\frac{\Delta \tilde{H}}{\tilde{H}} \right)^2 \right] + \left(\frac{\Delta \mu_0}{\mu_0} \right)^2 \left(\frac{\mu_0}{\mu + \mu_0} \right)^2}. \quad (9)$$

Note that aerosol optical depth is by far the greatest modulator of \tilde{H} , so we can easily find from equation (3) that

$$\left(\frac{\Delta \tilde{H}}{\tilde{H}} \right)^2 = \left(\frac{H_a}{\tilde{H}} - 1 \right)^2 \left(\frac{\Delta \tau_a}{\tilde{\tau}} \right)^2. \quad (10)$$

The Rayleigh component (τ_R) of the atmospheric optical depth at the ground is known to vary only slightly with air pressure and temperature, so $\Delta \tau_R \ll \Delta \tau_a$. Therefore, the uncertainty in the total optical depth is due mostly to uncertainty in its aerosol component, i.e. $\Delta \tilde{\tau} \cong \Delta \tau_a$. Then equation (9) transforms to the new form

$$\frac{\Delta W_0}{W_0} = \sqrt{\left(\frac{\Delta J_V}{J_V} \right)_{aD>5}^2 + \left(\frac{\Delta \tau_a}{\tilde{\tau}} \right)^2 \left(\frac{\tilde{\tau} D}{3\tilde{H}} \right)^2 \left[1 + \left(\frac{H_a}{\tilde{H}} - 1 \right)^2 \right] + \left(\frac{\Delta \mu_0}{\mu_0} \right)^2 \left(\frac{\mu_0}{\mu + \mu_0} \right)^2}. \quad (11)$$

Taking into account that H_a is typically less than half of \tilde{H} , the relative error $\Delta W_0/W_0$ never exceeds the value

$$\frac{\Delta W_0}{W_0} = \sqrt{\left(\frac{\Delta J_V}{J_V} \right)_{aD>5}^2 + \left(\frac{\Delta \tau_a}{\tilde{\tau}} \right)^2 \left(\frac{\tilde{\tau} D}{2\tilde{H}} \right)^2 + \left(\frac{\Delta \mu_0}{\mu_0} \right)^2 \left(\frac{\mu_0}{\mu + \mu_0} \right)^2}. \quad (12)$$

Lumen output in night-sky imaging 5011

On the one hand, the theoretical derivations in Kocifaj et al. (2019) dictate that the above equations cannot be used at short distances from a light source. On the other hand, it also follows from the second term under the square root of equation (12) that the error in ΔW_0 increases as D approaches very large values. Consequently, the optimum conditions to retrieve W_0 can be achieved if luminance data are captured at an intermediate distance, i.e. at D satisfying the condition $(\bar{\tau} D / 2\bar{H}) < 1$. In such a case, the relative error due to aerosol optical depth uncertainty is smaller than that due to potential measurement errors of J_V (comparing the first and second terms under the square root of equation 12). The data need to be collected under clear-sky conditions and ideally when the atmospheric turbidity is low. For a clear-sky optical depth of approximately $\bar{\tau} \approx 0.2$ at the scotopic peak and $\bar{H} \approx 5$ km, the above condition dictates $D < 50$ km. Assuming the luminance data are taken at distances of a few tens of kilometres from a city, the aforementioned second term in equation (12) becomes negligible compared with other terms. As an example, for $D = 20$ km the square of $\bar{\tau} D / 2\bar{H}$ is 0.16, resulting in a weighting factor of aerosol uncertainty six times smaller than that of the first term on the right-hand side of equation (12). The scaling parameter μ_0 is unknown and has to be obtained from the least-squares method (Kocifaj et al. 2019), and the relative error $\Delta\mu_0/\mu_0$ is computed from the sample standard deviation by matching modelled and observed data. The inequality $\mu_0/(\mu + \mu_0) < 1$ is valid for all combinations of μ_0 and μ , because both of these parameters range from 0–1. Therefore, we easily find that

$$\frac{\Delta W_0}{W_0} \leq \sqrt{\left(\frac{\Delta J}{J}\right)^2_{aD>5} + \left(\frac{\Delta \tau_a}{\bar{\tau}}\right)^2 + \left(\frac{\Delta \mu_0}{\mu_0}\right)^2}. \quad (13)$$

The relation

$$\frac{\Delta W_0}{W_0} \leq 0.2 \quad (14)$$

can be applied, if the relative error of the measured luminance data is below 10 per cent and the same is valid for the sample standard deviation and optical depth uncertainty, respectively. The error margin of lumen output retrieval would be reduced to less than 10 per cent, with input data showing an uncertainty within 5 per cent. Nevertheless, the optical depth is frequently unknown or inferred from the visibility using Koschmieder theory (Molnár et al. 2016). The following formula that links aerosol optical depth τ_a at a specific wavelength λ and visibility V has been introduced by Wu et al. (2014):

$$\tau_a = \left(\frac{3.912}{V} - 0.0116\right) \left(\frac{0.55}{\lambda}\right)^{2-\nu} [H_1 (e^{-h/H_1} - e^{-5.5/H_1}) + 12.5e^{-5.5/H_1} + H_2 e^{-5.5/H_1}], \quad (15)$$

where h is the station altitude, $H_1 = 0.866 + 0.222V$, $H_2 = 3.77$ km, $\lambda = 0.55 \mu\text{m}$ and ν is the so-called Ångström exponent (Wagner and Silva 2008), being most typically $\nu = 3$. The value of 3.912 is known as the Koschmieder constant for a distant target contrast equal to 0.02, a common reference value for the human detection threshold (Horvath 1995). The estimation of the limiting magnitude of visibility is too subjective for an individual observer, thus provoking potentially large errors in determination of τ_a . It is therefore not unlikely that $\Delta\tau_a/\tau_a$ could be as large as some tens of per cent. Assuming the same applies to $\Delta\mu_0/\mu_0$, the uncertainty in the total lumen output can rise up to 40 per cent or even more. Indeed, such an error margin yields a useful outcome, considering the fact that lumen outputs (W_0) for two different cities can differ by several orders of magnitude. Consequently, an estimate of W_0 within several tens of per cent of its correct value can generally be regarded as a suitable result.

3 DERIVATION OF THE INFLUENCE CAUSED BY SMALL/MEDIUM-SIZED CITIES

The great challenge we face is to distinguish between effects from possible existing dominating light-emitting sources and smaller ones. However, to model the night-sky brightness (NSB) distribution in all zenith angles z and azimuth angles A due solely to dominant light sources, we found that

$$NSB(z, A) = G(z) \sum_{i=1}^N J_i S(\theta_i) \quad (16)$$

can easily be used for N number i of light-emitting sources at all scattering angles θ_i . $G(z)$ describes the gradation function, which depends exclusively on zenith angle and atmospheric transmission function, with the latter being related to the optical depth. Furthermore, J_i is the brightness (luminance or radiance) of the i th source of light. As derived in Kittler, Kocifaj and Darula (2012), the scattering indicatrix $S(\theta)$ is defined as

$$S_i(\theta) \propto 1 + c_1 \{e^{d\theta} - e^{d\pi/2}\} + c_2 \cos^2 \theta, \quad (17)$$

with c_1 , c_2 and d being scaling constants. Equipped with substantial knowledge of azimuths A_i of all i apparent light sources, the scattering angles, as illustrated in Fig. 1, can be computed as

$$\cos(\theta_i) = \sin(z) \cos(A - A_i). \quad (18)$$

5012 *S. Wallner et al.*

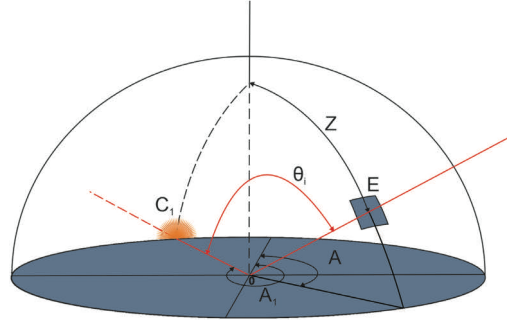


Figure 1. The spherical geometry, where scattering angle θ_i is the angle between the radius vector of the light source (OC_1) and the direction towards a sky element (OE).

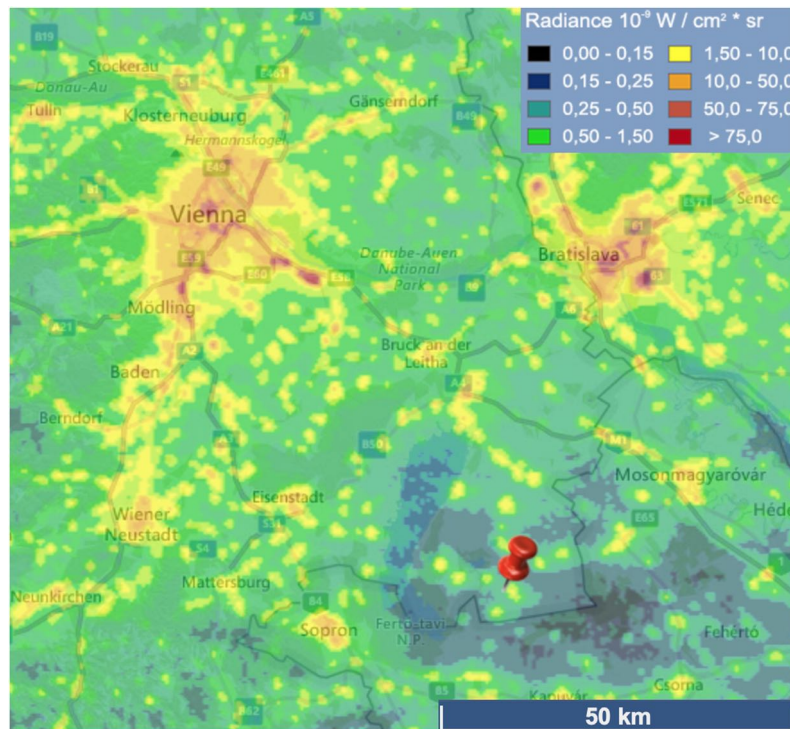


Figure 2. The measurement site in Eastern Austria, located at coordinates 47.7290 N, 16.9180E. The map shows radiance data from www.lightpollutionmap.info by Jurij Stare.

3.1 Field measurements

Field measurements were carried out in mid-June 2018 at locations in Eastern Austria, more precisely in a small area around the National Park Neusiedler See–Seewinkel. Care was taken to keep distances to the occurring dominating light sources, Vienna and Bratislava, high, i.e. 66 and 49 km, respectively. In order to provide an example of our approach, we show the derivations introduced before as calculated for one location, situated in the triangle of Vienna–Bratislava–Sopron. The observation point is illustrated in Fig. 2.

Measurements were taken using a digital single-lens reflex camera (Canon EOS 5D Mark II) equipped with a fisheye lens. The analysis of captured images, yielding a matrix indicating the luminance over the whole sky, was performed by the software ‘SKY QUALITY CAMERA’ (SQC), developed by Andrej Mohar from Euromix Ltd., Slovenia. Fig. 3 shows the input image as captured in cyclic format and the resulting

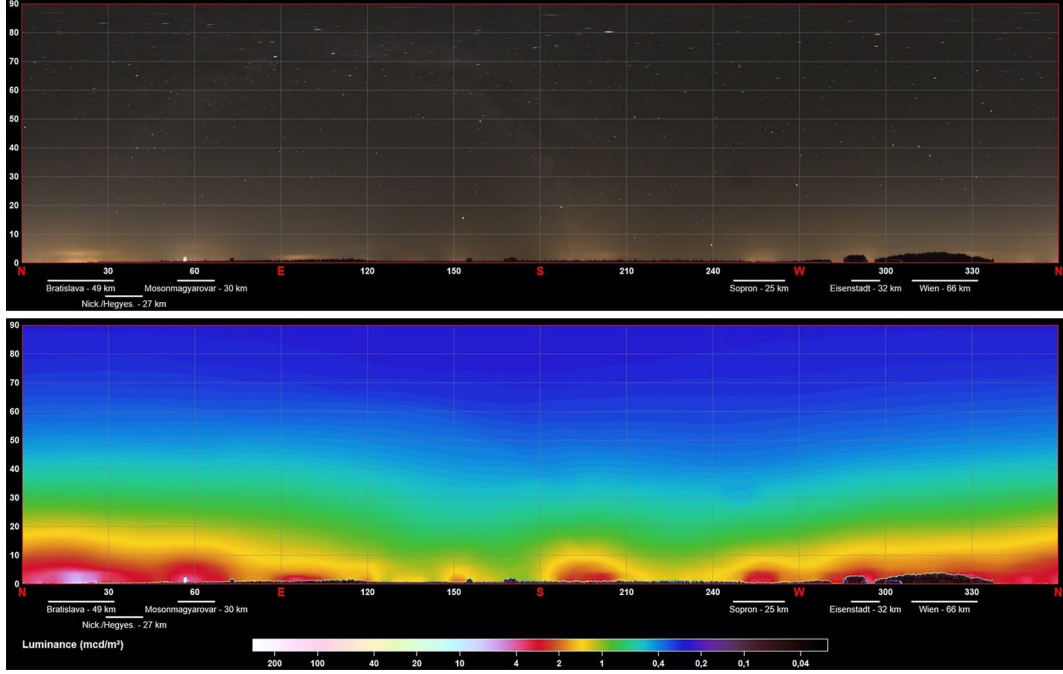


Figure 3. Top: image as captured at the observation site on 2018–06-19; 02.00 h local time. The cyclic format is the result of the SQC software. Bottom: luminance matrix of the input image resulting from SQC software.

luminance analysis. In the latter, light domes and their impact on the skyglow near the horizon become apparent. Since SQC provides the possibility of collecting data for the whole sky (i.e. a matrix consisting of zenith angles, azimuth angles and luminance values), fixed azimuths only, e.g. city centres, can also be examined.

3.2 Combining measurements with a theoretical approach

As can be seen from the radiance maps in Figs 2 and 3, there are two dominating cities, Bratislava and Vienna. Having collected luminance data from the azimuths of both city centres – Bratislava at $A_B = 18^\circ$, Vienna at $A_V = 322^\circ$ – the first step is to model the NSB at a local meridian that intersects a horizontal circle at the azimuth position of a radiating city. For Bratislava, i.e. $\theta_B = (\pi/2) - z$, we have

$$NSB_B(z, A_B) = G(z) \left\{ J_B S\left(\frac{\pi}{2} - z\right) + J_V S(\theta_z) \right\}. \quad (19)$$

In analogy, for Vienna, i.e. $\theta_V = (\pi/2) - z$, this results in

$$NSB_V(z, A_V) = G(z) \left\{ J_V S\left(\frac{\pi}{2} - z\right) + J_B S(\theta_z) \right\}. \quad (20)$$

The scattering angle θ_z , as illustrated in Fig. 4, is computed as follows:

$$\cos(\theta_z) = \sin(z) \cos(A_B - A_V). \quad (21)$$

For all zenith angles, the products $G(z)J_B$ and $G(z)J_V$ are generally unknown, but can be determined from the values $NSB_V(z, A_V)$ and $NSB_B(z, A_B)$ as measured at local meridians of Vienna and Bratislava. Specifically,

$$b(z) = G(z)J_B = \frac{S\left(\frac{\pi}{2} - z\right) NSB_B(z, A_B) - S(\theta_z) NSB_V(z, A_V)}{S^2\left(\frac{\pi}{2} - z\right) - S^2(\theta_z)} \quad (22)$$

provides the possibility of computing $G(z)J_V$ as

$$v(z) = G(z)J_V = \frac{NSB_V(z, A_V) - b(z)S(\theta_z)}{S\left(\frac{\pi}{2} - z\right)}. \quad (23)$$

5014 *S. Wallner et al.*

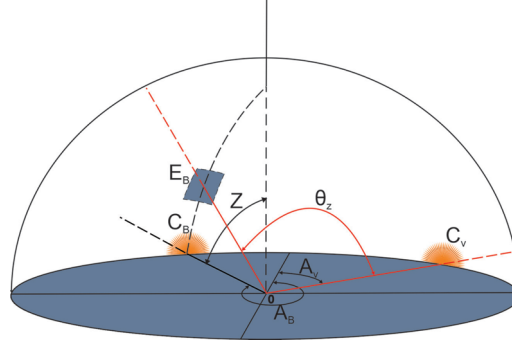


Figure 4. The same as in Fig. 1, but for scattering angle θ_z , which is the angle between the radius vector of Vienna (OC_V) and a sky element on the principal plane of Bratislava (OE_B).

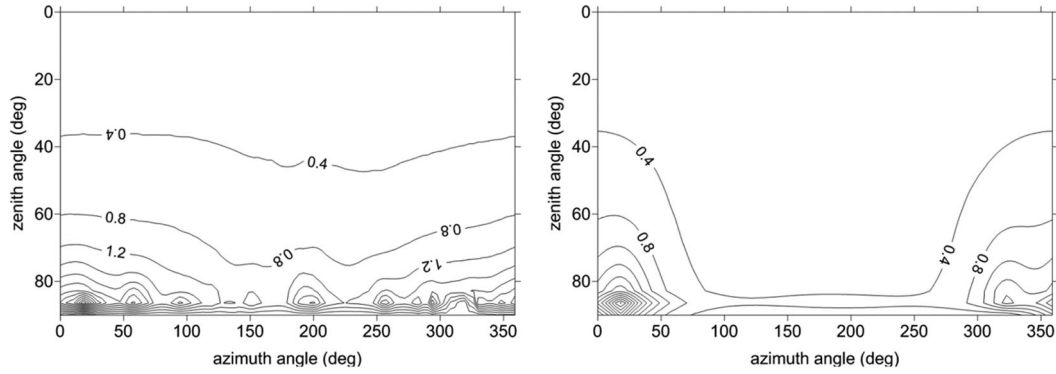


Figure 5. Left: digitized input image from data obtained from the SQC software as seen in Fig. 3. Right: computation showing the theoretical NSB only considering dominating light sources at the observation point, i.e. Bratislava and Vienna, as defined by equation (24). Data shown are in mcd m^{-2} .

The above formulae allow modelling of the theoretical NSB distribution (luminance or radiance map) due to two dominating light-emitting cities, Bratislava and Vienna, as

$$NSB_{\text{theoretical}}(z, A) = v(z) S(\theta_V) + b(z) S(\theta_B). \quad (24)$$

Fig. 5 compares the digitized input image, seen in Fig. 3 (lower), with the result of the computation provided by equation (24), which is now modelling the net contribution from both dominant cities.

The contribution from M small or medium-sized cities to the NSB is now obtained by subtracting the theoretical night-sky brightness caused by dominant cities solely from the measured NSB, i.e.

$$NSB_{\text{net}}(z, A_k) = NSB_{\text{measured}}(z, A_k) - NSB_{\text{theoretical}}(z, A_k) \quad k = 1 \dots M, \quad (25)$$

with M being the total number of small cities. Subsequently, the result now provides the contribution of small/medium-sized cities.

For the location of our observation point, we chose three smaller cities for exemplar computation: Mosonmagyaróvár ($A_{\text{center}} \approx 61^\circ$), Sopron ($A_{\text{center}} \approx 258^\circ$) and Eisenstadt ($A_{\text{center}} \approx 293^\circ$), so $M = 3$. The scaling coefficients used for calculation of the S function are: $c_1 = 16$, $c_2 = 0.3$ and $d = -3$ (Kittler et al. 2012). The result is shown in Fig. 6.

To estimate the amount W_{V0} of produced lumens radiated upwards by the cities, we use the formula introduced by (Garstang 1986), as follows:

$$W_{V0} = 2\pi \int_0^{\pi/2} I_{\text{up}}(z_0) \sin(z_0) dz_0 = LP [G(1 - F) + F], \quad (26)$$

with I_{up} being the cosine projected luminance, the uplight fraction chosen as $F = 0.15$ and the surface albedo chosen as $G = 0.35$, which are values typically found for unshielded luminaires and due to the high reflectance of urban areas as an average of the different materials typically used (Kotthaus et al. 2014; Wallner & Kocifaj 2019). The results can be found in Table 1.

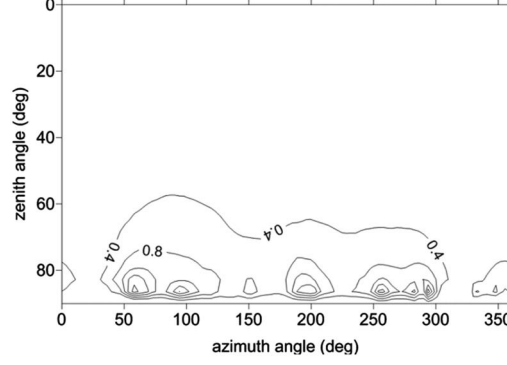


Figure 6. Result of equation (25), showing the net contribution of only small/medium-sized cities. Data shown are in mcd m^{-2} .

Table 1. Results of computations showing an estimation of the amount of lumens installed in the three small/medium-sized cities chosen.

	Mosonmagyaróvár	Sopron	Eisenstadt
W_{V0} (Mlm)	8.5	7.8	5.9
$W_{V0}^{\text{installed}}$ (Mlm)	22	17	13

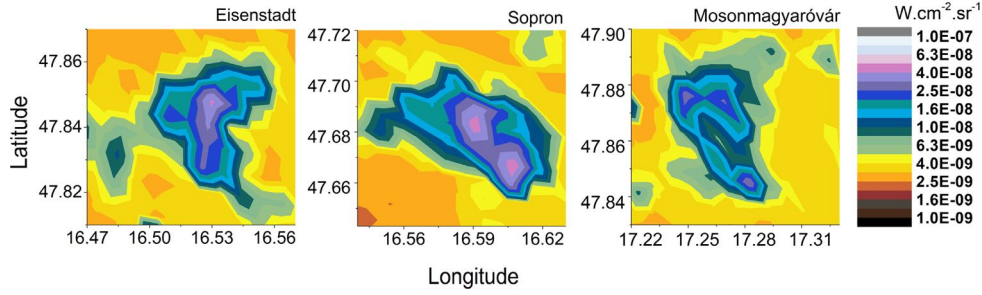


Figure 7. Satellite data obtained from VIIRS taken on 2018 May 17, for Eisenstadt, Sopron and Mosonmagyaróvár. Only pixels brighter than $10^{-8} \text{ W cm}^{-2} \text{ sr}^{-1}$ were considered, to focus on city centres and pixels radiating rather than scattering light.

Table 2. Estimation of total lumens installed in the three cities chosen as derived from satellite data only. The ranges show the results when using $F = 0.1 \dots 0.15$ and $G = 0.3 \dots 0.4$.

	Mosonmagyaróvár	Sopron	Eisenstadt
W_{V0} (Mlm)	9.4	12	9.8
$W_{V0}^{\text{installed}}$ (Mlm)	19–25	24–32	20–26

Taking into account that the satellite detection limit is $5 \times 10^{-11} \text{ W cm}^{-2} \text{ sr}^{-1}$ (Cao & Bai 2014), there is also the need to distinguish between scattered and radiated light. To ensure that only latter was included in our analysis, we focus exclusively on pixels brighter than $10^{-8} \text{ W cm}^{-2} \text{ sr}^{-1}$. In the conversion, we assume a uniform usage of high-pressure sodium (HPS) luminaires. In the case of at least Eisenstadt, the assumption of containing mostly HPS luminaires was certainly correct at the time of observations (Wallner 2019). In order to ensure comparability, satellite data taken on 2018 May 17, just shortly before the measurements took place, were collected. Furthermore, we also propose that cities produce a uniform angular output pattern, resulting from the calculation of emissions to the upward hemisphere, i.e.

$$W_{V0, \text{Satellite}} = L_{\text{mean}} A_{\text{tot}} \times 2\pi. \quad (27)$$

L_{mean} is the mean luminance of the total area of artificially lit pixels A_{tot} . The results are illustrated in Fig. 7 and the estimations of total lumens installed are given in Table 2.

4 DISCUSSION

The computations performed show that night-sky imagery via all-sky photometry, linked to the asymptotic formula introduced, can be used to provide information about the influence of small and medium-sized cities on the night-sky luminance. However, when comparing the simulated results with obtained satellite data, i.e. Tables 1 and 2, there are still some differences, e.g. for Eisenstadt the value of total lumens installed is less by 40 per cent than estimated from satellite. As mentioned before in Section 2, an estimate of this value within several tens of percent of its correct number can generally be applied as a suitable result. The differences found can be traced back to approximations made when satellite data were processed (see Section 3.3). One is uniform emission in all directions, which is clearly not the case seen realistically, but, since the emission function of cities is for the most part unknown, this is a native zero-order approximation. To go into detail, this means that if the satellite obtains data from low elevation angles, i.e. not from directly above a city, values for the theoretical uniform emission increase, since many cities appear to have stronger emission at low angles. Satellites are capable of detecting ‘cold’ and ‘hot’ spots, at which radiance is measurably weaker or stronger due to blockings (Li et al. 2019), but nevertheless cannot cover large viewing zenith angles close to 90°. Furthermore, limitations to HPS luminaires and minimum pixel brightness could also influence the results. Surprisingly, we found Mosonmagyaróvár to emit more light than Sopron, even if only containing half of the population. This outcome, however, appears correct when inspecting the localities in more detail. On the one hand, the surface of artificially lit areas seems to be smaller in Sopron, hence the density of luminaires appears to be higher and provides issues considering less efficient emission to low elevation angles, e.g. due to blockings. On the other hand, small towns close to the observation point, e.g. Jánossomorja (18 per cent population of Mosonmagyaróvár) or Mosonszolnok (5 per cent population of Mosonmagyaróvár), could have contributed to the NSB. Consequently, taking all comparisons into account, one might argue that satellites are not very accurate in providing information on light conditions perceived by an individual observer on the ground. However, considering that many approximations and assumptions had to be implemented to process the VIIRS dataset, both results, measurements and computations, are compatible.

In Eisenstadt, LED conversion started in 2018 July, so measurements were taken even before this process has started. Still, due to finished or upcoming LED conversions, VIIRS data cannot be used for comparison if cities use luminaires strongly emitting in short wavelengths. This provides an aggregated situation as regards long-term development of light pollution on Earth’s surface. The majority of data gathered originate either from one-dimensional photometric measurements detecting the luminance of the sky’s zenith luminosity, logged by so-called ‘Sky Quality Meter’ devices, or, as mentioned, from satellite data. Both methods will lead to difficulties in the long run, as their spectral sensitivities show weaknesses, being mostly blind to short wavelengths. Even if cities become brighter, by changing the colour of light-emitting sources, existing devices potentially predict a decrease in skyglow. This issue especially makes our approach even more essential for use as a possible measurement standard in the future.

The simulation performed in this work was conducted for two dominant light sources far away from the observation point. Congruously, the approach could be ineffective near dominant light-emitting sources, due to their strong influence on the night-sky luminance and their light domes camouflaging smaller sources, which are indistinguishable during measurement.

5 CONCLUSIONS

The approach used in this article combines in situ measurements via all-sky photometry and theoretical computations using the asymptotic formula introduced in past work. The aim is to provide information about the impact of small and medium-sized cities on the night-sky luminance, even with other occurring dominating sources, and additionally, an estimation of total lumens installed. This could be of great importance to astronomical observatories, since smaller cities or towns located in the surroundings can evolve and their impact on the NSB can increase. A comparison with performed computations was conducted via satellite data and has shown to be coherent, considering that approximations for processing satellite data were inevitable. We think that our approach can be of great value for quantifying and distinguishing different small or medium-sized light-emitting sources, but also especially for studying their long-term development, since, in future, the quality of data from e.g. VIIRS or Luojia 1–01 will decrease, due to their blindness in short wavelengths. The modelling approach can be used for all cities globally, although it is necessary not to obtain measurements inside light domes, to retain the possibility of these being separated from dominating ones within the course of the calculation. In addition, clear-sky conditions are necessary. However, only one measurement is required for inclusion in the theoretical modelling and therefore results are independent of any possible meteorological variations us, which usually occur if obtaining multiple images throughout the night. Another strength of the method used is that usually unknown atmospheric parameters, e.g. aerosol optical depth, which are necessary to include in models, need not be known, since the implementation of measurements from real conditions contains information about the environmental conditions. Consequently, the expenditure of computational time is lowered significantly by achieving even greater accuracy.

ACKNOWLEDGEMENTS

Open Access Funding provided by the University of Vienna. This work was supported by the Slovak Research and Development Agency under Project No. APVV-18–0014. Computational work was supported by the Slovak National Grant Agency VEGA (grant No. 2/0010/20).

REFERENCES

- Aubé M., 2015, *Phil. Trans. R. Soc. B*, 370, 20140117
 Bará S. et al., 2019, *Lighting Res. Technol.*, 51, 1092

MNRAS **494**, 5008–5017 (2020)

Lumen output in night-sky imaging 5017

- Bennie J. et al., 2016, *J. Ecol.*, 104, 611
- Cao C., Bai Y., 2014, *Remote Sens.*, 6, 11915
- Duriscoe D., Luginbuhl C. B., Elvidge C. D., 2014, *Lighting Res. Technol.*, 46, 35
- Garstang R. H., 1986, *PASP*, 98, 364
- Gaston K. J. et al., 2013, *Biol. Rev.*, 88, 912
- Horvath H., 1995, *Atmospheric Environ.*, 29, 241
- Jechow A. et al., 2017, *Sci. Rep.*, 7, 6741
- Joseph J. H., Kaufman Y. J., Mekler Y., 1991, *Appl. Opt.* 30, 3047
- Kinzey B. et al., 2017, Technical report, Pacific Northwest National Laboratory, Richland, Washington, 99352
- Kittler R., Kocifaj M., Darula S., 2012, *Daylight Science and Daylighting Technology*, in Springer Science+Business Media, LLC New York, 341
- Kocifaj M., 2018, *J. Quant. Spectrosc. Radiat. Transfer*, 206, 260
- Kocifaj M., Wallner S., Solano-Lamphar H. A., 2019, *MNRAS*, 485, 2214
- Kotthaus S. et al., 2014, *J. Photogr. Remote Sensing*, 94, 194
- Kyba C. C. M. et al., 2011, *Plos One*, 6, e17307
- Kyba C. C. M. et al., 2017, *Sci. Adv.*, 3, e1701528
- Li X. et al., 2019, *Remote Sens. Environ.*, 233, 111357
- Luginbuhl C. et al., 2009, *PASP*, 121, 204
- Luginbuhl C., Boley P., Davis D. R., 2014, *J. Quant. Spectrosc. Radiat. Transfer*, 139, 21
- Á. Molnár et al., 2016, *Időjárás*, 120, 163
- Perkin E. K. et al., 2011, *Ecosphere*, 2, 122
- Press W. H., Teukolsky S. A., Vetterling W. T., Flannery B. P., 2007, *Numerical Recipes 3rd Edition. The Art of Scientific Computing*, Cambridge University Press, Cambridge, New York
- Puschnig J., Posch T., Uttenthaler S., 2014, *J. Quant. Spectrosc. Radiat. Transfer*, 139, 64
- Solano-Lamphar H. A., 2018, *J. Quant. Spectrosc. Radiat. Transfer*, 211, 35
- Utrillas M. P. et al., 2000, *Sol. Energy*, 68, 197
- Wallner S., Kocifaj M., 2019, *J. Quant. Spectrosc. Radiat. Transfer*, 239, 106648
- Wallner S., 2019, *J. Imaging*, 5, 86
- Waquet F. et al., 2009, *J. Geophys. Res. Atmos.*, 114, D01206
- Wagner F., Silva A. M., 2008, *Atmos. Chem. Phys.*, 8, 481
- Wu D. et al., 2011, *J. Opt. Soc. Korea*, 15, 90
- Wu J. et al., 2014, *J. Geophys. Res. Atmos.*, 119, 13370

This paper has been typeset from a Microsoft Word file prepared by the author.

4.6 'Modelled impacts of a potential LED lighting system conversion and the influence of an extremely polluted atmosphere on light pollution in Mexico City'

Title: *Modelled impacts of a potential LED lighting system conversion and the influence of an extremely polluted atmosphere on light pollution in Mexico City*

Authors: S. Wallner¹ H. A. Solano-Lamphar¹, M. Kocifaj

Journal: Environment and Planning B: Urban Analytics and City Science

Status: Submitted on 12-Apr-2020, Manuscript ID: EPB-2020-0151

Personal contribution: This work bases on a first version as drafted by H. A. Solano-Lamphar. After his execution of computational work, I took charge of the entire data analysis, developed the idea how to represent results, and wrote the first version of the paper. As correspondent author, I was in charge of submission and will be in charge of a potential revision, if accepted for publication in the journal.

In the following, the paper as originally submitted to the journal is attached.

¹Co-first authorship

Modelled impacts of a potential LED lighting system conversion and the influence of an extremely polluted atmosphere in Mexico City

S. Wallner^{*,† 1,2}, H. Lamphar^{* 2,3}, M. Kocifaj^{2,4}

¹ *Department of Astrophysics, University of Vienna, Türkenschanzstrasse 17, 1180 Vienna, Austria*

² *ICA, Slovak Academy of Sciences, Dúbravská Road 9, 845 03 Bratislava, Slovak Republic*

³ *Cátedras CONACYT— The Center for Research in Geography and Geomatics Ing. Jorge L. Tamayo (CentroGeo). A.C., Contoy 137, Lomas de Padierna, Tlalpán, Ciudad de México, 14240, Mexico*

⁴ *Department of Experimental Physics, Faculty of Mathematics, Physics, and Informatics, Comenius University, Mlynská dolina, 842 48 Bratislava, Slovak Republic.*

** Co-first authorship, the two authors have contributed equally to the paper*

† Correspondent author: stefan.wallner@univie.ac.at

Abstract

Currently, many cities worldwide, are changing current existing and mostly outdated lighting situation systems from inefficient lamps to Light Emitting Diodes (LEDs). Providing the opportunity of energy savings they can help in preventing influences to the night sky and furthermore issues for human health, wildlife and environment. This work simulates a potential LED conversion for the megacity of Mexico City and investigates impacts to conservation areas. Modelled for the whole visible spectrum, the analysis places special focus on the effects of applying various colour temperatures. Additionally, a highly polluted atmosphere was included as theoretical model, something applying to megacities in particular, to see impacts on skyglow of such an environmental contingency. In general, results show that the night sky brightness increases significantly with increasing colour temperature of LEDs if the lumen output is kept constant. It is shown that a potential conversion requires a thorough adjustment, otherwise negative impacts on environment and health might rise. Furthermore, an increased aerosol optical thickness ends producing more diffuse light, identifying a major concern for the environment. The results obtained in this paper may be a strong motivation to ascertain measurements conducted in other large urban areas correlated to the computational results presented here.

Keywords: skyglow modelling; light pollution;; air pollution; aerosol optical thickness; night sky brightness; environmental impacts

Highlights

- Modelling of a potential lighting conversion for the whole visible spectrum
- Inclusion of air pollution, especially a highly polluted atmosphere, and the comparison to skyglow
- Simulation of a megacity with the possibility of applying to any other city globally
- Models show that night sky brightness increases significantly with increasing colour temperature of LEDs
- An increased aerosol optical thickness ends producing more diffuse light, identifying a major concern for the environment

1. Introduction

Since the 19th century, artificial lighting has changed both the living conditions and the socio-economic and cultural activities of the human being (O'Dea, 1951; Schernhammer and Schulmeister, 2004). These transformations are reflected in the urban environment where public and private lighting sources are part of the nocturnal landscape. Artificial light comprises a complex urban system designed to keep cities illuminated in an industrialized world. However, excessive nocturnal artificial lighting has been recognized as an environmental problem that requires the rearrangement of research priorities to act against its deteriorating growth. This has been an important topic of study in the literature for many years (Longcore and Rich, 2004; Navara and Nelson, 2007, Kocifaj and Lamphar, 2013; Pawson and Bader, 2014). Light pollution and skyglow are ubiquitous characteristics of modern society while the mechanisms of their formation, distribution and amplification should be understood better to address the basic consequences and plan remediation.

Skyglow is spreading continuously (Kyba et al. 2017) resulting not only in a waste of energy but as well in injudicious and harmful over-illumination of natural environments (Lamphar and Kocifaj, 2013). It is essential to comprehend properties of artificial light in modelling the nocturnal radiance in a diverse night-time atmosphere. In this sense, the distribution of the nocturnal radiant intensity is one of the most required properties which characterizes the collective emissions from the whole-city light sources. The artificial light emitted from urban settlements predetermines the sky brightness under arbitrary conditions, therefore attention is often paid to the diffuse light of the night sky. Fluctuations on the night sky radiance, not triggered by long-term seasonal effects like the change of surface albedo (Wallner and Kocifaj, 2019), are stubborn because of a variability of aerosol particles and air molecules which both are the greatest modulators of skyglow under clear sky conditions (Seinfeld and Pandis, 2016; Alvarado et al., 2016; Kerker, 2016). As a result, sky radiance distributions are distorted depending on many factors. Along with atmospheric effects, temporal and spatial changes of the artificial light at night are determined by the emission from terrestrial light emitting sources (Garstang, 1986; Cinzano and Castro, 1998; Aubé et al., 2005; Luginbuhl et al., 2009; Kocifaj and Lamphar, 2014; Kocifaj et al., 2019). Particularly important is the light output pattern as a function of zenith angle, otherwise called the city emission function (CEF) (Kocifaj et al., 2015; Lamphar, 2018).

The direct and indirect effects of artificial light on nocturnal environments escalated in recent decades with population and urban growth experienced in cities. The night sky radiance produced by urbanization depends on the socialized individuals and the particular characteristics that are part of an urban system. The spatial and temporal variations of these factors shape skyglow levels at local and global scales. Globally, cities carry a design process of the artificial lighting system with its main focus lying on reacting to new technologies and achieving a master plan that follows the demands of the agenda, e.g., security and infrastructure. As we are now seeing, many cities worldwide are changing current existing and mostly outdated lighting systems from inefficient past generation lamps to modern Light Emitting Diodes (LEDs) delivering significant amount of blue light to the ambient environment (Kinzey et al. 2017, Aubé et al., 2018; Baddiley, 2018; Barentine et al., 2018). Due to their high energy efficacy, they provide the possibility of energy savings but also danger originated from unintended misdirection and over-illumination features. One of the potential results of poorly designed lighting systems is urban skyglow. Especially blue parts of the emitting spectrum lead to huge issues for human health, environment and wildlife (Falchi et al., 2011). It is impossible to eradicate the impact of artificial lighting on the environment and its ecosystems, given the functional requirements of nightlight. However, the artificial light emissions can be adjusted properly in order to achieve optimum levels of illumination while reducing a few negative side effects such as skyglow. That is to say, those that the city needs once diverse environmental criteria are considered.

This work aims to develop a framework to investigate the consequences that a massive LED lighting system conversion could have on the skyglow produced from Mexico City. For the first time, theoretical modelling of light pollution has been applied to analyse a light conversion in a megacity for the whole visible spectrum.

2. Methods and technique

2.1 Location

The location chosen for detailed analysis is Mexico City, since it provides a variety of interesting conditions. First, it is one of the most inhabited cities on Earth with a population of nearly nine million people and a density of 6,000 people per km². The officially recognized extended land area of Greater Mexico City (metropolitan area) is home for more than 21

million people. Its growth was due to both the demographic increase of the native population and to the migratory flows from different parts of the country, mainly central Mexico. Industrial and urban growth motivated migrations from the countryside between the 1940s and 1960s. Further on, the city demonstrates a political structure creating concerns related to light pollution. Its area, talking only about the main city, is divided in 16 boroughs, all being decentralized and autonomous political-administrative bodies in their governmental actions.

Borough	Habitants	Lighting systems used			
		HPS	LED	MV	MH
Azcapotzalco	414,711	80%			20%
Coyoacán	620,416	20%		80%	
Cuajimalpa de Morelos	186,391	90%	10%		
Gustavo A. Madero	1,185,772	85%		15%	
Iztacalco	384,326		10%		90%
Iztapalapa	1,815,786	100%			
La Magdalena Contreras	239,086	80%	20%		
Milpa Alta	130,582	90%			10%
Álvaro Obregón	727,034	16%	84%		
Tláhuac	360,265			100%	
Tlalpan	650,567	80%		20%	
Xochimilco	415,007	70%			30%
Benito Juárez	385,439		95%		5%
Cuauhtémoc	531,831	80%			20%
Miguel Hidalgo	372,889		10%		90%
Venustiano Carranza	430,978	70%			30%
Average over all		54%	14%	13%	18%

Table 1 - Summary of all 16 boroughs of Mexico City, number of inhabitants (status of 2010), lighting systems and their percentage distribution. HPS = High pressure sodium lamp, LED = Light Emitting Diode, MV = Mercury-vapor lamp, MH = Metal-halide lamp

Each of the boroughs is headed by a Delegation Chief, who is elected by popular and direct vote. In this sense, given that there is the existence of a variety of administrations, decisions

regarding public lighting are by far not consistent, resulting in a multitude of lighting systems that foster a heterogeneity in the urban planning of the city. Data provided by all administrations, [Table 1](#), summarizes all boroughs and lighting installations therein. The numbers reflect that HPS lamps still are the most commonly used technology in Mexico city, only two boroughs seem to have converted to LEDs in the past and four in which LEDs are available in low amounts. Even if only 14% of all lighting systems in the whole city appear to be LEDs, their shift in colour temperature from orange coloured HPS lamps to white LEDs is visible from above as imaged by the International Space Station, pictured in [Figure 1](#). The observation sites, chosen for skyglow modelling, were selected in accordance to real existing protected natural areas, located inside and in the surrounding of Mexico City. The quantification of changes in lighting situation just in the above locations is preferred because these sites are extremely endangered by the influence of artificial light at night. More precise, the following habitats were opted: Reserva Ecológica del Pedregal de San Ángel (REPSA) and Parque Nacional Cumbres del Ajusco.

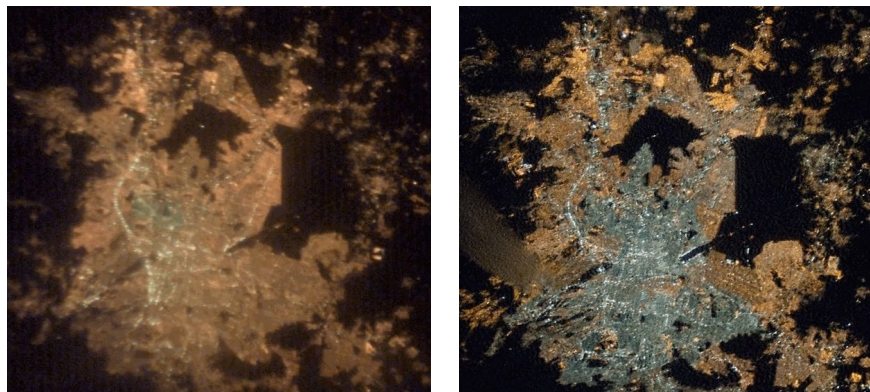


Figure 1 - Mexico City as seen from the International Space Station. The picture in the left side was taken in 2003 while the picture in the right side was taken in 2011. Clearly a shift from mostly HPS luminaires resulting in orange light to white LEDs is noticeable.

The *Reserva Ecológica del Pedregal de San Ángel (REPSA)*, has been under protection for 25 years by the National Autonomous University of Mexico (UNAM). It represents the last relict of the scree ecosystem of the basin of Mexico. This xerophilous scrub is located in the middle

of Mexico City, within the UNAM. From all vegetation types settled on the basaltic substrate of the Xitle volcano spill, the most common vegetation is just the one found in the protected area mentioned above. There are a few areas in the world such as the REPSA ecosystem, embedded in a mega metropolitan area and, at the same time, representing an exceptional natural laboratory for the study of the evolutionary processes of the communities present on a lava island. On the other hand, the environmental services that the natural reserve brings to the city are of vital importance for its inhabitants. Unfortunately, the accelerated growth of Mexico City led to a reduction of its extension to less than 10% of the original area. Urbanization causes loss of habitats and disappearances of numerous species.

Parque Nacional Cumbres del Ajusco is one of various National Parks near Mexico City. It is known for its high elevations reaching up to 3,900 meters (12,795 ft) above sea level and it is visible from all around Mexico City. The park is characterized by pine-oak forests and high mountain grassland. The area is key to the conservation of the ecosystem and is important to endemic species. Urbanization of Mexico City has posed several environmental concerns over the preservation of the habitats and ecosystems of the park. Even though the park is considered an area in jeopardy of being negatively affected by urban expansion, the Cumbres del Ajusco has a great diversity of flora and fauna endemic to Cordillera Neovolcanica that goes through the centre of Mexico.

2.2 Modelling approach

One of the key elements of this study is to model the consequences of LED conversion prior its physical realization, thus avoiding potential economic losses originated from unwanted skyglow effects. The basic prerequisite to do so is a simulating tool that allows for rapid numerical modelling of sky radiance on a large domain, while providing results within the specified error tolerance. The decision fell on the SkyGlow tool ([Kocifaj, 2017](#)) due to its easy use in modelling real shapes of Mexico City and evaluation of skyglow levels under various meteorological conditions. We have computed different scenarios considering current lamp technologies and a possible massive change to white LEDs. To model not only the city as a whole, but furthermore also being able to adapt lighting situations to real-world conditions, the modelled city was also divided into the 16 boroughs mentioned before. [Figure 2](#) illustrates the 'input city' and its division into sectors as customized for simulations.

Various set-up configurations were used according to the purpose of study:

- Clear sky
- Whole visible spectrum - 350 to 750nm
- Constant Background (to characterize the nature of aerosol particles)
- Fraction of the light that is isotropically reflected from the ground $G = 0.15$, and a fraction of the light radiated directly into the upward hemisphere $F = 0.25$
- Aerosol optical thickness at the reference wavelength 500 nm = 0.3, 0.9
- Ångström exponent = 1.3
- Scale height of molecular atmosphere = 8.0 km
- Vertical gradient of aerosol concentration = 0.65 km^{-1}

Figure 3 illustrates the position of the two natural protected areas which were chosen as observation points for computations. The quantity of light radiated to the upper hemisphere was computed following the Garstang's emission function, which is usually the only one choice considered in literature for cities when no other direct or indirect indicia on shapes of their light output patterns. The amount of light installed in cities is calculated following the lumens per habitant approach, i.e., 750 lumens per habitant. The number of inhabitants of each borough were individually adapted to be in accordance with Table 1. Since the number of inhabitants was not changed for computations of 'real' or 'current' conditions to hypothetical LED conversion, the lumen output is kept constant. Consequently, we are considering in our model that there are already massive energy savings due to the higher efficacy of LED luminaires. Considering also various colour temperatures of LEDs, Figure 4 shows input spectra used.

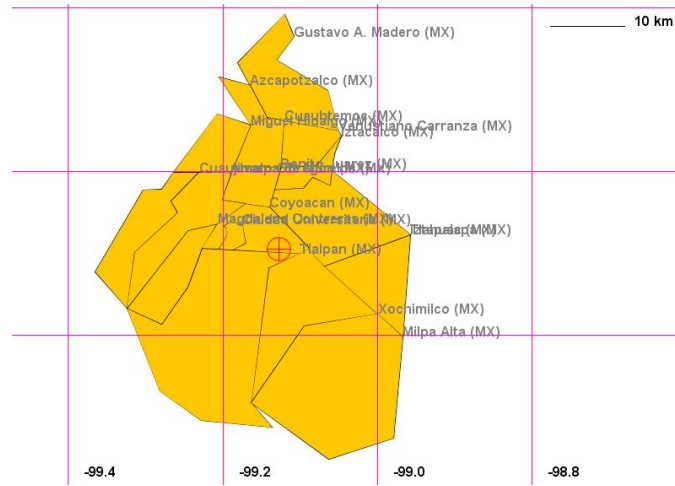


Figure 2 - Input city as customized for the SkyGlow model including the division into 16 boroughs. The red cross highlights a random observing site for skyglow simulation which is changeable. The magenta lines describe a coordinate system with latitude of 19.6° at the top horizontal, 19.0° at the bottom horizontal (not shown), and longitude -99.4° at the left vertical and -98.8° at the right vertical.

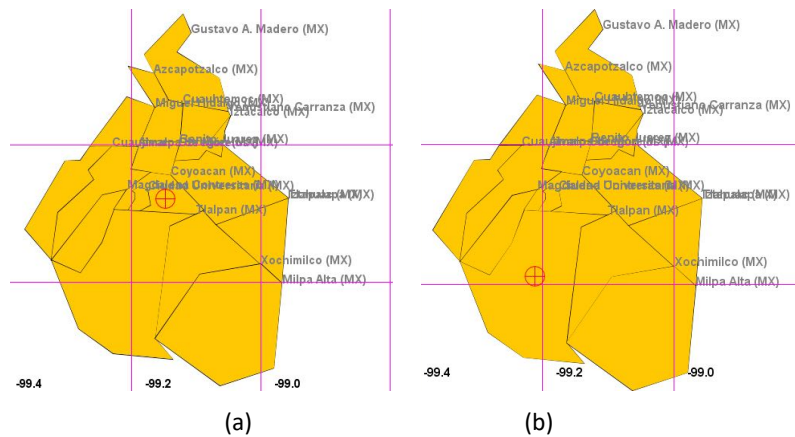


Figure 3 - The red crossed circles show locations chosen for simulations in Mexico City: (a) Reserva Ecológica del Pedregal de San Ángel (REPSA), (b) Parque Nacional Cumbres del Ajusco.

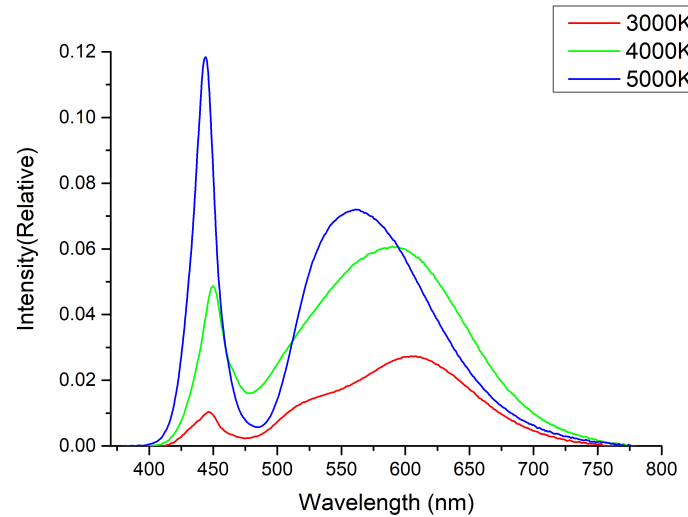


Figure 4 - Input spectra for LEDs with various colour temperatures as used for the computations.

2.3 Extremely polluted atmosphere

At the beginning of the century, Mexico City was ranked among the most air polluted cities on Earth, even being stated the most by the World Health Organization (WHO) in 1992. Conditions improved since then, still due to meteorological phenomena, there are appearances of dangerous air state quantities. In order to make qualitative assessments regarding this phenomenon in Mexico City, also a value of AOT=0.9, which is the upper limit for an exceptionally turbid atmosphere (Bäumer et al., 2008), was included to the computations. In the case of environmental contingencies due to air pollution, such as those occurring in Mexico City, there is a risk of respiratory diseases. There is some evidence suggesting that the relationship between pollutant monitoring and the frequencies of respiratory and ocular symptoms coincided with the highest frequencies of contamination. (Hernández-Garduño et al., 1997; Téllez-Rojo et al., 2000; Riojas-Rodriguez et al., 2014) In future works, it may be useful to study particular aspects of the effects of light pollution in human health. In the past, the relationship between the artificial night sky brightness and aerosols occurred empirically. In our case, it was possible to carry out an adequate simulation to analyse the results an environmental contingency entailed.

3. Results

In this section the computational results are analysed and intentionally separated in two subsections, since they show impacts of a LED conversion at two different applicable conditions, at low and elevated turbidity levels. This approach should make it possible to adopt results to any larger city in the world, being strongly air polluted or not.

3.1 LED conversion

To receive an impression on the importance of chosen colour temperatures, the results were illustrated as provided by computations and plotted for all zenith angles in cardinal directions, i.e., azimuths 0° (north), 90° (east), 180° (south) and 270° (west). Four input models were considered: the current state of lighting technology (most used luminaire spectrum chosen as seen in Table 1) and a conversion of the whole city light sources to 3000K, 4000K or 5000K LEDs, respectively.

Figures 5-8 illustrate the results of all four simulated models for Reserva Ecológica del Pedregal de San Ángel and Parque Nacional Cumbres del Ajusco. In general, one can see that luminance of the night sky at all azimuths shows the same behaviour, being brightest when considering the city being converted to the highest chosen colour temperature of 5000K. On the other hand, the current situation of used luminaires seem to have the least influence on the night sky brightness. Like discussed above, this results especially from keeping the lumen output constant for all lighting situations. At low elevation angles sky luminance can show significant changes with azimuth because of different population density in different parts of Mexico City. In other words, skyglow depends on lumen output not only from the borough the observer is situated in, but also from near boroughs around the observer's location. Unsurprisingly, the impact of various colour temperatures is increasingly important near the horizon. However, also zenith luminance values, summarized in Table 2, exemplify the influence on the night sky brightness. If, e.g., using LEDs with a colour temperature of 4000K, as very often used for public street lighting globally, the zenith brightens increases by a factor of 10 for the location situated near the city centre and a factor of 2 for the southwestern location. Astronomical magnitudes decrease by 2.5 or 0.8. It is no surprise that the observer near the centre of Mexico City is more affected by a potential LED conversion than farer away

from it. The differences occurring due to various colour temperatures, can especially be traced back to higher scattering efficiencies of light in short wavelengths.

	Reserva Ecológica del Pedregal de San Ángel	Parque Nacional Cumbres del Ajusco
Current Situation	$8.3639 \cdot 10^{-3} \text{ cd/m}^2$ $\cong 17.78 \text{ mag/arcsec}^2$	$1.3645 \cdot 10^{-3} \text{ cd/m}^2$ $\cong 19.75 \text{ mag/arcsec}^2$
3000K LEDs	$9.1455 \cdot 10^{-3} \text{ cd/m}^2$ $\cong 17.68 \text{ mag/arcsec}^2$	$2.1348 \cdot 10^{-3} \text{ cd/m}^2$ $\cong 19.26 \text{ mag/arcsec}^2$
4000K LEDs	$1.2145 \cdot 10^{-2} \text{ cd/m}^2$ $\cong 17.37 \text{ mag/arcsec}^2$	$2.8243 \cdot 10^{-3} \text{ cd/m}^2$ $\cong 18.96 \text{ mag/arcsec}^2$
5000K LEDs	$1.7223 \cdot 10^{-2} \text{ cd/m}^2$ $\cong 16.99 \text{ mag/arcsec}^2$	$3.9894 \cdot 10^{-3} \text{ cd/m}^2$ $\cong 18.58 \text{ mag/arcsec}^2$

Table 2 - Zenith luminance values as simulated for both locations with an AOT = 0.3.

3.2 Polluted atmosphere

Figures 9 and 10 show results of simulations for both locations for aerosol optical thickness as large as 0.9 while Table 3 compares the zenith luminance values of all models assumed. Analogously to what we have documented in Sec. 3.1, night sky brightening is also identified here when increasing colour temperature of luminaires used. Still, if comparing figures, a higher aerosol optical thickness (AOT) seem to result in reduced skyglow.

	Reserva Ecológica del Pedregal de San Ángel	Parque Nacional Cumbres del Ajusco
Current Situation	$7.777 \cdot 10^{-3} \text{ cd/m}^2$ $\cong 17.86 \text{ mag/arcsec}^2$	$1.1487 \cdot 10^{-3} \text{ cd/m}^2$ $\cong 19.93 \text{ mag/arcsec}^2$
3000K LEDs	$8.6806 \cdot 10^{-3} \text{ cd/m}^2$ $\cong 17.74 \text{ mag/arcsec}^2$	$1.8672 \cdot 10^{-3} \text{ cd/m}^2$ $\cong 19.41 \text{ mag/arcsec}^2$
4000K LEDs	$1.1302 \cdot 10^{-2} \text{ cd/m}^2$ $\cong 17.45 \text{ mag/arcsec}^2$	$2.4273 \cdot 10^{-3} \text{ cd/m}^2$ $\cong 19.12 \text{ mag/arcsec}^2$
5000K LEDs	$1.5700 \cdot 10^{-2} \text{ cd/m}^2$ $\cong 17.09 \text{ mag/arcsec}^2$	$3.3665 \cdot 10^{-3} \text{ cd/m}^2$ $\cong 18.77 \text{ mag/arcsec}^2$

Table 3 - Zenith luminance values as simulated for both locations with an AOT = 0.9.

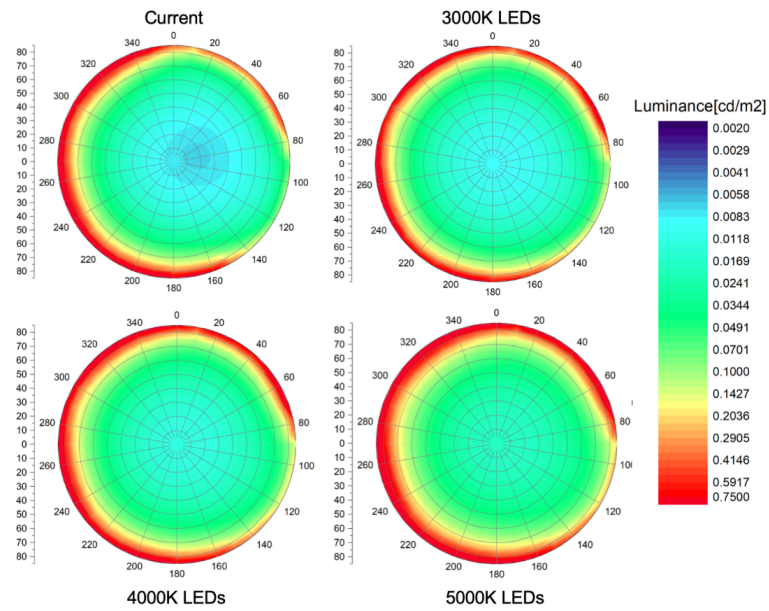


Figure FIG5: Results of simulations at the location of Reserva Ecológica del Pedregal de San Ángel with an AOT = 0.3.

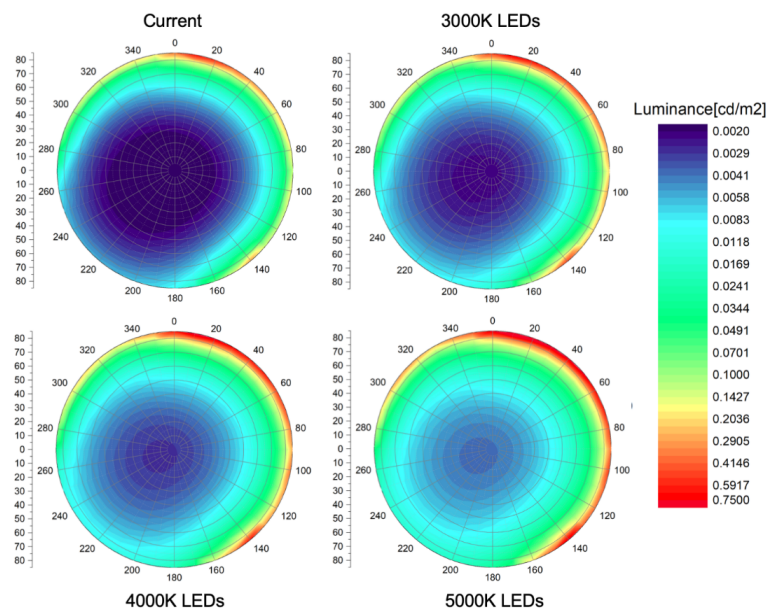


Figure FIG6: Results of simulations at the location of Parque Nacional Cumbres del Ajusco with an AOT = 0.3.

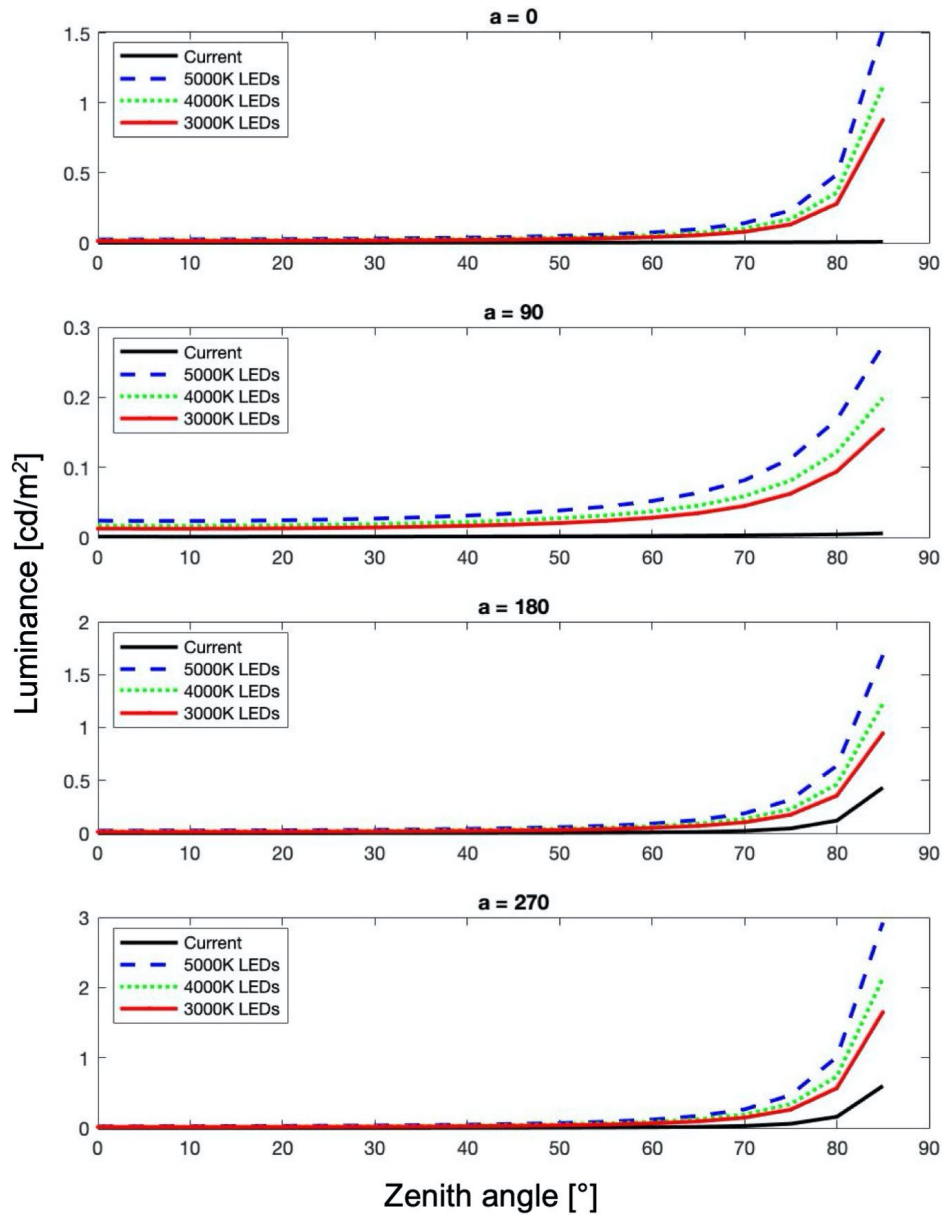


Figure FIG7. Results as provided by the simulations for Reserva Ecológica del Pedregal de San Ángel. 'Current' describes the current state of lamp technologies, '5000K' is for theoretical city-wide conversion to 5000K LEDs. The same applies to 4000K and 3000K. The four plots from top to the bottom are for azimuths of each cardinal direction: $a=0^\circ$ (north), 90° (east), 180° (south) and 270° (west).

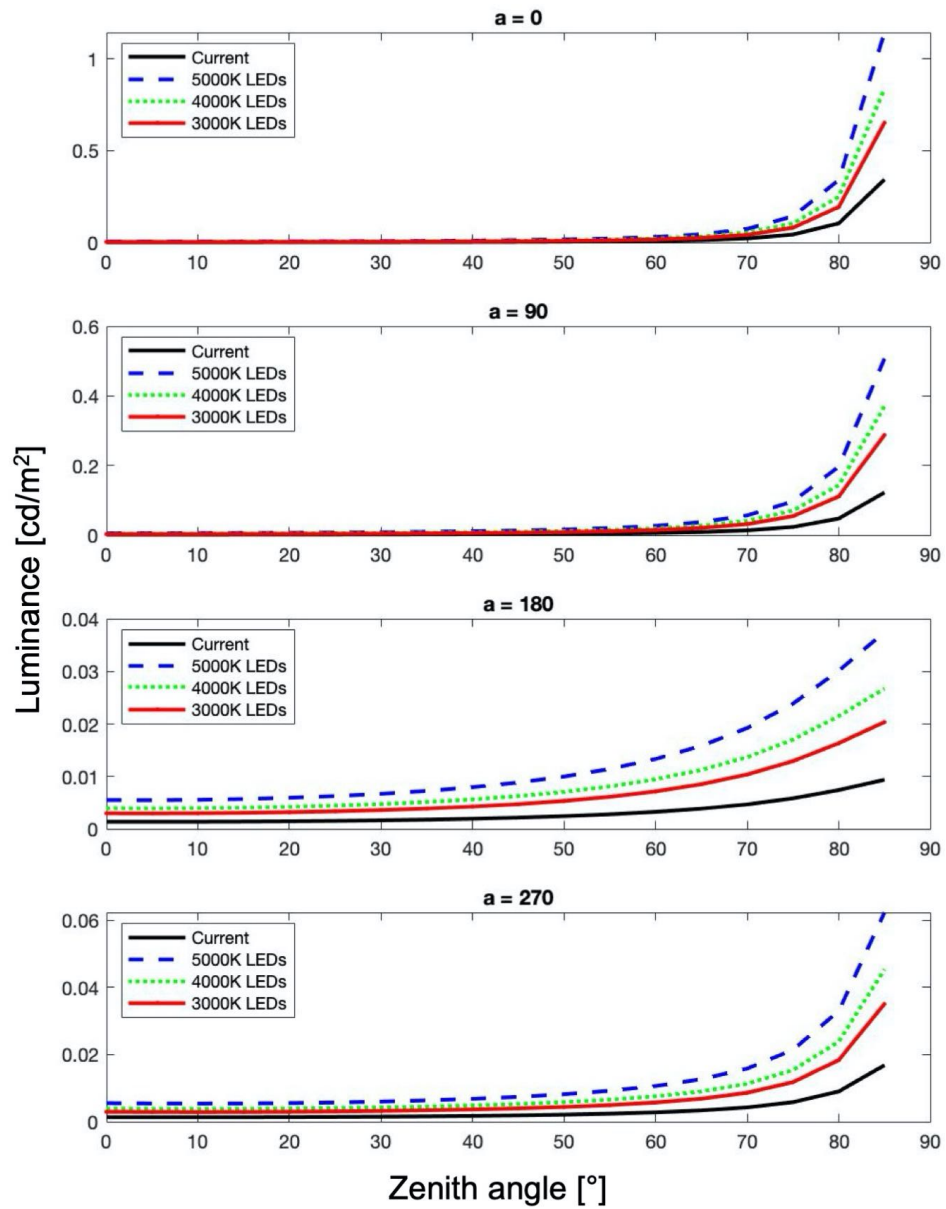


Figure FIG8. The same as in Figure FIG7, but for Parque Nacional Cumbres del Ajusco.

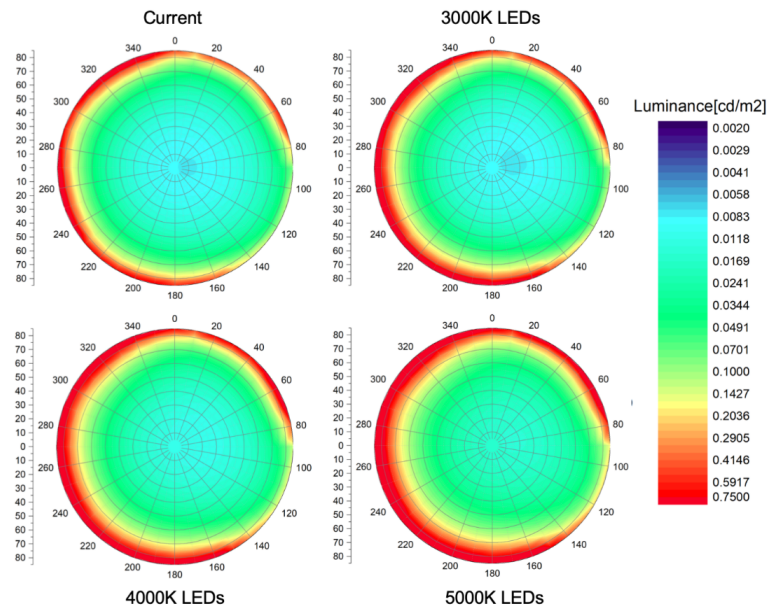


Figure FIG9: Results of simulations at the location of Reserva Ecológica del Pedregal de San Ángel with an AOT = 0.9.

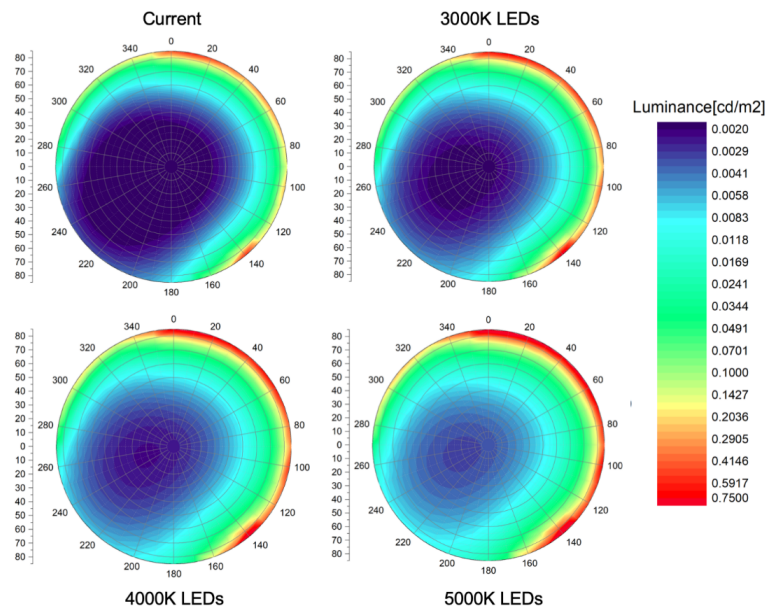


Figure FIG10: Results of simulations at the location of Parque Nacional Cumbres del Ajusco with an AOT = 0.9.

4. Discussion and Conclusion

Preserving human health and conserving wide diversity of living organisms in cities and their surroundings require increased effort and regulations to be implemented for an entire population at a municipal level. While emerging problems like air-, water-, ground-, or noise-pollution, are mostly all under specific control, the influence of artificial light at night has been overlooked for a long time or left apart from the public policy health agenda. Currently, there is a global movement in case to protect the natural night sky with the installation of new street lighting systems. It has shown that well-shielded LED lamps are on the one hand providing a high efficacy with the possibility of significant energy savings, and on the other hand can be adjusted better to the needs of certain areas. However, there is still the issue of poorly adapted installations, choosing high colour temperatures (> 3000 K) or over-illuminances. The result is a worsening of lighting conditions.

Our numerical simulations reveal the potential consequences to the skyglow expected in protected natural areas of Mexico City as a result of LED conversion if enforced in all 16 city-boroughs. The results of this analysis illustrate that in every case, the situation worsens in all locations selected if the amount of lumen output is kept constant. Specifically, the night sky patterns lose their natural structure due to significantly increased luminance amplitudes. This effect is strengthened with increasing colour temperature of LEDs. Results show that even if conducting the same lumen output and only changing light sources, scattering effects and differences in efficacy can end up in significant impacts on the night sky brightness. There is no doubt that potential conversions of lighting systems to LEDs require a thorough adjustment of other parameters, otherwise negative impacts on environment and health might rise significantly. Some of the useful measures are as follows: i) define a maximum illuminance for lamps and advertisements, ii) define a maximum colour temperature of 3000 Kelvin, iii) install only well-shielded lamps with no uplight, iv) dim (street lighting) or switch off (advertisements, buildings, etc.) light sources during the night.

The light emitted from artificial sources upwards undergoes intense scattering in a turbid atmosphere, especially when the aerosol optical thickness is extremely increased (see **Figure FIG11**). We know from radiative transfer theories that scattering efficiency increases proportionally with the cross section of scattering bodies. This is why aerosol particles, with sizes and cross sections exceeding significantly those of air molecules, have an important role in shaping the night sky brightness. The turbid environments in densely populated urban

areas are therefore found to produce more diffuse light compared to what we can observe in rural or even natural spaces. More scattering, however, also means strong attenuation and these two effects combine depending on particle sizes and compositions (chemistry). For instance, large particles cause the light emitted under low elevation angles not necessarily causes an increased illuminance at place of emission. Instead, it could amplify the diffuse illumination in surrounding areas, at the expense of backscattered light due to lowered amount of photons traveling backwards. By careful examining the data of our study, it is illustrated that the natural night does no longer exist in the two areas inspected, although one of them is outside of population centres. It is important to understand that zenith radiances can peak near large arbitrarily shaped cities with non-uniform distribution of upward emissions. In our case, sky luminance reveals significant increases in the vicinity of municipalities, which could help us to determine the effects on some plant and animal species with a nocturnal behaviour.

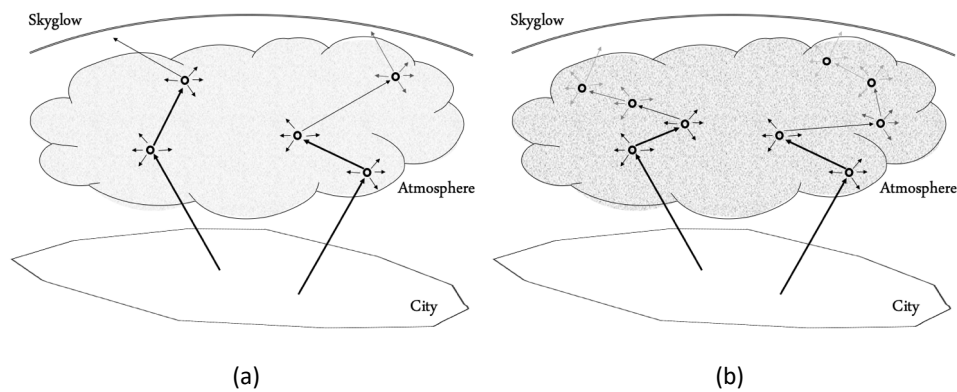


Figure FIG11. Photon trajectories in the atmosphere under low (a) and high (b) aerosol optical thickness. The mean free path of photons between two scattering events is short under elevated AOT conditions (b), causing the intensity of light rapidly decays as the optical path of photons increases.

The environmental concerns in the metropolitan areas of Mexico City identified imply the needs for alternative solutions for the formulation of public policies. The lighting system of the metropolitan areas is heterogeneous, meaning that the emission spectrum and light

output pattern (LOP) may both depend on the position within a city. A large fraction of artificial light at night comes from public lighting sources and there is no doubt that the problem requires a treatment on a local scale. The angular emission function is expected to be consistent with that of street lighting LOP, but the light emissions from building interiors, advertisement boards, cars, or sport stadiums can influence the emission curve. Therefore, the contribution from headlights, billboards, windows and monuments to the brightness of the night sky must not be ignored. Specifically, new urban lighting planning is needed to go further with the research introduced here. In this sense, design and implementation of policies must respond to the spatial criteria in which urban spaces have an influence. Studies should be carried out to propose zoning with lighting criteria that consider the environment and the needs of the city or cities within the metropolitan area according to scientific recommendations. The development of new and more appropriate regulations is a priority topic and a great challenge for experimentalists, urban modellers and light pollution researchers.

Acknowledgements

This work was supported by the Slovak Research and Development Agency under Project No. APVV-18-0014. Computational work was supported by the Slovak National Grant Agency VEGA (grant No. 2/0010/20).

References

- Alvarado, M. J., Lonsdale, C. R., Macintyre, H. L., Bian, H., Chin, M., Ridley, D. A., ... & Jimenez, J. L. (2016). Evaluating model parameterizations of submicron aerosol scattering and absorption with in situ data from ARCTAS 2008. *Atmospheric Chemistry and Physics*, 16(14), 9435-9455. <https://doi.org/10.5194/acp-16-9435-2016>
- Aubé, M., Franchomme-Fossé, L., Robert-Staehler, P., & Houle, V. (2005, agosto). Light pollution modeling and detection in a heterogeneous environment- Toward a night-time aerosol optical depth retrieval method. In *Proc. SPIE* (Vol. 5890, pp. 248-256). <https://doi:10.1117/12.615405>.

- Aubé, M., et al. Modelling the effects of phosphor converted LED lighting to the night sky of the Haleakala Observatory, Hawaii. *Monthly Notices of the Royal Astronomical Society* 478(2), 1776-1783.
- Baddiley, C. (2018) Light pollution modelling, and measurements at Malvern hills AONB, of county conversion to blue rich LEDs. *Journal of Quantitative Spectroscopy and Radiative Transfer* 219, 142-173.
- Barentine, J. C., et al. (2018) Skyglow changes over Tucson, Arizona, resulting from a municipal LED street lighting conversion. *Journal of Quantitative Spectroscopy and Radiative Transfer* 212, 10-23.
- Cinzano, P., & Castro, F. J. (1998). The artificial sky luminance and the emission angles of the upward light flux. *arXiv preprint astro-ph/9811297*.
- Falchi, F. et al. Limiting the impact of light pollution on human health, environment and stellar visibility. *J. Environ. Manag.* 2011, 92, 2714–2722.
- Garstang, R. H. (1986). Model for artificial night sky illumination. *Publications of the Astronomical Society of the Pacific*, 98(601), 364.
- Hernández-Garduño, E., et al. (1997). Air pollution and respiratory health in Mexico City. *J. Occup. Environ. Med.*, 39(4), 299-307.
- Kerker, M. (2016). *The scattering of light and other electromagnetic radiation*. Elsevier.
- Kocifaj, M., & Lamphar, H. S. (2013). Skyglow effects in UV and visible spectra: Radiative fluxes. *Journal of environmental management*, 127, 300-307.
- Kocifaj, M., & Lamphar, H. A. (2014). Skyglow: a retrieval of the approximate radiant intensity function of ground-based light sources. *Monthly Notices of the Royal Astronomical Society*, 439(4), 3405-3413. <https://doi:10.1093/mnras/stu180>
- Kocifaj, M., Lamphar, H. A., & Kundracik, F. (2015). Retrieval of Garstang's emission function from all-sky camera images. *Monthly Notices of the Royal Astronomical Society*, 453(1), 819-827. <https://doi:10.1093/mnras/stv1645>.
- Kocifaj M., 2017, SkyGlow Simulator, <http://skyglow.sav.sk/#simulator> (accessed Month Day, 2019).
- Kocifaj, M., Lamphar, H. A.S., & Videen, G. (2019). Night sky radiometry can revolutionize the characterization of light pollution sources globally. *Proceedings of the National Academy of Sciences*, 116(16), 7712-7717.

- Kyba, C.C.M. et al. Artificially lit surface of Earth at night increasing in radiance and extent. *Sci. Adv.* 2017, 3, e1701528.
- Kinzey, Bruce R., Perrin, Tess E., Miller, Naomi J., Kocifaj, Miroslav, Aube, Martin, & Lamphar, Hector. (2017). An Investigation of LED Street Lighting's Impact on Sky Glow. United States. doi:10.2172/1418092.
- Lamphar, H.A.S., Kocifaj, M., (2013). LP in ultraviolet and visible spectrum: effect on different visual perceptions. *Plos One* 8 (2), e56563.
- Lamphar, H.A.S. (2018). The emission function of ground-based light sources: state of the art and research challenges. *Journal of Quantitative Spectroscopy and Radiative Transfer*.
- Longcore, T., Rich, C., (2004). Ecological LP. *Front. Ecol. Environ.* 2 (4), 191-198.
- Luginbuhl, C. B., et al. (2009). From the ground up II: Sky glow and near-ground artificial light propagation in Flagstaff, Arizona. *Publications of the Astronomical Society of the Pacific*, 121(876), 204. <https://doi.10.1086/597626>
- Navara, K.J., Nelson, R.J., (2007). The dark side of light at night: physiological, epidemiological, and ecological consequences. *J. Pineal Res.* 43 (3), 215-224.
- O'Dea, W. T. (1951). Artificial lighting prior to 1800 and its social effects. *Folklore*, 62(2), 312-324.
- Pawson, S.M., Bader, M.F. (2014). LED lighting increases the ecological impact of LP irrespective of color temperature. *Ecol. Appl.* 24 (7), 1561-1568.
- Riojas-Rodríguez, H., et al. (2014) Health impact assessment of decreases in PM10 and ozone concentrations in the Mexico City Metropolitan Area. A basis for a new air quality management program, *Salud Publica Mex.*, 56(6):579-91.
- Seinfeld, J. H., & Pandis, S. N. (2016). *Atmospheric chemistry and physics: from air pollution to climate change*. John Wiley & Sons.
- Schernhammer, E. S., Schulmeister, K. (2004). Melatonin and cancer risk: does light at night compromise physiologic cancer protection by lowering serum melatonin levels? *British journal of cancer*, 90(5), 941-943.
- Téllez-Rojo, M. M., et al. (2000). Daily respiratory mortality and PM10 pollution in Mexico City: importance of considering place of death, *Eur Respir J.*, 16(3):391-6.
- Wallner, S., Kocifaj, M. (2019). Impacts of surface albedo variations on the night sky brightness - A numerical and experimental analysis, *Journal of Quantitative Spectroscopy and Radiative Transfer*, 239, 106648.

4.7 'Is the lumen output estimate from light-pollution sources suitable for bulk applications if based on population?'

Title: *Is the lumen output estimate from light-pollution sources suitable for bulk applications if based on population?*

Authors: M. Kocifaj, L. Komar, H. A. Solano-Lamphar, S. Wallner

Journal: Monthly Notices of the Royal Astronomical Society Letters (MNRASL)

Status: Published in MNRAS 496, L138-L141 (2020)

DOI: <https://doi.org/10.1093/mnrasl/slaa100>

Personal contribution: My contribution for this work was mainly in the development stage. Due to results from other studies, it was a joint idea towards this paper. I helped in the derivation of how to execute our idea and test it. Furthermore, I was involved in analysis of results and writing parts the letter. Additionally, I was involved in the revision process.



Are population-based models advantageous in estimating the lumen outputs from light-pollution sources?

M. Kocifaj,^{1,2★} L. Kómar,¹ H. Lamphar^{1,3} and S. Wallner^{①,4}

¹ICA, Slovak Academy of Sciences, Dúbravská cesta 9, 845 03 Bratislava, Slovakia

²Department of Experimental Physics, Faculty of Mathematics, Physics, and Informatics, Comenius University, Mlynská dolina, 842 48 Bratislava, Slovakia

³Cátedras CONACYT – The Center for Research in Geography and Geomatics "Ing. Jorge L. Tamayo" A.C. (CentroGeo), Contoy 137, Lomas de Padierna, Tlalpán, Ciudad de México 14240, Mexico

⁴Department of Astrophysics, University of Vienna, Türkenschanzstrasse 17, A-1180 Vienna, Austria

Accepted 2020 May 17. Received 2020 May 3; in original form 2020 March 21

ABSTRACT

The total lumen output (TLO) from ground-based artificial light sources is required in a wide range of light-pollution models currently in use. No realistic assessment of diffuse light levels in the nocturnal environment is possible if the information on TLO is missing. Traditional approaches to skyglow modelling, if no lighting inventory is available, foresee to estimate TLO based on population and average amount of lumens per capita. However, we show in this letter that a model based on the area of artificially lit surfaces can reduce uncertainties in estimating TLO by 25 per cent for compact urban areas of defined centres and autonomous character and even 50 per cent for diffuse cities with small satellite towns interacting closely with the main city. The new model could be of great significance to the community of light-pollution researchers, especially astronomers, physicists, and modellers who use TLO routinely in light-pollution characterization.

Key words: light pollution – methods: data analysis – methods: statistical.

1 INTRODUCTION

The primary influence of artificial light at night on skyglow is through its spectral power distribution, angular emission function, and total lumen output (TLO) of light sources. The TLO is indispensable in analysis of potential effects of artificial light sources on the night-sky brightness (NSB) level in city surroundings as the cumulative lumen output from whole-city light sources governs the amplitude of radiance variations. Due to the linearity of the radiative transfer equation, the NSB linearly scales down or up as TLO decreases or increases, respectively. TLO is therefore a key element in assessing the relative impacts of artificial lights on skyglow levels.

Unfortunately though, TLO is generally unknown for most of cities worldwide partly because the lighting inventory is either missing or incomplete, and partly because the potential methods of TLO retrieval require a certain experimental effort and mathematical workaround (see e.g. Duriscoe, Luginbuhl & Elvidge 2014; Kocifaj, Wallner & Solano-Lamphar 2019), and thus is not intended for routine use by non-specialists in the field. To make the TLO model useful to a wide community of researchers (including not only astronomers or physicists, but also engineers, city planners, biologists, environmentalists, or ecologists), it should be as simple as possible,

while allowing rapid computations and providing an estimate with reasonable error tolerance. A traditional approach used for over decades dates back to the classical works by Garstang (e.g. Garstang 1989), who assumed that the amount of light produced from a city is proportional to its population. The coefficient of proportionality is interpreted as light emission per head and can be arbitrary. Based on the inventory and modelling conducted one decade before this study, the coefficient of proportionality for North American cities was found to vary from a few hundreds to a few thousands of lumens per capita (see e.g. Luginbuhl et al. 2009), while typical values published three decades ago were about ≈ 1000 lm per head (see e.g. Lockwood, Floyd & Thompson 1990). Because of relatively wide interval, the proper value of the coefficient of proportionality is difficult to find. We have performed a set of modelling experiments in order to determine whether a more suitable model exists that is equally simple and rapid, but meets lower uncertainty needs. Of a few novel approaches under investigation, we introduce one that best matches all requirements and reduces uncertainties of the population-based model by 25–50 per cent.

2 DATA AND METHODS

Motivated by our modelling activities in the last few years, a hypothesis quickly arose that other than the population criterion would be useful to estimate TLO for different urbanized areas. Specifically, the use of the area of artificially lit surfaces seems to

★ E-mail: kocifaj@savba.sk



Figure 1. Geographical distribution of cities under consideration in our study (mostly eastern part of Germany). The map shows radiance data from www.lightpollutionmap.info by Jurij Stare.



Figure 2. The same as in Fig. 1 but for Spain.

have less trouble converging to a proper solution than the traditional approach based on the population. This property is easy to retrieve from publicly available VIIRS imagery of cities via Earth Observation Group of National Centers for Environmental Information NOAA website: <https://www.ngdc.noaa.gov/eog/index.html>, so the TLO estimation would remain as simple as up to now. VIIRS, the Visible Infrared Imaging Radiometer Suite equipped with day/night band (DNB) sensor, is an instrument onboard the *Suomi-NPP* satellite; see e.g. Levin & Zhang (2017) for VIIRS nighttime light imagery, or Miller et al. (2013) for VIIRS instrument capabilities. Although the method for obtaining the area of bright surfaces in a city or town is intrinsically simple (e.g. using the functionality of www.lightpollutionmap.info), its validation requires more effort to be spent before it will be released for a routine use.

For our analysis, 40 cities differing in population size (P) were randomly selected from Spain (P ranges from approximately 4000 to 200 000) and Germany ($P \approx 17\,000$ –550 000; mostly eastern part of Germany), 20 from each country (see Figs 1–2). We base on the premise that the territorial model of urbanization in these two countries has undergone a different evolution, going from an urban model of compact areas in Germany of defined centres and

Lumen output from light-pollution sources L139

autonomous character to a diffuse city model in Spain, motivated by different growing processes (cities and towns interacting closely with the main city), by universalization of car access, and by lowering the cost of transport. Radiance data were obtained from the standard annually averaged DNB VIIRS GeoTIFF file for the year 2018. This file contains cloud-free average radiance values that have undergone a process to filter out ephemeral lights. The file generated was processed using the geographic information system QGIS 3.12 in order to acquire pixel values. We established a threshold for the selection of the pixels. Due to the specified DNB radiance dynamic range declared (see e.g. Liao et al. 2013), we selected pixels with values higher than $3 \times 10^{-9} \text{ W cm}^{-2} \text{ sr}^{-1}$ only. In this sense, we can guarantee that the pixels with those values correspond only to the city lights and not to the scattered light around the light sources. (We mean here the threshold established regions of contiguous pixels above the cutoff. Those regions were converted to polygons and analysed in a GIS software.) Owing to the pixel selection in QGIS 3.12, we retrieved the shape of the area of interest. The average pixel radiance was converted to luminance in accordance with the following equation:

$$I_V = 683 \int_{500 \text{ nm}}^{900 \text{ nm}} S(\lambda) V(\lambda) I_e(\lambda) d\lambda, \quad (1)$$

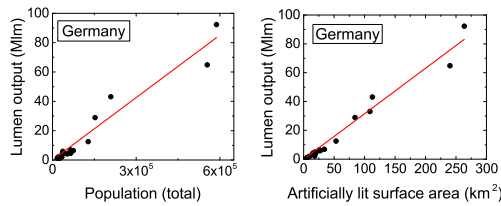
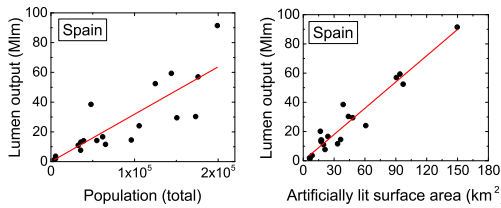
where the product of spectral power distribution $I_e(\lambda)$ of lights dominated in a city and the sensitivity $V(\lambda)$ of the retina for different wavelengths is multiplied by the spectral response $S(\lambda)$ of the VIIRS sensor. In other words, the spectral power distribution of the source ($\text{W m}^{-2} \text{ sr}^{-1} \text{ nm}^{-1}$) times the dimensionless VIIRS sensitivity (i.e. how much of the source VIIRS actually detects as a function of wavelength) times the normalized photopic luminous efficiency (the amount of that the eye actually sees) is integrated over the native bandpass of VIIRS and normalized by 683 lm W^{-1} . The result has luminance units (cd m^{-2}). I_V was determined by numerical integration within the spectral range of the sensor spectral sensitivity (see e.g. Cao & Bai 2014). TLO upwards can be computed using integration of I_V over all artificially lit surfaces in a city and all directions. Due to the fact that the emission function of the city is generally unknown, an isotropic radiator strategy is employed. Although this appears superficial compared with what we can potentially expect from various urban environments, the collective effect of differently oriented and sloped surfaces and complex arrangement of different types of light sources in the city is that the emission function usually slowly vary with zenith angle (see e.g. Kolláth & Kránicz 2014; Bará, private communication). Combining this model with the isotropic reflection from the ground (see e.g. Kastrov 1979) then appears to be a useful zero-order approximation. The lumen output computed as mentioned above was related to the total population and surface of bright city areas using linear regression performed by the least-squares method. The population was obtained from census data of the city of interest, while the area of bright parts of the city was determined by summation of surfaces over all pixels with brightness exceeding the threshold value of $3 \times 10^{-9} \text{ W cm}^{-2} \text{ sr}^{-1}$.

3 RESULTS

Based on analyses preceding this study, we decided to classify European cities into two categories, specifically of compact and diffuse type. Such classification is qualitative rather than quantitative, having its origin in urban planning theory. According to this theory, the compact city corresponds to a vertical model characterized by rather dense urbanization: vertical buildings, inserted in a wide

Table 1. Statistical indicators for two TLO models: the new one based on the area of artificially lit surfaces (left) and the traditional one based on population and average amount of lumens per capita (right).

	Surface area		Population	
	Germany	Spain	Germany	Spain
R^2	0.98	0.97	0.96	0.86
RMSE	4.23	6.32	5.89	12.8

**Figure 3.** TLO from cities displayed in Fig. 1. TLO is shown as a function of population (left) and area of artificially lit surfaces (right).**Figure 4.** TLO from cities displayed in Fig. 2. TLO is shown as a function of population (left) and area of artificially lit surfaces (right).

(preferably green) public space. The diffuse city often lacks an appropriate urban planning, while extending horizontally without limits. In result, compact cities tend to retain larger population in smaller spaces compared to what we observe in diffuse-like cities. The representative sets of both types are Spanish and German cities. The latter were found well isolated in most cases, while in Spain many cities are surrounded by several human settlements (some closely interacting with each other). This is why TLOs from German cities were found to be linked more tightly to the surface of illuminated area and population as well (see Table 1). This is elucidated by comparing data scatter for German cities (Fig. 3) and Spanish cities (Fig. 4). It should be highlighted that increasing either the area of artificially lit surface or population, the TLO for Spanish cities increases approximately two times faster than that for German cities. However, this is not surprising given that the populated urban areas in Spain extend farther to the surrounding environment. Computing TLO from surface of radiating area instead of population better matches the experimental data for both compact and diffuse-type cities. The improvement is best for diffuse cities [consult Table 1 for Spain and compare root-mean-square error (RMSE) = 6.32 related to the surface area against RMSE = 12.8 obtained assuming population as an input value]. In this case, the RMSE decreases by a factor of 2. For more compact cities with much faster brightness decays at their edges, the RMSE reduces by almost 30 per cent (see results for German cities in Table 1).

4 DISCUSSION AND CONCLUDING REMARKS

The qualitative analysis was introduced in Section 3, which, however, also comprises clear quantitative aspects. Averaging over all samples can be interpreted in terms of linear trends $TLO(P)$ and $TLO(S)$, where P is population and S is the surface of radiating area in SI units (i.e. m^2):

$$TLO_C(P) = c_C^{(P)} P \approx 140P,$$

$$TLO_D(P) = c_D^{(P)} P \approx 320P,$$

$$TLO_C(S) = c_C^{(S)} S \approx 0.3S,$$

$$TLO_D(S) = c_D^{(S)} S \approx 0.6S, \quad (2)$$

where index 'C' indicates the class of compact cities and 'D' the class of diffuse cities for both of which the representative data sets were taken in Germany and Spain, respectively. The coefficients of proportionality $c_{CorD}^{(P/S)}$ in equation (2) generally vary less for German cities ($c_C^{(P)} = 98-206$, $c_C^{(S)} = 0.23-0.38$) but much more for cities in Spain ($c_D^{(P)} = 151-804$, $c_D^{(S)} = 0.4-1.2$). The results show that TLO as a function of population is highly dependent on the city under evaluation and for the diffuse-like cities the coefficients of proportionality can span over a large range with maximum to minimum ratio up to 5.3: 1. This is nearly of the same order as the results reported by Luginbuhl et al. (2009). On the other hand, the spectrum of values $c_D^{(S)}$ is narrower by a factor of approximately 2, so the concept of linear scaling of TLO and the surface of a radiating area is more suitable than relating the TLO to the population. We suppose that especially future developments of urban areas will show a decreasing conformity with the lumen-per-capita approach. One potential reason could be a continuous change in number of inhabitants of a city. In general, urban areas are recording population growth. However, even if the number of population is rising, the area of metropolitan areas is usually not or only slightly due to buildings and apartments becoming taller in their design to offer a higher number of people at a certain area. It follows that, even with a varying number of residents, especially modernized areas already show a constant surface covering of artificial light at night. Consequently, only if a city increases in size, there is also the need of new public lighting installations. Due to the fact that information and parameters about population and density but also satellite imagery are generally easy to obtain, the approach introduced in this work gives the possibility of approximating the TLO of a city in a simple procedure.

Although the analysis is confined to a finite number of cities, this number is high enough to draw statistical inferences. Of course, the data set can always be extended by new records (new cities), and, in fact, we expect this work will motivate researchers to do so. The findings reported here can be significant because they deviate appreciably from what has been widely used until now. It is also challenging the light-pollution researchers who can use this new approach in estimating the variability of NSB due to different light emissions from different cities.

ACKNOWLEDGEMENTS

This work was supported by the Slovak Research and Development Agency under contract no. APVV-18-0014. Computational work was supported by the Slovak National Grant Agency VEGA (grant no. 2/0010/20).

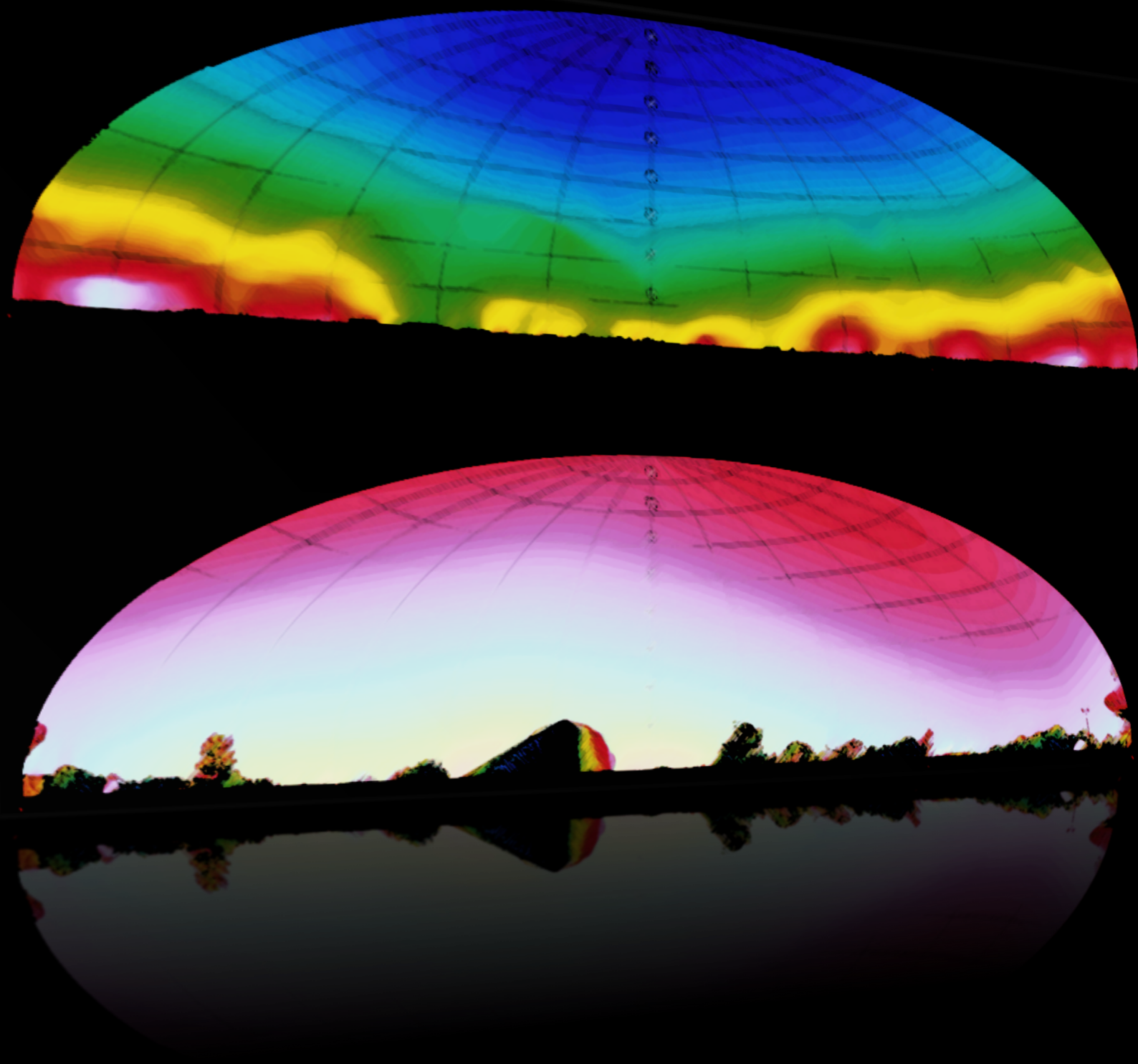
REFERENCES

- Cao C., Bai Y., 2014, *Remote Sens.*, 6, 11915
 Duriscoe D. M., Luginbuhl C. B., Elvidge C. D., 2014, *Light. Res. Technol.*, 46, 35
 Garstang R. H., 1989, *PASP*, 101, 306
 Kastrov V. G., 1979, *Works in Atmospheric Physics. Gidrometeoizdat, Leningrad*, p. 328
 Kocifaj M., Wallner S., Solano-Lamphar H. A., 2019, *MNRAS*, 485, 2214
 Kolláth Z., Kránicz B., 2014, *J. Quant. Spectrosc. Radiat. Transfer*, 139, 27

Lumen output from light-pollution sources L141

- Levin N., Zhang Q., 2017, *Remote Sens. Environ.*, 190, 366
 Liao L., Weiss S., Mills S., Hauss B., 2013, *J. Geophys. Res.*, 118, 12705
 Lockwood G. W., Floyd R. D., Thompson D. T., 1990, *PASP*, 102, 481
 Luginbuhl C. B., Lockwood G. W., Davis D. R., Pick K., Selders J., 2009, *PASP*, 121, 185
 Miller S. D. et al., 2013, *Remote Sens.*, 5, 6717

This paper has been typeset from a $\text{\TeX}/\text{\LaTeX}$ file prepared by the author.



CONCLUSIONS &
OUTLOOK

5

5 Conclusions and Outlook

5.1 Conclusions

The dissertation studied the global phenomenon of light pollution caused by artificial light at night. The focus of this work was to present fundamentals of the current state of research as well as to search for improvements and new developments helping to understand and examine potential impacts of the subject.

The works presented in Sections 4.3 and 4.4 can be assigned to the principle of measuring and analysing light pollution from ground-based observations. On the one hand, there was the development of a new measurement technique as not used in the light pollution community before. The utilisation of the 'vertical fisheye method' can be compared to luminance measurements as done in lighting engineering, but with the equipment and application as presented here, it was shown that there are lot more possibilities for light pollution researchers and commonly used instruments. It enables to quantify levels of light pollution in very small scales and can assist finding optimal solutions for every individual lighting situation. On the other hand, a new method of analysing long-term observational data was inspected via the Fast Fourier Transform. Usually a widely used tool for big data science, it was indicated that the night sky brightness data obtained from Austria were too unstable due to seasonal variations, although, with larger datasets of more observational years, the FFT-method can be optimally used to study impacts by certain amplitudes, like the circalunar cycle as done here. The evaluation of such amplitudes gives hints about the present intensity of light pollution at certain locations and its long-term evolution also.

The prediction of skyglow and the understanding of impacts by single parameters, especially of the highly variable atmosphere or other peripheral conditions, can be simulated via theoretical modelling. Sections 4.1, 4.6 and 4.7 participate in this activity and provided practical improvements for either modelling approaches or in understanding the aspects of external influences. First, there was the development of an asymptotical formula, aiming to simulate impacts from light pollution sources at far distances. Usually, such task is connected to high computational time due to its increasing complexity for larger domains. The introduced method entails only low amount of time for simulations while it was possible to keep a potential error level low and will be a useful assistance for skyglow modelling in the future. Second, the connection between light and air pollution, also currently presenting a research topic of high importance, was determined. It was demonstrated that turbid atmospheres do have significant impacts on the behaviour of skyglow and lighting situations are potentially exacerbated. Furthermore, there was discussion about light conversions, with the conclusion that there is the need of choosing optimal solutions with the important respect to being environmentally friendly. The aim was to bring our message to decision makers of urban and environmental planning, especially of megacities. Results shall stimulate to think about choices of lighting sources, since their parameters, like the correlated colour temperature or intensity, play a major role in protecting all living creatures against the influences of ALAN. Third, there was a questioning of an integral part of light pollution modelling which is substantially defining a city emission function. In detail, the derivation of total lumen output depending on the lumen-per-capita approach was challenged. The outline showed that this definition should be thoroughly scrutinised in the future, since it was shown that such usage leads to widely differing results, although, depending apparently stronger on other city properties like population density. Since here a fundamental basic concept of skyglow modelling was doubted, there is the expectation of focus on this issue in the future by researchers in the field.

Having displayed results of measuring and modelling light pollution individually, in Sections 4.2 and 4.5 works are presented which were facilitated by uniting both approaches. Since night sky brightness values are not constant over an area or time, there was a detailed analysis about the impact of surface albedo and its changes to skyglow. Furthermore, it was examined how such changes have to be treated in theoretical simulations. As the findings illustrate, seasonal trends as observed by ground-based devices were clearly visible over a year, underlining the importance of albedo to light pollution investigations. Consequently, also modelling tools have to deal with the reflectivity of the ground being a by far non-neglectable parameter. Additionally, findings have shown that theoretical results potentially show wide distinctions if either using an average albedo value over a city or clearly graduate various parts with values being chosen according to more realistic conditions. Consequently, results of this work provide a fundamental understanding of the importance of the surface albedo in observational or theoretical analysis of the night sky brightness and how to optimally treat this issue in modelling tools to refine predictions. Another objective of investigation was the question concerning the problem of the quantification of small and medium-sized cities solely while the night sky being influenced by more dominating and larger sources also. In fact, this work shall be of great advantages for future studies in light pollution, since unknown fundamental atmospheric parameters necessary to be included in theory, are implied via all-sky photometry, capturing the state of the environment. Due to leading to explicit reduction in computational time and also the requirement of only one in-situ measurement, there are expectations this technique, maybe in advanced forms, will become a well established approach for characterising smaller cities, e.g., situated around astronomical observatories, in future research.

As it was shown, the phenomenon of ALAN and its impacts are a global and interdisciplinary issue and especially due to the current trend of converting lighting systems, there is the must not to miss chances towards sustainability and environmental protection. Although, numbers of its development clarify that there is still large amount of work to do, especially to raise awareness of this problem. The main objective of this thesis is to be one of the potential actions against further increases by outlining the basics and studying ways of characterisation and quantification of light pollution. Consequently, outcomes shall also be used for research disciplines of other fields, since it creates new fundamentals for nature related studies in, e.g., ecology, (chrono-)biology and environmental physics, or even for technical studies like lighting management, sustainability and energy saving purposes.

5.2 Outlook

As we are now seeing, many cities worldwide, including Vienna, are changing current existing and mostly outdated lighting situation systems from inefficient lamps of past generations to Light Emitting Diodes (LEDs), often emitting large amounts of light in short wavelengths (blue). This foregoing will lead to major issues for light pollution research in the future. The majority of gathered data originate from either one-dimensional photometric measurements by detecting the brightness of the sky's zenith luminosity, logged by Sky Quality Meter-devices, or from satellite data, mostly obtained by the Visible Infrared Imaging Radiometer Suite (VIIRS) satellite. Both methods are going to lead to difficulties in the long run, as their spectral sensitivities show weaknesses, being mostly blind to short wavelengths. Even if cities increase the number of total lumen output, by changing the colour of light emitting sources to white-light LEDs, existing devices are going to predict a decrease in skyglow. Therefore, it is of great importance and one of the goals for the near future taking a closer look on the true effectiveness of current used devices and their data analyses. However, it is clear that there is the need to find either novel approaches in their usage or a completely new generation of instruments. Consequently, this is valid for ground-based observations and also those from space. Nevertheless,

this underlines that the significance of modelling tools and theoretical simulations will rise.

Another future goal to be studied in detail involves long-term measurements. Of course, like mentioned above, errors by used devices can influence them, but also the impact of meteorological parameters influence the amplification of light pollution substantial. Past works have shown that cloud coverage, humidity and also fine dust play important roles, mostly increasing skyglow around urban regions. Consequently, there is the need to conduct more detailed surveys regarding air pollution and the impacts of single particles at different atmospherical circumstances and at various environmental conditions. By conducting such data it shall be possible to make approaches of theoretical modelling of light pollution more exact, being able to predict skyglow with higher precision than at the time.

Furthermore, up-to-date there is one fundamental basis missing and its retrieval can be seen as one of the greatest challenges in light pollution research: a reference night sky. Although, it may be relatively easy to find areas on our planet with no light pollution or impact by ALAN at all, there are many open questions preventing this issue to be solved. Even if there were observations in deepest areas of the Pacific Ocean, one has to very critically question findings. What is the atmospheric condition characterising a 'reference sky'? What about the natural starlight or the brightness of other celestial objects moving across the sky and alternating in the process of time? Which conditions on the ground have no impact to the night sky? There are many open questions leading to this issue remaining unsolved until there will be a clear definition of a reference sky's character.

In general, light pollution research still faces many open goals to be reached in the future. With its increasing attention, there is the hope of more scientists and activists working together towards their solutions.

References

- M. Aubé and M. Kocifaj. Using two light-pollution models to investigate artificial sky radiances at Canary Island observatories. *Monthly Notices of the Royal Astronomical Society*, 422:819 – 830, 2012. doi: 10.1111/j.1365-2966.2012.20664.x.
- M. Aubé and A. Simoneau. New features to the night sky radiance model illumina: Hyperspectral support, improved obstacles and cloud reflection. *Journal of Quantitative Spectroscopy & Radiative Transfer*, 211:25 – 34, 2018. doi: 10.1016/j.jqsrt.2018.02.033.
- M. Aubé, L. Franchomme-Fossé, P. Robert-Staehler, and V. Houle. Light Pollution Modelling and Detection in a Heterogeneous Environment: Toward a Night Time Aerosol Optical Depth Retrieval Method. In H. A. Huang, H. J. Bloom, X. Xu, and G. J. Dittberner, editors, *Proceedings of SPIE Vol. 5890: Atmospheric and Environmental Remote Sensing Data Processing and Utilization: Numerical Atmospheric Prediction and Environmental Monitoring*, number 589012, 2005. doi: 10.1117/12.615405.
- M. Aubé, J. Roby, and M. Kocifaj. Evaluating Potential Spectral Impacts of Various Artificial Lights on Melatonin Suppression, Photosynthesis, and Star Visibility. *PLoS ONE*, 8(7)(e67798), 2013. doi: 10.1371/journal.pone.0067798.
- M. Aubé, M. Kocifaj, J. Zamorano, H. A. Solano-Lamphar, and A. Sanchez de Miguel. The spectral amplification effect of clouds to the night sky radiance in Madrid. *Journal of Quantitative Spectroscopy & Radiative Transfer*, 181:11 – 23, 2016. doi: 10.1016/j.jqsrt.2016.01.032.
- M. Ben-Attia et al. Blooming rhythms of cactus *Cereus peruvianus* with nocturnal peak at full moon during seasons of prolonged daytime photoperiod. *Chronobiology International*, 33(4):419–430, 2016. doi: 10.3109/07420528.2016.1157082.
- J. J. Bennie, J. P. Duffy, R. Inger, and K. J. Gaston. Biogeography of time partitioning in mammals. *Proceedings of the National Academy of Sciences of the United States of America*, 111(38):13727 – 13732, 2014. doi: 10.1073/pnas.1216063110.
- C. F. Bohren and D. R. Huffman. *Absorption and Scattering of Light by Small Particles*, chapter 8, pages 181–223. John Wiley & Sons, Ltd, 1983. ISBN 9783527618156. doi: 10.1002/9783527618156.ch8. URL <https://onlinelibrary.wiley.com/doi/abs/10.1002/9783527618156.ch8>.
- J. E. Bortle. The Bortle Dark-Sky Scale. *Sky Telescope*, 2:126 – 129, 2001.
- J. C. Braak, J. F. de Haan, C. V. M. Van der Mee, and J. W. Hovenier. Parameterized scattering matrices for small particles in planetary atmospheres. *Journal of Quantitative Spectroscopy and Radiative Transfer*, 69(5):585 – 604, 2001. doi: 10.1016/S0022-4073(00)00103-5.
- E. Bünning and I. Moser. Interference of moonlight with the photoperiodic measurement of time by plants and their adaptive reaction. *Proceedings of the National Academy of Sciences of the United States of America*, 62:1018 – 1022, 1969. doi: 10.1073/pnas.62.4.1018.
- C. Cajochen et al. Evening exposure to a light-emitting diodes (LED)-backlit computer screen affects circadian physiology and cognitive performance. *Journal of Applied Physiology*, 110(5):1432 – 1438, 2011. doi: 10.1152/jappphysiol.00165.2011.

- C. Cao, F. J. De Luccia, X. Xiong, R. Wolfe, and F. Weng. Early On-Orbit Performance of the Visible Infrared Imaging Radiometer Suite Onboard the Suomi National Polar-Orbiting Partnership (SNPP) Satellite. *IEEE Transactions on Geoscience and Remote Sensing*, 52(2):1142 – 1156, 2014. doi: 10.1109/TGRS.2013.2247768.
- C. Changyong et al. Visible Infrared Imaging Radiometer Suite (VIIRS) Sensor Data Record (SDR) User's Guide. Technical report, NOAA Technical Report NESDIS 142, 2017. <https://ncc.nesdis.noaa.gov/documents/documentation/viirs-users-guide-tech-report-142a-v1.3.pdf> [last accessed 22nd March, 2020].
- P. Cinzano. Night Sky Photometry with Sky Quality Meter. ISTIL Internal Report v1.4 nr. 9, ISTIL, Thiene, 2005. <http://www.lightpollution.it/download/sqmreport.pdf> [last accessed 18th March, 2020].
- P. Cinzano. Report on Sky Quality Meter, version L. ISTIL Internal Report v0.9, ISTIL, Thiene, 2007. <http://unihedron.com/projects/sqm-1/sqmreport2.pdf> [last accessed 18th March, 2020].
- P. Cinzano, F. Falchi, C. D. Elvidge, and K. E. Baugh. The artificial night sky brightness mapped from DMSP satellite Operational Linescan System measurements. *Monthly Notices of the Royal Astronomical Society*, 318(3):641 – 657, 2000. doi: 10.1046/j.1365-8711.2000.03562.x.
- J. Coesfeld, T. Kuester, H. U. Kuechly, and C. C. M. Kyba. Reducing Variability and Removing Natural Light from Nighttime Satellite Imagery: A Case Study Using the VIIRS DNB. *Sensors*, 20(3287), 2020. doi: 10.3390/s20113287.
- A. Crumey. Human contrast threshold and astronomical visibility. *Monthly Notices of the Royal Astronomical Society*, 442:2600 – 2619, 2014. doi: 10.1093/mnras/stu992.
- T. W. Davies and T. Smyth. Why artificial light at night should be a focus for global change research in the 21st century. *Global Change Biology*, 24(3):872–882, 2018. doi: 10.1111/gcb.13927.
- T. W. Davies, J. Bennie, R. Inger, N. H. De Ibarra, and K. J. Gaston. Artificial light pollution: Are shifting spectral signatures changing the balance of species interactions? . *Global Change Biology*, 19:1417 – 1423, 2013. doi: 10.1111/gcb.12166.
- D. M. Duriscoe, C. B. Luginbuhl, and C. A. Moore. Measuring night-sky brightness with a wide-field CCD camera. *Publications of the Astronomical Society of the Pacific*, 119(852):192, 2007. doi: 10.1086/512069.
- G. Eisenbeis and A. Hänel. *Ecology of Cities and Towns*, chapter 15: Light pollution and the impact of artificial night lighting on insects, pages 243 – 263. Cambridge University Press, 2009.
- F. Falchi, P. Cinzano, C. D. Elvidge, D. M. Keith, and A. Haim. Limiting the impact of light pollution on human health, environment and stellar visibility. *Journal of Environmental Management*, 92: 2714 – 2722, 2011. doi: 10.1016/j.jenvman.2011.06.029.
- F. Falchi, P. Cinzano, D. Duriscoe, C. C. M. Kyba, C. D. Elvidge, K. Baugh, B. Portnov, N. A. Rybnikova, and R. Furgoni. Supplement to: The New World Atlas of Artificial Night Sky Brightness. V. 1.1., 2016a.
- F. Falchi et al. The new world atlas of artificial night sky brightness. *Science Advances*, 2(6, e1600377), 2016b. doi: 10.1126/sciadv.1600377.

- R. H. Garstang. Model for artificial night-sky illumination. *Publications of the Astronomical Society of the Pacific*, 98:364 – 375, 1986. doi: 10.1086/131768.
- R. H. Garstang. Limiting visual magnitude and night sky brightness. *Memorie della Società Astronomia Italiana*, 71:83 – 92, 2000.
- K. J. Gaston, J. Bennie, T. W. Davies, and J. Hopkins. The ecological impacts of nighttime light pollution: a mechanistic appraisal. *Biological Reviews*, 88:912 – 927, 2013. doi: 10.1111/brv.12036.
- M. Grubisic, R. H. A. van Grunsven, A. Manfrin an M. T. Monaghan, and F. Hölker. A transition to white LED increases ecological impacts of nocturnal illumination on aquatic primary producers in a lowland agricultural drainage ditch. *Environmental Pollution*, 240:630 – 638, 2018. doi: 10.1016/j.envpol.2018.04.146.
- A. Hänel, T. Posch, S. J. Ribas, M. Aubé, D. Duriscoe, A. Jechow, Z. Kolláth, D. E. Lolkema, C. Moore, N. Schmidt, H. Spoelstra, G. Wuchterl, and C. C. M. Kyba. Measuring night sky brightness: methods and challenges. *Journal of Quantitative Spectroscopy & Radiative Transfer*, 205:278 – 290, 2018. doi: 10.1016/j.jqsrt.2017.09.008.
- S. Hecht. Visual Thresholds of Steady Point Sources of Light in Fields of Brightness from Dark to Daylight. *Journal of the Optical Society of America*, 37(1):59, 1947.
- G. H. Herbig. Stellar Magnitudes. *Astronomical Society of the Pacific Leaflets*, 4(198):386 – 393, 1945.
- F. Hölker, C. Wolter, E. K. Perkin, and K. Tockner. Light pollution as a biodiversity threat. *Trends in Ecology and Evolution*, 25(12), 2010. doi: 10.1016/j.tree.2010.09.007.
- N. Holonyak and S. F. Bevacqua. Coherent (Visible) Light Emission From Ga(As) As_{1-x}Px Junctions. *Applied Physics Letters*, 1(4):82–83, 1962. doi: 10.1063/1.1753706.
- D. C. Hood and M. A. Finkelstein. *Handbook of Perception and Human Performance*, volume 1, chapter 5: Sensitivity to light, pages 5–16 – 5–18. Wiley, New York, 1986.
- H. Horvath. Basic optics, aerosol optics, and the role of scattering for sky radiance. *Journal of Quantitative Spectroscopy & Radiative Transfer*, 139:3 – 12, 2014. doi: 10.1016/j.jqsrt.2013.08.009.
- International Dark Sky Association. LED Practical Guide, 2018a. URL <https://www.darksky.org/our-work/lighting/lighting-for-citizens/led-guide/>. Webpage [last accessed June 28th, 2020].
- International Dark Sky Association. International Dark Sky Park Program Guidelines June 2018. online, 2018b. <https://www.darksky.org/wp-content/uploads/2018/12/IDSP-Guidelines-2018.pdf> [last accessed July 4th, 2020].
- International Dark Sky Association. International Dark Sky Places, 2020. URL <https://www.darksky.org/our-work/conservation/idsp/>. [last accessed July 4th, 2020].
- A. Jechow and F. Hölker. Snowglow—The Amplification of Skyglow by Snow and Clouds Can Exceed Full Moon Illuminance in Suburban Areas. *Journal of Imaging*, 5(8)(69), 2019. doi: 10.3390/jimaging5080069.

- A. Jechow, F. Hölker, Z. Kolláth, M. O. Gessner, and C. C. M. Kyba. Evaluating the summer night sky brightness at a research field site on Lake Stechlin in northeastern Germany. *Journal of Quantitative Spectroscopy & Radiative Transfer*, 181:24 – 32, 2016. doi: 10.1016/j.jqsrt.2016.02.005.
- A. Jechow, Z. Kolláth, S. J. Ribas, H. Spoelstra, F. Hölker, and C. C. M. Kyba. Imaging and mapping the impact of clouds on skyglow with all-sky photometry. *Scientific Reports*, 7:6741, 2017. doi: 10.1038/s41598-017-06998-z.
- A. Jechow, F. Hölker, and C. C. M. Kyba. Using all-sky differential photometry to investigate how nocturnal clouds darken the night sky in rural areas. *Scientific Reports*, 9:1391, 2019. doi: 10.1038/s41598-018-37817-8.
- Andreas Jechow et al. Tracking the dynamics of skyglow with differential photometry using a digital camera with fisheye lens. *Journal of Quantitative Spectroscopy and Radiative Transfer*, 209:212 – 223, 2018. ISSN 0022-4073. doi: <https://doi.org/10.1016/j.jqsrt.2018.01.032>. URL <http://www.sciencedirect.com/science/article/pii/S0022407317308725>.
- W. Jiang, G. He, T. Long, H. Guo, R. Yin, W. Leng, H. Liu, and G. Wang. Potentiality of Using LuoJia 1-01 Nighttime Light Imagery to Investigate Artificial Light Pollution. *Sensors*, 18:2900, 2018. doi: 10.3390/s18092900.
- J. H. Joseph, Y. J. Kaufman, and Y. Mekler. Urban light pollution: the effect of atmospheric aerosols on astronomical observations at night. *Applied Optics*, 30(21):3047 – 3058, 1991. doi: 10.1364/AO.30.003047.
- M. Kocifaj. Light-pollution model for cloudy and cloudless night skies with ground-based light sources. *Applied Optics*, 46(15):3013 – 3022, 2007. doi: 10.1364/AO.46.003013.
- M. Kocifaj. Light pollution simulations for planar ground-based light source. *Applied Optics*, 47(6): 792 – 798, 2008. doi: 10.1364/AO.47.000792.
- M. Kocifaj. Modelling the spectral behaviour of night skylight close to artificial light sources. *Monthly Notices of the Royal Astronomical Society*, 403:2105 – 2110, 2010. doi: 10.1111/j.1365-2966.2010.16241.x.
- M. Kocifaj. Multiple scattering contribution to the diffuse light of a night sky: A model which embraces all orders of scattering. *Journal of Quantitative Spectroscopy & Radiative Transfer*, 206: 260 – 272, 2018a. doi: 10.1016/j.jqsrt.2017.11.020.
- M. Kocifaj. Towards a comprehensive city emission function (CCEF). *Journal of Quantitative Spectroscopy & Radiative Transfer*, 205:253 – 266, 2018b. doi: 10.1016/j.jqsrt.2017.10.006.
- M. Kocifaj and L. Kómar. A role of aerosol particles in forming urban skyglow and skyglow from distant cities. *Monthly Notices of the Royal Astronomical Society*, 458:438 – 448, 2016. doi: 10.1093/mnras/stw293.
- M. Kocifaj, I. Kapišinský, and F. Kundracik. Optical effects of irregular cosmic dust particle U2015 B10. *Journal of Quantitative Spectroscopy and Radiative Transfer*, 63(1):1 – 14, 1999. doi: 10.1016/S0022-4073(98)00130-7.
- M. Kocifaj, H. A. Solano-Lamphar, and F. Kundracik. Retrieval of Garstang’s emission function from all-sky camera images. *Monthly Notices of the Royal Astronomical Society*, 453:819 – 827, 2015. doi: 10.1093/mnras/stv1645.

- M. Kocifaj, S. Wallner, and H. A. Solano-Lamphar. An asymptotic formula for skyglow modelling over a large territory. *Monthly Notices of the Royal Astronomical Society*, 485:2214 – 2224, 2019. doi: 10.1093/mnras/stz520.
- M. Kocifaj, L. Kómar, H. A. Solano-Lamphar, and S. Wallner. Are population-based models advantageous in estimating the lumen outputs from light-pollution sources? *Monthly Notices of the Royal Astronomical Society: Letters*, 496(1):L138 – L141, 2020. doi: 10.1093/mnras/laa100.
- Z. Kolláth and A. Dömény. Night sky quality monitoring in existing and planned dark sky parks by digital cameras. *International Journal of Sustainable Lighting*, 19:61 – 68, 2017. doi: 10.26607/ijsl.v19i1.70.
- Z. Kolláth and B. Kránicz. On the feasibility of inversion methods based on models of urban sky glow. *Journal of Quantitative Spectroscopy & Radiative Transfer*, 139:27 – 34, 2014. doi: 10.1016/j.jqsrt.2014.01.008.
- Z. Kolláth, A. Dömény, K. Kolláth, and B. Nagy. Qualifying lighting remodelling in a Hungarian city based on light pollution effects. *Journal of Quantitative Spectroscopy & Radiative Transfer*, 181: 46 – 51, 2016. doi: 10.1016/j.jqsrt.2016.02.025.
- Z. Kolláth, A. Cool, A. Jechow, K. Kolláth, D. Száz, and K. Pong Tong. Introducing the dark sky unit for multi-spectral measurement of the night sky quality with commercial digital cameras. *Journal of Quantitative Spectroscopy and Radiative Transfer*, 253(107162), 2020. doi: <https://doi.org/10.1016/j.jqsrt.2020.107162>.
- S. Kotthaus, T. E. L. Smith, M. J. Wooster, and C. S. B. Grimmond. Derivation of an urban materials spectral library through emittance and reflectance spectroscopy. *ISPRS Journal of Photogrammetry and Remote Sensing*, 94:194 – 212, 2014. doi: 10.1016/j.isprsjprs.2014.05.005.
- C. C. M. Kyba, T. Kuester, A. Sánchez de Miguel, K. Baugh, A. Jechow, F. Hölker, J. Bennie, C. D. Elvidge, K. J. Gaston, and L. Guanter. Artificially lit surface of Earth at night increasing in radiance and extent. *Science Advances*, 3(11, e1701528), 2017. doi: 10.1126/sciadv.1701528.
- N. Levin et al. Remote sensing of night lights: A review and an outlook for the future. *Remote Sensing of Environment*, 237(111443), 2020. doi: 10.1016/j.rse.2019.111443.
- Lichttechnische Gesellschaft Österreichs. LED - Revolution in der Lichttechnik? online, 2012. Booklet. <http://aussenbeleuchtung.ltg.at/media/LED-2012.pdf> [last accessed June 28th, 2020].
- D. Liverington. *Babylon to Voyager and Beyond: A History of Planetary Astronomy*. Cambridge University Press, 2003.
- T. Longcore and C. Rich. Ecological light pollution. *Frontiers in Ecology and the Environment*, 2(4): 191 – 198, 2004. doi: 10.1890/1540-9295(2004)002[0191:ELP]2.0.CO;2.
- O. V. Lossev. CII. Luminous carborundum detector and detection effect and oscillations with crystals. *The London, Edinburgh, and Dublin Philosophical Magazine and Journal of Science*, 6(39):1024–1044, 1928. doi: 10.1080/14786441108564683.
- C. Luginbuhl et al. From the ground up II: sky glow and near-ground artificial light propagation in Flagstaff, Arizona. *Publications of the Astronomical Society of the Pacific*, 121:204 – 212, 2009. doi: 10.1086/597626.

- C. B. Luginbuhl, P. A. Boley, and D. R. Davis. The impact of light source spectral power distribution on sky glow. *Journal of Quantitative Spectroscopy & Radiative Transfer*, 139:21 – 26, 2014. doi: 10.1016/j.jqsrt.2013.12.004.
- C. S. McCamy. Correlated color temperature as an explicit function of chromaticity coordinates. *Color Research & Application*, 17(2):142 – 144, 1992. doi: 10.1002/col.5080170211.
- R. Y. Moore, J. C. Speh, and J. P. Card. The retinohypothalamic tract originates from a distinct subset of retinal ganglion cells. *Journal of Comparative Neurology*, 352(3):351–366, 1995. doi: 10.1002/cne.903520304.
- T. W. Murphy. Maximum spectral luminous efficacy of white light. *Journal of Applied Physics*, 111 (104909), 2012. doi: 10.1063/1.4721897.
- K. Nassau, editor. *Color for Science, Art and Technology*, volume 1. North Holland, 1997.
- D. B. Newell and E. Tiesinga, editors. *The International System of Units (SI)*, volume 330. National Institute of Standards and Technology, 2019. doi: <https://doi.org/10.6028/NIST.SP.330-2019>.
- D. E. Nye. *American Illuminations - Urban Lighting 1800-1920*, chapter 1: Illuminations, pages 11 – 33. Massachusetts Institute of Technology, 2018.
- Oberösterreichischer Energiesparverband. Straßenbeleuchtung mit LED. online, 2015. Booklet. https://www.richtig-hell.at/fileadmin/redakteure/ESV/Info_und_Service/Publikationen/Strassenbeleuchtung2015_dt.pdf [last accessed June 28th, 2020].
- ORF. Start zur Beleuchtung vor 325 Jahren, 2012. URL <https://wien.orf.at/v2/news/stories/2521725/>. Webpage. [last accessed June 28th].
- J. Palisa. Beobachtungen am 27-zölligen Refraktor. *Astronomische Nachrichten*, 222(11):161–172, 1924. doi: 10.1002/asna.19242221102.
- F. Patat. The Effects of Improper Lighting on Professional Astronomical Observations. 2010. <https://arxiv.org/pdf/1011.6175.pdf>
- M. Planck. On the law of distribution of energy in the normal spectrum. *Annalen der Physik*, 4(553), 1901.
- T. Posch, A. Freyhoff, and T. Uhlmann, editors. *Das Ende der Nacht - Lichtsmog: Gefahren - Perspektiven - Lösungen*, volume 1. Wiley-VCH, 2010.
- T. Posch, F. Binder, and J. Puschnig. Systematic measurements of the night sky brightness at 26 locations in Eastern Austria. *Journal of Quantitative Spectroscopy and Radiative Transfer*, 211: 144 – 165, 2018. doi: 10.1016/j.jqsrt.2018.03.010.
- T. Posch et al. Langzeitmessungen der Nachthimmelshelligkeit und Möglichkeiten für Nachthimmels-Schutzgebiete in Oberösterreich Endbericht der Studie des Instituts für Astrophysik an der Universitätssternwarte Wien, 2017. URL <http://www2.land-oberoesterreich.gv.at/internetpub/InternetPubPublikationDetail.jsp?SessionID=SID-BF9593AD-52BA835E&xmlid=Seiten%2F115999.htm&pbNr=300594&dest=ooe>. Technical Report. <http://www2.land-oberoesterreich.gv.at/internetpub/InternetPubPublikationDetail.jsp?SessionID=SID-BF9593AD-52BA835E&xmlid=Seiten%2F115999.htm&pbNr=300594&dest=ooe> [last accessed 19th March, 2020].

- P. Pracki. A proposal to classify road lighting energy efficiency. *Lighting Research Technology*, 43: 271 – 280, 2011. doi: 10.1177/1477153511407996.
- Province of Upper Austria. Austrian Guidelines for Outdoor Lighting. online, 2019. URL https://www.land-oberoesterreich.gv.at/files/publikationen/us_Leitfaden_Guidelines_Outdoor_lighting_english.pdf [last accessed July 4th, 2020].
- J. Puschnig, T. Posch, and S. Uttenthaler. Night sky photometry and spectroscopy performed at the Vienna University Observatory. *Journal of Quantitative Spectroscopy & Radiative Transfer*, 139: 64 – 75, 2014. doi: 10.1016/j.jqsrt.2013.08.019.
- J. Puschnig, S. Wallner, and T. Posch. Circalunar variations of the night sky brightness – an FFT perspective on the impact of light pollution. *Monthly Notices of the Royal Astronomical Society*, 492:2622 – 2637, 2020. doi: 10.1093/mnras/stz3514.
- R. J. Reiter et al. Light at Night, Chronodisruption, Melatonin Suppression, and Cancer Risk: A Review. *Critical Reviews in Oncogenesis*, 13(4):303 – 328, 2007. doi: 10.1615/critrevoncog.v13.i4.30.
- C. Rich and T. Longcore, editors. *Ecological Consequences of Artificial Night Lighting*, pages 15 – 42. Island Press, 2006.
- J. Roby and M. Aubé. LSPDD: Lamp Spectral Power Distribution Database. URL <http://www.lspdd.com> [last accessed July 3rd, 2020].
- H. J. Round. A note on Carborundum. *Electrical World*, 49:pp. 309, 1907.
- Royal Swedish Academy of Sciences. Scientific Background on the Nobel Prize in Physics 2014: Efficient Blue Light-Emitting Diodes Leading to Bright and Energy-Saving White Light Sources. online, 2014. URL <https://www.nobelprize.org/uploads/2018/06/advanced-physicsprize2014.pdf> [last accessed June 30th, 2020].
- S. Schroer, B. J. Huggins, C. Azam, and F. Hölker. Working with Inadequate Tools: Legislative Shortcomings in Protection against Ecological Effects of Artificial Light at Night. *Sustainability*, 12(2551), 2020. doi: 10.3390/su12062551.
- R. C. Shirkey. An Army Illumination Model (AAIM). Technical Report ARL-TR-4645, Army Research Laboratory, 2008. Technical Report. <https://apps.dtic.mil/dtic/tr/fulltext/u2/a493692.pdf> [last accessed 24th June, 2020].
- D. H. Sliney. What is light? The visible spectrum and beyond. *Eye*, 30(2):222 – 229, 2016. doi: 10.1038/eye.2015.252.
- H. Spoelstra. Sky brightness nomogram, 2009. URL <http://www.darkskiesawareness.org/nomogram.php> [last accessed on 18th March, 2020].
- R. G. Stevens and Y. Zhu. Electric light, particularly at night, disrupts human circadian rhythmicity: is that a problem? *Philosophical Transactions of the Royal Society B: Biological Sciences*, 370 (20140120), 2015. doi: 10.1098/rstb.2014.0120.

- R. G. Stevens et al. Meeting Report: The Role of Environmental Lighting and Circadian Disruption in Cancer and Other Diseases. *Environmental Health Perspectives*, 115(9):1357 – 1362, 2007. doi: 10.1289/ehp.10200.
- A. Stockman and L. T. Sharpe. Into the twilight zone: the complexities of mesopic vision and luminous efficiency. *Ophthalmic and Physiological Optics*, 26(3):225–239, 2006. doi: 10.1111/j.1475-1313.2006.00325.x.
- K. Thapan, J. Arendt, and D. J. Skene. An action spectrum for melatonin suppression: evidence for a novel non-rod, non-cone photoreceptor system in humans. *The Journal of Physiology*, 535(1): 261–267, 2001. doi: 10.1111/j.1469-7793.2001.t01-1-00261.x.
- D. Toublanc. Henyey–Greenstein and Mie phase functions in Monte Carlo radiative transfer computations. *Applied Optics*, 35(18):3270 – 3274, 1996. doi: 10.1364/AO.35.003270.
- J. B. Valencia, F. L. Giraldo, and J. V. Bonilla. Calibration method for Correlated Color Temperature (CCT) measurement using RGB color sensors. In *Symposium of Signals, Images and Artificial Vision - 2013: STSIVA - 2013*, pages 1–6. IEEE, 2013. doi: 10.1109/STSIVA.2013.6644921.
- S. Wallner. Eine Volkssternwarte für das Nordburgenland: Planungskonzept und Bedarfsanalyse. Master’s thesis, Department of Astrophysics, University of Vienna, 2017.
- S. Wallner. Usage of Vertical Fisheye-Images to Quantify Urban Light Pollution on Small Scales and the Impact of LED Conversion. *Journal of Imaging*, 5(86), 2019. doi: 10.3390/jimaging5110086.
- S. Wallner and M. Kocifaj. Impacts of surface albedo variations on the night sky brightness – A numerical and experimental analysis. *Journal of Quantitative Spectroscopy & Radiative Transfer*, 239(106648), 2019. doi: 10.1016/j.jqsrt.2019.106648.
- S. Wallner, M. Kocifaj, L. Kómar, and H. A. Solano-Lamphar. Night-sky imaging as a potential tool for characterization of total lumen output from small and medium-sized cities. *Monthly Notices of the Royal Astronomical Society*, 494:5008 – 5017, 2020. doi: 10.1093/mnras/staa925.
- C. Wang, Z. Chen, C. Yang, Q. Li, Q. Wu, J. Wu, G. Zhang, and B. Yu. Analyzing parcel-level relationships between Luojia 1-01 nighttime light intensity and artificial surface features across Shanghai, China: A comparison with NPP-VIIRS data. *International Journal of Applied Earth Observation and Geoinformation*, 85(101989), 2020. doi: 10.1016/j.jag.2019.101989.

Acknowledgements

There are numerous people I want to thank, and I hope to forget not one.

At first, I want to thank my family. My wife Anna, my two beautiful children Maximilian and Elisabeth. All three of them support me in my work day in, day out and naturally it took some time until this thesis was finished. So, let me tell you that I want to thank you with all of my heart, I love you and you are the most important part of my life. I am happy to share this work now with you. Biggest thanks to my parents Doris and Thomas also, who supported me throughout my educational career.

Another person I am deeply thankful is Miroslav Kocifaj. Without him, most of this thesis would not have been possible. It was the collaboration with him which resulted in a vast amount of ideas and works in this field. Thank you for being such a cooperative partner throughout my research career.

Another sincere thank goes to the Provincial Government of Upper Austria, especially Ing. Heribert Kaineder and Martin Waslmeier, for their cooperation in light pollution activities over the years.

Thank you to my supervisor, Franz Kerschbaum, who took charge over me in one of the most challenging times.

Furthermore, many thanks go out to: Franz Binder, Andreas Jechow, Martin Aubé, Zoltan Kolláth, Franz Hölker, Hector Solano-Lamphar, Ladislav Komar, Johannes Puschnig, and many more.

This dissertation is dedicated my beloved colleague Thomas Posch, he ought to take credit for everything I do in light pollution research. I hope you are well, this is for you, my friend!

Appendix

Scientific survey towards the establishment of the first official Dark Sky Park in Austria

by Stefan Wallner and Franz Binder

The authors are responsible for all results and figures in the following section.

According to the project end report 'Nachtlandschaftsschutzgebiete OÖ - Teil 2', May 2020.

The Nature Park Attersee-Traunsee

The first outline of the Dark Sky Park as wished was proposed by Nicole Eder (Mayor Steinbach am Attersee), Clemens Schnaitl (Director Nature Park Attersee-Traunsee), Heribert Kaineder (Office of the Provincial Government of Upper Austria) and Stefan Wallner (Department of Astrophysics). The boarder contains the entire Attersee-Traunsee Nature Park including the entire municipality of Steinbach am Attersee. Since the Nature Park appears very fragmented, especially on the outskirts, the borders there are designed as 'envelope'. The area thus reaches a size of approximately 155 km². Figure 38 shows the final boarder setting.

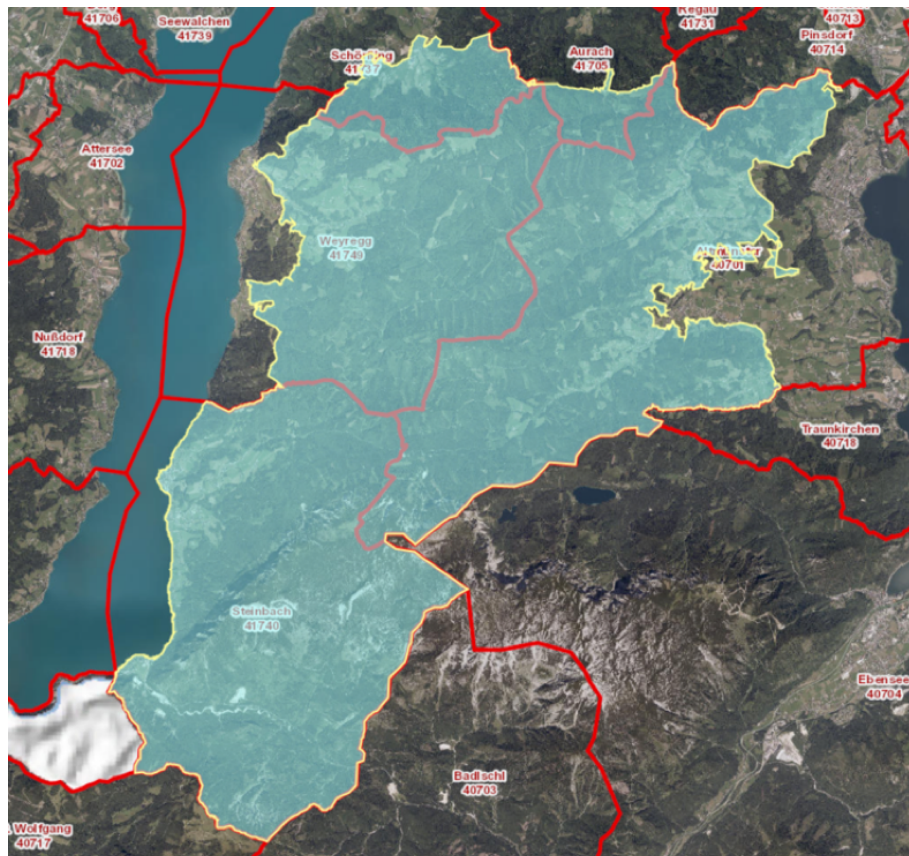


Figure 38 – Definition of borders of the Dark Sky Park as wished to be established. It is located at the Nature Park Attersee-Traunsee in Upper Austria.

Night sky quality in the Nature Park Attersee-Traunsee

Measurements of the night sky quality were carried out by the Department of Astrophysics, University of Vienna. Preconditions for measurements were cloudless nights with constant meteorological conditions, as well as an absence of the moon (new moon). Also no snow coverage on the ground was necessary in order to exclude the high albedo impacts of the snow. The following measurement methods were used for scientific analysis.

'Roadrunner' measurements

Sky Quality Meters, also known as SQM, take a one-dimensional point measurement at the zenith (highest point) of the sky. The result is immediately displayed in mag arcsec^{-2} . For this method, a SQM-LU from Unihedron was mounted on the roof of a car. The magnitudes and the associated coordinates, as well as altitude values, are saved by a connected mobile phone, see Figure 39. SQM measurements were carried out automatically at intervals of 30 seconds. More than 800 measuring points were collected this way over an entire night.

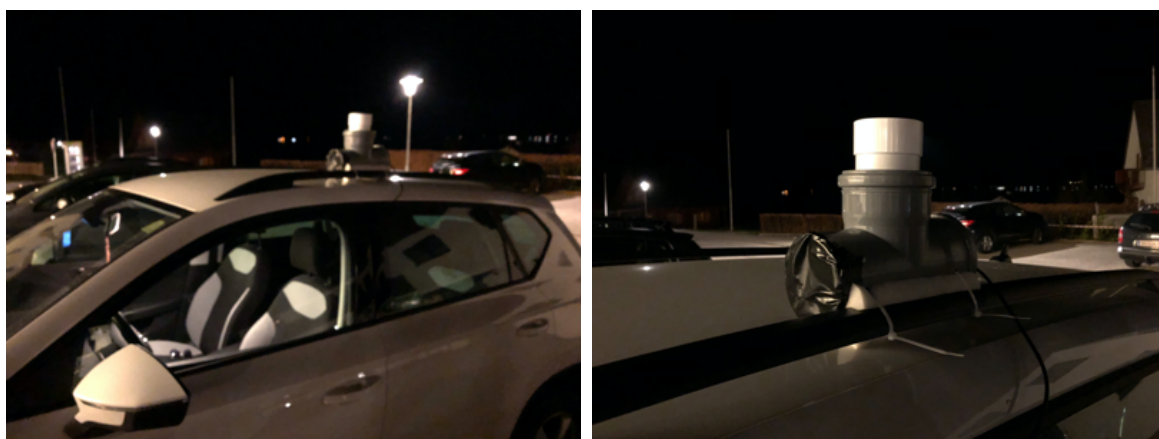


Figure 39 – 'Roadrunner' measurement technique, a SQM-LU device mounted on the roof of a car collecting night sky brightness data automatically. Via connection to a mobile phone, also location coordinates are recorded.

Two measurement runs were carried out in the area of the Attersee-Traunsee Nature Park. In order to obtain the results of two complementary seasons, the nights 30./31.3.2019 and 30./31.8.2019 were chosen. The results were cleaned with a filter to show values starting at $20.5 \text{ mag arcsec}^{-2}$. This was chosen with the aim to exclude the values caused by the stray light effects of the car headlights in, e.g., forest environments (see among others in the north of the area).

As expected, both nights show strongly fluctuating night sky brightness. This is mainly due to the brightness of the Milky Way, which stretched across the sky in August and was only observable in early morning measurements in March. The results show that the necessary sky brightness of $21.2 \text{ mag arcsec}^{-2}$ is achieved in the majority of the area in both nights. Figures 40 and 41 illustrate the measured values in the area.

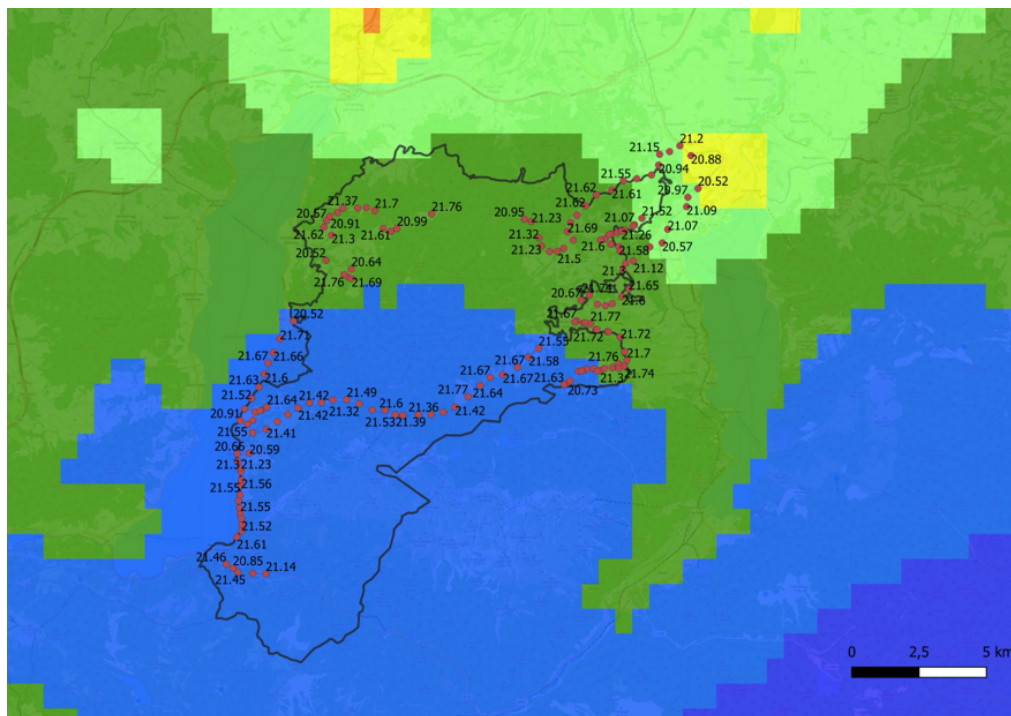


Figure 40 – Results of roadrunner measurement series as undertaken in March 2019.

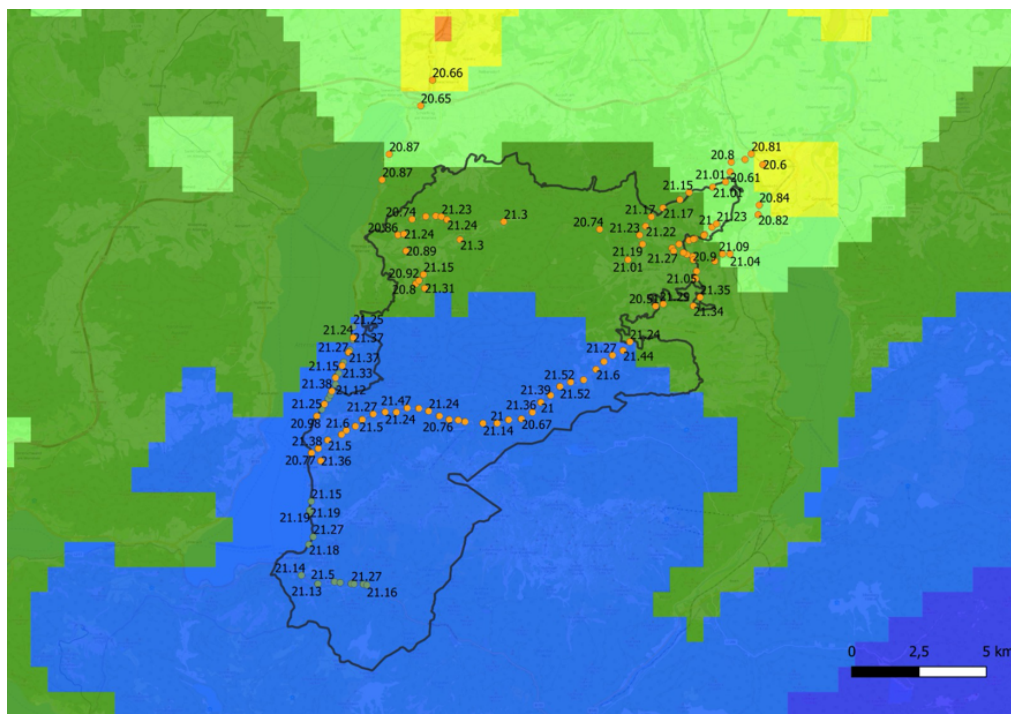


Figure 41 – Results of roadrunner measurement series as undertaken in August 2019.

All-sky measurements

These measurements are executed using a single-lens reflex camera with a fisheye lens attached to it. In contrast to an SQM, these types of observations offer the possibility to record not only one point, but the entire sky at a time. By processing these images, using special software, licensed for the working group at the Department of Astrophysics, a more detailed representation of the night sky quality is possible. This allows also to locate and analyse light domes especially at the horizon. According to requirements for a potential Dark Sky Park as provided by the IDA, such light domes must not be dominant in the sky. In order to be able to quantify the effects of light emissions around the potential area, this type of measurement should be carried out especially in the peripheral areas.

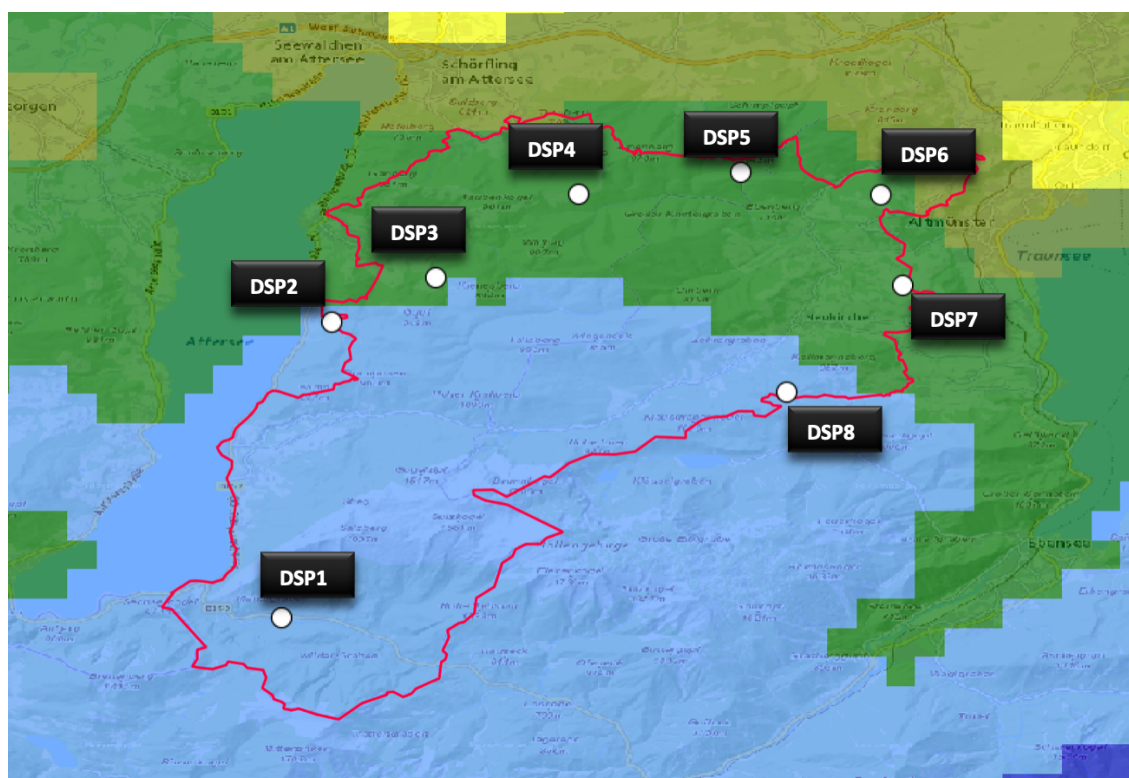


Figure 42 – Locations of all-sky measurements undertaken in the Nature Park in March 2019.

The all-sky measurement series at a total of eight locations, see Figure 42, were collected on the night of the first Roadrunner measurement series on March 30/31, 2019. A single series of measurements is sufficient, since the goal is not the value of the sky brightness, but the examination of skylights close to the horizon. The results and analyses as already carried out are shown in Figures 43-50. They show a light pollution matrix over the entire observable sky, each with values for brightness and correlated colour temperature.

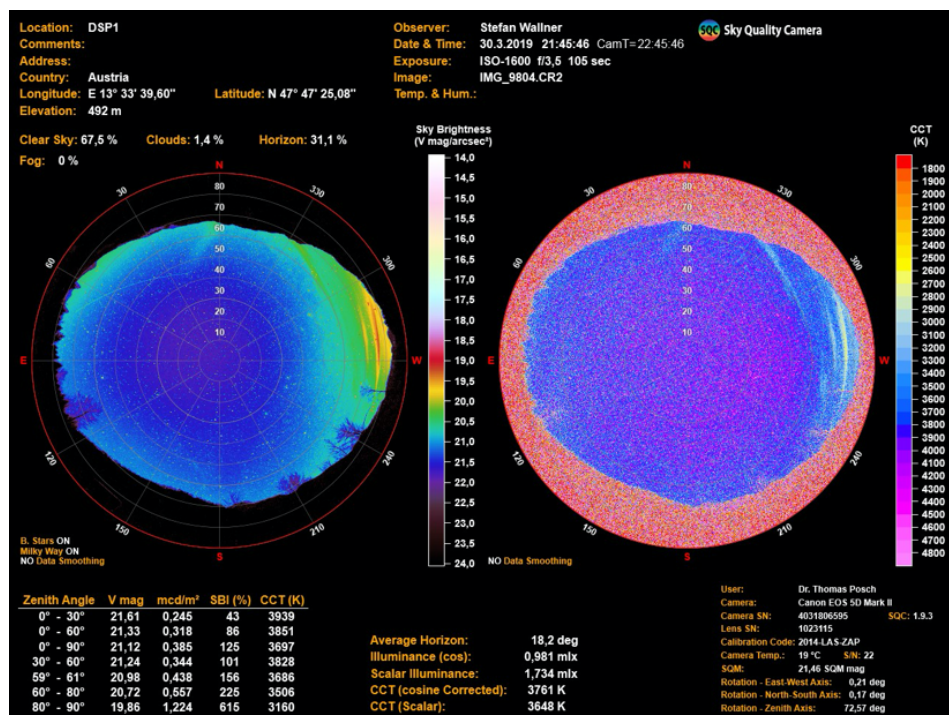


Figure 43 – SQC analysis of all-sky observation executed at location DSP1.

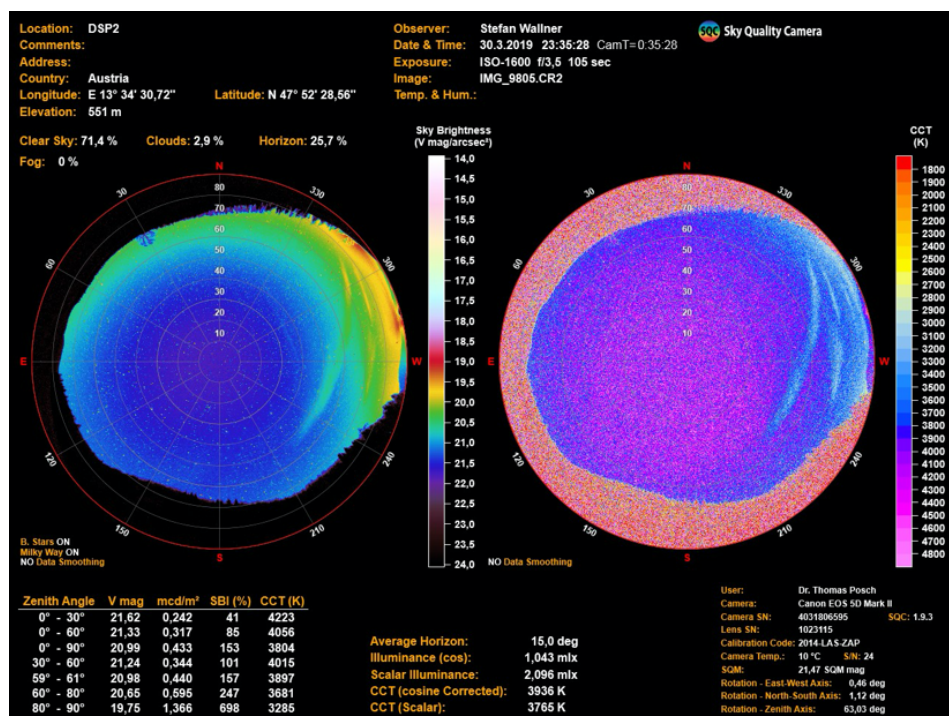


Figure 44 – SQC analysis of all-sky observation executed at location DSP2.

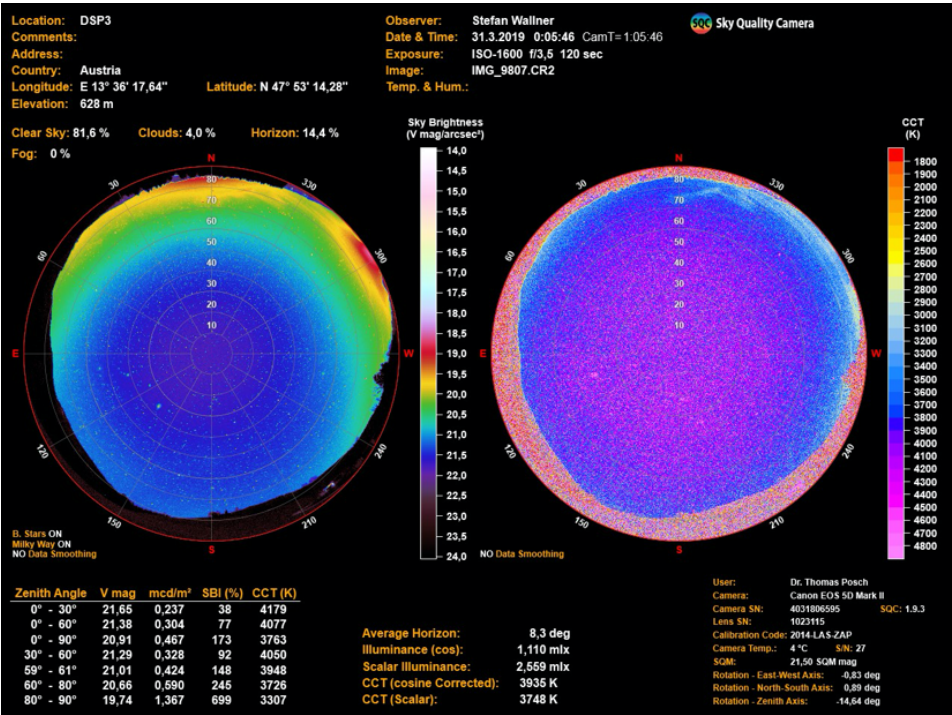


Figure 45 – SQC analysis of all-sky observation executed at location DSP3.

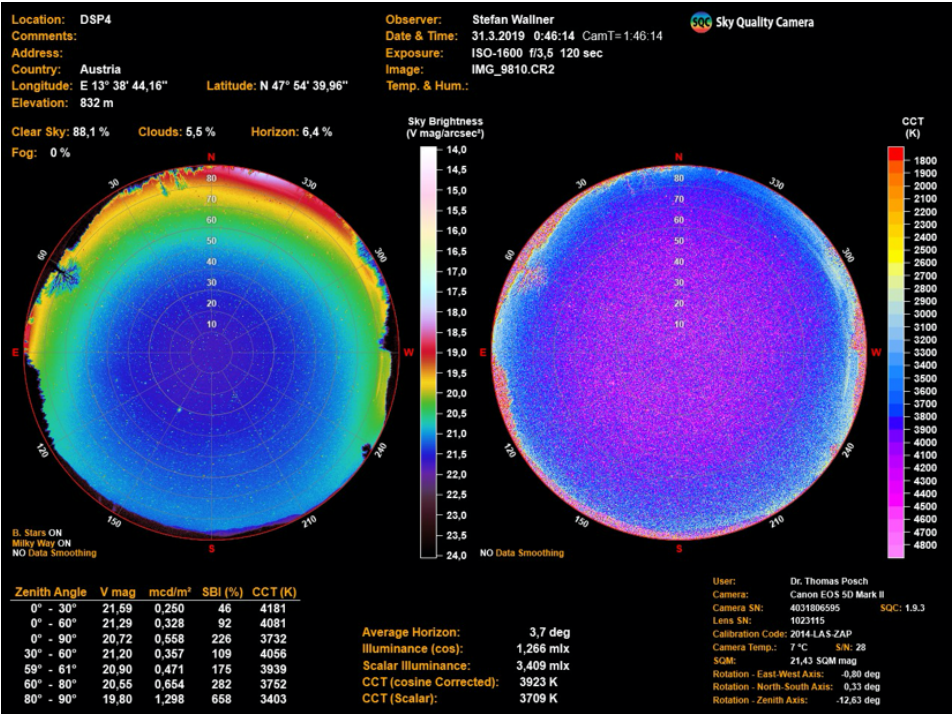


Figure 46 – SQC analysis of all-sky observation executed at location DSP4.

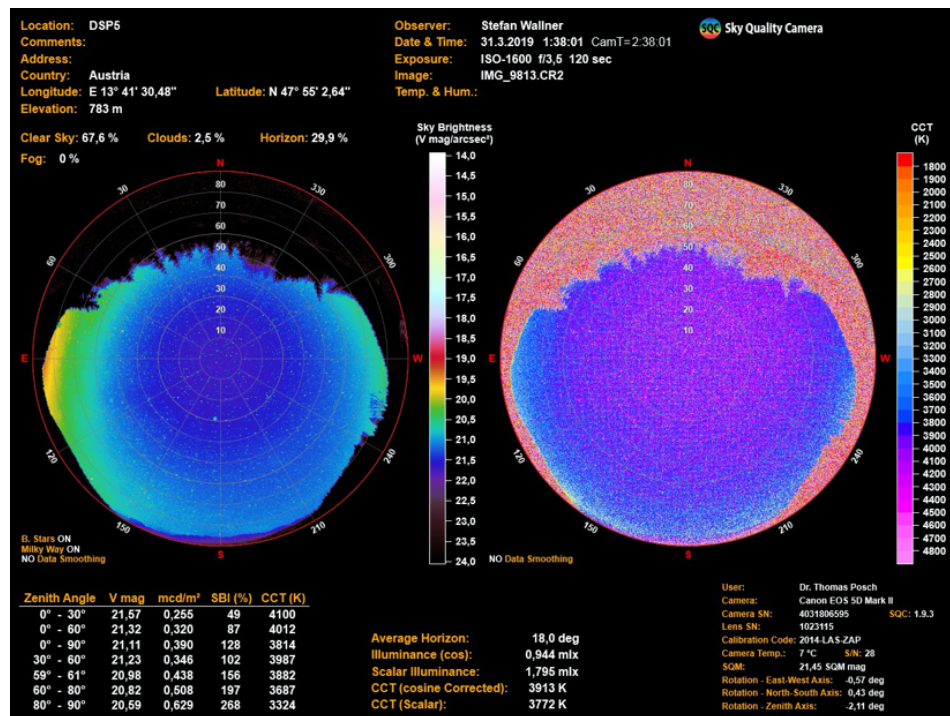


Figure 47 – SQC analysis of all-sky observation executed at location DSP5.

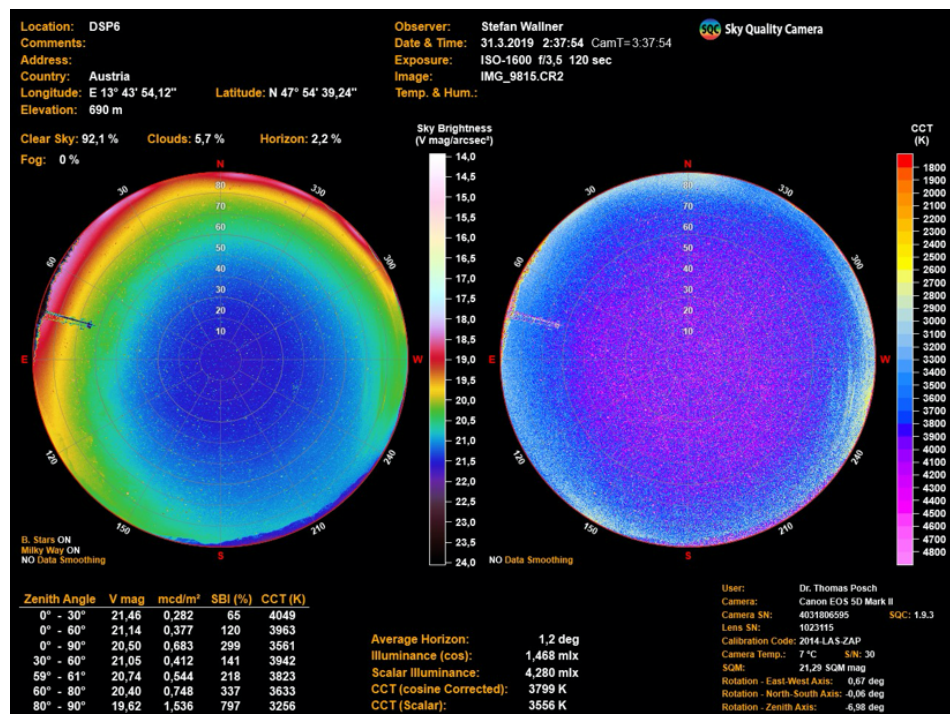


Figure 48 – SQC analysis of all-sky observation executed at location DSP6.

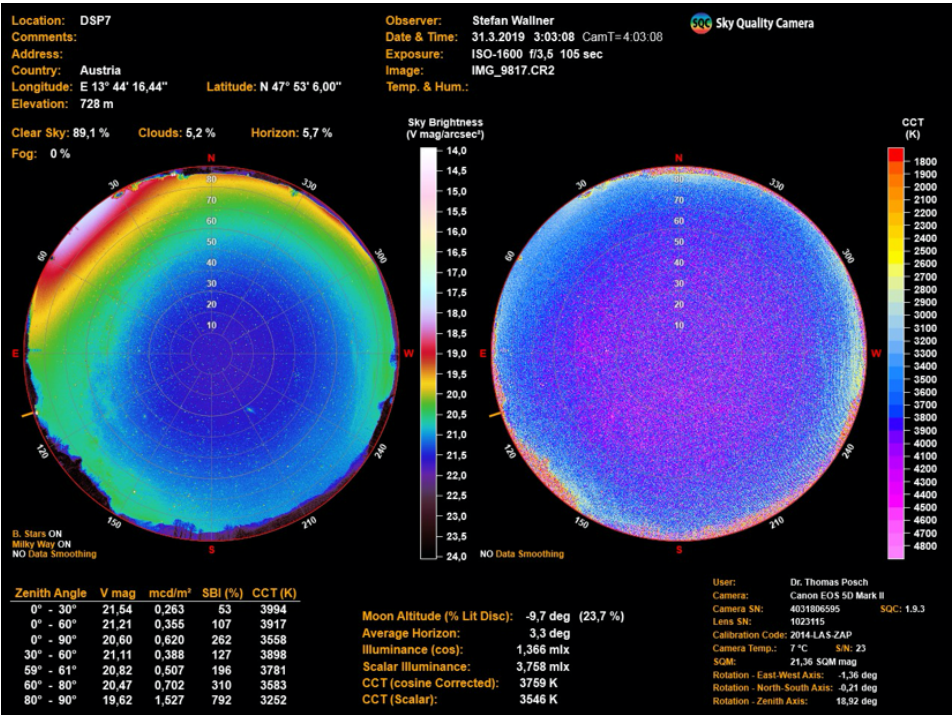


Figure 49 – SQC analysis of all-sky observation executed at location DSP7.

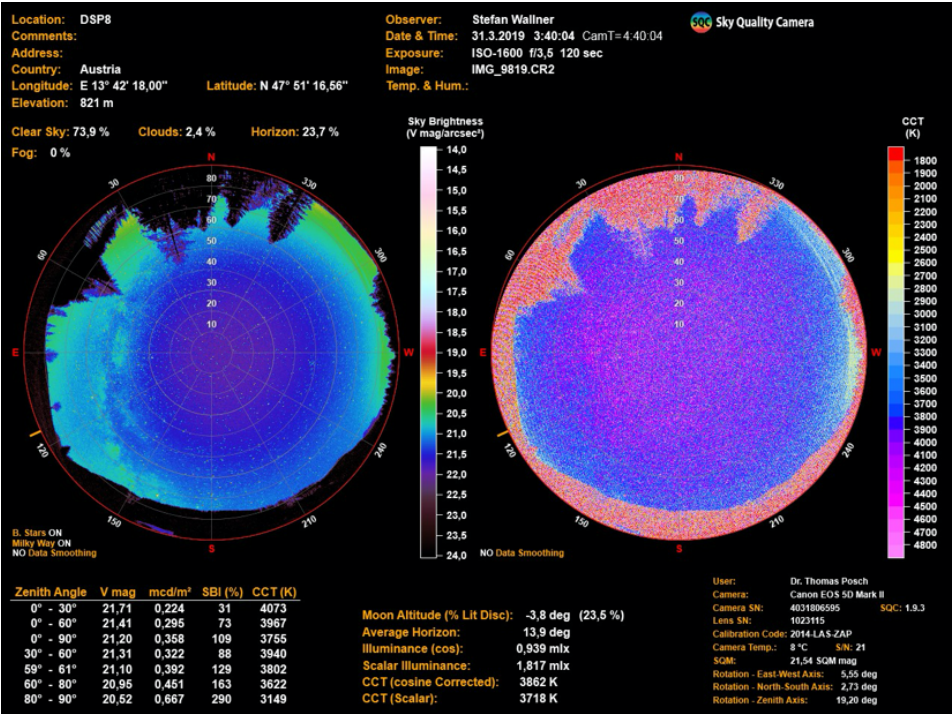


Figure 50 – SQC analysis of all-sky observation executed at location DSP8.

Lighting inventory

The lighting situation, as recorded aiming for a lighting management plan (LMP), as shown in Figure 51, is as follows: The municipality of Steinbach am Attersee is 100% compliant with the LMP, so there is no need for action here. The communities of Weyregg and Altmünster still have some lamps that need to be replaced.

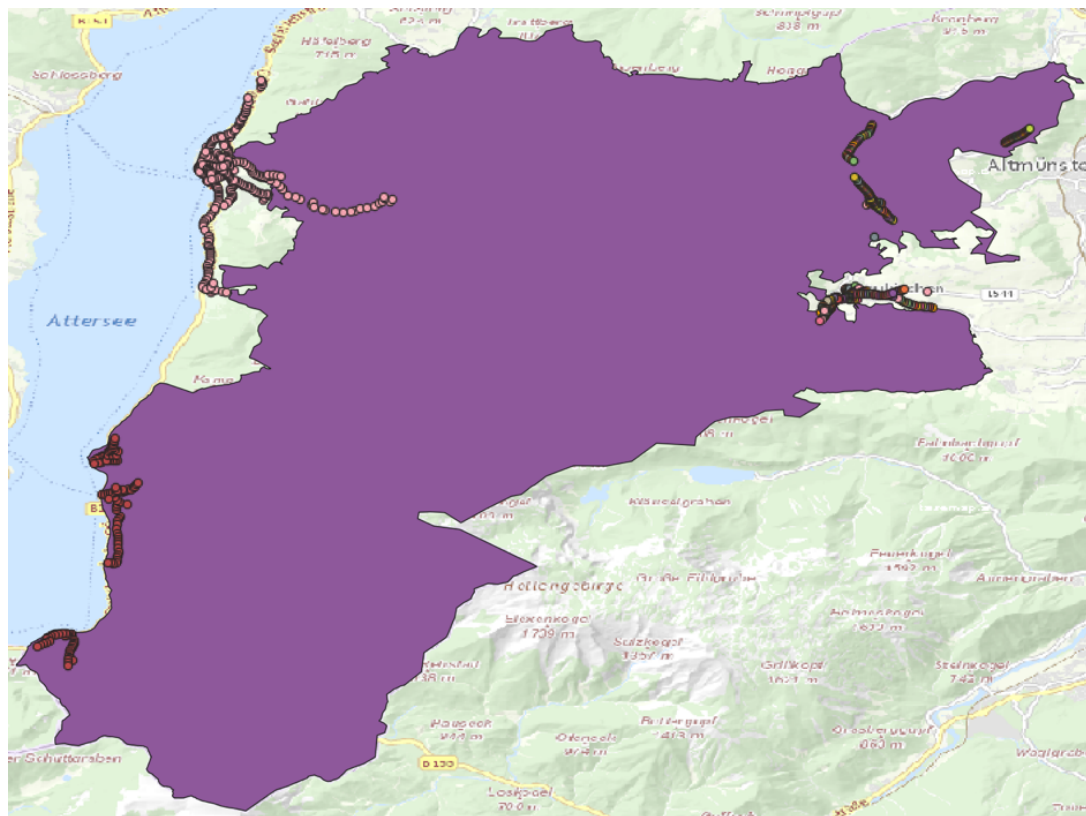


Figure 51 – Locations of all public streetlight sources in the area of the Nature Park Attersee-Traunsee.

The lamp counting carried out by AKUN Lichttechnik gave the following result for the area:

- **Steinbach am Attersee**
 existing lighting fixtures: 7x 1850 K LED (all full-cutoff), 97x 3000 K LED (all full-cutoff)
 compliant with LMP: 100%
 not compliant with LMP: 0%
 advertising and building illumination sources are available and need to be quantified
- **Weyregg**
 existing lighting fixtures: 36x 4000 K LED
 compliant with LMP: 0%
 not compliant with LMP: 100%
 advertising and building illumination sources are not available

- **Altmünster**

existing lighting fixtures: 53x 3000 LED, 38x 4000 K LED, 16x 4100 K LED

compliant with LMP: 49.53%

not compliant with LMP: 50.47%

advertising and building illumination sources are not available

With the decision of all available luminaires of the municipality Weyregg being changed to 3000 K LEDs, brings the percentage of luminaires that follow the LMP in total to 78.14%.

Reprint Permissions

I have tried to find all copyright holders of the image used and have obtained their consent to the use of the images in this work. Should a copyright infringement become known, I would like to be contacted.

I would like to thank the Oxford University Press and Elsevier for granting the reuse of all published papers in this thesis.

Curriculum Vitæ

Personal Details

Name Stefan Wallner, BSc MSc
 Date of Birth 26.08.1993
 Office adress Türkenschanzstrasse 17, 1180 Wien, Austria
 Mail stefan.wallner@univie.ac.at
 Phone +43 1 4277 53841 (Office)
 Marital status married, 2 children
 Website <https://ufind.univie.ac.at/en/person.html?id=58126>

Work Experience

01/2019 – today **Principal Investigator**, *Department of Astrophysics Vienna*.
 "Scientific survey for the establishment of official Dark Sky Places certified by the International Dark Sky Association in Upper Austria and Environmentally Friendly Lighting of Cultural and Natural Monuments"
 07/2019 – 12/2019 **Freelancer**, *Department of Astrophysics Vienna*.
 Responsible for all public outreach activities
 10/2018 – today **Freelancer**, *Event Management University of Vienna*.
 Coordination of the mobile planetarium and school visits
 07/2018 – 12/2018 **Research Assistant**, *Department of Astrophysics Vienna*.
 "Data Analysis of Light Pollution Monitoring Network in Upper Austria"
 05/2018 – today **Research Assistant**, *Institute of Construction and Architecture, Slovak Academy of Sciences, Bratislava*.
 Research field: Theoretical modelling and atmospherical effects of light pollution
 11/2017 – 08/2018 **Project Coordinator**, *Department of Astrophysics Vienna*.
 "Astronomy To Go" - Public outreach program with a portable planetarium visiting schools
 11/2016 – 11/2018 **Planetarium Operator**, *Natural History Museum Vienna*.
 09/2016 – today **Lecturer**, *University of Vienna*.
 05/2017 – 07/2017 **Project Staff**, *Department of Astrophysics Vienna*.
 "Long term measurements of the night sky brightness and possibilities for night sky protection areas in Upper Austria"
 12/2015 – 05/2017 **Student Assistant**, *Department of Astrophysics Vienna*.
 Responsible for public outreach
 03/2015 – 10/2016 **Freelancer**, *Planetarium and Public Observatories Vienna (VHS Wien)*.
 Responsible for tours and shows
 11/2014 – 06/2015 **Freelancer**, *Department of Astrophysics Vienna*.
 Responsible for public outreach programs (e.g. tours, school visits, talks)

Education

- 10/2015 – 09/2017 **Master's degree programme Astronomy**, *University of Vienna, successfully completed in September 2017.*
- 10/2011 – 09/2015 **Bachelor's degree programme Astronomy**, *University of Vienna, successfully completed in September 2015.*
- 09/2003 – 06/2011 **Gymnasium, Diözese Eisenstadt**, *Leaving certificate: Matura.*

Skills

- Languages German (native language)
English (C1)
Italian (A2)
Norwegian (A1)
- IT-Competences Microsoft Office
Mac, Windows, Linux
Typo3

Grants/Scholarships

- 2018 **Performance Scholarship**, *University of Vienna.*
- 2017 **Grant for the completion of my master's thesis**, *University of Vienna.*

Activities/Engagement

- Since 09/2018 Dark Sky Ambassador by the International Astronomical Union
- Since 09/2018 Executive board member of the Austrian Society for Astronomy and Astrophysics
- 08/2018 LOC-Member of the IAU General Assembly 2018 in Vienna
- Since 01/2018 Coordinator for public outreach and executive board member of the "Burgenländische Amateur Astronomen" (Amateur Astronomers of Burgenland)

Summary

Summary This thesis investigates various approaches in measuring and modelling of the global phenomenon of light pollution, artificial light at night which is misdirected, over-illuminated and/or makes use of harmful light. The ever-worsening phenomenon impairs not only the visibility of objects on the night sky, furthermore it is a major threat for all living beings worldwide, including human health suffering from impacts. By illustrating the fundamentals of lighting engineering, measurement techniques and theoretical model simulations, this dissertation aims to help understand the issue and provides studies presenting new ways of characterising light pollution. In summary, the thesis presented considers the quantification of light pollution from two angles, on the one hand by measurement approaches with especially ground-based observations being highlighted, on the other hand by computational modelling concepts. Both constitute basic needs when studying the issue, particularly to enable the recognition and prediction of its future development. It has been shown that measuring and modelling are contemplative aspects providing different strengths with the possibility of either individual application or an opportunity of fusion to receive optimal results. Overall, the aim of this dissertation was to refine current methods in theoretical modelling of skyglow, to find new ways in how to measure and analyse light pollution and to come solutions of the most pressing problems a step nearer. Results shall be of great value for the interdisciplinary research in the future as they give impulses in the way skyglow is observed and analysed.

Zusammenfassung Die Arbeit untersucht die Ansätze von Messtechniken sowie Möglichkeiten der Modellierung von Lichtverschmutzung, ein globales Phänomen, welches durch falsch gerichtetes, zu stark beleuchtendes oder schädliches, künstliches Licht bei Nacht verursacht wird. Das zunehmende Problem verursacht in der Astronomie, dass Himmelsobjekte nicht mehr sichtbar sind, ob für menschliches Auge oder Teleskop. Darüber hinaus ist es aber eine ernstzunehmende Gefahr für sämtliche Lebewesen auf der Erde, die menschliche Gesundheit inkludiert. Durch das Aufzeigen der Grundlagen der Lichttechnik, Messmethoden sowie theoretischen Modellsimulationen, möchte diese Dissertation die Thematik näherbringen sowie Studien präsentieren, die neue Wege aufzeigen, wie Lichtverschmutzung charakterisiert werden kann. Die Arbeit beleuchtet das Phänomen aus zwei Winkeln, einerseits durch unterschiedliche Messmethoden, besonders durch bodengebundene Instrumentarien, andererseits durch Modellierungen. Beide stellen fundamentale Notwendigkeiten bei der Behandlung der Thematik dar, besitzen sie doch unterschiedliche Stärken die entweder individuell einsetzbar sind oder fusioniert werden können um optimale Ergebnisse zu erhalten. Das Ziel der Dissertation war es zurzeit genutzte Modelle zu verbessern um Entwicklungen noch deutlicher vorhersagen zu können, neue Wege bei der Messung und Analyse von Lichtverschmutzung zu gehen sowie auf die aktuellsten Forschungsfragen einzugehen. Die Ergebnisse sollen wertvoll für die weitere, interdisziplinäre Arbeit in diesem Forschungsfeld sein und neue Impulse bei der Betrachtung der Thematik aufzeigen.